Hyaluronic Acid Vehicles for Cell Targeting

A thesis submitted to

The University of Manchester

for the degree of

Doctor of Philosophy (PhD)

in the Faculty of

Biology, Medicine and Health

2017

Julio Manuel Rios de la Rosa

NorthWest Nanoscience (NoWNANO) Doctoral Training Centre

School of Health Sciences

Contents

Word Count: 66,809

List of Figures

List of Schemes

List of Tables

Abstract

This thesis discusses the use of hyaluronic acid (HA) drug delivery vehicles as potential targeted therapies for cancer and inflammatory disease. We focus on the molecular design and processing of HA materials driven by the overexpression of its main endocytic receptor, CD44, in most solid tumors and the inflamed milieu. In particular, we have an interest in hijacking the natural mechanism of CD44-mediated HA endocytosis to deliver active pharmaceutical ingredients; however, CD44 has been described as "a molecule with a thousand faces" and the design of targeted strategies requires a solid understanding of its intricate cellular processing. As such, a comprehensive review is covered in **Chapter 1**.

Within the framework of CD44-targeted delivery, our group has previously developed a nucleic acid delivery platform based on HA-exposing chitosan nanoparticles prepared by ionotropic gelation. In **Chapter 2** we explored a simplified preparative method yielding nanoparticles with virtually identical physico-chemical properties and delivery capabilities. This procedure considerably improves the manufacturing process in terms of timing and risks. Additionally, it avoids loss of the nucleic acid payload, guarantees sterility and improves reproducibility and scalability. Further evaluation of these particles was carried out in **Chapter 3**, where we looked at the complex relationship between THP-1 macrophage polarization and the uptake of HA materials. We demonstrated that, paradoxically, a higher CD44 expression (M1 - classical activation) allows a more efficient capture of HA carriers, but a lower expression (M2 - alternative activation) is conducive to better internalization.

In **Chapter 4** we moved on to evaluate the transfection efficiency effects of chitosan macromolecular parameters by producing a library of nanoparticles that differed both in RNA binding strength (avidity) and in their internalization rate in HCT-116. Interestingly, we showed that the increase in chitosan molecular weight was detrimental for RNA release, had a complex influence on internalization rate, but proved a very positive factor for transfection efficiency. We ascribe this to an improved RNA protection and enhanced endosomolytic activity. The targeting behavior of the best performing formulations was finally assessed in **Chapter 5**, which explores feasibility of using chitosan/HA nanoparticles to preferentially deliver a siRNA payload into cancer cells (over normal cells). We found that CD44 expression correlated with nanoparticle internalization and silencing efficiency, overall higher in cancer cell lines; however, we depicted a remarkable lack of correlation in HT-29 colorectal cancer cells despite their high CD44 expression. We believe the puzzling behavior of this cell line is a wake-up call for researchers in the field to stress the role of the activation state and internalization capabilities of CD44 and of its variant isoforms rather than predicting the success of targeted drug delivery based on the overexpression of HA receptors alone.

Declaration

No portion of the work referred to in the thesis has been submitted in support of an application for another degree or qualification of this or any other university or other institute of learning.

Copyright statement

Dedication

I wish to dedicate this thesis to David, one of my closest and dearest friends unfortunately no longer with us. He passed away at the age of 23 after suffering with lung adenocarcinoma for several months, showing unprecedented courage during his treatment and keeping his ubiquitous smile and sense of humor until the very end. David was not like other people that I have met before; he was a humble, supportive, and determined guy whom with I shared over 18 years of laugher and fun, uncountable adventures, and a passion for videogames and technology. I will try my best to never forget your way of enjoying the simple things in life. Wherever you are, I hope you are proud of me and that this one tiny grain of sand that is my research might contribute somehow to the understanding and treatment of cancer in the future.

Acknowledgements

We say in Spain that “being thankful is a well-born people’s gift”. I believe this saying acquires high relevance in the context of a doctoral thesis, which requires our evolution as know-it-all (wannabe) independent scientists, but importantly as human beings. In the following lines, I have tried my best to publicly acknowledge everyone who has had an impact on my professional and personal life, leading me to where I stand today.

First and foremost, I owe everything to my parents, Julio and Rosa, for their love and unconditional support over the past 27 years including this challenging period of my professional life. I cannot thank them enough for all the sacrifices and struggles they have gone through, and I will be eternally grateful to them for putting my happiness before theirs. I also would like to thank my little brother Juan for the shared time since we were but kids. I would like to thank the rest of my family for what I consider a privileged childhood with memories that I will always cherish, and for all those big meals still taking place every now and then that help me disconnect and feel at home. Last, I am extremely thankful to my partner, Michael, for being by my side over the past three years. You are the kindest and most patient person I know, putting up with my stubbornness and supporting me through difficult times and big changes in my life. Thank you for encouraging me to keep working harder and moving forward. I feel fortunate to have you in my life and I hope this is just a *nano*-glimpse of the many adventures yet to live together, be it in Brexit island or our next destination.

For enlightening my mind and for their continuous support through my entire PhD, I have my supervisory team to thank: Prof. Nicola Tirelli, Dr. Annalisa Tirella, and Professor Ian J. Stratford. In particular, I would like to mention my supervisor Nicola for granting me the opportunity to develop this research project and so kindly hosting me in his group. Special mention also to my co-supervisor Annalisa, who gave me the freedom to make my own mistakes. Thank you for all the shared trips, conferences/meetings, coffee breaks (under the sun or even better complaining about the rain), and endless afternoons of formatting.

My most sincere thanks to all my colleagues and friends from The University of Manchester for providing invaluable help with many aspects of my research, for adding up to my own personal life and, most importantly, for making my time in Stopford Building so enjoyable! A big thank you to Maria (Pelliccia), Enrique, Alice, Roberto, Arianna, Richard, Jason, Wia,

Yusef, Charlotte, Will, Artal, and Irene. I am truly grateful for the support, amusement, and friendship. Also thanks to my flat mate Mario for all stuff geeky and for uncountable RuPaul episodes, lip-synch videos, and Wasabi dinners. It is only fair to also highlight the support from my NoWNANO friends who so kindly welcomed me to the UK about four years ago: Josh for your banter and 'essential' English lessons, Tom for sharing your 'boring' conversations and winning us pub quizzes, Daryl for living up to the drunken Irish stereotype, and Tommy C for being such a genuine and charismatic guy.

A big thank you goes to Dr. Stefano Pluchino from the University of Cambridge for hosting me in his lab earlier this year, as well as to all the welcoming and hard-working people in his group who made me enjoy of a short but unforgettable experience. In particular, I would like to thank my 'office mate' Bea for being such a sweetheart, Sara for those conversations over lunch or coffee, and of course Giulia for all her patience and help with my project in a very busy time of her studies. The special mention here goes to Maria Frias, whom I had the pleasure to meet back during my undergrads in Seville – I am really glad life brought us together once more and we got to share so many moments in this lovely English city.

Through the years I have been truly blessed with great friends who have been there through the good, but most remarkably the bad times. Starting with my life-long friends from Algeciras who have the pleasure (or curse) to know me far too well: Pao, Eze, Alvaro, Fati, Carmen, Vane, Eu, Fran. No words can express how fortunate I feel for having shared so many memories and moments with you all; this kind of friendship can only grow stronger with time. Moving on to A levels, I cannot help but mentioning Sergio and Maria for being a real support for me during those two years of transition from high school to university, intercalating long study hours with so many memorable moments, and Mª Angustias, who always believed in me and convinced me to become a biotechnologist – you got it all right from the very beginning, thank you very much for everything you have done for me. Bringing about university means mentioning more extraordinary people I had the pleasure to bump into during my 5-year stay in Seville. To all my *palmerienses*: Jesus, Sandra, Marta, Victor, Gemma and Patricia, a big thank you for all the joy you brought to my student life outside the classrooms; I hope we can manage to sort out that big reunion soon. In particular, thank you Jesus for being my closest friend. Thank you for all stuff silly and non-sense, for the music, for the trips, for your WhatsApp texts, for your calls. You are the real definition of a friend. And to my beloved biotechnologists whom with I spent practically all my hours in Seville,

mostly among lectures, lab, and AsBAn/FEBiotec. A huge thank you to my close circle of non-expendable scientists (sorry Paco for choosing this umbrella term): Marina, Tamara, Luis, Maria Jose, Cris, Sofi, Alvaro, Paco, Paula, and Dani. I could not have asked for better colleagues and friends – my memory cannot possibly cope with such array of wonderful memories, trips (I will never embark on a bus journey Seville-Barcelona ever again unless it is with you all guys), nerves before and after exams (to be frank I do not miss this at all), gossip, finding new places to end up eating far too much, 'enthralling' study sessions, and sing-alongs (Marina gets special acknowledgment here).

Last but not least, this work would not have been possible without the support of EPSRC in the form of a PhD studentship as part of the NoWNANO Doctoral Training Centre (EPSRC grant EP/G03737X/1). I would also like to thank AstraZeneca for the establishment of the NorthWest Centre for Advanced Drug Delivery, to the Bioimaging and Flow Cytometry Research Facilities at the University of Manchester, and to the Spanish Association of Researchers in the UK (SRUK) for the award of a travel grant.

Manuscript Organization and Author's Contribution

According to the current thesis policy at the University of Manchester, this thesis is presented in Journal Format. The main chapters stem from the articles listed below and the author's contribution to each individual chapter is made explicitly clear.

Chapter 1. Lost in Post-translation, Post-transcription and Other Identity Problems Affecting CD44 Targeting Through Hyaluronic Acid. Julio M. Rios de la Rosa, Annalisa Tirella, and Nicola Tirelli. *Manuscript in preparation.*

All the work was fully contributed by Julio. Nicola and Annalisa co-contributed to corrections to manuscript.

Chapter 2. Chitosan/HA Nanoparticles: What We Know and Don't. Julio M. Rios de la Rosa, Arianna Gennari, Maria Pelliccia, Enrique Lallana, Roberto Donno, Erwin Hohn, Annalisa Tirella, and Nicola Tirelli. *Manuscript in preparation.*

Julio contributed to the design and execution of all experiments with the exception of A4F analysis in Figure 2—3 and stability studies in Figure 2—7, which were fully contributed by Arianna and Erwin. Maria performed the fluorescent labelling of chitosan; Roberto helped with AFM experiments in Figure 2—2 and 2—8; Enrique and Annalisa contributed to RNA nanoparticle protection studies in Figure 2—9. Julio wrote the manuscript and Nicola co-contributed to corrections.

Chapter 3. The CD44-Mediated Uptake of Hyaluronic Acid-Based Carriers in Macrophages. Julio M. Rios de la Rosa, Annalisa Tirella, Arianna Gennari, Ian J. Stratford, and Nicola Tirelli. *Adv. Healthcare Mater*, 2017, 6, 1601012.

Julio performed all experimental parts of this study. Annalisa assisted with confocal microscopy acquisition in Figures 3—1, 3—3 and 3—4; Arianna prepared both high and low molecular weight chitosan used in the nanoparticle preparation. Julio wrote the manuscript, with Ian and Nicola co-contributing to the corrections to manuscript.

Chapter 4. Chitosan/Hyaluronic Acid Nanoparticles: Rational Design Revisited for RNA Delivery. Enrique Lallana[†], Julio M. Rios de la Rosa[†], Annalisa Tirella, Maria Pelliccia, Arianna Gennari, Ian J. Stratford, Sanyogitta Puri, Marianne Ashford, and Nicola Tirelli. *Mol.*

Pharmaceutics, 2017, 14 (7), pp 2422-2436. † Equal contribution.

Enrique and Julio contributed equally to the design and execution of all experimental parts of the study, as well as the elaboration of the manuscript. Annalisa was responsible for the acquisition of confocal microscopy pictures in Figure 4—6; Maria assisted with the amplification of Luciferase-encoding pDNA; Arianna contributed the preparation of chitosans (H84 and L84). Ian, Sanyogitta, Marianne, and Nicola co-contributed to corrections to manuscript.

Chapter 5. Target Specificity of Chitosan/HA Nanoparticles for siRNA Therapeutics: *An In Vitro* Study. Julio M. Rios de la Rosa, Annalisa Tirella, Alice Spadea, Maria Pelliccia, Ponpawee Pingrajai, Enrique Lallana, Arianna Gennari, Ian J. Stratford, and Nicola Tirelli. *Manuscript in preparation.*

Julio performed all experimental parts and wrote the manuscript. Maria carried out routinely maintenance of HUVEC and experiments related to these cells; Alice performed the CD44pan Western blotting at different exposure times in Figure 5—6; Annalisa assisted with confocal microscopy acquisition in Figure 5—1; Ponpawee contributed to the experimental reproduction of silencing experiments in Figure 5—5. Original training in chemistry lab, advice and guidance during the course of Julio's PhD was provided by Enrique and Arianna. Annalisa, Ian, and Nicola co-contributed to the corrections.

With the purpose of exposing the reader to a full breath of the work conducted within the framework of the NoWCADD, an additional chapter is included as annex:

Chapter 6. Nanomanufacturing through Microfluidic-Assisted Nanoprecipitation: Advanced Analytics and Structure-Activity Relationships. Roberto Donno, Arianna Gennari, Enrique Lallana, Julio M. Rios De La Rosa, Richard d'Arcy, Kevin Treacher, Kathryn Hill, Marianne Ashford, and Nicola Tirelli. *Manuscript accepted.*

Julio contributed cellular experiments in section 6.3.4. and Figures 6—8 and 6—12. Julio contributed ~5% to the final text.

Thesis Introduction

State of the Art Short Review

Cancer is a complex disease posing serious threat across the globe. Conventional chemotherapeutics have provided an effective means of tackling different types of cancer, in particular at early stage. Yet conventional therapies face a plethora of challenges such as poor patient acceptance and compliance, cancer drug resistance, lack of cell targeting ability, and numerous side effects. Inspired by Paul Ehrlich's vision of the magic bullet, scientists have devised novel strategies to target the specific molecular defects of cancer, aiming to overcome chemotherapy limitations [1]. The substantial development in nucleic acid therapeutics offers unprecedented opportunities for personalized cancer treatment; for example, the use of small interfering RNA (siRNA) can inhibit specific cellular pathways associated with tumor growth and metastasis. The potential of nucleic acid therapies is reflected in the more than 100 cancer clinical trials reported for RNA therapeutics alone (as of 2016) [2]. However, their success is still to come and is often hindered by the lack of efficient delivery strategies into diseased cells, immunogenicity, and optimization of target/off-target ratios [3].

Nanocarriers have been evolved as effective platforms for the controlled and selective delivery of nucleic acids in cancer therapy [4], with a recent emphasis on RNA payloads [5]. Special attention has been paid to nanoparticles made of (natural or synthetic) biocompatible and biodegradable polymers with inherent targeting capabilities. In this regard, the naturally occurring hyaluronic acid (HA; primary ligand for the cell surface receptor CD44) has become a popular choice for the targeted delivery of anticancer therapeutics into CD44-expressing cancer cells, as evidenced by the high number of publications on the delivery of cytostatic drugs or nucleic acids in the last few years (~150 papers in 2015 according to a recent review by Ana Cadete and María José Alonso [6]). In this review the authors have identified 18 HA-based nanocarriers designed for the delivery of cytotoxic drugs (mainly paclitaxel, docetaxel, or doxorubicin) which have returned positive pre-clinical, *in vivo* data; the number drops to 6 for those engineered for the delivery of small size nucleic acids (either miRNA or siRNA). Although no HA-based nanomedicine has yet moved from bench to bedside, two promising candidates are currently undergoing evaluation in clinical trials: ONCOFID™-P a paclitaxel-HA conjugate developed by Fidia Farmaceutici for the intravesical treatment of bladder cancer, in Phase II (EudraCT Number: 2009-012274-13, www.clinicaltrialregister.eu), and FOLF(HA)iri, a 'gel-like' system developed by Alchemia

Oncology for the delivery of irinotecan against metastatic colorectal cancer, in Phase III (NCT Number: NCT01290783, https://clinicaltrials.gov). Of note, one needs to bear in mind that the clinical translatability and success of current and future HA-based nanomedicine candidates proves especially challenging due to the still limited knowledge about the effects of these carriers in a complex biological scenario: systemic (e.g. off-target interactions, binding to HA receptors ubiquitously expressed in healthy cells), tissue (e.g. HA capture by soluble/vesicular CD44), and cellular (e.g. CD44 avidity/affinity, unclear link between CD44/HA binding and internalization).

References

[1] K. Strebhardt, A. Ullrich, Paul Ehrlich's magic bullet concept: 100 years of progress, Nat Rev Cancer 8(6) (2008) 473-80.

[2] P. Barata, A.K. Sood, D.S. Hong, RNA-targeted therapeutics in cancer clinical trials: Current status and future directions, Cancer Treat Rev 50 (2016) 35-47.

[3] F. McCormick, Cancer gene therapy: fringe or cutting edge?, Nat Rev Cancer 1(2) (2001) 130-41.

[4] A.R. Kirtane, J. Panyam, Polymer nanoparticles: Weighing up gene delivery, Nat Nanotechnol 8(11) (2013) 805-6.

[5] M.S. Singh, D. Peer, RNA nanomedicines: the next generation drugs?, Curr Opin Biotechnol 39 (2016) 28-34.

[6] A. Cadete, M.J. Alonso, Targeting cancer with hyaluronic acid-based nanocarriers: recent advances and translational perspectives, Nanomedicine 11(17) (2016) 2341-57.

Thesis Summary

The Laboratory of Polymers and Biomaterials led by Professor Nicola Tirelli is a multidisciplinary research group devoted to improving current treatments for cancer and inflammatory disease. The activity of the group encompasses polymer chemistry, nanomaterials, drug delivery, and regenerative medicine. Within this framework our group has developed an interest in the use of HA-based systems for the targeted delivery of active pharmaceutical principles to tumors. The great potential of HA as a component of drug delivery vehicles stems from its advantageous physico-chemical features including (1) its high hydrophilicity, which translates into an improved bioavailability, (2) its anionic character, which permits electrostatic interactions with cationic species (e.g. polymers or drugs) and

prevents binding of plasma proteins such as albumin, and (3) its excellent biocompatibility and immunotolerance. These favorable features are complemented by a promising therapeutic opportunity: CD44, the main endocytic surface receptor of HA, is overexpressed in malignant cells with key roles in tumorigenesis and metastasis. One of the most ambitious targeting strategies envisages the preferential delivery of drugs by hijacking the tumor's CD44-mediated mechanism of HA endocytosis. However, the almost ubiquitous expression of CD44 in healthy tissue has cast doubt on feasibility of such targeting strategies; their success would actually require further understanding of the target itself, i.e. how to exploit the differences in the expression and endocytic activity of CD44 between cancer and normal cells. Fittingly, a comprehensive overview of the biological complexity of CD44, its cellular processing, and relevant considerations for the targeting of active pharmaceutical principles to CD44-(over)expressing cells is covered in **Chapter 1**. Here we presented first a thorough background on the gene organization and protein structure of this receptor, discussing the main structural and functional differences between CD44 standard (CD44s) and variant (CD44v) isoforms to then map their differential expression in health and disease. We then went on to list the effects of CD44s/CD44v post-translational modifications on HA uptake (binding and internalization). Ultimately, we commented on the design of targeted strategies applicable to HA-based materials.

In the context of this thesis, we intend to target two features of solid tumors (one physical, the other biochemical) associated with aggressive phenotypes. With regard to physical parameters, human solid tumors are generally characterized by drastic modifications in the interstitial pH due to the pathological expression of a variety of enzymes; we are interested in exploiting this feature to maximize the efficacy of treatment. On the other hand, the widely reported overexpression of CD44 in most solid tumors seems appealing for the preferential targeting of therapeutics into cancer cells. Therefore, the aim of this thesis is to design HA-based drug delivery vehicles with an optimal performance in the tumoral environment (i.e. at slightly acidic pH) and to evaluate their suitability to deliver RNA therapeutics in a CD44-mediated fashion. These carriers can lay the basis for novel anticancer treatments that surpass the limitations of conventional therapy.

To that end, our group has previously developed an HA-based nanoparticle platform for potential use in gene delivery. These nanoparticles display a chitosan bulk cross-linked with TPP (ionotropic gelation) and a surface where HA concentrates, thus providing the means to

target HA receptors such as CD44, while creating a surface with a protein-repellent character. One of the main highlights of this research was the rationalization of the effect of chitosan $\bar{M}_v$ on the morphology of template chitosan-TPP nanoparticles and consequently on HA adsorption, which in turn influenced HA presentation to cell surface receptors and the uptake of these materials. Ionotropic gelation thus proves a robust method for nanoparticle preparation, although not without inconvenience. For example, it involves two dialysis purification steps (one to remove the acetate buffer used in the preparation of template particles, the second to remove the unbound excess HA) that may compromise the physico-chemical characteristics, cargo loading/protection, and sterility of the final formulation. For the sake of simplicity and experimental reproducibility, it would be more suitable to use a simpler preparative method that reduces the number of user-dependent operations and improves the clinical translatability of this platform. In **Chapter 2** we described a simplified approach to the sterile preparation of these particles based on the direct polyelectrolyte complexation of chitosan with HA (and RNA) that considerably minimizes handling of the formulation. Special attention was given to comparing the performance of ionotropic gelation and direct complexation particles. We found no significant effect of the preparative method on the physico-chemical properties or biological behavior of these nanoparticles; in fact, we demonstrated virtually identical siRNA delivery capabilities using two different CD44-expressing cell models. We also depicted an identical HA presentation for low and high $\bar{M}_v$ chitosan particles prepared by direct complexation, as opposed to those prepared by ionotropic gelation. Interestingly, we showed that the HA presentation did not play a major role in the uptake of these carriers, but this was heavily dependent on the cell type; we ascribe this to a different CD44 clustering and/or additional cell-specific factors, such as the contribution of other internalization pathways.

Chapter 3 sees a continuation towards the use of chitosan/HA nanoparticles prepared by direct polyelectrolyte complexation as targeted carriers for siRNA delivery. One of the main concerns for the use of these carriers in a tumor environment, however, is the ubiquitous expression of CD44 in the body, in particular by phagocytic cells such as tissue resident macrophages. These sentinel cells could theoretically compete with cancer cells for the uptake of HA-based materials. Many research groups have consequently focused efforts to study macrophage CD44 functionality, yet using murine cellular models. We believe the human translatability of such models is questionable due to remarkable differences not only in their resting phenotype (M0), but importantly in their classical (M1) and alternative (M2)

activation. Therefore, the use of a more physiologically relevant human model should be sought after in order to predict the likelihood of macrophages acting as off-target destination for a CD44-targeted therapy. Accordingly, we validated a robust human macrophage *in vitro* model to first study the relationship between macrophage polarization and CD44 expression. We demonstrated that the expression of CD44 is polarization-dependent and that the overall protein amount scaled as M1 > M0 ≥ M2. In addition, we reported the expression of the commonly tumor-associated CD44v6 in M2 macrophages. We suggest this variant isoform can be used for targeting this macrophage subpopulation, which is believed to promote cancer initiation and progression. We then focused our attention on the interaction of differently-polarized macrophages towards HA, both in its soluble and nanoparticulate form. A similar trend in the uptake of HA, analyzed via fluorimetry on cell lysates, spanning both membrane bound and internalized materials, was found: the higher the CD44 expression, the higher the capture of HA. In shocking contrast, the internalization of HA materials, analyzed on live cells after trypsinization (flow cytometry), which readily removes membrane bound HA, appeared to follow an inverse order (M1 < M0 < M2). We ascribe this effect to a slower/more difficult internalization of HA. This seemingly erratic behavior suggests that the common paradigm "higher CD44 expression = higher targetability" may be quite simplistic and needs to be considered in a cell-specific manner.

Chapter 4 aims to optimize chitosan/HA nanoparticles as tumor-targeting carriers for RNA delivery. In this instance, we aimed to link the macromolecular variables of chitosan ($\overline{M}_v$ and DD) with those of chitosan/HA nanoparticles (complexation strength, cargo protection, and cellular uptake) upon loading with two differently-sized RNA payloads (a 21bp siRNA or a ≈2000bp mRNA). In particular, we focused on the role of avidity on the transfection efficiency of CD44-overexpressing HCT-116 colorectal cancer cells. The RNA avidity for chitosan showed an expected inverse relationship: the higher the avidity, the higher the polyplex stability and the lower the transfection efficiency. Unexpectedly, the avidity of chitosan for RNA led to opposite effects: the higher the avidity, the higher the stability and transfection efficiency. Our results reveal that the performance of chitosan/HA nanoparticles cannot be simply predicted on the basis of the carrier characteristics or its payload, but instead additional factors need to be considered; for instance, the cellular uptake and the cytoplasmic bioavailability of the RNA payload after endosomal escape (which cannot be predicted *a priori*). Another important finding was the optimal performance of these carriers at pH 6.4, which suggests their suitability for applications in the tumoral microenvironment. Noteworthy,

we have for the first time described the delivery of mRNA using chitosan/HA nanoparticles under these conditions.

The interesting yet puzzling results seen in THP-1 macrophages raise concerns about the targeting behavior of HA-based vehicles in a tumor scenario. In fact, the success of a targeted therapy is often predicted on the basis of a differential CD44 expression between cancer and stromal cells, which is determined by mere protein analysis (Western blotting, flow cytometry, and immunohistochemistry). However, this view generally omits the functional state of CD44 receptors (i.e. their binding and internalization capabilities) across cell types. We could benefit from knowing more about the interactions of cancer cells and stromal cells with HA materials because it would hint at how to precisely tailor these materials in order to preferentially deliver a RNA payload into cancer cells. To that end, in **Chapter 5** we first selected a number of colorectal (HT-29, HCT-116) and pancreatic (PANC-1, AsPC-1) cancer cell lines commonly used in literature for the evaluation of HA-based delivery systems, as well as widely accepted macrophage (THP-1) and stromal cell models, namely fibroblasts (HDF) and endothelial cells (HUVEC). We then moved on to evaluate the CD44 fingerprint across these cell types. We depicted a very high CD44 expression in colorectal cancer cells, a moderate expression in pancreatic ones, comparable to that of fibroblasts and endothelial cells, and a low expression in macrophages. Noticeably, colorectal cancer cells but not pancreatic ones showed a preferential overexpression of CD44v. We then cross-correlated CD44 expression with the different phases of uptake (binding and internalization) of chitosan/HA nanoparticles (at pH 6.4) evidencing a preferential internalization and gene silencing in cancer cells, especially in the widely used metastatic models HCT-116 (high CD44v expression) and AsPC-1 (moderate CD44s expression). We also identified fibroblasts as the most likely off-target destination for these particles. Importantly, we found a totally unexpected behavior for the highest CD44-expressing cell line, HT-29, which showed reduced nanoparticle binding and internalization. Overall, these results revealed that both CD44 expression and HA uptake are cell dependent, and that the internalization state of CD44 could in fact prevail over its actual amounts on cell surface. We believe this finding stresses the need for CD44 activation screening prior to treatment, rather than assuming a positive therapeutic outcome based solely on the amounts of receptor expressed in target cells.

List of Abbreviations

A4F	Asymmetric Flow Field Flow Fractionation
AF	Alexa Fluor
AFM	Atomic Force Microscopy
AGO	Argonaute protein
APC	Allophycocyanin
AR	Androgen receptor
AREs	Adenylate/Uridylate-rich elements
ASPP	Apoptosis-stimulating of p53 protein
ATCC	American Tissue Cell Culture
$B(X_7)B$	HA-binding motif (B = basic residue, X = any non-acidic residue)
BaP	Benzo(a)pyrene
BCA	Bicinchoninic acid
bFGF	Basic fibroblast growth factor
bp	Base pair
BSA	Bovine serum albumin
CAMK	Ca^{2+}/calmodulin-dependent protein kinase
CD	Cluster of differentiation
CD44-st	Cluster of differentiation 44, tail-less isoform
CD44RC	Cluster of differentiation 44, alternatively spliced soluble
CD44s	Cluster of differentiation 44, standard isoform
CD44sol	Cluster of differentiation 44, soluble
CD44v	Cluster of differentiation 44, variant Isoform
cm^2	centimeter square
CnS	Chondroitin sulfate
COL	Collagen
CS	Chitosan
CSC	Cancer stem cell
CTF	C-terminal fragment
Cy	Cyanine
D	Fractal dimension
DAPI	4',6-diamino-2-fenilindol

DARPP	Dopamine- and cAMP-regulated neuronal phosphoprotein
DD	Degree of deacetylation
DLS	Dynamic Light Scattering
D_m	Mass fractal dimension
DMEM	Dulbecco's Modified Eagle's medium
DMSO	Dimethyl sulfoxide
DMTMM	4-(4,6-Dimethoxy-1,3,5-triazin-2-yl)-4-methylmorpholinium chloride
DNA	Deoxyribonucleic acid
DS	Dermatan sulfate
ECM	Extracellular matrix
EDTA	Ethylenediaminetetraacetic acid
EE	Encapsulation efficiency
EGFR	Epithelial growth factor receptor
ELISA	Enzyme-linked immunosorbent assay
Em	Emission
EMT	Epithelial mesenchymal transition
ER	Estrogen receptor
ERM	Ezrin, Radixin and Moesin proteins
ESCC	Esophageal squamous cell carcinoma
ESRP	epithelial splicing regulatory protein
Ex	Excitation
FBS	Foetal bovine serum
FN	Fibronectin
g	Gram
GAG	Glycosaminoglycan
GEF	Guanine nucleotide exchange factor
GEM	Glycolipid-enriched microdomains
Glu	Glucosamine
GSH	Glutathione
GSK-3B	Glycogen synthase kinase-3β
h	Hour
HA	Hyaluronic acid
HCC	Hepatocellular carcinoma
HEPES	4-(2-hydroxyethyl)-1-piperazineethanesulfonic Acid

HGF	Hepatocyte growth factor
HIF	Hypoxia-inducible factor
^{1}HNMR	Proton nuclear magnetic resonance spectroscopy
HNSCC	Head and neck squamous cell carcinoma
HPSCC	Hypopharyngeal squamous cell carcinoma
HS	Heparan sulfate
HSPG	Heparan-sulfated proteoglycan
HUVEC	Human umbilical vein endothelial cells
IFN	Interferon
Ig	Immunoglobulin
IGF	Insulin-like growth factor
IL	Interleukin
kb	Kilobase
kDa	10^{3} Dalton
KS	Keratan sulfate
kV	10^{3} Volts
L	Liter
LAM	Laminin
LPS	Lipopolysaccharides
LS	Light scattering
LTX	Low toxicity Lipofectamine
m	Meter
M	Molar
$\overline{M}_v$	Viscosity average molecular weight
$\overline{M}_w$	Weight average molecular weight
m/v	Mass-to-volume
M0	Non-polarized macrophages
M1	Classically-polarized macrophages
M2	Alternatively-polarized macrophages
mAb	Monoclonal antibody
MALS	Multiangle light scattering
MDa	10^{10} Dalton
mg	10^{-3} gram

MHC	Major histocompatibility complex
min	Minute
miRNAs	MicroRNA
mL	10^{-3} Liter
mm	10^{-3} meter
mM	10^{-3} molar
mmol	10^{-3} moles
MMP	Matrix metalloproteinase
Mo	Premonocytes
mol	Moles
mRNA	Messenger ribonucleic acid
MTS	3-(4,5-dimethylthiazol-2-yl)-5-(3-carboxymethoxyphenyl)-2-(4-sulfophenyl)-2H-tetrazolium
mV	10^{-3} Volts
MW	Molecular weight
MWCO	Molecular weight cut-off
ng	10^{-9} gram
Nm	10^{-9} meter
nM	10^{-9} molar
nmol	10^{-9} moles
NS	Non-structural protein
NSCLC	Non-small cell lung cancer
ºC	Degree Celsius
OPN	Osteopontin
OSCC	Oral squamous cell carcinoma
OSM	Oncostatin M
PBS	Phosphate buffer saline
PCBP	Poly(rC)-binding protein
PCR	Polymerase chain reaction
PDGF	Platelet-derived growth factor
PDI	Polydispersity
PE	Phycoerythrin
PEG	Polyethylene glycol
PKC	Protein kinase C

psi	Pound force per square inch
PZD	Post-synaptic density protein
RBM	RNA-binding motif protein
R_g	Radius of gyration
R_h	Hydrodynamic radius
RHAMM	Receptor for hyaluronic acid mediated motility
RI	Refractive Index
RIPA	Radioimmunoprecipitation assay
RITC	Rhodamine B isothiocyanate
RLU	Relative luminescence units
RNA	Ribonucleic acid
ROS	Reactive oxygen species
rpm	Revolutions per minute
RPMI	Roswell Park Memorial Institute medium
RT-PCR	Retro-transcriptase polymerase chain reaction
Sam	Src-associated in mitosis
sec	Second
SGSG	Double serine-glycine motif
siRNA	Silencing RNA
SLe^x	Sialyl-LewisX
SOS	Son of sevenless
SRm	Serine/Arginine-related nuclear matrix protein
SRp	Serine/Arginine-rich protein
TGF-β1	Transforming growth factor-β1
THPA	Thanatos-associated protein
TIC	Tumor-initiating cell
TLR	Toll-like receptor
TM	Transmembrane
TNF-α	Tumor necrosis factor alpha
TPA	12-O-tetradecanoyl phorbol-13-acetate
TPP	Triphosphate
TSG-6	Tumor necrosis factor-inducible gene 6 protein
Um	10^{-6} meter
UTR	Untranslated region

UV/Vis	Ultraviolet/Visible spectroscopy
V	Volts
v/v	Volume-to-volume
VEGF	Vascular endothelial growth factor
WNT	Wingless-type MMTV integration site family
wt.	Weight
XCT	Cysteine/glutamate transporter
YB	Y Box-Binding protein
µg	10^{-6} gram
µL	10^{-6} Liter
λ	Wavelength
ρ	Aspect ratio

Chapter 1 Lost in Post-translation, Post-transcription and Other Identity Problems Affecting CD44 Targeting Through Hyaluronic Acid

*Julio M. Rios de la Rosa, Annalisa Tirella, and Nicola Tirelli**

North West Centre for Advanced Drug Delivery (NoWCADD), Division of Pharmacy & Optometry, School of Health Sciences, Faculty of Biology, Medicine and Health, Stopford building, Manchester, M13 9PT, United Kingdom

Manuscript in preparation.

* to whom correspondence should be addressed:

Prof. Nicola Tirelli
NorthWest Centre for Advanced Drug Delivery (NoWCADD)
Division of Pharmacy and Optometry School of Health Sciences
University of Manchester Manchester, M13 9PT, UK
E-mail: nicola.tirelli@manchester.ac.uk
Tel.: +44 161 275 24 80.

1.1. Abstract

The glycoprotein CD44 is the major receptor of hyaluronic acid (HA) on cell membranes. The standard isoform of CD44 (CD44s) is ubiquitously present in the human body, where it modulates a variety of cellular processes in homeostasis and in pathology (e.g. cancer, inflammatory disease). In fact, higher molecular weight variant isoforms of the receptor (CD44v) are often overexpressed in most solid tumors with key roles in tumorigenesis and metastasis. Some of these variant isoforms are also associated to cancer initiating cells (TIC) / cancer stem cells (CSC), rendering this receptor a promising target for cancer therapy. One of the most common targeting strategies consists of hijacking the receptor's natural mechanism of HA endocytosis to deliver drugs preferentially into tumors (mainly through the use of HA-exposing nanocarriers and soluble HA derivatives). Yet the general overexpression of CD44 in disease tissue does not guarantee the success of a targeted therapy. For instance, CD44 receptors can exist in an active HA binding state (as a signaling anchor), while being inactive for its internalization. The design of such therapies and control over the interactions of HA with CD44 is therefore hampered by the limited understanding of the receptor's activation state across healthy and disease tissue and its impact on the different phases of HA uptake (i.e. binding and internalization). This review exposes the reader to a full breadth of the heterogeneous CD44 protein family and the potential impact of this biological complexity on the performance of HA-based therapies. In particular, the review will elaborate on the diversity of CD44 post-translational modifications and their effect on HA binding and internalization. Finally, additional factors such as receptor clustering or the role of soluble and exosomal CD44 will be discussed from a translational perspective.

Keywords: hyaluronic acid; CD44; CD44v; alternative splicing; post-translational modifications; targeted drug delivery; exosomes.

1.2. Introduction

CD44 is a type I (extracellular N terminus) transmembrane glycoprotein, identified in the 80s as (the) lymphocyte homing receptor [1, 2]. By the end of the century a number of its molecular functions were uncovered, recognizing it primarily as a receptor both for glycosoaminoglycans (GAGs) such as hyaluronic acid (HA) [3] and chondroitin sulfate [4], and for signaling proteins such as osteopontin [5] and galectin-8 [6], although being also capable of interactions with matrix proteins (collagen [7], fibronectin [8] and laminin [9]). As part of this sensitivity to both structural and signaling components, CD44 fulfills anchoring, signaling and endocytic functions and is therefore an important mediator in the response of cells to their microenvironment [10], be it in homeostasis or in pathological processes [11].

This multi-faceted role has an intricate intracellular regulation, controlling both the level of CD44 expression and its molecular heterogeneity, which has three main origins: post-transcriptional (a number of isoforms from alternative splicing), post-translational (extensive modification, mainly with glycosides and glycosaminoglycans) and epigenetic (hypermethylation of the *cd44* promoter region regulates CD44 silencing [12-14]). Although reviewing all these sources of heterogeneity, we will predominantly focus on the post-transcriptional one in order to underline the problems complicating the quantitative interpretation of CD44's real therapeutic value [15]. While the shorter standard isoform of the receptor (CD44s, also known as hematopoietic CD44H) is virtually ubiquitously present in mammalian cells already under homeostatic conditions [10], higher molecular weight variant isoforms (CD44v) are most often overexpressed in solid tumors [16]. In particular, some of the variants are also often associated to tumor initiating cells (TIC)/ cancer stem cells (CSC), above all of hematopoietic or epithelial origin [17-19]; this has led it to be considered both a diagnostic and prognostic marker (breast, prostate, bowel, head and neck, pancreas, and colorectal cancers [18, 20-30]) and a delivery target. The therapeutic agents used for the latter scope can be divided in two groups: 1) those that hijack the natural mechanism of CD44-mediated endocytosis of HA; this is typically the case of HA-exposing nanocarriers, and side-chain-modified soluble HA derivatives, as shown in two recent reviews [31, 32]; 2) those that have a specific affinity for CD44s, a specific isoform, or all of them, e.g. monoclonal antibodies common to all isoforms, such as RG7356 [33], as much as peptides against CD44v6 [34]. The advantages of HA-based therapies over their antibody counterpart are the lower cost, the easier combination with a variety of active principles and a better (but not necessarily completely) known mechanism of binding and internalization. The antibodies are

superior in the molecular precision of the targeted action, and therefore are more suitable for the abrogation of specific signaling pathways. In this review we focus on (intracellular) delivery, and therefore our attention polarizes on the first class of systems, and on the issues that affect their use in targeted delivery.

The main hurdle can be summarized as 'know your target': CD44 has been dubbed as "a molecule with a thousand faces" [35] not only because of its multiple functions, but also due to its molecular variability. For example, even if CD44v can be considered a hallmark of cancer, some CD44v can also be produced under non-pathological conditions (e.g. CD44v6 in M2-like macrophages [36]) and in general the CD44v/CD44s expression ratio is cell- and developmental stage-dependent, therefore potentially leading to significant off-target effects. In this context, we still lack clear if not quantitative relations between the post-transcriptional but also post-translational CD44 heterogeneity on one side and its interactions with HA on the other. For instance, N-glycosylation appears to be essential for CD44 to bind HA [37], but not many studies elaborate on the receptor functional state in both healthy and diseased cellular models. Further, the accuracy of these very models can strongly depend on their CD44 match with real pathologies.

In this review, we therefore provide an overview of 1) the intracellular processes responsible for the ubiquitous or restricted expression of CD44 isoforms in health and disease; 2) the effects of CD44s/CD44v post-translational modifications on HA uptake; 3) the resulting design strategies applicable to HA-based carriers.

1.3. Molecular structure of CD44

The human forms of CD44 have a rather constant isoelectric point between pH 4.2 and 5.8, where the predominantly negative charge at physiological pH is ascribed to terminal sialic acid residues in CD44-anchored sugar chains [16, 38]. CD44 is encoded by a single gene, which is located on the short arm of chromosome 11, spans approximately 50 kb of DNA [39-42], and encompasses 20 exons (10 constant and 10 variable) and 19 introns [40, 41] (Figure 1—1A). Despite the gene being highly conserved, the actual size of the receptor is highly variable; one common cause is that the CD44 transcripts are further edited to generate e.g. CD44s (no variable exon, the isoform typical of blood cells) or CD44v (where variable exons are added typically in the stem region, in blue in Figure 1—1B), in a fashion that depends on the cell type, the stage of development, or the pathophysiological condition [1, 39, 40, 43-45]. It is worth mentioning that size is not the only parameter differentiating; for example,

turnaround time may be affected. CD44 is estimated to have a half-life of about 8 h according to Naor *et al.* [35] or, possibly more likely, in the range of 12-48 h according to experimental data on normal and malignant cell lines [46, 47]; quantitative densitometry has shown a CD44s half-life of about 48 h in normal melanocytes, which is reduced to 20 h in MV3 metastatic melanoma cells [46] (highly expressing CD44v5 and CD44v6 [48]). Experiments on clonal MCDK cell lines expressing human CD44s also reveal a reduced half-life of 5-8 h for the tail-less (lacking intracellular domain) CD44 isoform, as opposed to 16-18 h for wild-type CD44s [49].

CD44 structural parameters are summarized in Table 1—1 and analyzed in detail in section 1.3 for CD44s, and in section 1.4 for the hypervariable stem region, broadly following the review of Williams *et al.* [50].

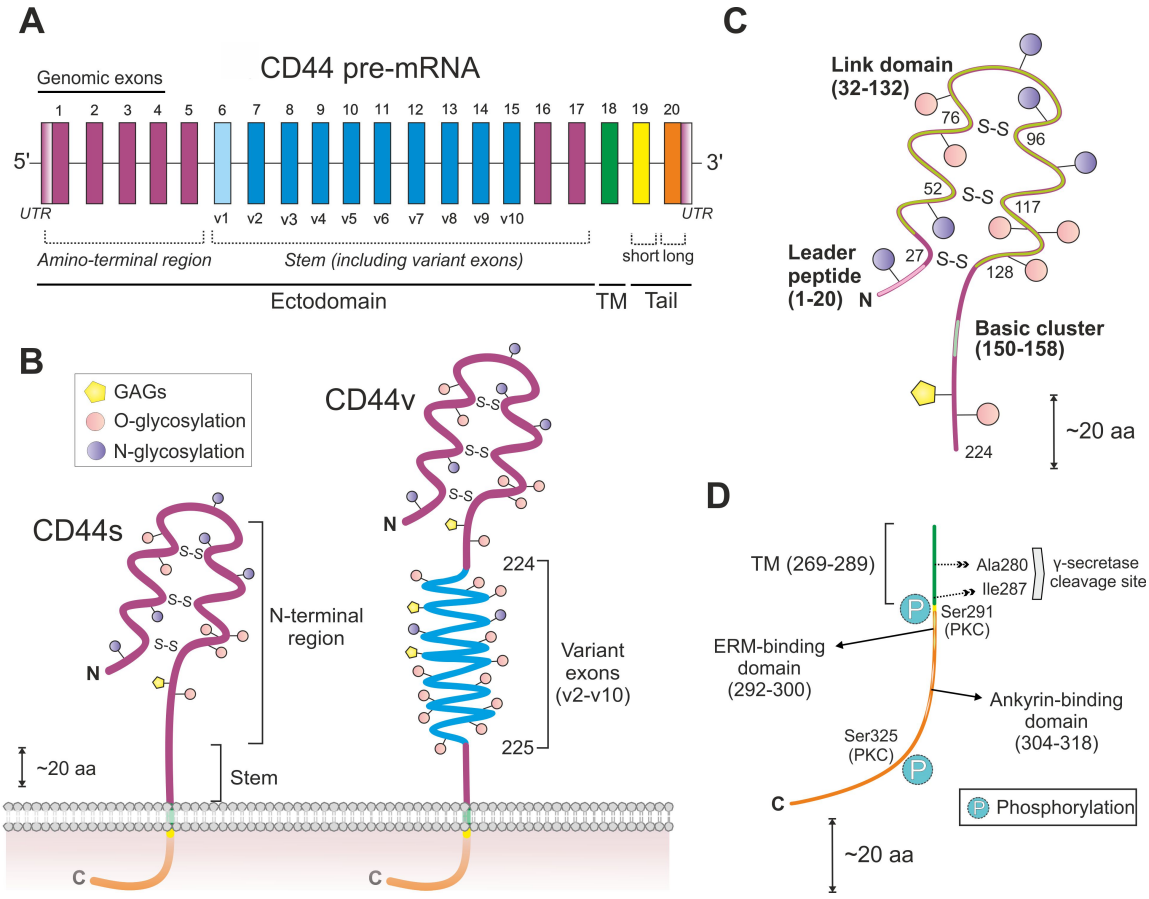

Figure 1—1. ***A.*** The CD44 pre-mRNA consists of 20 exons, some of them (highlighted in blue) prone to editing that originates variant isoforms. Purple exons are those utilized for the standard form of the extracellular domain. UTR: UnTranslated Region. ***B.*** CD44 features an extracellular domain (ectodomain, subdivided into the N-terminal and the stem region), a transmembrane (TM) domain, and an intracellular domain (endodomain). The inclusion of variant exons in the stem region through alternative splicing gives rise to much longer ectodomains (*right*) than what present in the receptor standard counterpart CD44s (*left*). ***C.*** Structure of CD44s ectodomain. The LINK domain and basic cluster of amino acids are essential for HA binding, and are localized close to the N-terminal region of CD44. ***D.*** Structure of the CD44 endodomain (encoded by exons 19 or 20 in A). This region regulates the interaction of CD44 with cytoskeletal elements and it is the only area characterized by phosphorylation sites. The endodomain may also affect HA binding by influencing the details of the receptor clustering.

Table 1—1. CD44 structural features.

Protein region (exons)		Structure
Ectodomain (Figure 1—1C)	*Globular domain* (exons 1-4)	• Disulfides from six highly conserved Cys residues stabilize globular domain and HA binding groove. • HA-binding region (amino acids 20-169) composed of the LINK domain (amino acids 32-132) and a basic motif (amino acids 150-158). • Two arginines and two tyrosines are critical for HA binding.
	Stem region (exons 4-17; exons 6-15 are also referred to as variant exons v1-v10)	• Fixed region of 46 amino acids in CD44s; incorporation of a variable region in CD44v. • Alternative splicing (variant exons skipping/inclusion) can lead to a 2-3-fold increase in size. • Variant exons may contain GAG-binding motifs.
Transmembrane domain (exon 18)		• Highly-conserved, 23 hydrophobic amino acids. • Allows lipid raft association (upon palmytoilation) and receptor clustering. • Cys286: CD44 dimerization. • Ala280/Ile287: γ-secretase cleavage site.
Intracellular domain (exons 19/20) (Figure 1—1D)		• Alternatively spliced in long-tail or a less common short-tail variant. • Long-tail CD44 contains a nuclear localization signal, which is involved in gene regulation). • Ankyrin (amino acids 304-318) and ERM (amino acids 292-300) binding sites couple CD44 with cytoskeleton. • C-terminus PZD-domain: putative phosphatase association and regulation (receptor signaling).

[s] HA, hyaluronic acid; GAGs, glycosaminoglycans; HS, heparan sulfate.

Another major source of size variability is post-translational modification. CD44s is ubiquitously expressed in most vertebrate cells [35, 42] and stems from the genomic exons 1-5, 16-18 and 20 giving rise to a 341-amino acid protein with an expected molar mass of 37 kDa [16]; however, the usual molar mass detected for CD44s is in the range of 85-95 kDa [39, 42], the increase being mostly due to glycosylation. These effects are reviewed in section 1.5.

1.3.1. Extracellular domain

The extracellular domain (ectodomain) is where most CD44 interactions with the external environment occur; it is also its most variable part (Figure 1—1B), which indicates the variability of the interactions themselves. The first five genomic exons are reported to be constant and encode the N-terminal globular region (from the N terminus to the basic cluster

in Figure 1—1C); exon 1 comprises the 5' untranslated region (UTR), the start codon and the leader peptide (amino acids 1-20) [10], and it is noteworthy that a specific variant, broadly homologous to CD44v5 but lacking the leader peptide, was seen in mature B cell malignancies [51]; probably also due to a unique C terminus, this variant has an intracellular localization, which therefore makes it impossible to target, even if overexpressed.

The CD44s ectodomain is normally subdivided in three regions [19]: the LINK domain (amino acids 32-132), the basic cluster (amino acids 150-158, mostly positively charged), and the stem structure (46 amino acids). The LINK domain has a ~35% homology with similar domains in hyaladherins, a family of proteins linked by their ability to bind HA through LINK sequences [1, 16, 39]. However, in CD44 the HA-binding region (amino acids 20-169 [52], encoded by genomic exons 2-4 [53]) spans the LINK domain and basic cluster [54, 55]; both include a putative HA-binding BX_7B motif, where B is a basic amino acid and X a generic (but not acidic) one. The first motif has reportedly a higher affinity for HA binding [16], but NMR studies identified as critical to HA binding residues both close to the LINK module (Arg58 and Tyr59) and within the a BX_7B motif of the basic cluster [35], thereby confirming a multidentate nature of HA binding and also the possibility of multiple modulation. Importantly, three disulfide bonds (Cys27-Cys128, Cys52-Cys117 and Cys76-Cys96) [1, 39] are necessary for the correct folding of the extracellular region [19], for the ensuing stability of the LINK module [56, 57] and therefore also to obtain stable HA interactions [56]. It is worth mentioning that CD44 possesses additional binding sites, contiguous to the HA binding region, for secondary ligands, such as osteopontin [5], collagen and laminin [9], fibronectin [8], selectins [58], serglycin/gp600 [59], the major histocompatibility complex class II (MHC-II) [16], or leukocytic receptors (e.g. CD62E and CD62L) [60]. It is not known to us whether any study has shown an agonistic or antagonistic influence of their occupancy on the strength of HA/CD44 interactions, whereas evidence has been reported that chondroitin sulfation, most likely at a site close to the basic cluster, reduces HA binding [61, 62].

The stem region (non-variable in CD44s) is encoded by genomic exons 4, 5, 16 and 17, and connects the extracellular domain to the transmembrane domain. This stalk-like structure contains proteolytic sites for membrane-associated proteases [63]. The insertion of variant exons due to alternative splicing increase the stem length and expand the diversity of its post-translational modifications [40, 64].

Finally, it is important to note that the capacity of CD44 clustering is critical to HA binding; for example, multifunctional CD44 antibodies can induce HA binding in cells that are constitutionally incapable of HA binding [65].

1.3.2. Transmembrane domain

The CD44 transmembrane region (encoded by genomic exon 18) is a single-pass domain of 23 hydrophobic amino acids that also provides a platform for protein interactions [50]. A cysteine residue (Cys286) is involved in the dimerization of CD44 receptors on cell surface [66, 67], while a γ-secretase cleavage site is located at Ala280/Ile287 and regulates intramembrane proteolysis [68]. Of relevance is the fact that the transmembrane domain is critical for the localization of CD44 in lipid rafts [69, 70] and hence for its clustering[59,60], where it associates to a variety of other receptors, such as ErbB2 [71] or sphingosine 1-phosphate receptor [72]. Of note, the disruption of lipid rafts leads to the loss of the signals induced by HA binding, similarly to what seen with CD44 blocking antibodies or CD44 silencing [72], and also appears to reduce the CD44 coupling (through its endodomain, see next section) to cytoskeletal elements [73].

1.3.3. Cytoplasmic (tail) domain

The CD44 cytoplasmic domain is affected by post-transcriptional modifications and can be encoded by genomic exons 19 or 20 depending on alternative splicing, and they respectively generate a rather uncommon short-tail and the more usual long-tail isoforms [39]. CD44s, for example, is a long-tail isoform that lacks exon 19, and also contains a nuclear localization signal and a C-terminal PZD-binding domain which may regulate phosphorylation, as seen in other receptors [53]. Motifs in intracellular regions are important for a membrane protein subcellular localization [10, 74], but also to allow its coupling to cytoskeletal components [10]. Indeed, CD44 interacts with ankyrin (binding domain: amino acids 304-318) [75] which in turn mediates contact with spectrin and participates in HA-dependent cell adhesion and motility [39, 76]. Additionally, a basic motif in the tail of CD44 is responsible for its interaction with ezrin, radixin and moesin (ERM) proteins (binding domain: amino acids 292-300) [77], linking the actin cytoskeleton to CD44. This action has important consequences in the regulation of cell migration, protein sorting, and lipid raft targeting [78-80]. Another important cytoplasmic partner is the ERM-related tumor suppressor merlin, which is able to inhibit cell growth through its interaction with CD44 [10, 81, 82]. The merlin-CD44 complex

can be seen as a molecular switch to control either cell growth arrest or proliferation depending on the participation of other ERM-proteins, on the phosphorylation state of merlin, and also on the HA molecular weight. When bound, high molecular weight HA can effectively cross-link several CD44 receptors, favoring thus the release of merlin, which in turn can be activated via dephosphorylation to function as an antiproliferation agent [83].

At the same time, it has been demonstrated that while post-translation modification of the cytoplasmic domain via phosphorylation does not affect HA binding [49], the complete abrogation of the cytoplasmic domain reduces it strongly [49, 84], and this can be recovered only by clustering CD44 with multifunctional antibodies [84], or by creating dimers of the "tail-less" CD44 [85]. However, it has been also shown that the induction of additional cytoplasmic clustering, e.g. by replacing the cytoplasmic CD44 domain with that of β5 integrin, does not significantly improve HA binding [86].

Therefore, CD44 clustering/oligomerization may play a role as important as the receptor own molecular structure in controlling HA binding, and "changes in the distribution of CD44 on the cell surface, induced by molecular interactions either from within the cell or from outside, may regulate its role as a receptor" [85].

1.4. Post-transcriptional regulation: alternative splicing

The expression of alternatively spliced isoforms of CD44 has attracted great attention because of their participation in the progression of several solid tumors [35], with important roles in the formation and maintenance of CSCs and (pre)metastatic niches [50]. Here we separately discuss the isoforms differing in extracellular domains (section 1.4.1), which can influence HA binding, and those in intracellular ones (section 1.4.2).

1.4.1. Ectodomain isoforms (CD44vx, CD44vx-x)

The alternative splicing of CD44 transcripts can lead to the insertion of individual (CD44v*x*) or multiple (CD44v*x*-*x*) variant exons between amino acids 224 and 225 [10, 87]. This addition translates into a significant elongation of the molecule. Most articles report a maximum value up to new 381 amino acids; we have been unable to find the original reference, but it seems reasonable to assume it to be the keratinocyte CD44v (CD44v3-10), which is the largest human form of the receptor with a molecular weight in the range of 250 kDa (180 kDa after deglycosylaton [88]). This equates to an almost 3-fold increase in size in comparison to CD44s and it seems more than likely that this may affect HA binding, either in

terms of steric hindrance (lower binding) or higher distance from the cell surface (higher binding due to better exposure). In terms of nomenclature, e.g. CD44v4 is the isoform obtained through the insertion of exon v4 only, whereas in CD44v8-10 the insertion involved the variant exons v8, v9 and v10. Importantly, CD44v8-10 corresponds to both the epithelial form of CD44 (CD44E), which does not bind to HA, but also to the CD44R1 isoform, typically associated to metastatic tumors, which differs from CD44E in three mutated amino acidic residues and is capable of HA binding [89]. A further difference may come from intron removal: it has been shown that the v8-v9 is removed more efficiently in CD44R1 than in CD44s [90], and this may apply also to the comparison with CD44E.

In theory, at least 800 splice variants of CD44 could be produced [39, 91, 92] and there is a general understanding that high CD44v expression often correlates with poor prognosis in cancer [35]. A reality check, however, shows that despite the number (vast but below 800) of isoforms indeed observed experimentally [39, 44, 93-95], only twelve appear to be commonly linked to disease progression [50]. For example, whereas CD44v3,8-10 is related to breast cancer progression [96] the larger CD44v3-10 is the usual form expressed by non-tumoral keratinocytes [88]. To further complicate the landscape, not only CD44v fingerprinting (i.e. the specific pattern of CD44v expression) but also its effects can be very disease-specific: for example, while the expression of CD44v3 and CD44v6 positively correlates with poor outcome in nasopharyngeal cancer [97] (as much as in lupus erythematosus [98]) that of CD44v5 in the latter had no correlation; however, CD44v5 is a prognostic factor in thymic neoplasms [99].

In Table 1—2, we report the expression of these isoforms both in normal and malignant cells.

Table 1—2. List of human cell types for which the expression of CD44s and CD44v has been reported[a,b].

CD44 isoform	(Over)expressed in		Relevance
	Physiological	**Pathological primary / lines**	
Absence	Protoplasmic astrocytes [100]. Platelets [15].	Jurkat cell line (Leukemia T lymphocyte cells) [101]. Some forms of OSCC [102]. Some forms of HNSCC [103].	Unknown.
CD44s	–Lymphohematopoietic cells [104]: lymphocytes, macrophages, dendritic cells, granulocytes and erythrocytes. –Epithelial cells [104]: epidermis, tonsils and pharynx, salivary glands, pancreas, thyroid follicles. –Glial and neuronal cells [100]: very high expression in "fibrous"-like astrocytes.	Carcinoma: renal [104], pancreatic [105-107], colorectal [108] and hepatocellular [109, 110]. HCC [109], NSCLC [111], osteosarcoma [112], biliary tract cancer [113]. Common human cancer cell lines [33]: PANC-1, AsPC-1, PC-3, SKOV-3, MOLM-13, HL60, THP-1, U87-MG, SK-Hep-1, Kasumi-1, Calu-6, A549, HEL 92.1.7, EOL-1.	–Associated with cell migration, invasion and survival [35],[99,100]. –Negative prognostic factor: primary colorectal carcinomas [98], HCC [99], NSCLC [108, 109, 113]. –Positive prognostic factor: myxofibrosarcoma [114] –Acquisition of mesenchymal phenotype and anchorage independent survival [110].
CD44v2	Normal urothelium [115].	Colorectal carcinoma [116], pancreatic cancer [117], breast cancer [106], ESCC [118].	–Marker for detection of transitional cell carcinoma [115]. – ESCC marker (indicates adjuvant therapy in patients with no lymph node metastasis) [118].
CD44v2-10	Normal colonic crypt epithelium, predominantly in the crypt base [119].	Breast solid tumors and cancer cell lines (e.g. MDA-MB-231, MCF-7) [120].	Positive steroid receptor status, low proliferation and luminal A subtype [120].
CD44v3	–Apical ectodermal ridge cells [121, 122]. –Polymorphonuclear leukocytes [123].	OSCC [124], HNSCC [125], breast [126] and endometrial [127] carcinomas.	–CSC marker for HNSCC, increases proliferation and enhances cisplatin resistance [124]. –Marker for cell migration [125].
CD44v3,8-10	Not reported in healthy tissues.	Colorectal adenomas and carcinomas [128, 129].	Overexpressed in >70% of colorectal liver metastases [128].

		Synovial fluid cells in arthritis [6], HNSCC [125].	
CD44v3-10	Keratinocytes [39].	Cancer cell lines [33]: MKN45, HCC1937, KPL4, JIMT-1, NCI-N87, FaDu, Detroit-562, Cal-27, NCI-H520, NCI-H1993, Colo205.	Considered as a marker for tumor progression and aggressiveness [125].
CD44v4	–Choroid plexus cells [130]. –Neurons [100].	Breast carcinoma and breast cancer cell lines [131]: MDA-MB-231, MDA-MB-435, MDA-MB-468.	Incorporation of E-selectin ligand facilitates tumor cell migration [131].
CD44v5	Choroid plexus cells, Purkinje cells [130].	Renal [132] and breast [133] carcinoma, osteosarcoma [112]. Cervix cancer cell lines: HeLa [134].	Associated with increased metastatic behavior [112].
CD44v6	–Choroid plexus cells [130]. –Mammary epithelial cells, non-proliferating ductal epithelium [135]. –THP-1 M2-like macrophages [36].	ESCC [136], OSCC [137], HNSCC [138, 139] and HPSCC [140], tongue [141], pancreatic [107] and cervical carcinoma [142]. Colorectal CSCs [143], osteosarcoma [112], prostate [144], biliary tract [113] and breast cancer [145].	–Pancreatic carcinoma metastasis and progression [107] ($CD446^{+}/CD44s^{-}$ is an independent survival factor). –Involved in c-Met signaling [146]. –Down-regulation promotes metastasis in OSCC [137]. –Useful marker of tumor invasion and metastasis [147].
CD44v8-10 (CD44E, or CD44R1)	Very low expression in normal tissue [148].	Hepatocellular [110], gastric and colorectal carcinomas [148-150]. Cancer cell lines [148-150]: BT-20, AGS, KATOIII, HCT-116, HT-29.	–Human gastric CSC marker [148]. –Promotes GSH synthesis [149] (enhanced oxidative defense). –EGFR signaling preferentially cooperates with CD44v8-v10 [120].
CD44v9	Normal endometrial glandular cell membrane [151].	Endocervical adenocarcinoma [152], pancreatic carcinoma [107], cervical precancerous lesions [153], OSCC [137]; gastric [154, 155], esophageal [155], colon [156, 157], prostate [158] and ovarian cancer [159]; colorectal CSCs [160].	–Pancreatic carcinoma metastasis and progression [107]. –Associated with proliferative activity, GSK-3β activity, EMT and inhibition of apoptosis [161]. –Down-regulation promotes metastasis in OSCC [137]. –Most likely candidate CSC marker [162].

CD44v10	–Choroid plexus cells [130]. –Bone marrow stromal cells [163, 164].	Hepatocellular carcinoma [110]. Prostate [165] and pancreatic cancer [166].	Allows differentiation between metastatic and non-metastatic prostate cancer cells. Putatively involved in counteracting metastases *in vivo* [166].

[a] HCC, hepatocellular carcinoma; NSCLC, non-small cell lung cancer; ESCC, esophageal squamous cell carcinoma; HNSCC, head and neck squamous cell carcinoma; HPSCC, hypopharyngeal squamous cell carcinoma; OSCC, oral squamous cell carcinoma; GSK-3β, glycogen synthase kinase-3β.

[b] Table 2 does not include the variant exon 1: this is expressed in rats and mice [43], but due to the presence of an early termination codon it remains silent in humans [158, 167, 168]. However, point mutations may trigger the expression of isoform CD44v1 in human cells, as described for fibroblasts isolated from rejecting cardiac allografts, even though its functional implications remain unknown [169].

To date the regulation of CD44 alternative splicing has not been completely elucidated due to its complex genomic organization, to the variety of cell specific *cis*- and *trans*-acting mechanisms involved in the process, but also to the possibility of the presence of single mutations (e.g. distinguishing CD44E from CD44R1). A number of carcinogenesis-promoting genes can modulate CD44 expression, often in a mitogenic signal-dependent fashion [10], and spliced isoforms can therefore be up or down-regulated upon stimulation with cytokines and growth factors. For example, interleukin-1 induces the expression of v3 and v6 isoforms in a process mediated by the early growth response element-1 [170]. Secondary ligands of CD44 may also regulate alternative splicing. For instance, osteopontin favors the expression of variants v6 and v9 in breast cancer cells [171]. A list of the most frequent alternative splicing regulators is enclosed in Table 1—3. Please note that the use of these regulators or the genetic modification of related pathways may be useful to change the CD44v/CD44s expression ratio of cancer cell lines, obtaining a CD44-fingerprint relevant for specific *in vitro* and *in vivo* experiments. For instance, Hu *et al.* modified the CD44v/CD44s ratio of breast cancer cells by regulating the expression of epithelial splicing regulatory protein 1 (ESRP1), thereby demonstrating the higher capacity of lung metastasis of $CD44s^{low}CD44v^{high}$ breast CSC with respect to $CD44s^{high}CD44^{low}$ ones [172].

Table 1—3. CD44 alternative splicing regulators[a].

Type	Effector	Impact on alternative splicing / target CD44 mRNA	Cell line or tissue
Up-regulators	TPA, IGF1, PDFG [173]	Exons v3, v5, v6, v7, v8 and v9.	SK-N-SH
	MAPK/ERK [174]	Exon v5.	LB-17
	IL-1 [170]	Exons v3 and v6.	ECV304
	SRm160 [134] Sam68 [175] ASPP1 [176]	Exon v5 (in a Ras-dependent manner).	HeLa and 293T [134], T-lymphoma [175], HEK293 [176]
	BaP [177]	Exon v10.	HeLa
	bFGF [178]	Exons v3, v4 and v5-10.	HUVEC
	OPN [161, 171]	Exons v6 and v9.	21NT
	TNF-α [179]	Exons v3 and v6 (via JNK pathway).	MCF-7
		CD44s and exons v3 and v6 (via p38 pathway).	MDA-MB-231
	DARPP-32 [180]	Exons v8-10.	AGS, MKN-45
	AGO1 and AGO2 [181]	Variant exons (through spliceosome recruitment and modulation of RNA polymerase II elongation rate).	HeLa S3
	YB-1 [182]	Activation of exon v5 keeping via multiple CAUC motifs.	MDA-MB-231
	PP2Cγ [183] p72 RNA helicase [184]	Inclusion of exons v4 and v5 (co-regulated by YB-1).	HeLa
	SRp55 [185]	Depletion of SRp55 favors inclusion of exon v7.	U2OS
	SRp40 [186]	Exons v2, v3, v5 and v6.	Breast cancer
	Tra2-β1 [187]	Exons v4 and v5 (synergy with YB-1).	Breast cancer

Down-regulators	HIF-1α [188]	Up-regulation of CD44s and isoforms (CD44v6, CD44v7/8) mature mRNA under hypoxic conditions.	MDA-MB-231, SUM-149
	HGF, EGF [189]	General alternative splicing.	HeLa
	ESRP1[172, 190]	ESRP1 depletion triggers a switch from CD44v to CD44s.	4T1 [190] MCF10CA1h [172]
	Mitomycin-C [185]	CD44s mRNA and mRNA spanning v6 exon.	U2OSE6AS
		Exons v7 and v10.	
	ESRP2 [191]	ESRP1/2 depletion down-regulates CD44v8-10 in favor of CD44s.	PNT2
	WNT5A [192]	Exons v4, v5 and v6.	MDA-MB-231, MDA-MB-4T1
Inhibitors	AR [193]	General CD44 splicing (p68 enhanced).	LNCaP
	PCBP1 [194]	Exons v3, v5, v6, v8 and v10.	HepG2
	THAP11 [195]	Exons v3, v6 and v8	HepG2
	Silibinin [196]	~90% total mRNA and ~70% decrease in CD44v7-10 mRNA.	PC-3M
	RBM3 [197]	CD44v8-v10 mRNA (in favor of CD44s mRNA).	PC-3
	NS5A (HCV) [198]	CD44v6 mRNA.	SB-HCV Molt-4

[a] TPA, 12-O-tetradecanoyl phorbol-13-acetate; IGF1, insulin-like growth factor-1; PDGF, platelet-derived growth factor; IL-1, interleukin 1; PCBP1, poly(rC) binding protein 1; THPA11, Thanatos-associated protein 11; SRm160, Serine/arginine -related nuclear matrix protein 160; Sam68, Src-associated in mitosis 68; ASPP1, apoptosis-stimulating of p53 protein 1; RBM3, RNA-binding motif protein 3; WNT5A, Wingless-type MMTV integration site family, member 5A; BaP, benzo(a)pyrene; bFGF, basic fibroblast growth factor; ESRP1 and ESRP2, epithelial splicing regulatory protein 1 and 2; OPN, osteopontin; DARPP-32, dopamine- and cAMP-regulated neuronal phosphoprotein; SRp55, Serine/arginine-rich protein 55; AGO1 and AGO2, argonaute proteins 1 and 2; YB-1, Y box-binding protein 1; NS5A, non-structural 5A protein (HCV); AR, androgen receptor; HIF-1α, hypoxia-inducible factor 1-α.

1.4.2. Intracellular isoforms (CD44-st, CD44-lt)

Most literature dealing with CD44 mRNA processing has traditionally focused on ectodomain variants, i.e. those traditionally referred to as CD44v, although the exons encoding for the

cytoplasmic tail domain are also susceptible to alternative splicing [199]. The two existing CD44 tail isoforms share three arginine residues encoded by exon 18 [39, 40] and differ in the presence of exon 19. If this exon is spliced out, the amino acids codified by exon 18/exon 20 give raise to the long-tail CD44 isoform (CD44-lt, tail domain 72 amino acids long) [16]. On the contrary, when exon 19 is included, there is an in-frame termination signal that causes the short-tail or 'tail-less' CD44 isoform (CD44-st, tail domain 3 amino acids long [16] terminating at Arg294) [1], characterized by a drastically reduced half-life [49]. RT-PCR studies reveal that the CD44-lt transcript of the hematopoietic form of the receptor (CD44H, i.e. CD44s) is much more abundant than its truncated counterpart [199]. CD44-st has only been identified as a dominant-negative receptor in chondrocytes [200], and its inhibition seems to enhance HA internalization [199]. Importantly, the DNA sequence of the 3'-UTR for the short-tail isoform carries poly-(A+T) tracts [40], which suggests the expression of CD44-st may be strictly downregulated by means of mRNA rapid turnover.

1.4.3. MicroRNAs

MicroRNAs can target the 3'-UTR of CD44 and strongly reduce its expression at the protein level. For example, down-regulation of miR-328 due to oxidative stress in the tumor microenvironment up-regulates CD44 expression and promotes cancer cells growth and drug resistance [201].

1.5. Post-translational modifications

CD44 heterogeneity is further augmented through a variety of post-translational modifications [202-205]. In this section, we address: 1) the main post-translational modifications reported in literature for CD44, 2) their functional role at the cellular level, and 3) the impact of these modifications on the uptake of HA. All points are summarized in Table 1—4.

1.5.1. Glycosylation

CD44s can undergo N-glycosylation at six sites (Asn25, Asn57, Asn100, Asn110, Asn120 and Asn255, the first five located within the HA binding domain [206]) and O-glycosylation at seven sites (Ser/Thr residues in the extracellular region proximal to the membrane) [16, 39]. CD44 glycosylation is considered to be a regulatory mechanism of CD44 binding to HA [10, 37], which would appear to hinge on three states with different activation: (1) an active form that constitutively binds HA, (2) an inducible form which binds HA upon cell stimulation,

and (3) an inactive state which does not (or weakly) bind HA [16]. Typically, the active HA-binding form of CD44 is poorly glycosylated, whereas inactive receptors are characterized by an extensive glycosylation [202]; it has been suggested that this effect is due to conformational changes in the extracellular domain caused by N-glycosylation [74], although saccharidic side-chains may also reduce the extent of receptor clustering, or, when negatively charged, interact with the positively charged residues critical to HA binding.

The CD44 variable region contains four additional N-glycosylation sites and a large number of O-glycosylation sites in the case of exons v2, v8, v9 and v10, rich in Ser/Thr moieties [39]. The decoration of CD44v with additional sugar chains is usually considered to reduce HA binding [37, 95, 207], although others have reported the opposite [208]. Noteworthy, certain glycosylation patterns of CD44v are frequently linked to malignant processes in cancer. For instance, tumor hypoxia promotes the decoration of CD44v with the sialyl-Lewis^X carbohydrate antigen (sLe^X), a common ligand of selectins with a role in metastasis of estrogen receptor-positive tumors to the bone [209], which indeed renders CD44v a ligand for endothelial E-selectins during metastasis [131, 210, 211]. This effect is not reported with CD44s.

It is noteworthy that CD44 glycosylation of CD44v has a number of roles in addition to the modulation of HA binding; for example, it is also involved in the quenching of intracellular reactive oxygen species (ROS) in CSCs, associated with the survival of pre-neoplastic foci and with radio/chemotherapy resistance mechanisms [212]. CSC maintain low ROS levels due to the high expression of glutathione (GSH) [213], synthesized in a process mediated by the cysteine/glutamate transporter XCT [149]. This enzyme is key for tumor development [214] and is docked and stabilized by N-glycosylated CD44v [149, 215], which up-regulates GSH [216].

A further source of post-translational heterogeneity is provided by the modification of CD44-associated carbohydrates. For example, sulfation typically occurs upon stimulation with inflammatory cytokines and seems to increase the affinity of CD44 for HA [204, 217-219]. Probably even more common is sialylation [38], which introduces additional negative charges and reduces HA binding to CD44 possibly due to electrostatic repulsion [59, 203, 220]. It has been speculated that sialylation / de-sialylation of CD44 may function as a switch to modulate the ability of CD44 to act as an HA-anchoring receptor. For example, hypersialylation of an N-glycosylation site within the HA-binding domain has been associated with an increased cell adhesion to selectins and metastatic behavior (in SW1990 pancreatic cancer cells) [221].

1.5.2. Glycosaminoglycanation

The region of CD44 proximal to the cellular membrane contains a chondroitin sulfate (CnS) binding site (Ser-Gly motif) common to all isoforms [16, 39, 222]. CnS attachment occurs at Ser180 and may negatively regulate HA binding [61, 62], which could be due to an induced structural change in the ectodomain conformation or by direct competition of CnS-modified proteins with HA for the binding to CD44, or electrostatic repulsion [4, 59].

CD44v can be extensively modified through the attachment of GAGs, which allows to recruit growth factors and cytokines [16, 61] and through their presentation on the cell surface enables autocrine or paracrine signaling [223]. CD44 isoforms including exon v3 contain a double serine-glycine motif (SGSG), i.e. an attachment site for CnS, and preferential sites for HS that make CD44 a heparan-sulfated proteoglycan (HSPG) [224], which implies a role of CD44v in inflammatory processes [223]. Additional binding sites within the variable region have also been described for dermatan sulfate (DS) [224], keratan sulfate (KS) [225] and heparan sulfate (HS) [222]. Exon v6 adds a site each for hepatocyte growth factor (HGF) and a vascular endothelial growth factor (VEGF) [226, 227]; additionally, it also increases GAG binding probably through a coordinated binding that involves the HA-binding N-terminal region, as also happens for v7-containing variants [94]. The attachment of GAGs to CD44v causes the receptor to interact with Met signaling, which in turn activates a broad range of cellular pathways involved in cell proliferation, motility, migration, and invasion [146, 228]. Of special importance is the role of CD44v6 as in the presentation of HGF and the formation of a ternary complex between CD44v6, HGF, and Met [146]. Besides, the intracellular tail links c-Met signaling to the actin cytoskeleton by means of partner proteins in order to recruit the guanine nucleotide exchange factor (GEF) son of sevenless (SOS), which amplifies MAPK/ERK signaling [229]. A feedback up-regulation of CD44v6 in melanoma cells after HGF binding has also been described [230].

In summary, the variant-dependent presence of GAGs adds another level of modulation to the interactions of CD44 with its ligands (not only HA).

1.5.3. Palmitoylation

CD44 can undergo reversible palmitoylation (formation of thioesters between palmitate and cysteine residues) at the highly conserved Cys286 (within the transmembrane domain) and Cys295 (within the proximal cytoplasmic domain) [231]. This modification not only seems to enhance the binding of ankyrin and possibly of ERM proteins [53], but also interferes with

CD3-mediated signaling on human T-lymphocytes [232] and influences CD44 raft targeting [53, 231]. What's more, depalmitoylated and palmytoilation-defective CD44 mutants appear not to be sufficiently hydrophobic for their association with lipid rafts and as a result the internalization of both HA and the receptor itself are inhibited [231]. It may therefore reasonable to assume the effect of palmitoylation to be similar to the other (membrane and intracellular) factors regulating CD44 clustering (section 1.3.2 and 1.3.3).

1.5.4. Phosphorylation

The cytoplasmic tail of CD44 contains six potential phosphorylation sites [39, 233], out of which Ser303 and Ser305 (mainly) have been shown to be the two most highly phosphorylated residues *in vivo* [16], although also Ser323 is also possibly necessary for the phosphorylation of CD44 *in vivo* [234]; in cultured resting cells CD44 is also phosphorylated at Ser325 [53, 235] in a process mediated by protein kinase II (CAMKII) [236]. Interestingly, the activation of protein kinase C (PKC) switches off Ser325 phosphorylation and leads to phosphorylation of Ser291, which in turn modulates the interaction of CD44 with ERM proteins and is consequently paramount to cell motility [235]. The activation of downstream Ser316 kinases by PKC has proved essential for CD44-mediated chemotaxis towards a phorbol ester gradient, which also suggests a role of this receptor in directional cell migration [233, 237]. The presence of certain variant domains such as CD44v4-7 may enhance phosphorylation of the cytoplasmic tail [39] and thus influence the interaction of the receptor with other intracellular proteins. For example, Rho-kinase A has been reported to promote the interaction of isoform CD44v3,8-10 with ankyrin, stimulating tumor cell migration in metastatic breast lines [96]. However, despite of this rich signaling behavior, mutations in all the above-mentioned Ser residues have shown that HA binding is an essentially phosphorylation-independent process [49].

1.5.5. Proteolytic cleavage (production of CD44sol)

The CD44 extracellular domain can be proteolytically cleaved, generating the so-called soluble CD44 (CD44sol) [238, 239]; it is noteworthy that CD44sol can also be produced *de novo* as an isoform lacking the cytoplasmic and transmembrane domains [240], but it is overwhelmingly produced via proteolytic cleavage [63]. Mechanistically, the cleavage of the stem region requires the intervention of metalloproteases (MMPs), such as MT1-MMP (also known as MMP14) and MT3-MMP (MMP16) [241]; however, the shedding of CD44 is

probably a multi-component process, which has been associated to the expression of cytokines such as oncostatin M (OSM) and transforming growth factor-β1 (TGF-β1) [242], as well as the epithelial growth factor (EGF) [243], and possibly also involving interactions with matrix elements such as laminin-5 gamma 2 chains [244, 245]. The C-terminal fragment (CTF) remains embedded in the plasma and is further processed by a presenilin-1/γ-secretase (cleavage of Ala280/Ile287); this process is known as regulated intramembranous proteolysis (RIP) [68], and results in the secretion of a CD44β-like peptide and of an intracellular domain fragment (CD44-ICD), which translocates to the nucleus and promotes the transcription of target genes (including *cd44* itself) via a phorbol ester response element [246].

Because of the increased CD44sol levels reported in several cell lines [63] and human tumors [247], it has been suggested that CD44sol could be a useful biomarker for tumor growth and invasion [248-250]; however, it should be noted that CD44sol is also produced during homeostatic phenonema of migration, e.g. by thymocytes [251].

The important point is that CD44 can exist therefore not only as a transmembrane cell surface receptor, but also in the fluid phase, and from there it can be sequestered and become an integral component of extracellular matrices [239]. In either case, these two forms can compete with the membrane-anchored form for HA binding [242].

Table 1—4. Summary of the effects of post-translational modifications on HA binding.

Post-translational modification	Effect on CD44/HA interactions	Proposed explanation
N-glycosylation	Negative [252-254]	Interferes with basic amino acids clusters and/or prevents HA binding by steric hindrance. Possible effect on CD44 mobility and clustering.
O-glycosylation	Positive [253, 255] Negative [37] Unclear [202, 256]	Effects on HA interactions strongly depend on the cell type and growth conditions, and need to be evaluated in a case-by-case basis.
Sialylation	Negative [59, 203, 220]	Possibly interferes with HA binding by increasing CD44 overall negative charge (HA-CD44 repulsion, interactions with basic cluster).
Chondroitin sulfate addition	Negative [61, 62, 254]	CnS-associated proteins may bind to/near the HA binding site, cause a conformational change in the ectodomain that blocks HA binding, or simply increase the negative charge (see sialylation).
Carbohydrate sulfation	Positive [204, 217-219]	It may facilitate CD44 clustering, both enhancing the affinity for HA and increasing avidity.
Keratan sulfate addition	Negative [225]	KS may modulate adhesion to HA via changes in protein conformation (LINK domain).

Palmitoylation	None [231]	It is relevant for lipid raft targeting and HA internalization, but does not influence binding.
Phosphorylation	None [49]	Phosphorylation-defective mutants show that HA binding and internalization are both phosphorylation-independent processes.
Proteolytic cleavage	Competition [242, 249]	CD44sol has the ability to compete with membrane-anchored CD44s/CD44v for HA binding.

1.6. Considerations for the design of HA-based targeted therapies

The numerous publications and patents published to date suggest feasibility of utilizing HA-based materials for the targeted delivery of active principles to CD44-expressing cancer cells, reporting positive results with enhanced drug efficacy and tumor shrinkage. Nonetheless, there are still many gaps with regard to the biological complexity of CD44 receptors and the molecular engineering of HA-based materials that need to be filled in order to predict biodistribution, targeting and efficacy *in vivo*.

For example, it is not clear how unique CD44s/CD44v fingerprints and the dynamic activation state of these receptors will impact the uptake of HA in healthy and diseased cells, or even whether these fingerprints will match those of real tissue from patients. Overall, the complex relations existing between the CD44 expression and the different phases of HA uptake need to be further analyzed from a rather fundamental perspective, as well as the possible interaction with other key hyaladherins in the body.

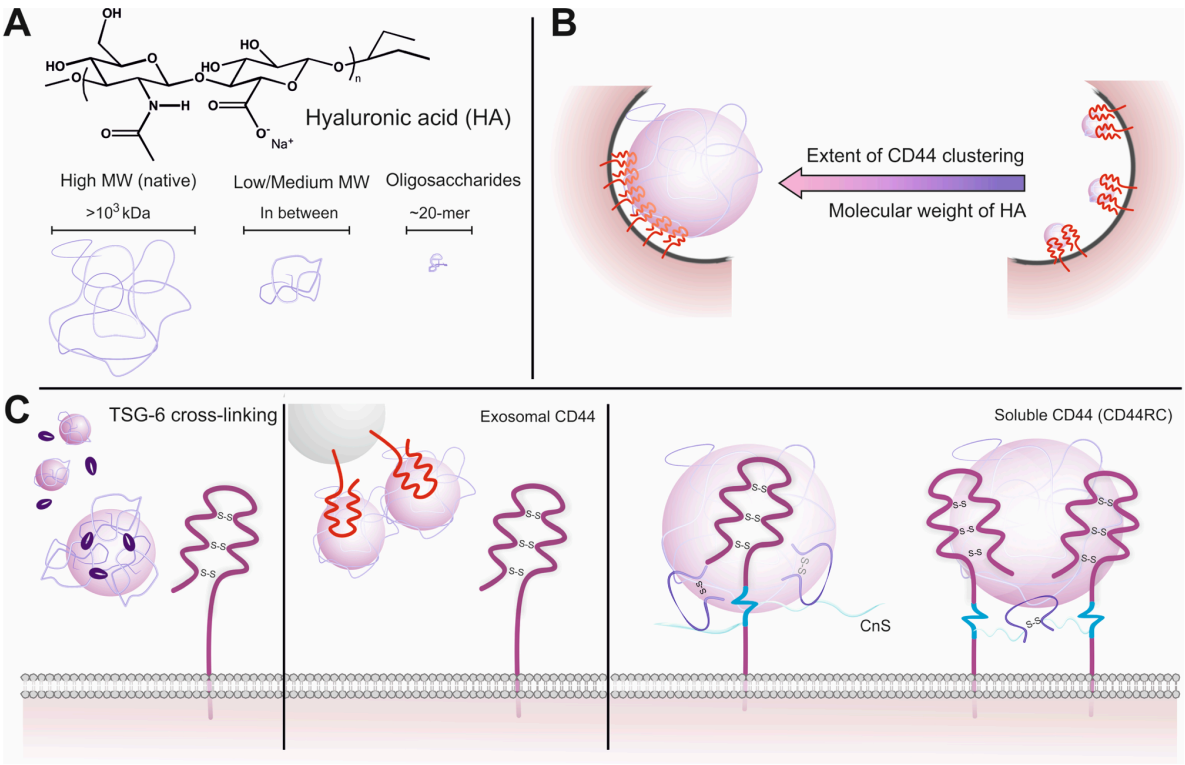

Figure 1—2. Focus on HA-materials and CD44 targeting. ***A.*** Chemical structure of hyaluronic acid (HA), composed of repeating disaccharide units D-glucuronic acid and D-N-acetylglucosamine, bound through alternating β-1,4 and β-1,3 glycosidic bonds. The size of HA proves paramount to its biological effects. Here we are using the nomenclature described in a recent review [257]: HA of around 20 monosaccharides in length are oligosaccharides; HA of ~10^3 kDa or bigger (resembling native HA) is high molecular weight; everything in between is low/medium molecular weight. ***B.*** The size of HA is thought to determine the degree of clustering (i.e. the local density) of CD44 receptors on cell membrane, which has an impact in the internalization of HA and in downstream signaling. ***C.*** *Left:* TSG-6 is a soluble hyaladherin that appears in inflammation and binds HA with high affinity. TSG-6 can enhance the presentation of cross-linked HA structures to CD44. *Centre:* exosomes have been reported as a novel mechanism for cancer cells to transfer CD44 protein to other target cells; we speculate that $CD44^+$ exosomes may be able to immobilize HA in order to present it to CD44 in a high avidity fashion. *Right:* soluble CD44, in particular CD44RC, is likely to enhance HA binding avidity of CD44 via binding to chondroitin sulfate (CnS) side-chains, generating a multivalent complex, or by simply inducing CD44 clustering.

1.6.1. Interaction of HA materials with healthy cells

The ubiquitous expression of CD44s and other HA receptors in healthy tissue is often seen as the most obvious caveat of HA-based therapies, raising concerns about potential side effects and reduced targeting efficiencies. The main predicted side effect of a systemic therapy is liver toxicity because of the high expression of Hyaluronan Receptor for Endocytosis (HARE) in endothelial cells. HARE is the main receptor involved in the uptake of HA from the blood [258] and its blocking results in the inhibition of HA clearance in the liver [259]. It has been discussed, however, that the *a priori* saturation of HARE in the liver, e.g. by pre-administration of soluble HA [260], should suffice to saturate HARE and mitigate against

potential side effects of a systemic HA therapy. On the other hand, the reduction in the efficiency of a potential tumor targeting strategy stems from the physiological expression and function of CD44 in the human body. The presence of CD44s in healthy tissue would account for the unspecific uptake of HA carriers, thus reducing the amount of drug delivered to tumor cells. For instance, macrophages are seen as the most likely off-target destination of any generic drug carrier in the tumor microenvironment, but especially of HA carriers due to the relatively high CD44 expression reported for macrophages and their major role in HA uptake and degradation [261]. The HA binding capabilities of CD44, however, depend on several factors, such as the presence of an intact cytoplasmic domain [84, 262], receptor clustering [65], and, as previously discussed, tissue-specific expression of variant isoforms and their post-translational modifications. This array of biological events determines the binding affinity of HA for CD44s/CD44v both in cancer and healthy tissue, which is normally seen as an inherent disadvantage of HA-based targeted systems. Therefore, the main challenge is to find a precise way to engineer HA-based materials in order to increase their affinity to cancer-associated CD44 receptors (e.g. CD44v), while minimizing interactions with healthy tissue. For example, the conjugation of HA with folate [263] or EGFR-targeting peptides [264] has been explored for the dual targeting of CD44 and other secondary receptors overexpressed in ovarian and breast cancer cells. Our group has also evaluated the use of HA as a platform for the presentation of additional ligands, such as RGD [265] or mannose [266], thus allowing for synergic targeting of specific cell populations.

1.6.2. Relationship between CD44 expression and HA uptake

In cell membranes CD44 is virtually never dispersed as an individual macromolecule, but instead it associates with lipid rafts [69, 70, 267]. This association seems to be strongly influenced by the expression of CD44v [37, 74, 268, 269], but not of CD44s [37]. The binding of HA to CD44 receptors occurs via multiple weak interactions (low affinity, K_d = 10-100 μM) dominated by hydrogen bonds and Van der Waals forces [270]; however, the individual CD44/HA bonds have a remarkably high tensile strength [271]. Under the enhanced local concentration typical of lipid rafts, the strength of CD44 binding to HA will strongly be influenced on the possibility of cooperative binding, i.e. avidity - how many receptors can cluster around a single ligand. The presentation of HA to cell surface receptors is also key to CD44 clustering (Figure 1—2B). In fact, FRET experiments have confirmed that native high molecular weight HA (~10^4 kDa), which possesses multivalent sites

$(GlcNAc_{\beta 1\text{-}4}GlcUA)_n$ for CD44 binding [272], stimulates CD44 clustering; while low molecular weight HA oligosaccharides, which only have 1 or 2 binding sites, ablate it (on CD44-transfected COS-7 cells, HK-2 and BT549 cells) [273]. Therefore, both the cell specific interaction of CD44 receptors with lipid rafts and the apparent hydrodynamic size of HA materials can influence receptor clustering around these materials, most likely having an impact on their uptake and therapeutic performance. Another difficult aspect to deal with in the targeting of CD44 with HA materials is the complex and sometimes unpredictable relationship between the expression of CD44 on cell membranes and the different phases of HA uptake (i.e. binding to CD44 receptors and receptor-mediated internalization). For example, we have recorded a negative correlation between HA internalization and CD44 expression in differently-polarized THP-1 macrophages, i.e. the amount of internalized HA material appeared to reduce with increasing CD44 levels [36]. Although this event is most likely cell line specific, further knowledge about the mechanistic details of receptor presentation and ligand association (e.g. participation of secondary protein partners in the uptake process which slow down internalization) is needed due to the profound effect such an unexpected behavior will have on a HA-based delivery approach.

1.6.3. HA capture and presentation by soluble (and exosomal?) CD44

Additionally, and as discussed in section 1.5.5, CD44 can exist in the fluid phase and become an integral component of extracellular matrices, potentially competing with membrane-anchored receptors for HA binding or, on the contrary, act as a platform for the enhanced presentation of HA to these surface receptors. The latter would mirror the behavior of the soluble hyaladherin TSG-6, whose interaction with HA is of much higher affinity (K_d = 0.2-2 μM) [274, 275] than that of CD44. Evidence suggests that very large HA structures cross-linked by TSG-6 (Figure 1—2C, left) proteins may in fact have an enhanced binding to membrane CD44 [276]. Likewise, a naturally occurring soluble form of CD44, CD44RC, may be involved in a different, likely better HA presentation. CD44RC is generated by alternative splicing and comprises a unique C-terminus that spans two HA-binding $[B(X_6)B]$ motifs [277]. Evidence suggests that CD44RC is likely to enhance HA binding avidity of CD44 via two mechanisms. On the one hand, CD44RC may bind to CnS side-chains attached to membrane-anchored CD44, generating a multivalent complex with increased avidity for HA. On the other hand, CD44RC may cross-link CnS moieties attached to different CD44 receptors, thus inducing their clustering [269]. In our opinion, these mechanisms are

particularly plausible for CD44 isoforms spanning additional CnS binding-sites, such as CD44v3 (Figure 1—2C, right).

Interestingly, it has been recently reported that exosomes derived from ovarian cancer cells are enriched in CD44 and that these vesicles are able to transfer CD44 receptors to human peritoneal mesothelial cells, promoting metastasis [278]. Although to the best of our knowledge there is no experimental evidence that exosomal CD44 can act as an off-target destination of HA, it is tempting to speculate that $CD44^+$ exosomes or extracellular vesicles in general could bind this ligand, and possibly other GAGs, to bring them back to cells in an immobilized, high-avidity fashion, as discussed for TSG-6 (Figure 1—2C, center).

1.7. Conclusions

The current state of knowledge of CD44s and CD44v in terms of their dynamic expression and ligand interaction is insufficient to establish a consensus opinion about the optimal strategy to exploit the overexpression of CD44 in cancer cells utilizing HA-based materials. CD44 targeting proves especially challenging due to the numerous cell-specific factors in place, such as post-translational modifications that affect the binding of HA to cell surface receptors or their internalization via endocytosis, the presence of CD44 in normal tissue, and the intervention of secondary protein partners involved in the uptake of HA. In order to effectively use HA as a targeting ligand in drug delivery we need to know its target better: the interplay between the expression of CD44 in healthy and diseased cells both in terms of amounts and isoforms, its dynamic functionality as a signaling and endocytic receptor, and its clustering capabilities. This aspect requires first the optimization and validation of current cellular models to obtain a more physiological relevant CD44 fingerprint; only then the molecular engineering of HA materials, both in their soluble or nanoparticulate form, holds the potential not only for enhancing the synergistic uptake of these materials by specific target cell populations, but also for mitigating against unspecific uptake mechanism and rapid clearance from the body. Taking all together, the points discussed in this review should contribute to the understanding of CD44 as a target in cancer therapy with a view on the design of targeted therapies, their evaluation *in vitro*, and ultimately in translating *in vitro* findings to the multicellular *in vivo* scenario.

1.8. References

[1] L.A. Goldstein, D.F.H. Zhou, L.J. Picker, C.N. Minty, R.F. Bargatze, J.F. Ding, E.C. Butcher, A Human-Lymphocyte Homing Receptor, the Hermes Antigen, Is Related to Cartilage Proteoglycan Core and Link Proteins, Cell 56(6) (1989) 1063-1072.

[2] W.M. Gallatin, I.L. Weissman, E.C. Butcher, A Cell-Surface Molecule Involved in Organ-Specific Homing of Lymphocytes, Nature 304(5921) (1983) 30-34.

[3] S. Oliferenko, I. Kaverina, J.V. Small, L.A. Huber, Hyaluronic acid (HA) binding to CD44 activates Rac1 and induces lamellipodia outgrowth, J Cell Biol 148(6) (2000) 1159-1164.

[4] M.F. Naujokas, M. Morin, M.S. Anderson, M. Peterson, J. Miller, The Chondroitin Sulfate Form of Invariant Chain Can Enhance Stimulation of T-Cell Responses through Interaction with Cd44, Cell 74(2) (1993) 257-268.

[5] G.F. Weber, S. Ashkar, M.J. Glimcher, H. Cantor, Receptor-ligand interaction between CD44 and osteopontin (Eta-1), Science 271(5248) (1996) 509-512.

[6] L.E. Sebban, D. Ronen, D. Levartovsky, O. Elkayam, D. Caspi, S. Aamar, H. Amital, A. Rubinow, I. Golan, D. Naor, Y. Zick, I. Golan, The involvement of CD44 and its novel ligand galectin-8 in apoptotic regulation of autoimmune inflammation, Journal of immunology 179(2) (2007) 1225-1235.

[7] W.M. Gallatin, E.A. Wayner, P.A. Hoffman, T. Stjohn, E.C. Butcher, W.G. Carter, Structural homology between lymphocyte receptors for high endothelium and class-iii extracellular-matrix receptor, P Natl Acad Sci USA 86(12) (1989) 4654-4658.

[8] S. Jalkanen, M. Jalkanen, Lymphocyte Cd44 Binds the Cooh-Terminal Heparin-Binding Domain of Fibronectin, J Cell Biol 116(3) (1992) 817-825.

[9] S. Ishii, R. Ford, P. Thomas, A. Nachman, G. Steele, J.M. Jessup, Cd44 Participates in the Adhesion of Human Colorectal-Carcinoma Cells to Laminin and Type-Iv Collagen, Surg Oncol 2(4) (1993) 255-264.

[10] H. Ponta, L. Sherman, P.A. Herrlich, CD44: From adhesion molecules to signalling regulators, Nat Rev Mol Cell Bio 4(1) (2003) 33-45.

[11] K. Gee, M. Kryworuchko, A. Kumar, Recent advances in the regulation of CD44 expression and its role in inflammation and autoimmune diseases, Arch Immunol Ther Ex 52(1) (2004) 13-26.

[12] N.S. Verkaik, G.J. van Steenbrugge, W.M. van Weerden, M.J. Bussemakers, T.H. van der Kwast, Silencing of CD44 expression in prostate cancer by hypermethylation of the CD44 promoter region, Lab Invest 80(8) (2000) 1291-1298.

[13] H. Kito, H. Suzuki, T. Ichikawa, N. Sekita, N. Kamiya, K. Akakura, T. Igarashi, T. Nakayama, M. Watanabe, K. Harigaya, H. Ito, Hypermethylation of the CD44 gene is associated with progression and metastasis of human prostate cancer, Prostate 49(2) (2001) 110-115.

[14] A. Stallmach, B.M. Wittig, K. Kremp, R. Goebel, S. Santourlidis, M. Zeitz, M. Menges, J. Raedle, S. Zeuzem, W.A. Schulz, Downregulation of CD44v6 in colorectal carcinomas is associated with hypermethylation of the CD44 promoter region, Exp Mol Pathol 74(3) (2003) 262-266.

[15] A.R. Jordan, R.R. Racine, M.J. Hennig, V.B. Lokeshwar, The Role of CD44 in Disease Pathophysiology and Targeted Treatment, Frontiers in immunology 6 (2015) 182.

[16] D. Naor, S. Nedvetzki, I. Golan, L. Melnik, Y. Faitelson, CD44 in cancer, Crit Rev Cl Lab Sci 39(6) (2002) 527-579.

[17] R. Thapa, G.D. Wilson, The Importance of CD44 as a Stem Cell Biomarker and Therapeutic Target in Cancer, Stem Cells Int (2016).

[18] Y.M. Yan, X.S. Zuo, D.Y. Wei, Concise Review: Emerging Role of CD44 in Cancer Stem Cells: A Promising Biomarker and Therapeutic Target, Stem Cell Transl Med 4(9) (2015) 1033-1043.

[19] M. Zoller, CD44: can a cancer-initiating cell profit from an abundantly expressed molecule?, Nat Rev Cancer 11(4) (2011) 254-267.

[20] A.P. Rybak, L.Z. He, A. Kapoor, J.C. Cutz, D. Tang, Characterization of sphere-propagating cells with stem-like properties from DU145 prostate cancer cells, Bba-Mol Cell Res 1813(5) (2011) 683-694.

[21] L. Patrawala, T. Calhoun, R. Schneider-Broussard, H. Li, B. Bhatia, S. Tang, J.G. Reilly, D. Chandra, J. Zhou, K. Claypool, L. Coghlan, D.G. Tang, Highly purified CD44(+) prostate cancer cells from xenograft human tumors are enriched in tumorigenic and metastatic progenitor cells, Oncogene 25(12) (2006) 1696-1708.

[22] W. Guo, P.S. Frenette, Alternative CD44 splicing in intestinal stem cells and tumorigenesis, Oncogene 33(5) (2014) 537-538.

[23] M.E. Prince, R. Sivanandan, A. Kaczorowski, G.T. Wolf, M.J. Kaplan, P. Dalerba, I.L. Weissman, M.F. Clarke, L.E. Ailles, Identification of a subpopulation of cells with cancer

stem cell properties in head and neck squamous cell carcinoma, P Natl Acad Sci USA 104(3) (2007) 973-978.
[24] C.W. Li, C.J. Lee, D.M. Simeone, Identification of Human Pancreatic Cancer Stem Cells, Methods Mol Biol 568 (2009) 161-173.
[25] C.W. Li, D.G. Heidt, P. Dalerba, C.F. Burant, L.J. Zhang, V. Adsay, M. Wicha, M.F. Clarke, D.M. Simeone, Identification of pancreatic cancer stem cells, Cancer Res 67(3) (2007) 1030-1037.
[26] L. Du, H.Y. Wang, L.Y. He, J.Y. Zhang, B.Y. Ni, X.H. Wang, H.J. Jin, N. Cahuzac, M. Mehrpour, Y.Y. Lu, Q. Chen, CD44 is of Functional Importance for Colorectal Cancer Stem Cells, Clin Cancer Res 14(21) (2008) 6751-6760.
[27] P. Dalerba, S.J. Dylla, I.K. Park, R. Liu, X.H. Wang, R.W. Cho, T. Hoey, A. Gurney, E.H. Huang, D.M. Simeone, A.A. Shelton, G. Parmiani, C. Castelli, M.F. Clarke, Phenotypic characterization of human colorectal cancer stem cells, P Natl Acad Sci USA 104(24) (2007) 10158-10163.
[28] M. Al-Hajj, M.S. Wicha, A. Benito-Hernandez, S.J. Morrison, M.F. Clarke, Prospective identification of tumorigenic breast cancer cells, P Natl Acad Sci USA 100(7) (2003) 3983-3988.
[29] D. Ponti, A. Costa, N. Zaffaroni, G. Pratesi, G. Petrangolini, D. Coradini, S. Pilotti, M.A. Pierotti, M.G. Daidone, Isolation and in vitro propagation of tumorigenic breast cancer cells with stem/progenitor cell properties, Cancer Res 65(13) (2005) 5506-5511.
[30] A.T. Collins, P.A. Berry, C. Hyde, M.J. Stower, N.J. Maitland, Prospective identification of tumorigenic prostate cancer stem cells, Cancer Res 65(23) (2005) 10946-10951.
[31] A. Cadete, M.J. Alonso, Targeting cancer with hyaluronic acid-based nanocarriers: recent advances and translational perspectives, Nanomedicine 11(17) (2016) 2341-57.
[32] J.M. Wickens, H.O. Alsaab, P. Kesharwani, K. Bhise, M. Amin, R.K. Tekade, U. Gupta, A.K. Iyer, Recent advances in hyaluronic acid-decorated nanocarriers for targeted cancer therapy, Drug discovery today 22(4) (2017) 665-680.
[33] F. Birzele, E. Voss, A. Nopora, K. Honold, F. Heil, S. Lohmann, H. Verheul, C. Le Tourneau, J.P. Delord, C. van Herpen, D. Mahalingam, A.L. Coveler, V. Meresse, S. Weigand, V. Runza, M. Cannarile, CD44 Isoform Status Predicts Response to Treatment with Anti-CD44 Antibody in Cancer Patients, Clin Cancer Res 21(12) (2015) 2753-2762.
[34] L. Li, M. Schmitt, A. Matzke-Ogi, P. Wadhwani, V. Orian-Rousseau, P.A. Levkin, CD44v6-Peptide Functionalized Nanoparticles Selectively Bind to Metastatic Cancer Cells, Adv Sci (Weinh) 4(1) (2017) 1600202.

[35] D. Naor, S.B. Wallach-Dayan, M.A. Zahalka, R.V. Sionov, Involvement of CD44, a molecule with a thousand faces, in cancer dissemination, Semin Cancer Biol 18(4) (2008) 260-267.
[36] J.M.R. de la Rosa, A. Tirella, A. Gennari, I.J. Stratford, N. Tirelli, The CD44-Mediated Uptake of Hyaluronic Acid-Based Carriers in Macrophages, Adv Healthc Mater 6(4) (2017).
[37] K.L. Bennett, B. Modrell, B. Greenfield, A. Bartolazzi, I. Stamenkovic, R. Peach, D.G. Jackson, F. Spring, A. Aruffo, Regulation of Cd44 Binding to Hyaluronan by Glycosylation of Variably Spliced Exons, J Cell Biol 131(6) (1995) 1623-1633.
[38] B. Byrne, G.G. Donohoe, R. O'Kennedy, Sialic acids: carbohydrate moieties that influence the biological and physical properties of biopharmaceutical proteins and living cells, Drug discovery today 12(7-8) (2007) 319-326.
[39] D. Naor, R.V. Sionov, D. IshShalom, CD44: Structure, function, and association with the malignant process, Adv Cancer Res 71 (1997) 241-319.
[40] G.R. Screaton, M.V. Bell, D.G. Jackson, F.B. Cornelis, U. Gerth, J.I. Bell, Genomic Structure of DNA Encoding the Lymphocyte Homing Receptor Cd44 Reveals at Least 12 Alternatively Spliced Exons, P Natl Acad Sci USA 89(24) (1992) 12160-12164.
[41] M.V. Bell, G.R. Screaton, D.G. Jackson, J.I. Bell, The Genomic Organization of the Human Cd44 Gene, J Cell Biochem (1993) 332-332.
[42] C.M. Isacke, H. Yarwood, The hyaluronan receptor, CD44, Int J Biochem Cell B 34(7) (2002) 718-721.
[43] G.R. Screaton, M.V. Bell, J.I. Bell, D.G. Jackson, The Identification of a New Alternative Exon with Highly Restricted Tissue Expression in Transcripts Encoding the Mouse Pgp-1 (Cd44) Homing Receptor - Comparison of All 10 Variable Exons between Mouse, Human, and Rat, J Biol Chem 268(17) (1993) 12235-12238.
[44] U. Gunthert, M. Hofmann, W. Rudy, S. Reber, M. Zoller, I. Haussmann, S. Matzku, A. Wenzel, H. Ponta, P. Herrlich, A New Variant of Glycoprotein Cd44 Confers Metastatic Potential to Rat Carcinoma-Cells, Cell 65(1) (1991) 13-24.
[45] D. Naor, S. Nedvetzki, M. Walmsley, A. Yayon, E.A. Turleyd, I. Golan, D. Caspi, L.E. Sebban, Y. Zick, T. Garin, D. Karussis, N. Assayag-Asherie, I. Raz, L. Weiss, S. Slavin, I. Golan, CD44 involvement in autoimmune Inflammations - The lesson to be learned from CD44-Targeting by antibody or from knockout mice, Ann Ny Acad Sci 1110 (2007) 233-247.
[46] M. Goebeler, D. Kaufmann, E.B. Brocker, C.E. Klein, Migration of highly aggressive melanoma cells on hyaluronic acid is associated with functional changes, increased turnover and shedding of CD44 receptors, J Cell Sci 109 (1996) 1957-1964.

[47] A.R. Gunthert, J. Strater, U. vonReyher, C. Henne, S. Joos, K. Koretz, G. Moldenhauer, P.H. Krammer, P. Moller, Early detachment of colon carcinoma cells during CD95(APO-1/Fas)-mediated apoptosis .1. De-adhesion from hyaluronate by shedding of CD44, J Cell Biol 134(4) (1996) 1089-1096.

[48] E. Mantenhorst, E.H.J. Danen, L. Smith, M. Snoek, I.C. Lepoole, G.N.P. Vanmuijen, S.T. Pals, D.J. Ruiter, Expression of Cd44 Splice Variants in Human Cutaneous Melanoma and Melanoma Cell-Lines Is Related to Tumor Progression and Metastatic Potential, Int J Cancer 64(3) (1995) 182-188.

[49] C.R. Uff, S.J. Neame, C.M. Isacke, Hyaluronan-Binding by Cd44 Is Regulated by a Phosphorylation-Independent Mechanism, Eur J Immunol 25(7) (1995) 1883-1887.

[50] K. Williams, K. Motiani, P.V. Giridhar, S. Kasper, CD44 integrates signaling in normal stem cell, cancer stem cell and (pre)metastatic niches, Exp Biol Med 238(3) (2013) 324-338.

[51] X.T. Hu, Y.W. Chen, A.C.T. Liang, W.Y. Au, K.Y. Wong, T.S.K. Wan, M.L.Y. Wong, L.J. Shen, K.K. Chan, T.H. Guo, K.M. Chu, Q. Tao, C.S. Chim, F. Loong, W.W.L. Choi, L.W. Lu, C.C. So, L.C. Chan, Y.L. Kwong, R.H.S. Liang, G. Srivastava, CD44 activation in mature B-cell malignancies by a novel recurrent IGH translocation, Blood 115(12) (2010) 2458-2461.

[52] P. Teriete, S. Banerji, M. Noble, C.D. Blundell, A.J. Wright, A.R. Pickford, E. Lowe, D.J. Mahoney, M.I. Tammi, J.D. Kahmann, I.D. Campbell, A.J. Day, D.G. Jackson, Structure of the regulatory hyaluronan binding domain in the inflammatory leukocyte homing receptor CD44, Mol Cell 13(4) (2004) 483-496.

[53] R.F. Thorne, J.W. Legg, C.M. Isacke, The role of the CD44 transmembrane and cytoplasmic domains in co-ordinating adhesive and signalling events, J Cell Sci 117(3) (2004) 373-380.

[54] T.E. Hardingham, A.J. Fosang, Proteoglycans - Many Forms and Many Functions, Faseb J 6(3) (1992) 861-870.

[55] A.J. Day, G.D. Prestwich, Hyaluronan-binding proteins: Tying up the giant, J Biol Chem 277(7) (2002) 4585-4588.

[56] S. Banerji, A.J. Day, J.D. Kahmann, D.G. Jackson, Characterization of a functional hyaluronan-binding domain from the human CD44 molecule expressed in Escherichia coli, Protein Expression and Purification 14(3) (1998) 371-381.

[57] A.J. Day, J.K. Sheehan, Hyaluronan: polysaccharide chaos to protein organisation, Curr Opin Struc Biol 11(5) (2001) 617-622.

[58] C.J. Dimitroff, J.Y. Lee, S. Rafii, R.C. Fuhlbrigge, R. Sackstein, CD44 is a major E-selectin ligand on human hematopoietic progenitor cells, J Cell Biol 153(6) (2001) 1277-1286.
[59] N. Toyamasorimachi, H. Sorimachi, Y. Tobita, F. Kitamura, H. Yagita, K. Suzuki, M. Miyasaka, A Novel Ligand for Cd44 Is Serglycin, a Hematopoietic-Cell Lineage-Specific Proteoglycan - Possible Involvement in Lymphoid-Cell Adherence and Activation, J Biol Chem 270(13) (1995) 7437-7444.
[60] K. Konstantopoulos, S.N. Thomas, Cancer Cells in Transit: The Vascular Interactions of Tumor Cells, Annu Rev Biomed Eng 11 (2009) 177-202.
[61] B. Ruffell, P. Johnson, Chondroitin sulfate addition to CD44H negatively regulates hyaluronan binding, Biochem Bioph Res Co 334(2) (2005) 306-312.
[62] B. Ruffell, G.F.T. Poon, S.S.M. Lee, K.L. Brown, S.L. Tjew, J. Cooper, P. Johnson, Differential Use of Chondroitin Sulfate to Regulate Hyaluronan Binding by Receptor CD44 in Inflammatory and Interleukin 4-activated Macrophages, J Biol Chem 286(22) (2011) 19179-19190.
[63] I. Okamoto, Y. Kawano, H. Tsuiki, J. Sasaki, M. Nakao, M. Matsumoto, M. Suga, M. Ando, M. Nakajima, H. Saya, CD44 cleavage induced by a membrane-associated metalloprotease plays a critical role in tumor cell migration, Oncogene 18(7) (1999) 1435-1446.
[64] Z. Kalnina, P. Zayakin, K. Silina, A. Line, Alterations of pre-mRNA splicing in cancer, Genes, chromosomes & cancer 42(4) (2005) 342-57.
[65] J. Lesley, P.W. Kincade, R. Hyman, Antibody-Induced Activation of the Hyaluronan Receptor Function of Cd44 Requires Multivalent Binding by Antibody, Eur J Immunol 23(8) (1993) 1902-1909.
[66] D. Liu, M.S. Sy, A cysteine residue located in the transmembrane domain of CD44 is important in binding of CD44 to hyaluronic, J Exp Med 183(5) (1996) 1987-1994.
[67] D. Liu, M.S. Sy, Phorbol myristate acetate stimulates the dimerization of CD44 involving a cysteine in the transmembrane domain, Journal of immunology 159(6) (1997) 2702-11.
[68] M.S. Brown, J. Ye, R.B. Rawson, J.L. Goldstein, Regulated intramembrane proteolysis: A control mechanism conserved from bacteria to humans, Cell 100(4) (2000) 391-398.
[69] S.J. Neame, C.R. Uff, H. Sheikh, S.C. Wheatley, C.M. Isacke, Cd44 Exhibits a Cell-Type Dependent Interaction with Triton X-100 Insoluble, Lipid Rich, Plasma-Membrane Domains, J Cell Sci 108 (1995) 3127-3135.

[70] A. Perschl, J. Lesley, N. English, R. Hyman, I.S. Trowbridge, Transmembrane Domain of CD44 Is Required for Its Detergent Insolubility in Fibroblasts, J Cell Sci 108 (1995) 1033-1041.

[71] S. Ghatak, S. Misra, B.P. Toole, Hyaluronan constitutively regulates ErbB2 phosphorylation and signaling complex formation in carcinoma cells, J Biol Chem 280(10) (2005) 8875-8883.

[72] P.A. Singleton, S.M. Dudek, S.F. Ma, J.G.N. Garcia, Transactivation of sphingosine 1-phosphate receptors is essential for vascular barrier regulation - Novel role for hyaluronan and CD44 receptor family, J Biol Chem 281(45) (2006) 34381-34393.

[73] P.A. Singleton, L.Y.W. Bourguignon, CD44 interaction with ankyrin and IP3 receptor in lipid rafts promotes hyaluronan-mediated Ca2+ signaling leading to nitric oxide production and endothelial cell adhesion and proliferation, Exp. Cell Res. 295(1) (2004) 102-118.

[74] J. Sleeman, W. Rudy, M. Hofmann, J. Moll, P. Herrlich, H. Ponta, Regulated clustering of variant CD44 proteins increases their hyaluronate binding capacity, J Cell Biol 135(4) (1996) 1139-1150.

[75] V.B. Lokeshwar, L.Y.W. Bourguignon, Tyrosine Phosphatase-Activity of Lymphoma Cd45 (Gp180) Is Regulated by a Direct Interaction with the Cytoskeleton, J Biol Chem 267(30) (1992) 21551-21557.

[76] V.B. Lokeshwar, N. Fregien, L.Y.W. Bourguignon, Ankyrin-Binding Domain of Cd44(Gp85) Is Required for the Expression of Hyaluronic Acid-Mediated Adhesion Function, J Cell Biol 126(4) (1994) 1099-1109.

[77] J.W. Legg, C.M. Isacke, Identification and functional analysis of the ezrin-binding site in the hyaluronan receptor, CD44, Curr Biol 8(12) (1998) 705-708.

[78] R.G. Fehon, A.I. McClatchey, A. Bretscher, Organizing the cell cortex: the role of ERM proteins, Nat Rev Mol Cell Bio 11(4) (2010) 276-287.

[79] S. Tsukita, K. Oishi, N. Sato, J. Sagara, A. Kawai, S. Tsukita, Erm Family Members as Molecular Linkers between the Cell-Surface Glycoprotein Cd44 and Actin-Based Cytoskeletons, J Cell Biol 126(2) (1994) 391-401.

[80] J.L. Lee, M.J. Wang, P.R. Sudhir, J.Y. Chen, CD44 engagement promotes matrix-derived survival through the CD44-Src-integrin axis in lipid rafts, Mol Cell Biol 28(18) (2008) 5710-5723.

[81] H. Morrison, L.S. Sherman, J. Legg, F. Banine, G. Isacke, C.A. Haipek, D.H. Gutmann, H. Ponta, P. Herrlich, The NF2 tumor suppressor gene product, merlin, mediates contact inhibition of growth through interactions with CD44, Gene Dev 15(8) (2001) 968-980.

[82] I. Stamenkovic, Q. Yu, Merlin, a "Magic" Linker Between the Extracellular Cues and Intracellular Signaling Pathways that Regulate Cell Motility, Proliferation, and Survival, Curr Protein Pept Sc 11(6) (2010) 471-484.
[83] Y. Bai, Y.J. Liu, H. Wang, Y. Xu, I. Stamenkovic, Q. Yu, Inhibition of the hyaluronan-CD44 interaction by merlin contributes to the tumor-suppressor activity of merlin, Oncogene 26(6) (2007) 836-850.
[84] J. Lesley, Q. He, K. Miyake, A. Hamann, R. Hyman, P.W. Kincade, Requirements for Hyaluronic-Acid Binding by Cd44 - a Role for the Cytoplasmic Domain and Activation by Antibody, J Exp Med 175(1) (1992) 257-266.
[85] A. Perschl, J. Lesley, N. English, I. Trowbridge, R. Hyman, Role of CD44 cytoplasmic domain in hyaluronan binding, Eur J Immunol 25(2) (1995) 495-501.
[86] J. Lesley, N. English, C. Charles, R. Hyman, The role of the CD44 cytoplasmic and transmembrane domains in constitutive and inducible hyaluronan binding, Eur J Immunol 30(1) (2000) 245-253.
[87] M. Giovingo, M. Nolan, R. McCarty, I.H. Pang, A.F. Clark, R.M. Beverley, S. Schwartz, W.D. Stamer, L. Walker, A. Grybauskas, K. Skuran, P.V. Kuprys, B.Y.J.T. Yue, P.A. Knepper, sCD44 overexpression increases intraocular pressure and aqueous outflow resistance, Mol Vis 19 (2013) 2151-2164.
[88] J.G. Haggerty, R.H. Bretton, L.M. Milstone, Identification and characterization of a cell-surface proteoglycan on keratinocytes, J Invest Dermatol 99(4) (1992) 374-380.
[89] G.J. Dougherty, D.L. Cooper, J.F. Memory, R.K. Chiu, Ligand-binding specificity of alternatively spliced cd44 isoforms - recognition and binding of hyaluronan by CD44R1, J Biol Chem 269(12) (1994) 9074-9078.
[90] G.M. Hayes, C. Carpenito, P.D. Davis, S.T. Dougherty, J.F. Dirks, G.J. Dougherty, Alternative splicing as a novel of means of regulating the expression of therapeutic genes, Cancer Gene Therapy 9(2) (2002) 133-141.
[91] M.V. Bell, A.E. Cowper, M.P. Lefranc, J.I. Bell, G.R. Screaton, Influence of intron length on alternative splicing of CD44, Mol Cell Biol 18(10) (1998) 5930-5941.
[92] D.H.J. Vanweering, P.D. Baas, J.L. Bos, A Pcr-Based Method for the Analysis of Human Cd44 Splice Products, Pcr Meth Appl 3(2) (1993) 100-106.
[93] G. Borland, J.A. Ross, K. Guy, Forms and functions of CD44, Immunology 93(2) (1998) 139-148.

[94] J.P. Sleeman, K. Kondo, J. Moll, H. Ponta, P. Herrlich, Variant exons v6 and v7 together expand the repertoire of glycosaminoglycans bound by CD44, J Biol Chem 272(50) (1997) 31837-31844.
[95] I. Stamenkovic, A. Aruffo, M. Amiot, B. Seed, The Hematopoietic and Epithelial Forms of Cd44 Are Distinct Polypeptides with Different Adhesion Potentials for Hyaluronate-Bearing Cells, Embo J 10(2) (1991) 343-348.
[96] L.Y.W. Bourguignon, H.B. Zhu, L.J. Shao, D. Zhu, Y.W. Chen, Rho-kinase (ROK) promotes CD44v(3,8-10)-ankyrin interaction and tumor cell migration in metastatic breast cancer cells, Cell Motil Cytoskel 43(4) (1999) 269-287.
[97] K. Sagawa, N. Uwa, T. Daimon, M. Sakagami, T. Tsujimura, Expression of CD44 variant isoforms, CD44v3 and CD44v6, are associated with prognosis in nasopharyngeal carcinoma, Journal of Laryngology and Otology 130(9) (2016) 843-849.
[98] J.C. Crispin, B.T. Keenan, M.D. Finnell, B.L. Bermas, P. Schur, E. Massarotti, E.W. Karlson, L.M. Fitzgerald, S. Ergin, V.C. Kyttaris, G.C. Tsokos, K.H. Costenbader, Expression of CD44 Variant Isoforms CD44v3 and CD44v6 Is Increased on T Cells From Patients With Systemic Lupus Erythematosus and Is Correlated With Disease Activity, Arthritis Rheum 62(5) (2010) 1431-1437.
[99] S.C. Lee, H.J. Harn, T.S. Lin, K.T. Yeh, Y.C. Liu, C.S. Tsai, Y.L. Cheng, Prognostic significance of CD44v5 expression in human thymic epithelial neoplasms, Annals of Thoracic Surgery 76(1) (2003) 213-218.
[100] J. Dzwonek, G.M. Wilczynski, CD44: molecular interactions, signaling and functions in the nervous system, Front Cell Neurosci 9 (2015).
[101] R.R. Racine, N.A. Manalo, J.M.F. Hall, A. Dibas, G.D. Raffel, M.E. Mummert, CD44 induced enhancement of phosphatase activity and calcium influx: Modifications of EGR-1 expression and cell proliferation, Biochemistry and Biophysics Reports 6 (2016) 172-178.
[102] A. Nasman, C. Nordfors, N. Grun, E. Munck-Wikland, T. Ramqvist, L. Marklund, D. Lindquist, T. Dalianis, Absent/weak CD44 intensity and positive human papillomavirus (HPV) status in oropharyngeal squamous cell carcinoma indicates a very high survival, Cancer Med-Us 2(4) (2013) 507-518.
[103] S.Y. Oh, H.J. Kang, Y.S. Kim, H. Kim, Y.C. Lim, CD44-negative cells in head and neck squamous carcinoma also have stem-cell like traits, Eur J Cancer 49(1) (2013) 272-280.
[104] M.Z. Gilcrease, M. Guzman-Paz, G. Niehans, D. Cherwitz, J.B. McCarthy, J. Albores-Saavedra, Correlation of CD44S expression in renal clear cell carcinomas with subsequent tumor progression or recurrence, Cancer 86(11) (1999) 2320-2326.

[105] L. Li, X. Hao, J. Qin, W. Tang, F. He, A. Smith, M. Zhang, D.M. Simeone, X.T. Qiao, Z.N. Chen, T.S. Lawrence, L. Xu, Antibody against CD44s inhibits pancreatic tumor initiation and postradiation recurrence in mice, Gastroenterology 146(4) (2014) 1108-18.
[106] Y. Tokue, Y. Matsumura, N. Katsumata, T. Watanabe, D. Tarin, T. Kakizoe, CD44 variant isoform expression and breast cancer prognosis, Jpn J Cancer Res 89(3) (1998) 283-290.
[107] Z. Li, K. Chen, P. Jiang, X. Zhang, X. Li, Z. Li, CD44v/CD44s expression patterns are associated with the survival of pancreatic carcinoma patients, Diagnostic pathology 9(1) (2014) 79.
[108] J.W. Huh, H.R. Kim, Y.J. Kim, J.H. Lee, Y.S. Park, S.H. Cho, J.K. Joo, Expression of standard CD44 in human colorectal carcinoma: Association with prognosis, Pathol Int 59(4) (2009) 241-246.
[109] K. Mima, H. Okabe, T. Ishimoto, H. Hayashi, S. Nakagawa, H. Kuroki, M. Watanabe, T. Beppu, M. Tamada, O. Nagano, H. Saya, H. Baba, CD44s Regulates the TGF-beta-Mediated Mesenchymal Phenotype and Is Associated with Poor Prognosis in Patients with Hepatocellular Carcinoma, Cancer Res 72(13) (2012) 3414-3423.
[110] H. Okabe, T. Ishimoto, K. Mima, S. Nakagawa, H. Hayashi, H. Kuroki, K. Imai, H. Nitta, S. Saito, D. Hashimoto, A. Chikamoto, T. Ishiko, M. Watanabe, O. Nagano, T. Beppu, H. Saya, H. Baba, CD44s signals the acquisition of the mesenchymal phenotype required for anchorage-independent cell survival in hepatocellular carcinoma, Brit J Cancer 110(4) (2014) 958-966.
[111] Y.H. Ko, H.S. Won, E.K. Jeon, S.H. Hong, S.Y. Roh, Y.S. Hong, J.H. Byun, C.K. Jung, J.H. Kang, Prognostic significance of CD44s expression in resected non-small cell lung cancer, Bmc Cancer 11 (2011).
[112] H.S. Kim, Y.B. Park, J.H. Oh, J. Jeong, C.J. Kim, S.H. Lee, Expression of CD44 isoforms correlates with the metastatic potential of osteosarcoma, Clin Orthop Relat R (396) (2002) 184-190.
[113] S.M. Lee, K.E. Lee, H.J. Chang, M.Y. Choi, M.S. Cho, S.K. Min, H.K. Lee, Y.C. Mun, E.M. Nam, C.M. Seong, S.N. Lee, Prognostic significance of CD44s expression in biliary tract cancers, Ann Surg Oncol 15(4) (2008) 1155-1160.
[114] C. Matuschek, M. Lehnhardt, P.A. Gerber, C. Poremba, J. Hamilton, G. Lammering, K. Orth, W. Budach, H. Bojar, E. Bolke, M. Peiper, Increased CD44s and decreased CD44v6 RNA expression are associated with better survival in myxofibrosarcoma patients: a pilot study, Eur J Med Res 19 (2014).

[115] M. Muller, R. Heicappell, F. Habermann, M. Kaufmann, U. Steiner, K. Miller, Expression of CD44V2 in transitional cell carcinoma of the urinary bladder and in urine, Urol Res 25(3) (1997) 187-192.
[116] K. Haruyama, Y. Matsumura, Y. Moriya, T. Kakizoe, A. Ochiai, M. Kawaguchi, T. Saito, Clinicopathological significance of the expression of CD44v2 in colorectal cancer, Anticancer Res 19(5C) (1999) 4421-4428.
[117] T. Gotoda, Y. Matsumura, H. Kondo, D. Saitoh, Y. Shimada, T. Kosuge, Y. Kanai, T. Kakizoe, Expression of CD44 variants and its association with survival in pancreatic cancer, Jpn J Cancer Res 89(10) (1998) 1033-1040.
[118] T. Gotoda, Y. Matsumura, H. Kondo, H. Ono, A. Kanamoto, H. Kato, H. Watanabe, Y. Tachimori, Y. Nakanishi, T. Kakizoe, Expression of CD44 variants and prognosis in oesophageal squamous cell carcinoma, Gut 46(1) (2000) 14-19.
[119] D.C. Gotley, J. Fawcett, M.D. Walsh, J.A. Reeder, D.L. Simmons, T.M. Antalis, Alternatively spliced variants of the cell adhesion molecule CD44 and tumour progression in colorectal cancer, Brit J Cancer 74(3) (1996) 342-351.
[120] E. Olsson, G. Honeth, P.O. Bendahl, L.H. Saal, S. Gruvberger-Saal, M. Ringner, J. Vallon-Christersson, G. Jonsson, K. Holm, K. Lovgren, M. Ferno, D. Grabau, A. Borg, C. Hegardt, CD44 isoforms are heterogeneously expressed in breast cancer and correlate with tumor subtypes and cancer stem cell markers, Bmc Cancer 11 (2011).
[121] L. Sherman, D. Wainwright, H. Ponta, P. Herrlich, A splice variant of CD44 expressed in the apical ectodermal ridge presents to limb mesenchyme and is required for limb outgrowth, Gene Dev 12(7) (1998) 1058-1071.
[122] V. Orian-Rousseau, CD44, a therapeutic target for metastasising tumours, Eur J Cancer 46(7) (2010) 1271-1277.
[123] K. Zen, D.Q. Liu, L.M. Li, C.X.J. Chen, Y.L. Guo, B. Ha, X. Chen, C.Y. Zhang, Y. Liu, The Heparan Sulfate Proteoglycan Form of Epithelial CD44v3 Serves as a CD11b/CD18 Counter-receptor during Polymorphonuclear Leukocyte Transepithelial Migration, J Biol Chem 284(6) (2009) 3768-3776.
[124] L.Y.W. Bourguignon, G. Wong, C. Earle, L.Q. Chen, Hyaluronan-CD44v3 Interaction with Oct4-Sox2-Nanog Promotes miR-302 Expression Leading to Self-renewal, Clonal Formation, and Cisplatin Resistance in Cancer Stem Cells from Head and Neck Squamous Cell Carcinoma, J Biol Chem 287(39) (2012) 32800-32824.

[125] E.P. Reategui, A.A. de Mayolo, P.M. Das, F.C. Astor, R. Singal, K.L. Hamilton, W.J. Goodwin, K.L. Carraway, E.J. Franzmann, Characterization of CD44v3-containing isoforms in head and neck cancer, Cancer Biol Ther 5(9) (2006) 1163-1168.
[126] X. Roca, J.L. Mate, A. Ariza, A.M. Munoz-Marmol, C. von Uexkull-Guldeband, I. Pellicer, J.J. Navas-Palacios, M. Isamat, CD44 isoform expression follows two alternative splicing pathways in breast tissue, Am J Pathol 153(1) (1998) 183-190.
[127] E. Laas, M. Ballester, A. Cortez, J. Gonin, E. Daraï, O. Graesslin, Supervised clustering of immunohistochemical markers to distinguish atypical endometrial hyperplasia from grade 1 endometrial cancer, Gynecol Oncol 133(2) (2014) 205-210.
[128] R. Kopp, M. Fichter, G. Schalhorn, J. Danescu, S. Classen, Frequent expression of the high molecular, 673-bp CD44v3,v8-10 variant in colorectal adenomas and carcinomas, Int J Mol Med 24(5) (2009) 677-683.
[129] M. Barshishat, I. Levi, D. Benharroch, B. Schwartz, Butyrate down-regulates CD44 transcription and liver colonisation in a highly metastatic human colon carcinoma cell line, Brit J Cancer 87(11) (2002) 1314-1320.
[130] P. Kaaijk, S.T. Pals, F. Morsink, D.A. Bosch, D. Troost, Differential expression of CD44 splice variants in the normal human central nervous system, J Neuroimmunol 73(1-2) (1997) 70-76.
[131] K. Zen, D.Q. Liu, Y.L. Guo, C. Wang, J. Shan, M. Fang, C.Y. Zhang, Y. Liu, CD44v4 Is a Major E-Selectin Ligand that Mediates Breast Cancer Cell Transendothelial Migration, Plos One 3(3) (2008).
[132] S.T. Wu, G.H. Sun, D.S. Hsieh, A. Chen, H.I. Chen, S.Y. Chang, D. Yu, Correlation of CD44v5 expression with invasiveness and prognosis in renal cell carcinoma, Journal of the Formosan Medical Association = Taiwan yi zhi 102(4) (2003) 229-33.
[133] C. Tempfer, A. Losch, H. Heinzl, G. Hausler, E. Hanzal, H. Kolbl, G. Breitenecker, C. Kainz, Prognostic value of immunohistochemically detected CD44 isoforms CD44v5, CD44v6 and CD44v7-8 in human breast cancer, Eur J Cancer 32A(11) (1996) 2023-5.
[134] C.H. Cheng, P.A. Sharp, Regulation of CD44 alternative splicing by SRm160 and its potential role in tumor cell invasion, Mol Cell Biol 26(1) (2006) 362-370.
[135] L. Hebbard, A. Steffen, V. Zawadzki, C. Fieber, N. Howells, J. Moll, H. Ponta, M. Hofmann, J. Sleeman, CD44 expression and regulation during mammary gland development and function, J Cell Sci 113(14) (2000) 2619-2630.

[136] H. Yang, J.L. Liu, H. Yu, P. Sun, Y. Hu, J.D. Zhong, Z.H. Zhu, Expression and association of CD44v6 with prognosis in T2-3N0M0 esophageal squamous cell carcinoma, J Thorac Dis 6(2) (2014) 91-98.
[137] S. Sato, M. Miyauchi, M. Kato, S. Kitajima, S. Kitagawa, M. Hiraoka, Y. Kudo, I. Ogawa, T. Takata, Upregulated CD44v9 expression inhibits the invasion of oral squamous cell carcinoma cells, Pathobiology 71(4) (2004) 171-175.
[138] D. Spiegelberg, M. Nestor, Characterization of CD44 Variant Expression in Cultured Head & Neck Squamous Cell Carcinomas for Possible Use in Radio-Immunotargeting, Eur J Nucl Med Mol I 39 (2012) S354-S354.
[139] K.H. Heider, H. Kuthan, G. Stehle, G. Munzert, CD44v6: a target for antibody-based cancer therapy, Cancer Immunol Immun 53(7) (2004) 567-579.
[140] Q. Yang, Y.H. Liu, Y. Huang, D.K. Huang, Y.F. Li, J. Wu, M.L. Duan, Expression of COX-2, CD44v6 and CD147 and Relationship with Invasion and Lymph Node Metastasis in Hypopharyngeal Squamous Cell Carcinoma, Plos One 8(9) (2013).
[141] S. Yanamoto, S. Yamada, H. Takahashi, T. Naruse, Y. Matsushita, H. Ikeda, T. Shiraishi, S. Seki, S. Fujita, T. Ikeda, I. Asahina, M. Umeda, Expression of the cancer stem cell markers CD44v6 and ABCG2 in tongue cancer: effect of neoadjuvant chemotherapy on local recurrence, International journal of oncology 44(4) (2014) 1153-62.
[142] S. Costa, P. Terzano, A. Bovicelli, A. Martoni, B. Angelelli, D. Santini, C. Ceccarelli, P. Lipponen, M. Erzen, S. Syrjanen, K. Syrjanen, CD44 isoform 6 (CD44v6) is a prognostic indicator of the response to neoadjuvant chemotherapy in cervical carcinoma, Gynecol Oncol 80(1) (2001) 67-73.
[143] M. Todaro, M. Gaggianesi, V. Catalano, A. Benfante, F. Iovino, M. Biffoni, T. Apuzzo, I. Sperduti, S. Volpe, G. Cocorullo, G. Gulotta, F. Dieli, R. De Maria, G. Stassi, CD44v6 Is a Marker of Constitutive and Reprogrammed Cancer Stem Cells Driving Colon Cancer Metastasis, Cell Stem Cell 14(3) (2014) 342-356.
[144] J. Ni, P.J. Cozzi, J.L. Hao, J. Beretov, L. Chang, W. Duan, S. Shigdar, W.J. Delprado, P.H. Graham, J. Bucci, J.H. Kearsley, Y. Li, CD44 variant 6 is associated with prostate cancer metastasis and chemo-/radioresistance, The Prostate 74(6) (2014) 602-617.
[145] M. Kaufmann, K.H. Heider, H.P. Sinn, G. Vonminckwitz, H. Ponta, P. Herrlich, Cd44 Variant Exon Epitopes in Primary Breast-Cancer and Length of Survival, Lancet 345(8950) (1995) 615-619.
[146] V. Orian-Rousseau, L.F. Chen, J.P. Sleeman, P. Herrlich, H. Ponta, CD44 is required for two consecutive steps in HGF/c-Met signaling, Gene Dev 16(23) (2002) 3074-3086.

[147] Y.J. Liu, P.S. Yan, J. Li, J.F. Jia, Expression and significance of CD44s, CD44v6, and nm23 mRNA in human cancer, World J Gastroentero 11(42) (2005) 6601-6606.
[148] W.M. Lau, E. Teng, H.S. Chong, K.A. Lopez, A.Y. Tay, M. Salto-Tellez, A. Shabbir, J.B. So, S.L. Chan, CD44v8-10 Is a Cancer-Specific Marker for Gastric Cancer Stem Cells, Cancer Res 74(9) (2014) 2630-41.
[149] T. Ishimoto, O. Nagano, T. Yae, M. Tamada, T. Motohara, H. Oshima, M. Oshima, T. Ikeda, R. Asaba, H. Yagi, T. Masuko, T. Shimizu, T. Ishikawa, K. Kai, E. Takahashi, Y. Imamura, Y. Baba, M. Ohmura, M. Suematsu, H. Baba, H. Saya, CD44 Variant Regulates Redox Status in Cancer Cells by Stabilizing the xCT Subunit of System xc(-) and Thereby Promotes Tumor Growth, Cancer Cell 19(3) (2011) 387-400.
[150] A. Yamaguchi, T. Urano, T. Goi, M. Saito, K. Takeuchi, K. Hirose, G. Nakagawara, H. Shiku, K. Furukawa, Expression of a CD44 variant containing exons 8 to 10 is a useful independent factor for the prediction of prognosis in colorectal cancer patients, J Clin Oncol 14(4) (1996) 1122-1127.
[151] K. Ketola, M. Hilvo, T. Hyotylainen, A. Vuoristo, A.L. Ruskeepaa, M. Oresic, O. Kallioniemi, K. Iljin, Salinomycin inhibits prostate cancer growth and migration via induction of oxidative stress, Brit J Cancer 106(1) (2012) 99-106.
[152] D. Lu, O. Tawfik, C. Pantazis, W. Hobart, J. Chapman, K. Iczkowski, Altered expression of CD44 and variant isoforms in human adenocarcinoma of the endocervix during progression, Gynecol Oncol 75(1) (1999) 84-90.
[153] A. Dellas, E. Schultheiss, A.C. Almendral, J. Torhost, F. Gudat, Expression of CD44 and variant isoforms in cervical intraepithelial neoplasia, Gynecol Oncol 62(2) (1996) 218-225.
[154] B. Mayer, K.W. Jauch, U. Gunthert, C.G. Figdor, F.W. Schildberg, I. Funke, J.P. Johnson, De-Novo Expression of Cd44 and Survival in Gastric-Cancer, Lancet 342(8878) (1993) 1019-1022.
[155] S. Koyama, T. Maruyama, S. Adachi, Expression of epidermal growth factor receptor and CD44 splicing variants sharing exons 6 and 9 on gastric and esophageal carcinomas: a two-color flow-cytometric analysis, J Cancer Res Clin 125(1) (1999) 47-54.
[156] T. Goi, K. Koneri, K. Katayama, K. Hirose, A. Yamaguchi, Evaluation of clinicopathological factors and the correlation between the adhesion molecule CD44 variant 9 expression and pulmonary metastases from colorectal cancers, Int Surg 87(2) (2002) 130-136.
[157] K. Okano, T. Shimoda, Y. Matsumura, Clinicopathologic and immunohistochemical study of early colorectal cancer with liver metastases, J Gastroenterol 34(3) (1999) 334-340.

[158] A.L. Omara-Opyene, J.X. Qiu, G.V. Shah, K.A. Iczkowski, Prostate cancer invasion is influenced more by expression of a CD44 isoform including variant 9 than by Muc18, Lab Invest 84(7) (2004) 894-907.
[159] L. Rodriguez-Rodriguez, I. Sancho-Torres, P. Leakey, D.G. Gibbon, J.T. Comerci, J.W. Ludlow, C. Mesonero, CD44 splice variant expression in clear cell carcinoma of the ovary, Gynecol Oncol 71(2) (1998) 223-229.
[160] Y. Kimura, T. Goi, T. Nakazawa, Y. Hirono, K. Katayama, T. Urano, A. Yamaguchi, CD44variant exon 9 plays an important role in colon cancer initiating cells, Oncotarget 4(5) (2013) 785-91.
[161] J. Akasaka, C. Uekuri, H. Shigetomi, M. Koike, H. Kobayashi, Hepatocyte nuclear factor (HNF)-1beta and its physiological importance in endometriosis, Biomedical reports 1(1) (2013) 13-17.
[162] B.I. Jang, Y. Li, D.Y. Graham, P.T. Cen, The Role of CD44 in the Pathogenesis, Diagnosis, and Therapy of Gastric Cancer, Gut Liver 5(4) (2011) 397-405.
[163] M. Rosel, S. Khaldoyanidi, V. Zawadzki, M. Zoller, Involvement of CD44 variant isoform v10 in progenitor cell adhesion and maturation, Exp Hematol 27(4) (1999) 698-711.
[164] M. Zoeller, CD44v10 in hematopoiesis and stem cell mobilization, Leukemia Lymphoma 38(5-6) (2000) 463-480.
[165] H. Tei, H. Miyake, K.I. Harada, M. Fujisawa, Expression profile of CD44s, CD44v6, and CD44v10 in localized prostate cancer: Effect on prognostic outcomes following radical prostatectomy, Urologic oncology (2014).
[166] F. Navaglia, P. Fogar, E. Greco, D. Basso, A.L. Stefani, S. Mazza, C.F. Zambon, W. Habeler, G. Altavilla, A. Amadori, A. Cecchetto, M. Plebani, CD44v10: An antimetastatic membrane glycoprotein for pancreatic cancer, Int J Biol Marker 18(2) (2003) 130-138.
[167] K.A. Iczkowski, A.L. Omara-Opyene, G.V. Shah, The predominant CD44 splice variant in prostate cancer binds fibronectin, and calcitonin stimulates its expression, Anticancer Res 26(4B) (2006) 2863-2872.
[168] S. Goodison, V. Urquidi, D. Tarin, CD44 cell adhesion molecules, J Clin Pathol-Mol Pa 52(4) (1999) 189-196.
[169] G.D. Wu, H. Wang, H. Zhu, Y. He, M.L. Barr, A.S. Klein, Genetic Modulation of CD44 Expression by Intragraft Fibroblasts, J Biochem 144(5) (2008) 571-580.
[170] K.A. Fitzgerald, L.A.J. O'Neill, Characterization of CD44 induction by IL-1: A critical role for Egr-1, Journal of immunology 162(8) (1999) 4920-4927.

[171] S.A. Khan, A.C. Cook, M. Kappil, U. Gunthert, A.F. Chambers, A.B. Tuck, D.T. Denhardt, Enhanced cell surface CD44 variant (v6, v9) expression by osteopontin in breast cancer epithelial cells facilitates tumor cell migration: Novel post-transcriptional, post-translational regulation, Clin Exp Metastas 22(8) (2005) 663-673.
[172] J. Hu, G. Li, P. Zhang, X. Zhuang, G. Hu, A CD44v+ subpopulation of breast cancer stem-like cells with enhanced lung metastasis capacity, Cell death & disease 8(3) (2017) e2679.
[173] M. Fichter, R. Hinrichs, G. Eissner, B. Scheffer, S. Classen, M. Ueffing, Expression of CD44 isoforms in neuroblastoma cells is regulated by PI 3-kinase and protein kinase C, Oncogene 14(23) (1997) 2817-2824.
[174] S. Weg-Remers, H. Ponta, P. Herrlich, H. Konig, Regulation of alternative pre-mRNA splicing by the ERK MAP-kinase pathway, Embo J 20(15) (2001) 4194-4203.
[175] N. Matter, P. Herrlich, H. Konig, Signal-dependent regulation of splicing via phosphorylation of Sam68, Nature 420(6916) (2002) 691-695.
[176] J.K. Thornton, C. Dalgleish, J.P. Venables, K.A. Sergeant, I.E. Ehrmann, X. Lu, P.T.K. Saunders, D.J. Elliott, The tumour-suppressor protein ASPP1 is nuclear in human germ cells and can modulate ratios of CD44 exon V5 spliced isoforms in vivo, Oncogene 25(22) (2006) 3104-3112.
[177] C.L. Yan, W. Wu, H.Y. Li, G.L. Zhang, P.J. Duerksen-Hughes, X.Q. Zhu, J. Yang, Benzo[a]pyrene treatment leads to changes in nuclear protein expression and alternative splicing, Mutat Res-Fund Mol M 686(1-2) (2010) 47-56.
[178] A.W. Griffioen, M.J.H. Coenen, C.A. Damen, S.M.M. Hellwig, D.H.J. vanWeering, W. Vooys, G.H. Blijham, G. Groenewegen, CD44 is involved in tumor angiogenesis; an activation antigen on human endothelial cells, Blood 90(3) (1997) 1150-1159.
[179] J. Li, X.M. Zha, R. Wang, X.D. Li, B. Xu, Y.J. Xu, Y.M. Yin, Regulation of CD44 expression by tumor necrosis factor-alpha and its potential role in breast cancer cell migration, Biomed Pharmacother 66(2) (2012) 144-150.
[180] S.M. Zhu, Z. Chen, J. Hong, A. Belkhiri, W. El-Rifai, Regulation of Splicing of CD44 by DARPP-32 in Gastric Cancers, Gastroenterology 144(5) (2013) S526-S527.
[181] M. Ameyar-Zazoua, C. Rachez, M. Souidi, P. Robin, L. Fritsch, R. Young, N. Morozova, R. Fenouil, N. Descostes, J.C. Andrau, J. Mathieu, A. Hamiche, S. Ait-Si-Ali, C. Muchardt, E. Batsche, A. Harel-Bellan, Argonaute proteins couple chromatin silencing to alternative splicing, Nat Struct Mol Biol 19(10) (2012) 998-U46.

[182] W.J. Wei, S.R. Mu, M. Heiner, X. Fu, L.J. Cao, X.F. Gong, A. Bindereif, J.Y. Hui, YB-1 binds to CAUC motifs and stimulates exon inclusion by enhancing the recruitment of U2AF to weak polypyrimidine tracts, Nucleic Acids Res 40(17) (2012) 8622-8636.
[183] E. Allemand, M.L. Hastings, M.V. Murray, M.P. Myers, A.R. Krainer, Alternative splicing regulation by interaction of phosphatase PP2C gamma with nucleic acid-binding protein YB-1, Nat Struct Mol Biol 14(7) (2007) 630-638.
[184] A. Honig, D. Auboeuf, M.M. Parker, B.W. O'Malley, S.M. Berget, Regulation of alternative splicing by the ATP-dependent DEAD-box RNA helicase p72, Mol Cell Biol 22(16) (2002) 5698-5707.
[185] V. Filippov, M. Filippova, P.J. Duerksen-Hughes, The early response to DNA damage can lead to activation of alternative splicing activity resulting in CD44 splice pattern changes, Cancer Res 67(16) (2007) 7621-7630.
[186] C.S. Huang, C.Y. Shen, H.W. Wang, P.E. Wu, C.W. Cheng, Increased expression of SRp40 affecting CD44 splicing is associated with the clinical outcome of lymph node metastasis in human breast cancer, Clin Chim Acta 384(1-2) (2007) 69-74.
[187] D.O. Watermann, Y.S. Tang, A. zur Hausen, M. Jager, S. Stamm, E. Stickeler, Splicing factor Tra2-beta 1 is specifically induced in breast cancer and regulates alternative splicing of the CD44 gene, Cancer Res 66(9) (2006) 4774-4780.
[188] B. Krishnamachary, M.F. Penet, S. Nimmagadda, Y. Mironchik, V. Raman, M. Solaiyappan, G.L. Semenza, M.G. Pomper, Z.M. Bhujwalla, Hypoxia Regulates CD44 and Its Variant Isoforms through HIF-1 alpha in Triple Negative Breast Cancer, Plos One 7(8) (2012).
[189] C.H. Cheng, M.B. Yaffe, P.A. Sharp, A positive feedback loop couples Ras activation and CD44 alternative splicing, Gene Dev 20(13) (2006) 1715-1720.
[190] T. Yae, K. Tsuchihashi, T. Ishimoto, T. Motohara, M. Yoshikawa, G.J. Yoshida, T. Wada, T. Masuko, K. Mogushi, H. Tanaka, T. Osawa, Y. Kanki, T. Minami, H. Aburatani, M. Ohmura, A. Kubo, M. Suematsu, K. Takahashi, H. Saya, O. Nagano, Alternative splicing of CD44 mRNA by ESRP1 enhances lung colonization of metastatic cancer cell, Nat Commun 3 (2012).
[191] C.C. Warzecha, T.K. Sato, B. Nabet, J.B. Hogenesch, R.P. Carstens, ESRP1 and ESRP2 Are Epithelial Cell-Type-Specific Regulators of FGFR2 Splicing, Mol Cell 33(5) (2009) 591-601.
[192] W. Jiang, D.K. Crossman, E.H. Mitchell, P. Sohn, M.R. Crowley, R. Serra, WNT5A Inhibits Metastasis and Alters Splicing of Cd44 in Breast Cancer Cells, Plos One 8(3) (2013).

[193] E.L. Clark, A. Coulson, C. Dalgliesh, P. Rajan, S.M. Nicol, S. Fleming, R. Heer, L. Gaughan, H.Y. Leung, D.J. Elliott, F.V. Fuller-Pace, C.N. Robson, The RNA helicase p68 is a novel androgen receptor coactivator involved in splicing and is overexpressed in prostate cancer, Cancer Res 68(19) (2008) 7938-7946.

[194] T. Zhang, X.H. Huang, L. Dong, D.Q. Hu, C.H. Ge, Y.Q. Zhan, W.X. Xu, M. Yu, W. Li, X.H. Wang, L.J. Tang, C.Y. Li, X.M. Yang, PCBP-1 regulates alternative splicing of the CD44 gene and inhibits invasion in human hepatoma cell line HepG2 cells, Mol Cancer 9 (2010).

[195] W.X. Lian, R.H. Yin, X.Z. Kong, T. Zhang, X.H. Huang, W.W. Zheng, Y. Yang, Y.Q. Zhan, W.X. Xu, M. Yu, C.H. Ge, J.T. Guo, C.Y. Li, X.M. Yang, THAP11, a novel binding protein of PCBP1, negatively regulates CD44 alternative splicing and cell invasion in a human hepatoma cell line, Febs Lett 586(10) (2012) 1431-1438.

[196] A.M. Handorean, K. Yang, E.W. Robbins, T.W. Flaig, K.A. Iczkowski, Silibinin suppresses CD44 expression in prostate cancer cells, Am J Transl Res 1(1) (2009) 80-86.

[197] Y. Zeng, D. Wodzenski, D. Gao, T. Shiraishi, N. Terada, Y.Q. Li, D.J.V. Griend, J. Luo, C.Z. Kong, R.H. Getzenberg, P. Kulkarni, Stress-Response Protein RBM3 Attenuates the Stem-like Properties of Prostate Cancer Cells by Interfering with CD44 Variant Splicing, Cancer Res 73(13) (2013) 4123-4133.

[198] Y. Kondo, K. Machida, H.M. Liu, Y. Ueno, K. Kobayashi, T. Wakita, T. Shimosegawa, M.M.C. Lai, Hepatitis C Virus Infection of T Cells Inhibits Proliferation and Enhances Fas-Mediated Apoptosis by Down-Regulating the Expression of CD44 Splicing Variant 6, J Infect Dis 199(5) (2009) 726-736.

[199] L.A. Goldstein, E.C. Butcher, Identification of Messenger-Rna That Encodes an Alternative Form of H-Cam(Cd44) in Lymphoid and Nonlymphoid Tissues, Immunogenetics 32(6) (1990) 389-397.

[200] H. Jiang, C.B. Knudson, W. Knudson, Antisense inhibition of CD44 tailless splice variant in human articular chondrocytes promotes hyaluronan internalization, Arthritis Rheum 44(11) (2001) 2599-2610.

[201] T. Ishimoto, H. Sugihara, M. Watanabe, H. Sawayama, M. Iwatsuki, Y. Baba, H. Okabe, K. Hidaka, N. Yokoyama, K. Miyake, M. Yoshikawa, O. Nagano, Y. Komohara, M. Takeya, H. Saya, H. Baba, Macrophage-derived reactive oxygen species suppress miR-328 targeting CD44 in cancer cells and promote redox adaptation, Carcinogenesis 35(5) (2014) 1003-11.

[202] J. Lesley, N. English, A. Perschl, J. Gregoroff, R. Hyman, Variant Cell-Lines Selected for Alterations in the Function of the Hyaluronan Receptor Cd44 Show Differences in Glycosylation, J Exp Med 182(2) (1995) 431-437.
[203] S. Katoh, Z. Zheng, K. Oritani, T. Shimozato, P.W. Kincade, Glycosylation of Cd44 Negatively Regulates Its Recognition of Hyaluronan, J Exp Med 182(2) (1995) 419-429.
[204] A. Maiti, G. Maki, P. Johnson, TNF-alpha induction of CD44-mediated leukocyte adhesion by sulfation, Science 282(5390) (1998) 941-943.
[205] M. Delcommenne, R. Kannagi, P. Johnson, TNF-alpha increases the carbohydrate sulfation of CD44: induction of 6-sulfo N-acetyl lactosamine on N- and O-linked glycans, Glycobiology 12(10) (2002) 613-622.
[206] P.P. Jacobs, R. Sackstein, CD44 and HCELL: Preventing hematogenous metastasis at step 1, Febs Lett 585(20) (2011) 3148-3158.
[207] D.G. Jackson, J.I. Bell, R. Dickinson, J. Timans, J. Shields, N. Whittle, Proteoglycan Forms of the Lymphocyte Homing Receptor Cd44 Are Alternatively Spliced Variants Containing the V3 Exon, J Cell Biol 128(4) (1995) 673-685.
[208] J.P. Sleeman, S. Arming, J.F. Moll, A. Hekele, W. Rudy, L.S. Sherman, G. Kreil, H. Ponta, P. Herrlich, Hyaluronate-independent metastatic behavior of CD44 variant-expressing pancreatic carcinoma cells, Cancer Res 56(13) (1996) 3134-3141.
[209] S. Julien, A. Ivetic, A. Grigoriadis, D. Qize, B. Burford, D. Sproviero, G. Picco, C. Gillett, S.L. Papp, L. Schaffer, A. Tutt, J. Taylor-Papadimitriou, S.E. Pinder, J.M. Burchell, Selectin Ligand Sialyl-Lewis x Antigen Drives Metastasis of Hormone-Dependent Breast Cancers, Cancer Res 71(24) (2011) 7683-7693.
[210] R. Kannagi, K. Sakuma, K. Miyazaki, K.T. Lim, A. Yusa, J. Yin, M. Izawa, Altered expression of glycan genes in cancers induced by epigenetic silencing and tumor hypoxia: Clues in the ongoing search for new tumor markers, Cancer Sci 101(3) (2010) 586-593.
[211] W.D. Hanley, M.M. Burdick, K. Konstantopoulos, R. Sackstein, CD44 on LS174T colon carcinoma cells possesses E-selectin ligand activity, Cancer Res 65(13) (2005) 5812-5817.
[212] C. Gorrini, I.S. Harris, T.W. Mak, Modulation of oxidative stress as an anticancer strategy, Nat Rev Drug Discov 12(12) (2013) 931-947.
[213] A. Meister, Glutathione Deficiency Produced by Inhibition of Its Synthesis, and Its Reversal - Applications in Research and Therapy, Pharmacol Therapeut 51(2) (1991) 155-194.
[214] W. Zhang, D. Trachootham, J.Y. Liu, G. Chen, H. Pelicano, C. Garcia-Prieto, W.Q. Lu, J.A. Burger, C.M. Croce, W. Plunkett, M.J. Keating, P. Huang, Stromal control of cystine

metabolism promotes cancer cell survival in chronic lymphocytic leukaemia, Nat Cell Biol 14(3) (2012) 276-+.
[215] M. Diehn, R.W. Cho, N.A. Lobo, T. Kalisky, M.J. Dorie, A.N. Kulp, D.L. Qian, J.S. Lam, L.E. Ailles, M.Z. Wong, B. Joshua, M.J. Kaplan, I. Wapnir, F.M. Dirbas, G. Somlo, C. Garberoglio, B. Paz, J. Shen, S.K. Lau, S.R. Quake, J.M. Brown, I.L. Weissman, M.F. Clarke, Association of reactive oxygen species levels and radioresistance in cancer stem cells, Nature 458(7239) (2009) 780-U123.
[216] O. Nagano, S. Okazaki, H. Saya, Redox regulation in stem-like cancer cells by CD44 variant isoforms, Oncogene 32(44) (2013) 5191-5198.
[217] K.L. Brown, A. Maiti, P. Johnson, Role of sulfation in CD44-mediated hyaluronan binding induced by inflammatory mediators in human CD14(+) peripheral blood monocytes, Journal of immunology 167(9) (2001) 5367-5374.
[218] H.C. DeGrendele, P. Estess, M.H. Siegelman, Requirement for CD44 in activated T cell extravasation into an inflammatory site, Science 278(5338) (1997) 672-675.
[219] A. Nandi, P. Estess, M.H. Siegelman, Hyaluronan anchoring and regulation on the surface of vascular endothelial cells is mediated through the functionally active form of CD44, J Biol Chem 275(20) (2000) 14939-14948.
[220] S. Katoh, T. Miyagi, H. Taniguchi, Y. Matsubara, J. Kadota, A. Tominaga, P.W. Kincade, S. Matsukura, S. Kohno, Cutting edge: An inducible sialidase regulates the hyaluronic acid binding ability of CD44-bearing human monocytes, Journal of immunology 162(9) (1999) 5058-5061.
[221] R.T. Almaraz, Y. Tian, R. Bhattarcharya, E. Tan, S.H. Chen, M.R. Dallas, L. Chen, Z. Zhang, H. Zhang, K. Konstantopoulos, K.J. Yarema, Metabolic Flux Increases Glycoprotein Sialylation: Implications for Cell Adhesion and Cancer Metastasis, Mol Cell Proteomics 11(7) (2012).
[222] B. Greenfield, W.C. Wang, H. Marquardt, M. Piepkorn, E.A. Wolff, A. Aruffo, K.L. Bennett, Characterization of the heparan sulfate and chondroitin sulfate assembly sites in CD44, J Biol Chem 274(4) (1999) 2511-2517.
[223] K.L. Bennett, D.G. Jackson, J.C. Simon, E. Tanczos, R. Peach, B. Modrell, I. Stamenkovic, G. Plowman, A. Aruffo, Cd44 Isoforms Containing Exon V3 Are Responsible for the Presentation of Heparin-Binding Growth-Factor, J Cell Biol 128(4) (1995) 687-698.
[224] R.A.F. Clark, F.B. Lin, D. Greiling, J.Q. An, J.R. Couchman, Fibroblast invasive migration into fibronectin/fibrin gels requires a previously uncharacterized dermatan sulfate-CD44 proteoglycan, J Invest Dermatol 122(2) (2004) 266-277.

[225] K. Takahashi, I. Stamenkovic, M. Cutler, A. Dasgupta, K.K. Tanabe, Keratan sulfate modification of CD44 modulates adhesion to hyaluronate, J Biol Chem 271(16) (1996) 9490-9496.
[226] V. Orian-Rousseau, H. Ponta, Adhesion Proteins Meet Receptors: A Common Theme?, Advances in Cancer Research, Vol 101 101 (2008) 63-+.
[227] M. Tremmel, A. Matzke, I. Albrecht, A.M. Laib, V. Olaku, K. Ballmer-Hofer, G. Christofori, M. Heroult, H.G. Augustin, H. Ponta, V. Orian-Rousseau, A CD44v6 peptide reveals a role of CD44 in VEGFR-2 signaling and angiogenesis, Blood 114(25) (2009) 5236-5244.
[228] S.L. Organ, M.S. Tsao, An overview of the c-MET signaling pathway, Therapeutic advances in medical oncology 3(1 Suppl) (2011) S7-S19.
[229] W. Orian-Rousseau, H. Morrison, A. Matzke, T. Kastilan, G. Pace, P. Herrlich, H. Ponta, Hepatocyte growth factor-induced Ras activation requires ERM proteins linked to both CD44v6 and F-Actin, Mol Biol Cell 18(1) (2007) 76-83.
[230] J.A. Recio, G. Merlino, Hepatocyte growth factor/scatter factor induces feedback up-regulation of CD44v6 in melanoma cells through Egr-1, Cancer Res 63(7) (2003) 1576-1582.
[231] S.P. Thankamony, W. Knudson, Acylation of CD44 and its association with lipid rafts are required for receptor and hyaluronan endocytosis, J Biol Chem 281(45) (2006) 34601-34609.
[232] Y.J. Guo, S.C. Lin, J.H. Wang, M. Bigby, M.S. Sy, Palmitoylation of Cd44 Interferes with Cd3-Mediated Signaling in Human T-Lymphocytes, Int Immunol 6(2) (1994) 213-221.
[233] D. Peck, C.M. Isacke, CD44 phosphorylation regulates melanoma cell and fibroblast migration on, but not attachment to, a hyaluronan substratum, Curr Biol 6(7) (1996) 884-890.
[234] S.J. Neame, C.M. Isacke, Phosphorylation of Cd44 Invivo Requires Both Ser323 and Ser325, but Does Not Regulate Membrane Localization or Cytoskeletal Interaction in Epithelial-Cells, Embo J 11(13) (1992) 4733-4738.
[235] J.W. Legg, C.A. Lewis, M. Parsons, T. Ng, C.M. Isacke, A novel PKC-regulated mechanism controls CD44-ezrin association and directional cell motility, Nat Cell Biol 4(6) (2002) 399-407.
[236] C.A. Lewis, P.A. Townsend, C.M. Isacke, Ca2+/calmodulin-dependent protein kinase mediates the phosphorylation of CD44 required for cell migration on hyaluronan, Biochem J 357 (2001) 843-850.

[237] G. Tzircotis, R.F. Thorne, C.M. Isacke, Directional sensing of a phorbol ester gradient requires CD44 and is regulated by CD44 phosphorylation, Oncogene 25(56) (2006) 7401-7410.
[238] L. Mellor, C.B. Knudson, D. Hida, E.B. Askew, W. Knudson, Intracellular Domain Fragment of CD44 Alters CD44 Function in Chondrocytes, J Biol Chem 288(36) (2013) 25838-25850.
[239] J. Cichy, E. Pure, The liberation of CD44, J Cell Biol 161(5) (2003) 839-843.
[240] Q. Yu, B.P. Toole, A new alternatively spliced exon between v9 and v10 provides a molecular basis for synthesis of soluble CD44, J Biol Chem 271(34) (1996) 20603-20607.
[241] M. Kajita, Y. Itoh, T. Chiba, H. Mori, A. Okada, H. Kinoh, M. Seiki, Membrane-type 1 matrix metalloproteinase cleaves CD44 and promotes cell migration, J Cell Biol 153(5) (2001) 893-904.
[242] J. Cichy, E. Pure, Cytokines regulate the affinity of soluble CD44 for hyaluronan, Febs Lett 556(1-3) (2004) 69-74.
[243] T. Murai, T. Miyauchi, T. Yanagida, Y. Sako, Epidermal growth factor-regulated activation of Rac GTPase enhances CD44 cleavage by metalloproteinase disintegrin ADAM10, Biochem J 395 (2006) 65-71.
[244] S. Murai, T. Umemiya, M. Seiki, K. Harigaya, Expression and localization of membrane-type-1 matrix metalloproteinase, CD44, and laminin-5 gamma 2 chain during colorectal carcinoma tumor progression, Virchows Arch. 445(3) (2004) 271-278.
[245] H. Sato, S. Higashi, K. Miyazaki, Amino-terminal fragments of laminin gamma 2 chain stimulate migration of metastatic breast cancer cells by interacting with CD44, Clin Exp Metastas 32(5) (2015) 405-415.
[246] I. Okamoto, Y. Kawano, D. Murakami, T. Sasayama, N. Araki, T. Miki, A.J. Wong, H. Saya, Proteolytic release of CD44 intracellular domain and its role in the CD44 signaling pathway, J Cell Biol 155(5) (2001) 755-762.
[247] I. Okamoto, H. Tsuiki, L.C. Kenyon, A.K. Godwin, D.R. Emlet, M. Holgado-Madruga, I.S. Lanham, C.J. Joynes, K.T. Vo, A. Guha, M. Matsumoto, Y. Ushio, H. Saya, A.J. Wong, Proteolytic cleavage of the CD44 adhesion molecule in multiple human tumors, Am J Pathol 160(2) (2002) 441-447.
[248] V. Subramaniam, H. Gardner, S. Jothy, Soluble CD44 secretion contributes to the acquisition of aggressive tumor phenotype in human colon cancer cells, Exp Mol Pathol 83(3) (2007) 341-346.

[249] T. Ahrens, J.P. Sleeman, C.M. Schempp, N. Howells, M. Hofmann, H. Ponta, P. Herrlich, J.C. Simon, Soluble CD44 inhibits melanoma tumor growth by blocking cell surface CD44 binding to hyaluronic acid, Oncogene 20(26) (2001) 3399-3408.
[250] E.J. Franzmann, E.P. Reategui, F. Pedroso, F.G. Pernas, B.M. Karakullukcu, K.L. Carraway, K. Hamilton, R. Singal, W.J. Goodwinl, Soluble CD44 is a potential marker for the early detection of head and neck cancer, Cancer Epidem Biomar 16(7) (2007) 1348-1355.
[251] M. Vivinus-Nebot, P. Rousselle, J.P. Breittmayer, C. Cenciarini, S. Berrih-Aknin, S. Spong, P. Nokelainen, F. Cottrez, M.P. Marinkovich, A. Bernard, Mature human thymocytes migrate on laminin-5 with activation of metalloproteinase-14 and cleavage of CD44, Journal of immunology 172(3) (2004) 1397-1406.
[252] N.M. English, J.F. Lesley, R. Hyman, Site-specific de-N-glycosylation of CD44 can activate hyaluronan binding, and CD44 activation states show distinct threshold densities for hyaluronan binding, Cancer Res 58(16) (1998) 3736-3742.
[253] T.P. Skelton, C.X. Zeng, A. Nocks, I. Stamenkovic, Glycosylation provides both stimulatory and inhibitory effects on cell surface and soluble CD44 binding to hyaluronan, J Cell Biol 140(2) (1998) 431-446.
[254] M.C. Levesque, B.F. Haynes, TNF alpha and IL-4 regulation of hyaluronan binding to monocyte CD44 involves posttranslational modification of CD44, Cell Immunol 193(2) (1999) 209-218.
[255] A. Dasgupta, K. Takahashi, M. Cutler, K.K. Tanabe, O-linked glycosylation modifies CD44 adhesion to hyaluronate in colon carcinoma cells, Biochem Bioph Res Co 227(1) (1996) 110-117.
[256] Z. Zheng, R.D. Cummings, P.E. Pummill, P.W. Kincade, Growth as a solid tumor or reduced glucose concentrations in culture reversibly induce CD44-mediated hyaluronan recognition by Chinese hamster ovary cells, J Clin Invest 100(5) (1997) 1217-1229.
[257] J.M. Cyphert, C.S. Trempus, S. Garantziotis, Size Matters: Molecular Weight Specificity of Hyaluronan Effects in Cell Biology, International journal of cell biology 2015 (2015) 563818.
[258] E.N. Harris, S.V. Kyosseva, J.A. Weigel, P.H. Weigel, Expression, processing, and glycosaminoglycan binding activity of the recombinant human 315-kDa hyaluronic acid receptor for endocytosis (HARE), J Biol Chem 282(5) (2007) 2785-2797.
[259] J.A. Weigel, R.C. Raymond, C. McGary, A. Singh, P.H. Weigel, A blocking antibody to the hyaluronan receptor for endocytosis (HARE) inhibits hyaluronan clearance by perfused liver, J Biol Chem 278(11) (2003) 9808-9812.

[260] F.A. Venning, L. Wullkopf, J.T. Erler, Targeting ECM disrupts cancer progression, Front Oncol 5 (2015).
[261] M. Culty, H.A. Nguyen, C.B. Underhill, The Hyaluronan Receptor (Cd44) Participates in the Uptake and Degradation of Hyaluronan, J Cell Biol 116(4) (1992) 1055-1062.
[262] H.X. Liao, M.C. Levesque, K. Patton, B. Bergamo, D. Jones, M.A. Moody, M.J. Telen, B.F. Haynes, Regulation of Human Cd44h and Cd44e Isoform Binding to Hyaluronan by Phorbol-Myristate Acetate and Anti-Cd44 Monoclonal and Polyclonal Antibodies, Journal of immunology 151(11) (1993) 6490-6499.
[263] Y. Liu, J. Sun, W. Cao, J. Yang, H. Lian, X. Li, Y. Sun, Y. Wang, S. Wang, Z. He, Dual targeting folate-conjugated hyaluronic acid polymeric micelles for paclitaxel delivery, International journal of pharmaceutics 421(1) (2011) 160-9.
[264] J. Chen, J. Ouyang, Q. Chen, C. Deng, F. Meng, J. Zhang, R. Cheng, Q. Lan, Z. Zhong, EGFR and CD44 Dual-Targeted Multifunctional Hyaluronic Acid Nanogels Boost Protein Delivery to Ovarian and Breast Cancers In Vitro and In Vivo, ACS applied materials & interfaces 9(28) (2017) 24140-24147.
[265] S. Ouasti, P.J. Kingham, G. Terenghi, N. Tirelli, The CD44/integrins interplay and the significance of receptor binding and re-presentation in the uptake of RGD-functionalized hyaluronic acid, Biomaterials 33(4) (2012) 1120-1134.
[266] A. Gennari, M. Pelliccia, R. Donno, I. Kimber, N. Tirelli, Mannosylation Allows for Synergic (CD44/C-Type Lectin) Uptake of Hyaluronic Acid Nanoparticles in Dendritic Cells, but Only upon Correct Ligand Presentation, Adv Healthc Mater 5(8) (2016) 966-976.
[267] S. Oliferenko, K. Paiha, T. Harder, V. Gerke, C. Schwarzler, H. Schwarz, H. Beug, U. Gunthert, L.A. Huber, Analysis of CD44-containing lipid rafts: Recruitment of annexin II and stabilization by the actin cytoskeleton, J Cell Biol 146(4) (1999) 843-854.
[268] L.Y.W. Bourguignon, Z. Gunja-Smith, N. Iida, H.B. Zhu, L.J.T. Young, W.J. Muller, R.D. Cardiff, CD44v(3,8-10) is involved in cytoskeleton-mediated tumor cell migration and matrix metalloproteinase (MMP-9) association in metastatic breast cancer cells, J Cell Physiol 176(1) (1998) 206-215.
[269] R.K. Chiu, C. Carpenito, S.T. Dougherty, G.M. Hayes, G.J. Dougherty, Identification and characterization of CD44RC, a novel alternatively spliced soluble CD44 isoform that can potentiate the hyaluronan binding activity of cell surface CD44, Neoplasia 1(5) (1999) 446-52.
[270] S. Banerji, A.J. Wright, M. Noble, D.J. Mahoney, I.D. Campbell, A.J. Day, D.G. Jackson, Structures of the Cd44-hyaluronan complex provide insight into a fundamental carbohydrate-protein interaction, Nat Struct Mol Biol 14(3) (2007) 234-239.

[271] F. Bano, S. Banerji, M. Howarth, D.G. Jackson, R.P. Richter, A single molecule assay to probe monovalent and multivalent bonds between hyaluronan and its key leukocyte receptor CD44 under force, Sci Rep-Uk 6 (2016).
[272] C.X. Yang, M.L. Cao, H. Liu, Y.Q. He, J. Xu, Y. Du, Y.W. Liu, W.J. Wang, L. Cui, J.J. Hu, F. Gao, The High and Low Molecular Weight Forms of Hyaluronan Have Distinct Effects on CD44 Clustering, J Biol Chem 287(51) (2012) 43094-43107.
[273] C.X. Yang, M.L. Cao, H. Liu, Y.Q. He, J. Xu, Y. Du, Y.W. Liu, W.J. Wang, L. Cui, J.J. Hu, F. Gao, The high and low molecular weight forms of hyaluronan have distinct effects on CD44 clustering (vol 287, 43097, 2012), J Biol Chem 288(46) (2013) 33323-33323.
[274] J.D. Kahmann, R. O'Brien, J.M. Werner, D. Heinegard, J.E. Ladbury, I.D. Campbell, A.J. Day, Localization and characterization of the hyaluronan-binding site on the Link module from human TSG-6, Structure 8(7) (2000) 763-774.
[275] V.A. Higman, D.C. Briggs, D.J. Mahoney, C.D. Blundell, B.M. Sattelle, D.P. Dyer, D.E. Green, P.L. DeAngelis, A. Almond, C.M. Milner, A.J. Day, A Refined Model for the TSG-6 Link Module in Complex with Hyaluronan Use of defines oligosaccharides to probe structure and function, J Biol Chem 289(9) (2014) 5619-5634.
[276] J. Lesley, I. Gal, D.J. Mahoney, M.R. Cordell, M.S. Rugg, R. Hyman, A.J. Day, K. Mikecz, TSG-6 modulates the interaction between hyaluronan and cell surface CD44, J Biol Chem 279(24) (2004) 25745-25754.
[277] B.H. Yang, B.L. Yang, R.C. Savani, E.A. Turley, Identification of a Common Hyaluronan-Binding Motif in the Hyaluronan-Binding Proteins Rhamm, Cd44 and Link Protein, Embo J 13(2) (1994) 286-296.
[278] K. Nakamura, K. Sawada, Y. Kinose, A. Yoshimura, A. Toda, E. Nakatsuka, K. Hashimoto, S. Mabuchi, K. Morishige, H. Kurachi, E. Lengyel, T. Kimura, Exosomes Promote Ovarian Cancer Cell Invasion through Transfer of CD44 to Peritoneal Mesothelial Cells, Mol Cancer Res 15(1) (2017) 78-92.

Chapter 2 Chitosan/HA Nanoparticles: What We Know and Don't

Julio M. Rios de la Rosa[1], Arianna Gennari[1], Maria Pelliccia[1†], Enrique Lallana[1], Roberto Donno[1], Erwin Hohn[1‡], Annalisa Tirella[1], and Nicola Tirelli[1]*

[1] NorthWest Centre for Advanced Drug Delivery (NoWCADD), School of Health Sciences, University of Manchester, Oxford Road, Manchester, M13 9PT, United Kingdom.

[†] Current address: GSK R&D, Gunnels Wood Road, Stevenage, Herts, SG1 2NY, United Kingdom.

[‡] Current address: Sandoz Biopharmaceuticals and Oncology Injectables, Lehenau 10a, 5325 Plainfield, Austria.

Manuscript in preparation.

* to whom correspondence should be addressed:

Prof. Nicola Tirelli
NorthWest Centre for Advanced Drug Delivery (NoWCADD)
Division of Pharmacy and Optometry School of Health Sciences
University of Manchester Manchester, M13 9PT, UK
E-mail: nicola.tirelli@manchester.ac.uk
Tel.: +44 161 275 24 80.

2.1. Abstract

Hyaluronic acid (HA) has emerged as an active targeting ligand in cancer and anti-inflammatory disease due to its inherent ability to interact with receptors overexpressed under these conditions, chiefly CD44. Chitosan has been commonly used in the formulation of HA-exposing nanocarriers owing to its excellent biocompatibility and versatily for the entrapping of negatively charged nucleic acid payloads. Chitosan/HA nanocarriers can be easily prepared via either ionotropic gelation (templated method) or direct polyelectroylate complexation (non-templated method); yet the relative effects of the preparative method on the properties of carrier particles and on their delivery capabilities remain unclear due to the apparent lack of direct comparison studies. In this work we have compared templated and non-templated chitosan/HA nanoparticles using two different chitosans, i.e. low and high molecular weight ($\overline{M}_v$), that differ in their binding strength with polyanions. The two preparative methods yielded nanoparticles with virtually identical physico-chemical properties but a different morphology in the case of templated low $\overline{M}_v$ chitosan particles, characterized by a higher surface exposure of HA (an "HA corona"). The toxicity profile, kinetics of uptake (on cell lysates) and silencing efficiencies of these carriers, however, were indistinguishable between templated and non-templated particles. Nanoparticle-cell interactions suggest a negligible effect of the preparative method, but unveil a major influence of the cellular model on the uptake of chitosan/HA nanoparticles. Nevertheless, the detailed cell type-specific mechanisms involved in the intracellular processing of these carriers still need to be elucidated.

Keywords: chitosan; hyaluronic acid; ionotropic gelation; polyelectrolyte complexation; siRNA delivery; A4F.

2.2. Introduction

Chitosan, a cationic linear copolymer of β-1,4-D-glucose-2-amine and N-acetyl-D-glucose-2-amine, has reached a prominent position in the formulation of nucleic acids because of its excellent biocompatibility, biodegradability and low toxicity [1-4]. Despite the huge diversity of preparative methods reported in literature to produce chitosan-based nanoparticles [5-8], ionotropic gelation and direct polyelectrolyte complexation remain widely the methods of choice due to their simplicity and benign character (absence of chemical reactions and use of very mild hydrophilic conditions) [2, 9].

In ionotropic gelation chitosan is first mixed with a cross-linker, typically sodium triphosphate (TPP), or a mixture of cross-linker and nucleic acids, in order to obtain respectively empty or loaded cationic template particles. These pre-complexed templates can be further decorated, e.g. with anionic polysaccharides like hyaluronic acid (HA) or alginate [10-12], in order to increase selectivity for cell populations of interest and/or to reduce serum proteins adsorption [13]. Our group has previously optimized the conditions for the preparation of chitosan-TPP/HA nanoparticles and evaluated the effect of chitosan molecular weight on the morphology/structure of the chitosan-TPP template on the adsorption of HA [14], linking the uptake of HA-coated carriers to a different HA presentation to CD44 receptors (both in RAW264.7 macrophages [10, 15] and XS106 dendritic cells [16]).

Direct complexation, on the other hand, relies on simple electrostatic interactions between chitosan and nucleic acids [17] (in the case of binary uncoated particles) or a mixture of nucleic acids and HA (for ternary coated ones) [18]. Although this method is in principle more advantageous due to the reduced number of user-dependent operations, it remains unknown whether the absence of a pre-complexed chitosan nanoparticle has a significant impact on the nanoparticle characteristics and overall uptake of HA-coated carriers.

In the framework of siRNA delivery, a poor transfection efficiency has been reported for binary chitosan-siRNA particles prepared by direct complexation, allegedly due to poor nanoparticle stability in cell culture medium and/or nanoparticle dissociation/aggregation prior to cell uptake [19]. However, there is a lack of consensus on the role of TPP on transfection efficiency: on the one hand, it seems that this cross-linker strengthens interactions between siRNA and chitosan and enhances transfection [20], but on the other hand some have reported the opposite effect [21]. Despite the many papers dealing with chitosan-mediated siRNA delivery, there is a gap between the understanding of the effect of nanoparticle preparation on chitosan's delivery capabilities and the role of HA in these polyplexes.

In the present study, we focused first on assessing the effect of the preparative method on the physico-chemical properties, siRNA encapsulation and morphology/structure of chitosan/HA nanoparticles. We then assessed whether the preparative procedure influences the nanoparticle's biological activity using RAW264.7 macrophages and HCT-116 cells; these are popular cellular models for the study of HA-based materials since they offer a high CD44 expression and receptor-mediated endocytosis [15, 22].

2.3. Materials and Methods

The list of materials used is provided in Supporting Information, section SI1.1. Chitosan of viscosimetric average molecular weight 36 and 656 kDa was obtained and purified as previously described [16]. The synthesis of fluorescently labelled polymer is described in Supporting Information, section SI1.1.3.

2.3.1. Preparation of chitosan/HA nanoparticles

In all cases, nanoparticles were prepared in sterile conditions (Cat. II cabinet) with surfaces previously treated with RNaseZap® solution (Thermo Scientific, UK) for nucleic acids handling. All the steps were performed under vigorous magnetic stirring (1,000 rpm) and at 25°C.

A) Template-based (TPP) method. In a typical experiment, nanoparticles were prepared by the addition of 72 μL of 0.1%wt. solution of TPP in deionized water (pH = 5 adjusted with 0.1 M HCl) to 928 μL of a 0.069%wt. solution of low or high $\overline{M}_v$ chitosan in 4.6 mM HCl (pH = 5 adjusted with 0.1 M NaOH), always at a 1:9 TPP/chitosan weight ratio. In the case of siRNA-loaded nanoparticles, TPP was dissolved in deionized nuclease-free water containing siRNA. The chitosan-TPP nanoparticle (template) dispersion was stirred for 30 min and then mixed with an equal volume of acetate buffer (200 mM, pH = 5). After 30 min an equal volume (i.e. 1 mL) of a 1.5 mg/mL HA in acetate buffer (100 mM, pH = 5) was added and kept under stirring for 30 min, always at 25°C. The resulting nanoparticle (chitosan-TPP/HA) suspension was then dialyzed against deionized water (MWCO = 1,000 kDa) for 5 h, changing the water every 20 min.

B) Direct complexation. 0.069%wt. chitosan solutions prepared as described above were mixed with an equal volume of deionized and nuclease-free water containing siRNA or simply with deionized water for 10 min at 25°C. The resulting dispersions were added to an

equal volume of a 1.5 mg/mL HA solution in water (previously adjusted to pH = 5) and stirred for 30 min.

2.3.2. Nanoparticle characterization

2.3.2.1. Elemental analysis

The composition of freeze-dried nanoparticles was analyzed using a Thermo Flash 2000 Organic Elemental Analyzer for carbon (C) and nitrogen (N), and a Thermo Scientific iCAP 6300 DUO ICP Spectrometer for phosphorus (P). Theoretical compositions were calculated under assumption that all complexations were quantitative, i.e. all TPP and HA were complexed with chitosan.

2.3.2.2. Hydrodynamic size and ζ potential

Z-average hydrodynamic size, polydispersity index (PDI), and ζ potential were measured on three independent samples at 25°C using a Zetasizer Nano ZS instrument (Model ZEN3600, Malvern Instruments Ltd., UK) equipped with a solid state HeNe laser (λ=633 nm) at a scattering angle of 173°. Size measurement data were obtained by using the General Purpose algorithm. The electrophoretic mobility of nanoparticles was converted into ζ potential values by means of the Smoluchowski equation using Malvern Zetasizer software (v7.11).

2.3.2.3. Capillary electrophoresis

Electrophoresis measurements were performed at 25 °C on a P/ACE MDQ Plus (SCIEX, Warrington, UK) equipped with a 50 cm effective length (70 cm total length) capillary with 75 μm internal diameter (Beckam Coulter, Brea, USA) and a photodiode array detector operating at 214 nm. The capillary was first conditioned by successive rinsing steps (all performed at 20 psi): 5 minutes with 1M HCl, 2 min with deionized water, 10 min with 0.1 M NaOH, 2 min with deionized water, 5 min with 20 mM phosphate buffer at pH 7.4 (running buffer), 1 min with 0.1 M NaOH, 1 min with deionized water, and finally 1.5 min with the running buffer. Each sample was then injected at 0.5 psi for 10 seconds, applying 15 kV between the anode and the injection site (normal polarity) for 60 min. At the end of each measurement, the capillary was rinsed with water for 1 min at 20 psi. Data acquisition and analysis were performed respectively with software packages 32 Karat (SCIEX) and OriginPro 8.5.1 (OriginLab Corporation, US). A calibration curve was obtained by injecting HA at known concentration (47, 188 and 750 μg/mL), thus allowing to quantify the amount of unbound HA from the area of its peak at 22 min.

2.3.2.4. Asymmetric Flow Field-Flow Fractionation (AF_4)

An AF2000 TM (Postnova Analytics, Landsberg, Germany) featuring an A4F channel an equipped with a 350 μm spacer and a regenerated cellulose 10 kDa MWCO membrane as accumulation wall was employed in connection with a UV/Vis detector operating at 220 nm (S3210, Laserchrom, Rochester, UK), a MALS detector (Viscotek SEC-MALS20, Malvern Instruments, Worcestershire, UK), a refractive index detector (Optilab T-rEX, Wyatt Technology, Dernbach, Germany) and a DLS (Zetasizer Nano SZ, Malvern) in the given order. A 0.02% (w/v) NaN_3 solution filtered through a 0.1 μm pore size filter was used as the eluent. Prior to injection, the volume of the nanoparticle suspensions was reduced by 2/3 (i.e. the particles were concentrated) *via* ultrafiltration by using a membrane with MWCO of 10 kDa. In a typical experiment, parameters were set as: 1) the detector flow rate 0.5 mL/min, 2) 100 μL of samples injected over 10 min at 0.3 mL/min, 3) cross flow rate 2.0 mL/min, and 4) focusing flow rate 2.70 mL/min (focusing step). During the elution step, the cross flow was kept constant at 2.0 mL/min for 0.5 min and then exponentially decreased (exponent = 0.40) to 0.09 mL/min over 30 min, and further exponentially decreased (exponent = 0.90) to 0.07 mL/min over 7 min, and kept constant to this value (0.07 mL/min) for 20 min. A rinse step was finally performed for 2 min, i.e. setting cross flow at 0 mL/min and purge valve on. UV/Vis, MALS and refractive index data were analyzed using AF2000 software (Postnova Analytics GmbH, Germany) and fitted with a Sphere model to obtain the $\overline{M}_v$ and radius of gyration (R_g) distributions. DLS data were analyzed using the Zetasizer Nano software (Malvern). From MALS and DLS data, two parameters were calculated:

A) $\rho = R_g/R_h$ (aspect ratio). This parameter defines some key geometrical characteristics of a colloid, and ρ values are tabulated in literature [23] for a variety of particle morphologies. For example, the ρ = 0.775 for a hard, uniform sphere, 1.0 for vesicles with thin walls (hollow spheres), and close to 1.5 for random polymer coil conformations [23, 24].

B) Fractal dimension (D). When applied to particulates, the fractal geometry analysis is another important morphological indicator; for example, aggregation of colloidal suspensions typically produces objects where the mass can be expressed as fractal power of the size (mass fractals [25, 26]), i.e. $M(R) \approx R^{Dm}$, where D_m (≤ 3) is the so-called mass fractal dimension of the particle aggregate system [27]. For instance, this parameter takes values > 2.5 for densely packed particle aggregates, whereas lower D_m values have been ascribed to more branched structures. Interestingly, the concept of fractal dimension can be also extended on a much smaller scale than individual aggregates due to the fractal scaling invariance [28, 29]; thus, R

can represent an imaginary spherical boundary center on a particle, and M the amount of mass contained within. Mass fractal dimensions of selected topologies have been calculated and can be found elsewhere [23].

2.3.2.5. siRNA loading

Encapsulation efficiency (EE): EE values (%) were calculated as $\mathrm{EE} = \frac{(A-B)}{A}\ x\ 100$, where A is the siRNA in the feed and B is the amount of non-complexed siRNA. The latter was quantified by separating as-prepared nanoparticles from the supernatant through centrifugation at 13,000 rpm for 60 min, and detecting siRNA in the supernatant with RiboGreen® following the manufacturer's instructions and using a Synergy2 Biotek plate reader.

2.3.2.6. Atomic Force Microscopy (AFM)

Drops (~35 μL) of chitosan/HA nanoparticle suspensions were deposited on a clean mica surface and left to dry overnight in petri dishes at room temperature. A Molecular Force Probe 3D AFM (MFP-3D, Asylum Research, Oxford Instruments, Abingdon, UK) equipped with an OTESPA-R3 cantilever (Bruker, Camarillo, CA, USA) was used to acquire AFM images in air at room temperature in tapping mode. Igor-Pro AFM software (Oxford Instrument, UK) was used to analyze the images.

2.3.3. Cellular studies

HCT-116 and RAW 264.7 cell lines were cultured in complete media (McCoy's 5A or high glucose DMEM, respectively) under standard conditions for cell culture (5% v/v CO_2 in air, 37°C).

2.3.3.1. Preparation of double-concentrated (2X) cell culture growth media

5.95 g McCoy's 5A powder or 6.75 g of DMEM powder, respectively, were dissolved in 175 mL of distilled water followed by addition of 3 g of HEPES. The pH was then adjusted to 7.4 by adding 1 M HCl and the volume brought to 195 mL with distilled water. The resulting medium was filtered using Disposable Sterile Filter Systems (0.22 μm) and supplemented accordingly (20% v/v FBS, 2% v/v Penicilin-Streptomycin), referred to a final volume of 250 mL.

Nanoparticle solutions for cellular experiments were prepared by addition of a given volume of double-concentrated (2X) full growth medium to an equal volume of double-concentrated nanoparticle dispersion (water).

2.3.3.2. Cytotoxicity experiments

HCT-116 (20,000 cells/cm^2) and RAW 264.7 (30,000 cells/cm^2) were seeded in 48-well plates and left to adhere overnight (5% v/v CO_2 in air, 37°C). Cells were then exposed to 0.25 mL of nanoparticle suspensions in full medium (concentration: 0.01-0.5 mg/mL) for 24 h, then determining viability using the CellTiter 96® AQueous One Solution Cell Proliferation Assay (MTS assay). Briefly, cells were washed with PBS and incubated for 1 h at 37°C in medium containing 5% (v/v) of MTS solution. Cell viability was measured by reading the absorbance values at 490 nm (Synergy2 Biotek plate reader using Gen5 software) and normalized against the total protein content in each well (BCA assay). Please note that any influence of phenol-red was ruled out by using medium as blank and subtracting its absorbance to all wells before calculating metabolic activity.

2.3.3.3. Quantification of cell uptake

HCT-116 (20,000 cells/cm^2) and RAW 264.7 (30,000 cells/cm^2) were seeded in 12-well plates and left to adhere overnight (5% v/v CO_2 in air, 37°C). Cells were then incubated with 1 mL of fluorescently-labeled nanoparticles (using chitosan-RITC for their preparation; see Supporting Information, section SI1.2, for the preparation of the labeled polymers) diluted in full medium (125 μg/mL) at 37°C for specified incubation times i.e. 0, 2, 4, 8, 16, and 24 h. Afterwards, cells were washed three times with pre-warmed PBS and lysed in 100 μL RIPA Buffer. The total uptake (combined membrane-bound and internalized materials) was calculated from fluorescence measurements of the cell lysates using a calibration curve from nanoparticle aqueous suspensions diluted in cell lysates (range 0.12-125 μg/mL). Uptake results were normalized against the total protein content per well (BCA assay). Synergy2 Biotek plate reader (Ex 540/25, Em 620/40 nm), Gen5 software; top 50% optical position.

2.3.3.4. Silencing experiments

HCT-116 (20,000 cells/cm^2) and RAW 264.7 (30,000 cells/cm^2) were seeded in 48-well plates and left to adhere overnight (5% v/v CO_2 in air, 37°C). Cells were pre-transfected for 4 h with 0.25 μg of pGL3 vector encapsulated in Lipofectamine™ LTX according to manufacturer's instructions. After subsequent removal of medium and gentle washing with warmed PBS, 0.25 mL of complete medium containing 0.67 μg of anti-Luc siRNA (200 nM) encapsulated in nanoparticles (125 μg/mL) were added to each well, with anti-Luc siRNA/LTX complex used as a positive control for transfection. Cells were incubated for 4 h with the nanoparticles, then medium was discarded and cells were washed with PBS, and further incubated with 0.25 mL of complete medium for 24 h. Finally, cells were washed with

PBS and lysed with Glo-Lysis buffer (10 min, 25°C). The luciferase activity was measured after cell lysate centrifugation (4,500 rpm, 2 min) using the ONE Glo luciferase assay following manufacturer's instructions. The relative luminescence units (RLU) were measured using a Synergy2 Biotek plate reader (Gen5 data acquisition software), and normalized against the total protein content (BCA assay) for each well.

2.4. Results and Discussion

2.4.1. Physicochemical properties of chitosan/HA and chitosan-TPP/HA nanoparticles

We first analyzed the physicochemical properties of nanoparticles prepared using the two preparative procedures: the direct polyelectrolyte complexation, where chitosan directly forms complexes with HA, *versus* the templated approach, where first chitosan is cross-linked with the trianion (i.e. at pH = 5) TPP, and then the resulting chitosan-TPP template is added over an HA solution (i.e. ionotropic gelation chitosan-TPP/HA nanoparticles). The two preparative methods yielded rather similar nanoparticles, with a strongly negative surface charge and a size distribution with similar dispersity (Table 2—1) and completely confined in the range of a few hundred nanometers (Figure 2—1, compare dashed and solid lines) for both high and low $\overline{M}_v$ chitosans. Both types of nanoparticles showed quantitative entrapping of siRNA (EE >99%), and its amount did not significantly affect the nanoparticle characteristics up to a loading of 25% wt. siRNA in relation to chitosan (Figure 2—1, Table 2—1). In addition, the stability of nanoparticles prepared by the templated method upon dialysis, storage and dilution with different solvents (Supporting Information SI1 and Figure 2—7) was comparable to that previously reported by our group for the templated method [30].

Table 2—1. Physico-chemical characteristics[a] and elemental ratios of the nanoparticles prepared in this study.

	Z-average size (nm)	PDI[b]	ζ-potential (mV)	siRNA loading		C/N[d]	P/N[d]
				Size increase[c]	EE[b]		
36 kDa chitosan							
chit-TPP *(template)*	180 ± 30	0.21 ± 0.02	+37 ± 1	1%	>99%	6.16 (5.72)	0.48 (0.36)
chit-TPP/HA *(templated)*	310 ± 50	0.17 ± 0.06	-38 ± 5	3%	>99%	11.56 (9.71)	nd (0.11)
Chit/HA *(direct)*	220 ± 30	0.19 ± 0.07	-39 ± 2	0%	>99%	10.08 (9.28)	nd (0)

656 kDa chitosan							
chit-TPP *(template)*	290 ± 20	0.20 ± 0.03	+38 ± 3	1%	>99%	6.49 (5.72)	0.31 (0.36)
chit-TPP/HA *(templated)*	320 ± 30	0.17 ± 0.06	-38 ± 4	6%	>99%	11.91 (9.71)	nd (0.11)
Chit/HA *(direct)*	260 ± 40	0.20 ± 0.05	-40 ± 2	0%	>99%	9.7 (9.28)	nd (0)

[a] In deionized water, room temperature, concentration of 1 mg/mL. Data are averages ± standard deviation from three separate experiments
[b] PDI = polydispersity index; EE= encapsulation efficiency.
[c] Ratio between Z-average size with and without siRNA (25% wt. in comparison to chitosan).
[c] Theoretical values in brackets. The detection limit for P/N analysis is 0.07.

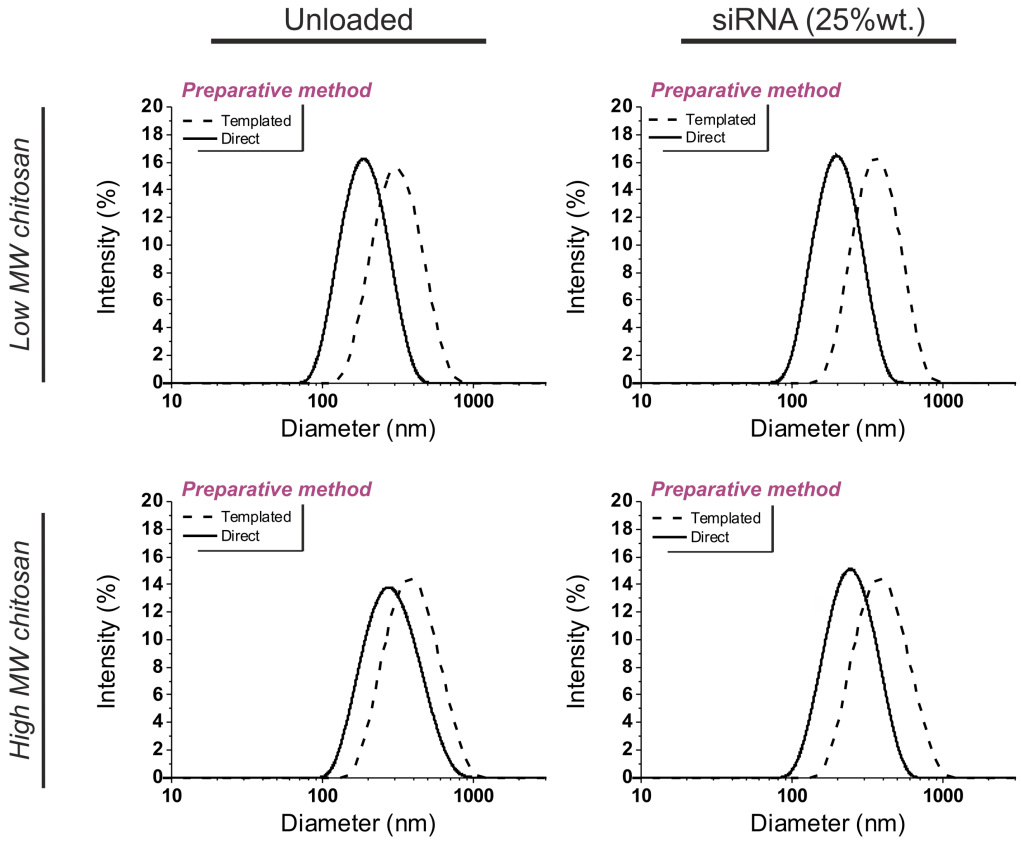

Figure 2—1. Size distribution of chitosan-HA nanoparticles (1 mg/mL, deionized water) prepared from 36 (top) and 656 (bottom) kDa chitosan using a templated (dashed lines) or direct (solid lines) complexation in the absence (left) or presence (right) of siRNA (25%wt. in relation to chitosan).

We report the nanoparticle elemental composition by means of the amount of C and P (related to the presence of TPP, chitosan, and HA) normalized by the N content to minimize the effect of the possible presence of water traces in the samples, for the same reason we discarded the analysis of hydrogen and oxygen atoms. As reported in Table 2—1, nanoparticles with

comparable C/N and P/N ratios were obtained using the two preparative methods. Most noticeably, the P/N ratio revealed that the presence of TPP could no longer be detected in chitosan-TPP/HA particles, although it was still retained in the uncoated chitosan-TPP complexes in accordance to the theoretical elemental composition. It is therefore clear that the chitosan-TPP complex (templated nanoparticles) undergoes a significant structural reorganization during the incubation step with HA. We believe that the quantitative loss of TPP is due to the weakening of the chitosan-TPP interactions by HA, possibly accentuated by the high ionic strength of the surrounding solvent (100 mM acetate buffer), which eventually results in the leakage of TPP from the nanoparticle matrix and removal during dialysis. Indeed, leakage issues during dialysis of templated chitosan/HA nanoparticles have been recently discussed [31]. Additionally, HA has been reported to weaken the electrostatic interactions of polyelectrolyte complexes between chitosan and small size polyphosphates e.g. siRNA [32]. Nevertheless, the loss of TPP from the final ionotropic formulation may play only a secondary role, as the key characteristic of this preparative procedure is the presence of a templated (pre-complexed) chitosan prior to interaction with HA, which in turn is expected to influence other important parameters such as the complexation to and presentation of HA.

2.4.2. Effect of preparative method on nanoparticle morphology

In terms of morphological characterization of resulting nanoparticles, our group has previously demonstrated with AFM images on dried samples that templated low $\overline{M}_v$ chitosan nanoparticles present a higher surface exposure of HA (i.e. an HA 'corona') than their high $\overline{M}_v$ chitosan counterpart [10, 30]. We attributed this to a different pore structure of the chitosan-TPP complex: the smaller pore (more densely cross-linked) structure of the low $\overline{M}_v$ chitosan/TPP template would favor a higher surface exposure of HA, as opposed to the larger pore (less densely cross-linked) structure of the high $\overline{M}_v$ chitosan-TPP template that would allow a deeper penetration of HA in the nanoparticle bulk, hence a lower surface presence of this polymer [10, 30]. In the case of non-templated nanoparticles, AFM images (Figure 2—2) did not show a different HA surface exposure for either low or high $\overline{M}_v$ chitosan particles (no evident HA corona). This effect could be directly ascribed to the absence of a pre-complexed chitosan, so that regardless of the chitosan $\overline{M}_v$ HA is more likely to integrate within the bulk of the nanoparticle structure to a higher extent and in a more uniformly cross-linked fashion than in the case of templated particles.

Another interesting tool for the structural elucidation and characterization of particle aggregates and discrete nanoparticles is light scattering (LS) [33]. LS permits the study of fractal geometry, which in this framework acquires special relevance since many colloid systems have been identified as mass fractals [25] (i.e. their mass M scales with their radius R following the relationship M (R) ~ R^{Dm}). Indeed, the mass fractal dimension (D_m) has been used to determine the morphologies of a plethora of nanocarriers including liposomes [26], self-assembled nanostructures [34], and gold nanoparticles [35].

In order to shed light on the morphology of our nanoparticles we analyzed suspensions prepared by either a templated or a non-templated approach using A4F coupled to RI, MALS and DLS detectors (Figure 2—3). It is worth mentioning that this analytical set-up represents an excellent tool for on-line morphological characterization of size-fractionated particles, as opposed to the batch analysis of the formulation as a whole. First, the ρ-ratio (i.e. R_g/R_h) of the eluted nanoparticles revealed average values in the range 0.75-1 for all formulations (Figure 2—3A), in agreement with a hard-uniform spherical topology [36]. Second, further analysis of the mass fractal characteristics (calculated from the slope of the fitting-line log MW vs log R_g) of the nanoparticles revealed significant differences as a function of chitosan $\overline{M}_v$ although independent on the preparative method.

In summary:

1) all nanoparticle formulations presented a $D_m \geqslant 2$, characteristic of a 3D object with spherical shape (in agreement with the ρ-ratio values and AFM data);

2) templated nanoparticles prepared from high $\overline{M}_v$ chitosan and non-templated nanoparticles prepared from both chitosans presented a D_m between 2.5-3.0, generally ascribed to objects with a moderate-to-high degree of compactness;

3) templated low $\overline{M}_v$ chitosan nanoparticles presented a D_m = 2.0, representative of a less compact structure.

We attempt to correlate these results with a different aggregation growth of the polyelectrolyte complex that in turn determines the degree of surface presentation of HA. As already mentioned, we had previously tentatively linked the presence/absence (via AFM) of an HA corona in template nanoparticles to a structural dependency of the chitosan/TPP template on the $\overline{M}_v$ of chitosan. This hypothesis seems to be corroborated by our fractal dimension results, which revealed a rather compact structure for templated high $\overline{M}_v$ chitosan particles and non-templated particles (D_m ~ 2.5-3.0), as opposed to that observed for low $\overline{M}_v$ chitosan particles (D_m = 2.0).

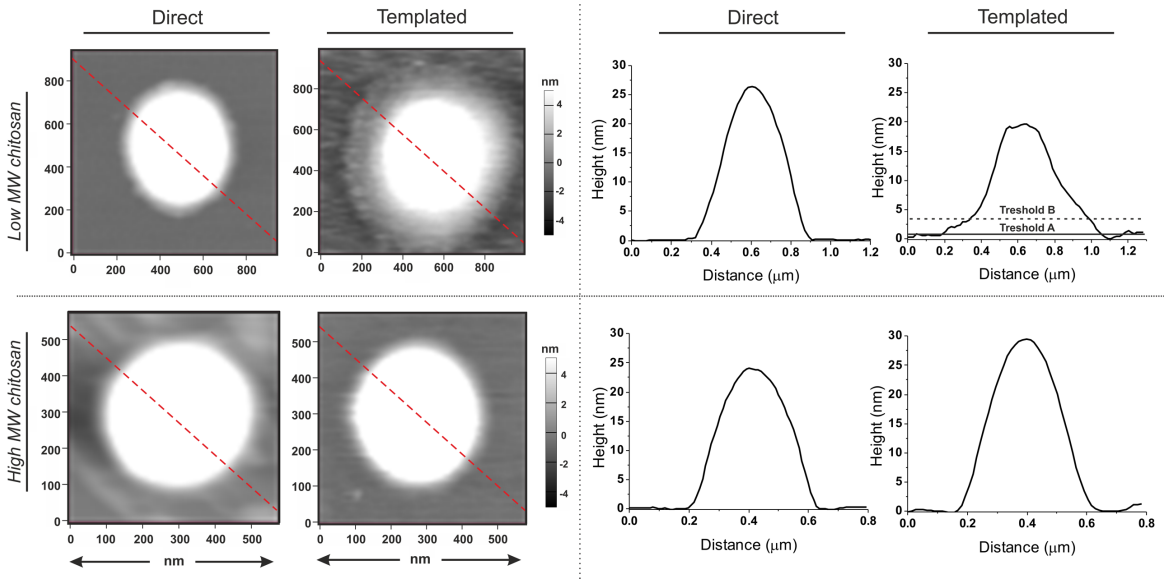

Figure 2—2. AFM characterization in dry state of nanoparticles obtained from low and high $\overline{M}_v$ chitosans *via* the two preparative methods. ***Left*:** representative AFM height images of nanoparticles. ***Right*:** Nanoparticle height profile calculated from the red dashed lines in the AFM images. Please note that for low $\overline{M}_v$ chitosan-TPP/HA nanoparticles the two thresholds used to calculate the volume distributions of the nanoparticle corona and core are highlighted.

2.4.3. Quantification of non-complexed HA

One of the most important limitations in the use of HA for drug delivery purposes is the apparent saturable behavior of its main biological target, the CD44 receptor [37, 38]. As a result, an essential factor to foresee in the design of HA-based systems is the competition not only with the host's own HA, but also with unbound, soluble HA possibly not incorporated into the engineered material. This putative competition gains more relevance when considering the use of medium-to-large HA species (>30 kDa) whose initial binding to CD44 has been described as being essentially irreversible in competition experiments with soluble HA [38]; therefore, the presence of soluble HA could potentially translate in a significant binding competition with e.g. a delivery carrier, thus hindering the therapeutic outcome. With this in mind, the amount of free (un-complexed) HA present in our nanoparticle formulations was studied by capillary electrophoresis, and precisely by analyzing nanoparticles as prepared (mixture of bound and free HA) and after a dialysis purification (only bound HA). For quantification purposes, membranes with a sufficiently large MWCO (1,000 kDa) were used and the complete removal of unbound HA after the purification step was assessed by AFM (Figure 2—3B, *right*). Interestingly, our analysis revealed that the vast majority of the HA in the feed (ca. 80%) was incorporated (complexed) in the nanoparticle structure with no significant differences between chitosan $\overline{M}_v$ or preparative methods (Figure 2—3B, *left*). However, it is important to mention that the templated preparative procedure incorporates the

same dialysis purification step; therefore, for competitive purposes, only direct complexation nanoparticles would present a low amount of free HA in solution that may presumably influence (to a low extent) nanoparticle binding and uptake.

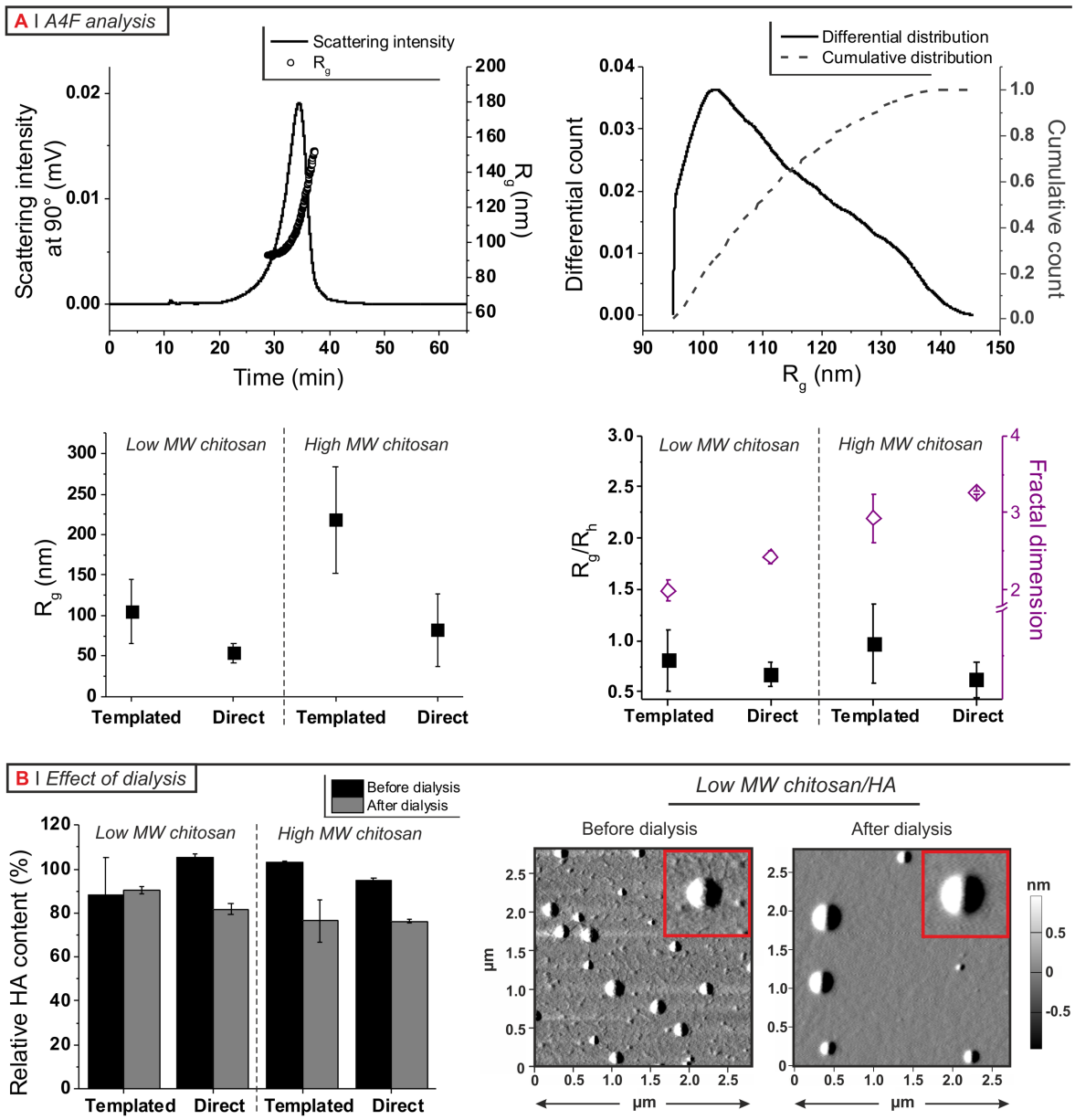

Figure 2—3. ***A:*** Asymmetric flow field-flow fractionation (A4F) characterization of nanoparticles. Top: Representative A4F elugram (left) and the corresponding differential and cumulative R_g distribution plots (right) obtained for low $\overline{M}_v$ chitosan TPP/HA nanoparticles (ionic gelation). *Bottom:* Average R_g (obtained from the maximum of the LogNormal curve fitting the differential distributions; error bars refer to the full width at half maximum) (left); mass fractal dimension and R_g/R_h ratio (calculated as reported in the experimental part, please note that the error bars reported for the fractal dimension refers to the error of the fitting) of the different nanoparticles (right). ***B:*** Quantification of free HA after nanoparticle preparation. *Left:* The HA content of the different nanoparticle formulations (1 mg/mL, deionized water) was measured by capillary electrophoresis before and after dialysis (MWCO = 1,000 kDa). Results are expressed as the relative amount of complexed HA (incorporated in the nanoparticle) relative to the total amount of HA in the nanoparticle feed (n=3). *Right:* AFM images of (low $\overline{M}_v$ chitosan) nanoparticles after dialysis showing the complete removal of unbound HA (note the absence of "debris" material on the mica surface after purification).

2.4.4. Evaluation of CD44-targeted delivery of siRNA

After thorough physico-chemical and structural characterization of the nanoparticles, we proceeded to evaluate their suitability to deliver a functional small interfering nucleic acid (siRNA). One of the most fundamental aspects to a successful intracellular siRNA delivery is the ability of the carrier to protect the cargo from enzymatic degradation to allow its release in the cytoplasm, where the RNAi machinery is located. Hence, as a first step we ruled out any differences in the protective behavior of our nanoparticles between preparative methods (Supporting Information SI3, Figure 2—9). Secondly, we evaluated the biocompatibility of these nanoparticles using two relevant cellular models: the murine RAW 264.7 macrophages (already used in our previous studies with chitosan-TPP/HA nanoparticles [10, 39]) due to their relatively high CD44 expression [40], and the human colorectal HCT-116, a CD44-overexpressing colorectal cell line whose suitability for HA-based targeting therapies has been reported in literature [22, 41, 42]. The cytotoxicity of the nanoparticles was assessed using the MTS assay, a colorimetric method that measures mitochondrial metabolic activity (data normalized against the protein content, assumed roughly proportional to the cell number). Independently of the preparative method and chitosan $\overline{M}_v$, all the formulations had a negligible effect on the cell viability up to 0.5 mg/mL in both models (Figure 2—4). Despite the fragile nature of macrophages, the low toxicity effects seen for HA-coated chitosan nanoparticles are in accordance with those reported in RAW 264.7 macrophages for other HA-based nanomaterials, such as HA-coated liposomes [43] and a library of lipid nanoparticles with surface-anchored HA [44], or chitosan-based carriers, such as mannosylated chitosan nanoparticles [45] or siRNA-entrapped chitosan nanoparticles (with or without TPP) [46]. The innocuous character of HA-coated chitosan nanoparticles in HCT-116 is also consistent with previous studies on HA-based cationic nanocarriers [47, 48].

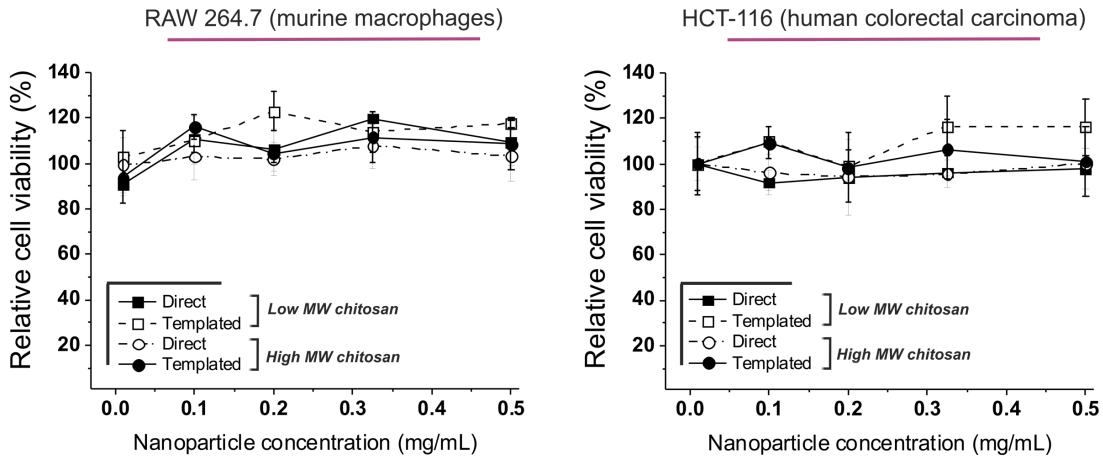

Figure 2—4. Relative cell viability of RAW 264.7 (left) and HCT-116 (right) cell lines as a function of nanoparticle concentrations (0.01-0.5 mg/mL, 24 h incubation), with mitochondrial activity values normalized against the total protein content. Percentages are relative to the normalized mitochondrial activity of untreated cells. Error bars represent standard deviation (n=3). No statistical differences were found between preparative methods.

Next we analyzed the nanoparticle uptake on cell lysates (comprising both membrane-bound and internalized materials [18]). Tracking the fluorescence of RITC-labelled nanoparticles on cell lysates up to 24 h did not reveal any significant effect of the nanoparticle preparative method in their uptake (Figure 2—5A). Our group has previously reported that the presentation of HA seems to play an important role in the uptake of nanoparticles (in RAW264.7 macrophages) [39]: the HA corona present in low $\overline{M}_v$ chitosan-TPP nanoparticles (ionotropic gelation) increases their binding affinity to CD44 receptors (faster uptake *plateau*), but conversely decreases the amount of nanoparticles taken up at saturation compared to high $\overline{M}_v$ chitosan-TPP nanoparticles (Figure 2—5). Despite the apparent lack of an HA corona in the dried state analysis for non-templated particles (AFM images in Figure 2—2), low $\overline{M}_v$ chitosan nanoparticles followed a comparatively similar uptake trend in this macrophage model (Figure 2—5A, *left*). This biological interaction therefore suggests a minor role of the HA presentation in the uptake of chitosan/HA particles. However, the nature and extent of the particle-cell interactions seem to be cell type dependent, as no differences in uptake were observed for HCT-116, regardless of the preparative method or chitosan $\overline{M}_v$ (Figure 2—5A, *right*). This seemingly erratic behavior could be ascribed to differences in the CD44 clustering between the two cell types due to a cell-specific interaction with other receptors. Interestingly, one major difference between the two cellular models in terms of their lipid raft composition is the expression levels of the toll-like receptor 4 (TLR4), an HA-related protein involved in the modulation of lipid raft-associated interactions between HA with CD44[49, 50]: while RAW264.7 macrophages are commonly used as a good model for inflammation

studies due to a readily expression of TLR4, HCT-116 are used as a model of limited TLR4 signaling [51]. Therefore, we are tempted to speculate that a differential expression of TLR4 between the two cell models could putatively lead to a distinct CD44 clustering behavior. Another possibility is that other non-receptor mediated pathways may act in concert with CD44 in the uptake of these particles. In HCT-116, it has been reported that micropinocytosis, but not CD44-mediated internalization, accounts for the majority of the uptake of octaarginine-functionalized HA-materials [22]. In RAW264.7 macrophages, CD44 has been depicted not only as an endocytic receptor, but also as a fully competent phagocytic receptor for the digestion of large particles [52]. On another note, it is also worth mentioning that the similar uptake behavior of both templated and non-templated nanoparticles seems to indicate that the small amount of soluble HA present in non-templated nanoparticles do not compete with the HA-coated chitosan nanoparticles for the cell's binding sites.

As a final step, we evaluated the silencing efficiency of nanoparticles loaded with a functional anti-luciferase (anti-Luc) siRNA. To this end, cells were first pre-transfected with a luciferase-encoding plasmid (pGL3) using low toxicity Lipofectamine (LTX) as a vector, and then cells were treated with anti-Luc siRNA vectored either in nanoparticles or LTX complexes in order to silence luciferase expression. For comparison purposes, we reproduced the experimental conditions previously reported by our group for chitosan-TPP/HA particles (i.e. delivery of 200 nM anti-Luc per well) on the difficult to transfect RAW264.7 macrophages [39]. Under our experimental conditions, both high and low $\overline{M}_v$ chitosan nanoparticles rendered similar functional readings for both preparative methods, independently of the cellular model used (Figure 2—5B). In addition, and in parallel with uptake results (Figure 2—6), we again observed a distinct cell-specific behavior: while in RAW264.7 macrophages low $\overline{M}_v$ chitosan showed a higher luciferase knockdown than high $\overline{M}_v$ chitosan, the contrary was observed in HCT-116 cells. This supports the fact that both composition and HA presentation have a lower biological impact than possibly anticipated, and in turn reveals the higher importance of cell-dependent parameters.

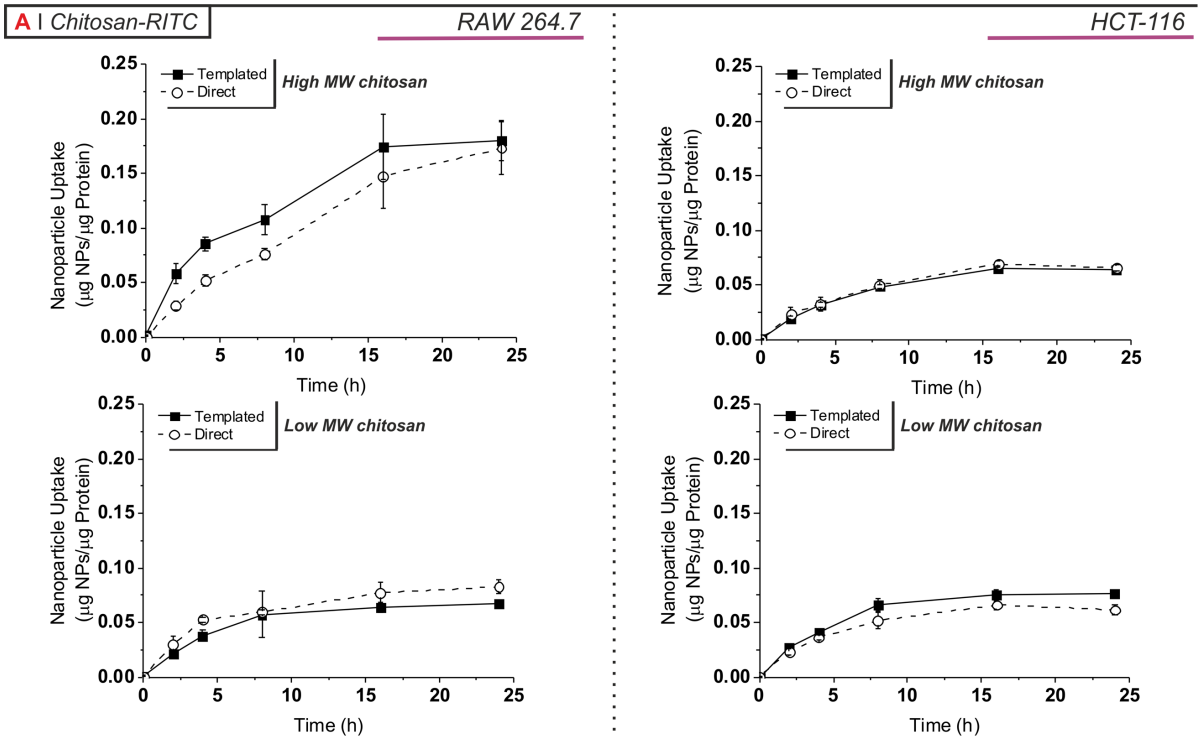

Figure 2—5. Uptake of templated (chitosan-TPP/HA) and of direct (chitosan/HA) nanoparticles followed via fluorimetry of cell lysates (normalized against the protein content) in RAW 264.7 macrophages (*left*) and HCT-116 cells (*right*). The uptake kinetics were followed by tracking chitosan labelled with RITC.

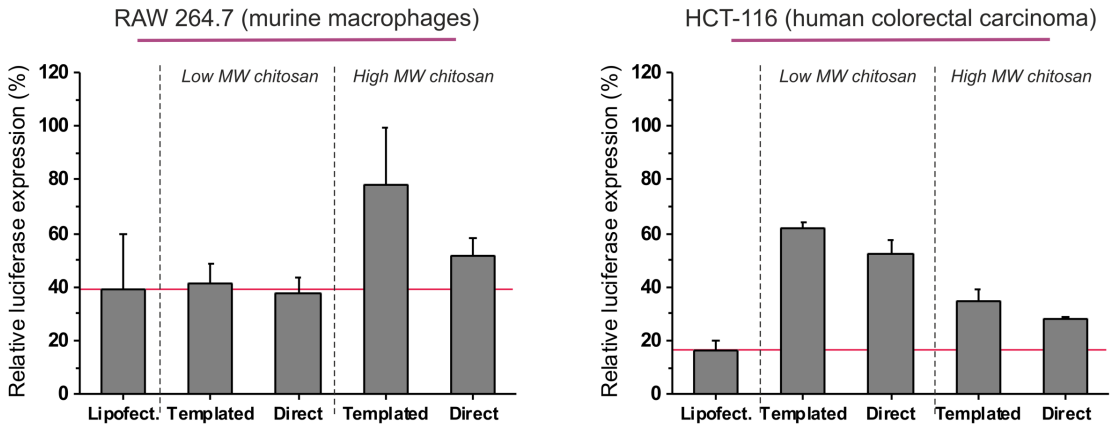

Figure 2—6. Comparison of siRNA transfection efficiencies in both cell lines using nanoparticles obtained via a templated or direct preparative method. The results are expressed as the percentage of luciferase expression relative to the average RLUs of the negative control (i.e. cells pre-transfected with the pGL3 plasmid DNA, without anti-Luc siRNA treatment) (n=3). Statistical analysis (T-test, Two-tailed) showed no significant differences between preparative methods.

2.5. Conclusion

We have compared two mainstream methods for the preparation of chitosan/HA nanoparticles, namely ionotropic gelation (templated method) and direct polyelectrolyte complexation (non-templated method) in terms of the physico-chemical properties, morphological characteristics

and biological interactions of resulting siRNA-loaded carriers with RAW264.7 macrophages and HCT-116 colorectal cancer cells. We have varied the chitosan $\overline{M}_v$ to produce nanoparticles that differed both in siRNA and HA binding strength. The results of our comparison study demonstrate that both preparative methods yield chitosan/HA nanoparticles with rather similar physico-chemical properties, but the morphology and compactness of templated low $\overline{M}_v$ chitosan nanoparticles differ from those of the other formulations (likely due to the presence of an HA corona). On the biological side, the biocompatibility, uptake kinetics and siRNA delivery are virtually identical for both preparative procedures, suggesting an almost negligible effect of the HA corona (for templated carriers) and of uncomplexed HA (for non-templated ones) on the uptake rate of chitosan/HA nanoparticles. However, we currently lack a plausible explanation for the inverted behavior of chitosan $\overline{M}_v$ on the gene silencing efficiency of RAW264.7 and HCT-116 cells. We believe it to be related to significant differences in CD44 clustering around the carriers or to additional cell-specific factors, such as the effect of the endosomal environment on the chitosan decomplexation from ternary polyplexes. These questions still need to be addressed for the design of an optimal siRNA targeted delivery strategy through chitosan/HA nanoparticles.

2.6. Acknowledgements

Kyowa Hakko Bio Italia S.r.l. (Miloano, Italy) is gratefully acknowledged for the provision of hyaluronic acid. This study was supported by EPSRC (PhD studentship for Mr. Rios de la Rosa as part of the North-West Nanoscience (NoWNano) Doctoral Training Centre, EPSRC grant EP/G03737X/1). The Bioimaging Facility of the Faculty of Life Sciences (University of Manchester) is maintained with grants from BBSRC, Wellcome Trust, and the University of Manchester Strategic Fund. AFM images were acquired at the BioAFM Facility of the University of Manchester.

The research leading to these results has received funding from the European Community's Seventh Framework Programme (FP7/2007-2013) under grant agreement n° 601738.

2.7. References

[1] A. Bernkop-Schnurch, S. Dunnhaupt, Chitosan-based drug delivery systems, Eur J Pharm Biopharm 81(3) (2012) 463-9.

[2] H. Ragelle, G. Vandermeulen, V. Preat, Chitosan-based siRNA delivery systems, J Control Release 172(1) (2013) 207-18.

[3] M.D. Buschmann, A. Merzouki, M. Lavertu, M. Thibault, M. Jean, V. Darras, Chitosans for delivery of nucleic acids, Adv Drug Deliv Rev 65(9) (2013) 1234-70.
[4] W.F. Lai, M.C. Lin, Nucleic acid delivery with chitosan and its derivatives, J Control Release 134(3) (2009) 158-68.
[5] M. Prabaharan, J.F. Mano, Chitosan-Based Particles as Controlled Drug Delivery Systems, Drug Delivery 12(1) (2004) 41-57.
[6] A. Grenha, Chitosan nanoparticles: a survey of preparation methods, J Drug Target 20(4) (2012) 291-300.
[7] K.G. Desai, Chitosan Nanoparticles Prepared by Ionotropic Gelation: An Overview of Recent Advances, Crit Rev Ther Drug Carrier Syst 33(2) (2016) 107-58.
[8] M. Garcia-Fuentes, M.J. Alonso, Chitosan-based drug nanocarriers: Where do we stand?, Journal of Controlled Release 161(2) (2012) 496-504.
[9] A. Babu, R. Ramesh, Multifaceted Applications of Chitosan in Cancer Drug Delivery and Therapy, Mar Drugs 15(4) (2017).
[10] A. Almalik, S. Karimi, S. Ouasti, R. Donno, C. Wandrey, P.J. Day, N. Tirelli, Hyaluronic acid (HA) presentation as a tool to modulate and control the receptor-mediated uptake of HA-coated nanoparticles, Biomaterials 34(21) (2013) 5369-80.
[11] M. de la Fuente, B. Seijo, M.J. Alonso, Novel hyaluronic acid-chitosan nanoparticles for ocular gene therapy, Invest Ophthalmol Vis Sci 49(5) (2008) 2016-24.
[12] C. Lemarchand, R. Gref, P. Couvreur, Polysaccharide-decorated nanoparticles, Eur J Pharm Biopharm 58(2) (2004) 327-41.
[13] A. Almalik, H. Benabdelkamel, A. Masood, I.O. Alanazi, I. Alradwan, M.A. Majrashi, A.A. Alfadda, W.M. Alghamdi, H. Alrabiah, N. Tirelli, A.H. Alhasan, Hyaluronic Acid Coated Chitosan Nanoparticles Reduced the Immunogenicity of the Formed Protein Corona, Sci Rep 7(1) (2017) 10542.
[14] A. Almalik, R. Donno, C.J. Cadman, F. Cellesi, P.J. Day, N. Tirelli, Hyaluronic acid-coated chitosan nanoparticles: molecular weight-dependent effects on morphology and hyaluronic acid presentation, J Control Release 172(3) (2013) 1142-50.
[15] A. Almalik, P.J. Day, N. Tirelli, HA-coated chitosan nanoparticles for CD44-mediated nucleic acid delivery, Macromol Biosci 13(12) (2013) 1671-80.
[16] A. Gennari, M. Pelliccia, R. Donno, I. Kimber, N. Tirelli, Mannosylation Allows for Synergic (CD44/C-Type Lectin) Uptake of Hyaluronic Acid Nanoparticles in Dendritic Cells, but Only upon Correct Ligand Presentation, Adv Healthc Mater 5(8) (2016) 966-76.

[17] X. Liu, K.A. Howard, M. Dong, M.O. Andersen, U.L. Rahbek, M.G. Johnsen, O.C. Hansen, F. Besenbacher, J. Kjems, The influence of polymeric properties on chitosan/siRNA nanoparticle formulation and gene silencing, Biomaterials 28(6) (2007) 1280-8.
[18] J.M. Rios de la Rosa, A. Tirella, A. Gennari, I.J. Stratford, N. Tirelli, The CD44-Mediated Uptake of Hyaluronic Acid-Based Carriers in Macrophages, Advanced Healthcare Materials 6(4) (2017) 1601012-n/a.
[19] H. Katas, H.O. Alpar, Development and characterisation of chitosan nanoparticles for siRNA delivery, J Control Release 115(2) (2006) 216-25.
[20] M. Ravina, E. Cubillo, D. Olmeda, R. Novoa-Carballal, E. Fernandez-Megia, R. Riguera, A. Sanchez, A. Cano, M.J. Alonso, Hyaluronic acid/chitosan-g-poly(ethylene glycol) nanoparticles for gene therapy: an application for pDNA and siRNA delivery, Pharm Res 27(12) (2010) 2544-55.
[21] S. Al-Qadi, M. Alatorre-Meda, E.M. Zaghloul, P. Taboada, C. Remunan-Lopez, Chitosan-hyaluronic acid nanoparticles for gene silencing: the role of hyaluronic acid on the nanoparticles' formation and activity, Colloids Surf B Biointerfaces 103 (2013) 615-23.
[22] Y. Yamada, M. Hashida, H. Harashima, Hyaluronic acid controls the uptake pathway and intracellular trafficking of an octaarginine-modified gene vector in CD44 positive- and CD44 negative-cells, Biomaterials 52 (2015) 189-98.
[23] W. Schartl, Light Scattering from Polymer Solutions and Nanoparticle Dispersions, Springer Lab Man Pol (2007) 1-191.
[24] W. Burchard, Static and Dynamic Light-Scattering from Branched Polymers and Bio-Polymers, Adv Polym Sci 48 (1983) 1-124.
[25] G. Stiny, Fractals - Form, Chance, and Dimension - Mandelbrot,Bb, Environ Plann B 4(2) (1977) 248-250.
[26] S. Roldan-Vargas, R. Barnadas-Rodriguez, M. Quesada-Perez, J. Estelrich, J. Callejas-Fernandez, Surface fractals in liposome aggregation, Phys Rev E 79(1) (2009).
[27] D.A. Weitz, J.S. Huang, M.Y. Lin, J. Sung, Limits of the Fractal Dimension for Irreversible Kinetic Aggregation of Gold Colloids, Phys Rev Lett 54(13) (1985) 1416-1419.
[28] J. Sabin, G. Prieto, J.M. Ruso, F. Sarmiento, Fractal aggregates induced by liposome-liposome interaction in the presence of Ca2+, Eur Phys J E 24(2) (2007) 201-210.
[29] N. Pippa, A. Dokoumetzidis, C. Demetzos, P. Macheras, On the ubiquitous presence of fractals and fractal concepts in pharmaceutical sciences: A review, Int J Pharmaceut 456(2) (2013) 340-352.

[30] A. Almalik, R. Donno, C.J. Cadman, F. Cellesi, P.J. Day, N. Tirelli, Hyaluronic acid-coated chitosan nanoparticles: Molecular weight-dependent effects on morphology and hyaluronic acid presentation, J Control Release 172(3) (2013) 1142-1150.

[31] P. Sacco, E. Decleva, F. Tentor, R. Menegazzi, M. Borgogna, S. Paoletti, K.A. Kristiansen, K.M. Varum, E. Marsich, Butyrate-Loaded Chitosan/Hyaluronan Nanoparticles: A Suitable Tool for Sustained Inhibition of ROS Release by Activated Neutrophils, Macromol Biosci (2017).

[32] S. Al-Qadi, M. Alatorre-Meda, E.M. Zaghloul, P. Taboada, C. Remunan-Lopez, Chitosan-hyaluronic acid nanoparticles for gene silencing: The role of hyaluronic acid on the nanoparticles' formation and activity, Colloid Surface B 103 (2013) 615-623.

[33] N. Pippa, S. Pispas, C. Demetzos, The fractal hologram and elucidation of the structure of liposomal carriers in aqueous and biological media, Int J Pharmaceut 430(1-2) (2012) 65-73.

[34] N. Pippa, M. Mariaki, S. Pispas, C. Demetzos, Preparation, development and in vitro release evaluation of amphotericin B-loaded amphiphilic block copolymer vectors, Int J Pharmaceut 473(1-2) (2014) 80-86.

[35] T. Kim, C.H. Lee, S.W. Joo, K. Lee, Kinetics of gold nanoparticle aggregation: Experiments and modeling, J Colloid Interf Sci 318(2) (2008) 238-243.

[36] J.P. Patterson, M.P. Robin, C. Chassenieux, O. Colombani, R.K. O'Reilly, The analysis of solution self-assembled polymeric nanomaterials, Chemical Society reviews 43(8) (2014) 2412-25.

[37] S. Ouasti, P.J. Kingham, G. Terenghi, N. Tirelli, The CD44/integrins interplay and the significance of receptor binding and re-presentation in the uptake of RGD-functionalized hyaluronic acid, Biomaterials 33(4) (2012) 1120-1134.

[38] P.M. Wolny, S. Banerji, C. Gounou, A.R. Brisson, A.J. Day, D.G. Jackson, R.P. Richter, Analysis of CD44-Hyaluronan Interactions in an Artificial Membrane System Insights into the distinct binding properties of high and low molecular weight hyaluronan, J Biol Chem 285(39) (2010) 30170-30180.

[39] A. Almalik, P.J. Day, N. Tirelli, HA-Coated Chitosan Nanoparticles for CD44-Mediated Nucleic Acid Delivery, Macromol Biosci 13(12) (2013) 1671-1680.

[40] E. Vachon, R. Martin, J. Plumb, V. Kwok, R.W. Vandivier, M. Glogauer, A. Kapus, X.M. Wang, C.W. Chow, S. Grinstein, G.P. Downey, CD44 is a phagocytic receptor, Blood 107(10) (2006) 4149-4158.

[41] K. Liang, K.H. Bae, F. Lee, K.F. Xu, J.E. Chung, S.J. Gao, M. Kurisawa, Self-assembled ternary complexes stabilized with hyaluronic acid-green tea catechin conjugates for targeted gene delivery, J Control Release 226 (2016) 205-216.
[42] O.P. Oommen, C. Duehrkop, B. Nilsson, J. Hilborn, O.P. Varghese, Multifunctional Hyaluronic Acid and Chondroitin Sulfate Nanoparticles: Impact of Glycosaminoglycan Presentation on Receptor Mediated Cellular Uptake and Immune Activation, Acs Appl Mater Inter 8(32) (2016) 20614-20624.
[43] Y. Glucksam-Galnoy, T. Zor, R. Margalit, Hyaluronan-modified and regular multilamellar liposomes provide sub-cellular targeting to macrophages, without eliciting a pro-inflammatory response, J Control Release 160(2) (2012) 388-393.
[44] S. Mizrahy, S.R. Raz, M. Hasgaard, H. Liu, N. Soffer-Tsur, K. Cohen, R. Dvash, D. Landsman-Milo, M.G.E.G. Bremer, S.M. Moghimi, D. Peer, Hyaluronan-coated nanoparticles: The influence of the molecular weight on CD44-hyaluronan interactions and on the immune response, J Control Release 156(2) (2011) 231-238.
[45] G.S. Asthana, A. Asthana, D.V. Kohli, S.P. Vyas, Mannosylated Chitosan Nanoparticles for Delivery of Antisense Oligonucleotides for Macrophage Targeting, Biomed Res Int (2014).
[46] B. Xiao, P. Ma, L. Ma, Q. Chen, X. Si, L. Walter, D. Merlin, Effects of tripolyphosphate on cellular uptake and RNA interference efficiency of chitosan-based nanoparticles in Raw 264.7 macrophages, J Colloid Interf Sci 490 (2017) 520-528.
[47] B.P. Jiang, L. Zhang, Y. Zhu, X.C. Shen, S.C. Ji, X.Y. Tan, L. Cheng, H. Liang, Water-soluble hyaluronic acid-hybridized polyaniline nanoparticles for effectively targeted photothermal therapy, J Mater Chem B 3(18) (2015) 3767-3776.
[48] G. Liang, Y. Zhu, A. Jing, J. Wang, F. Hu, W. Feng, Z. Xiao, B. Chen, Cationic microRNA-delivering nanocarriers for efficient treatment of colon carcinoma in xenograft model, Gene Ther 23(12) (2016) 829-838.
[49] H. Yamawaki, S. Hirohata, T. Miyoshi, K. Takahashi, H. Ogawa, R. Shinohata, K. Demircan, S. Kusachi, K. Yamamoto, Y. Ninomiya, Hyaluronan receptors involved in cytokine induction in monocytes, Glycobiology 19(1) (2009) 83-92.
[50] A. Higashi, Y. Dohi, N. Uraoka, K. Sentani, S. Uga, H. Kinoshita, Y. Sada, T. Kitagawa, T. Hidaka, S. Kurisu, H. Yamamoto, W. Yasui, Y. Kihara, The Potential Role of Inflammation Associated with Interaction between Osteopontin and CD44 in a Case of Pulmonary Tumor Thrombotic Microangiopathy Caused by Breast Cancer, Internal Med 54(22) (2015) 2877-2880.

[51] J.M. Rutkowsky, T.A. Knotts, K.D. Ono-Moore, C.S. McCoin, S.R. Huang, D. Schneider, S. Singh, S.H. Adams, D.H. Hwang, Acylcarnitines activate proinflammatory signaling pathways, Am J Physiol-Endoc M 306(12) (2014) E1378-E1387.
[52] E. Vachon, R. Martin, V. Kwok, V. Cherepanov, C.W. Chow, C.M. Doerschuk, J. Plumb, S. Grinstein, G.P. Downey, CD44-mediated phagocytosis induces inside-out activation of complement receptor-3 in murine macrophages, Blood 110(13) (2007) 4492-4502.
[53] A. Gennari, M. Pelliccia, R. Donno, I. Kimber, N. Tirelli, Mannosylation Allows for Synergic (CD44/C-Type Lectin) Uptake of Hyaluronic Acid Nanoparticles in Dendritic Cells, but Only upon Correct Ligand Presentation, Adv Healthc Mater 5(8) (2016) 966-976.

2.8. Supporting Information

SI1. Additional Experimental Descriptions

SI1.1. Chemicals

Chitosan of viscosity average molecular weight ($\overline{M_v}$) 656 kDa and a degree of deacetylation (DD) of 85% (from ^{1}H NMR; hereafter referred to as high $\overline{M}_v$ chitosan) was purchased from Sigma-Aldrich (Gillingham, UK) and purified in-house prior to use, as previously described [53]. Chitosan with $\overline{M_v}$ = 36 kDa and a DD = 85% (hereafter referred to as low $\overline{M}_v$ chitosan) was obtained by oxidative degradation of the above high $\overline{M}_v$ chitosan (1% wt. in 0.1 M HCl / 3 mM sodium nitrite, room temperature, 12 h) [30]. Hyaluronic acid (HA) of weight average molecular weight ($\overline{M}_w$) 180 kDa was kindly donated by Kyowa Hakko Bio Italia S.r.l. (Milano, Italy). 1 M hydrochloric acid (HCl, J/4320/15), 1 M sodium hydroxide (NaOH, J/7620/15), dimethyl sulfoxide (DMSO, D/14120/PB08) 1,2-propanol (P/7490/17) and Lissamine™ Rhodamine B Ethylenediamine (L2424) were all purchased from Thermo Fisher Scientific (Loughborough, UK). Sodium triphosphate pentabasic (TPP, #72061), rhodamine B isothiocyanate (RITC, #283924), 4-(2-hydroxyethyl)-1-piperazineethanesulfonic acid (HEPES, #90909C), 4-(4,6-dimethoxy-1,3,5-triazin-2-yl)-4-methylmorpholinium chloride (DMT-MM, #74104), BCA assay kit (BCA1 and B963), phosphate buffered saline (PBS, P4417), sodium azide (S2002) and RIPA buffer (R0278) were obtained from Sigma-Aldrich (Gillingham, UK). Glacial acetic acid and sodium acetate were purchased from VWR BDH Chemicals (Poole, UK). Chitosanase from *Streptomyces griseus* and RNAse I were purchased from Merck (Nottingham, UK). RNA Low Molecular Weight Marker Ladder (10-100 nt), GelRed™ nucleic acid gel stain, and Quant-iT™ RiboGreen® RNA assay kit reagent were purchased respectively from Affymetrix (High Wycombe, UK), Biotium (CA, USA) and

Molecular Probes (OR, USA). UltraPure™ DNase/RNase-free distilled water and low toxicity Lipofectamine® LTX reagent were purchased from Invitrogen (Paisley, UK). CellTiter 96® AQueous One Solution Cell Proliferation Assay – MTS (3-(4,5-dimethylthiazol-2-yl)-5-(3-carboxymethoxyphenyl)-2-(4-sulfophenyl)-2H-tetrazolium), pGL3 - Control Luciferase Reporter Vector, and ONE Glo Luciferase Assay System were purchased from Promega (WN, USA). Anti-Luc siRNA-1 (D-002050-01-05) with target sequence 5'-GAT TAT GTC CGG TTA TGT ATT-3' was purchased from GE-Dharmacon (UK).

SI1.2. Cell Culture

The human colorectal cancer cell line HCT-116 (CCL-247™) and the murine macrophagic cell line RAW 264.7 (TIB-71™) were purchased from ATCC (VA, USA) and cultured respectively in McCoy's 5A (M8403) or high glucose DMEM (D5671), each supplemented with 10% (v/v) foetal bovine serum (FBS) (F7524), 2 mM L-Glutamine (G7513), and 1% (v/v) Penicilin-Streptomycin (P4333). DMEM, high glucose powder (D5648) and McCoy's 5A powder (M4892) were also used to prepare double concentrated media. All products were purchased from Sigma-Aldrich (Gillingham, UK). Disposable Sterile Filter Systems (0.22 μm), cell culture flasks and well plates were purchased from Corning, UK.

SI1.3. Fluorescent labelling of chitosan

100 mg of chitosan (high or low $\bar{M}_v$), corresponding to 0.5 mmol of glucosamine (Glu) units, were dissolved in 18 mL 0.1 M acetic acid (aq) overnight and the pH was then adjusted to 4 with 0.1 M NaOH (aq). 8 mg of RITC (0.015 mmol of isothiocyanate groups) dissolved in 1.6 mL of dry DMSO were then added dropwise to the above chitosan solution. The reaction mixture was stirred (300 rpm) overnight at 25°C in the dark. Afterward, the reaction solution was diluted with 19.6 mL of deionized water and purified via centrifugal ultrafiltration against deionized water using Amicon Ultra-4 devices (MWCO 50 kDa for high $\bar{M}_v$ chitosan, 10 KDa for low $\bar{M}_v$ chitosan) until the conductivity and pH values of the wastewater reached those of deionized water. Finally, the chitosan-RITC samples were freeze-dried and stored at 4°C (Mass recovery = 85%). The degree of functionalization was determined by measuring the fluorescence intensity of the RITC-labeled chitosan products, using a calibration curve of free RITC to link the emission to the molar concentrations of the fluorophore (please note that this is then transformed in a molar ratio between functionalized and total number of Glu units in the polymer). Typical degree of derivatization achieved is 0.25-0.30% mol of Glu units.

SI2. Nanoparticle Physico-chemical Characterization and Stability

Table 2—2. Physico-chemical characteristics of nanoparticles in deionized water, room temperature, concentration of 1 mg/mL. Data are averages ± standard deviation from three separate experiments (n=3 each).

	- siRNA		**+ siRNA (25% wt.)**	
Chitosan $\overline{M}_v$	35 kDa	670 kDa	35 kDa	670 kDa
Template method				
Z-average size (nm)	310 ± 50	320 ± 30	320 ± 70	340 ± 60
PDI[a]	0.17 ± 0.06	0.22 ± 0.06	0.20 ± 0.04	0.24 ± 0.05
ζ-potential (mV)	-38 ± 5	-38 ± 4	-41 ± 5	-39 ± 6
EE (% wt.)	-	-	>99	>99
Direct complexation				
Z-average size (nm)	220 ± 30	260 ± 40	220 ± 20	260 ± 30
PDI	0.19 ± 0.07	0.20 ± 0.05	0.21 ± 0.05	0.23 ± 0.04
ζ-potential (mV)	-39 ± 2	-40 ± 2	-40 ± 2	-40 ± 2
EE (% wt.)	-	-	>99	>99

[a] PDI = polydispersity index; EE= encapsulation efficiency.

The stability of high and low $\overline{M}_v$ chitosan/HA nanoparticles was checked against:

A and B) Dialysis and storage: after preparation the particles were dialyzed against MilliQ water for 5 hours changing the water every 20 minutes. Aliquots of both dialyzed and non-dialyzed particles were then stored at 4 °C for 14 days and their stability over time was checked by DLS.

C) Dilution with different media: 1 mL of freshly prepared nanoparticles was diluted with an equal volume of either MilliQ water, 2X saline (i.e. 1.8 w/v% NaCl), 200 mM acetate buffer at pH 5 or 2X PBS, their hydrodynamic size and zeta potential were then measured by DLS.

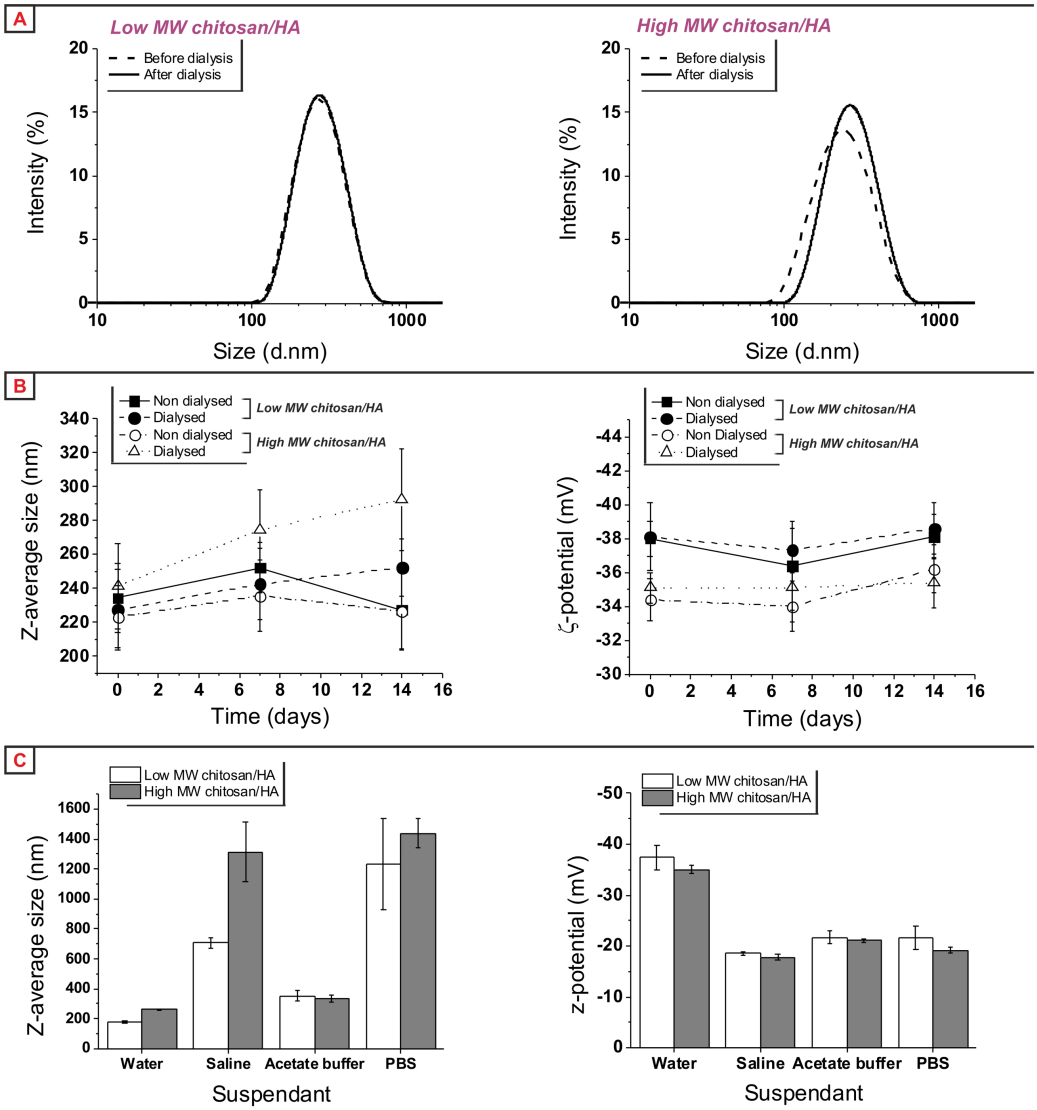

Figure 2—7. Stability of chitosan/HA nanoparticles prepared following a direct preparative method upon dialysis against water (A and B), storage for up to two weeks (B) and dilution with different media (C).

SI3. Atomic Force Microscopy (AFM)

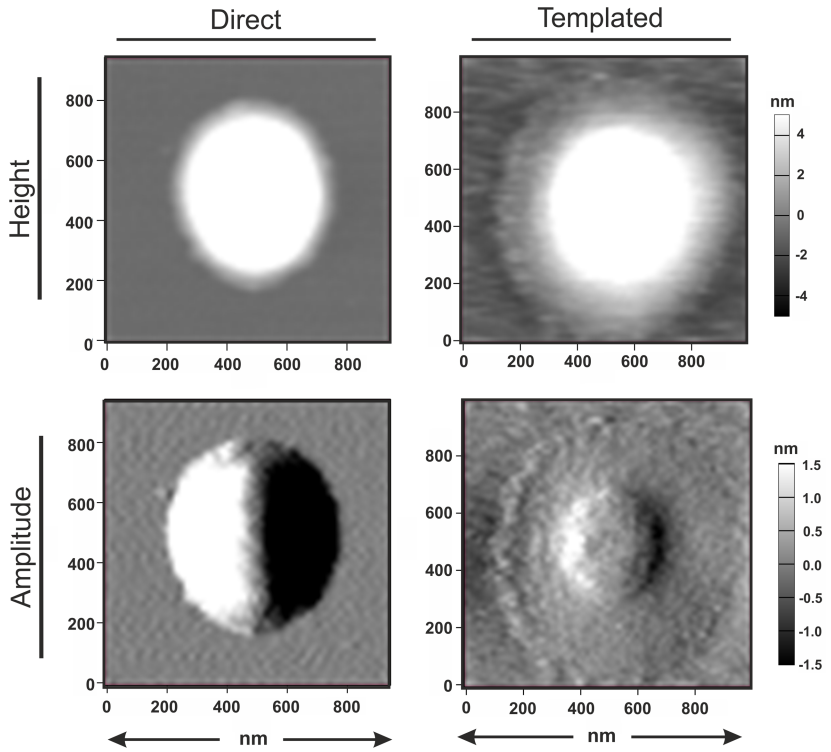

Figure 2—8. Height and Amplitude images of HA-coated low $\bar{M}_v$ chitosan nanoparticles (obtained through different preparative methods) deposited on a mica substrate. Please note the absence of the HA corona in the nanoparticles prepared via direct complexation with respect to those prepared via the templated method.

SI4. Nuclease protection assay: chitosanase/heparin-mediated siRNA release

The protection effect against nuclease degradation of low and high $\bar{M}_v$ chitosan nanoparticles prepared by ionotropic gelation or direct polyelectrolyte complexation was assayed by gel electrophoresis after nuclease and chitosanase/heparin treatment. Briefly, 44 µL of siRNA-loaded nanoparticles (25% wt. loading with respect to chitosan, a high siRNA loading for precise gel analysis) were incubated with 22 µL of a solution of RNAse I (15 mM Tris buffer, 0.3 M NaCl, pH 7.0) at a concentration of 0, 0.33 and 3.33 U (corresponding to 0, 0.5, and 5 U of enzymes per 100 µL of final reaction volume, respectively) at 37°C for 30 min. The nuclease reaction was then quenched with the addition of 7.6 µL of 1.0% SDS (aq). Afterwards, 3 µL of chitosanase (0.084 units/µL, 50 mM acetate buffer, pH 5.0) were added to the mixture, and the enzymatic reaction was allowed to occur for 3 h. Finally, 4.7 µL of a solution of heparin (200 mg/mL in nuclease-free water; corresponding approximately to a z-Hep/z-siRNA ratio of 250) were added. The resulting mixture was incubated overnight at 25°C. After centrifugation (13,000 rpm, 30 min), the nucleic acid released in solution was quantified using polyacrylamide gel electrophoresis (PAGE, 18-well/30µL, 15% Criterion

TM TBE-Urea Gel, Biorad; 70 min, 120V). Gels were imaged with a UV trans-illuminator (ChemiDoc™ MP System #170-8280) adjusting the exposure time to avoid saturation, and the acquired images were analyzed using ImageJ software (v1.49p, http://rsb.info.nih.gov/ij).

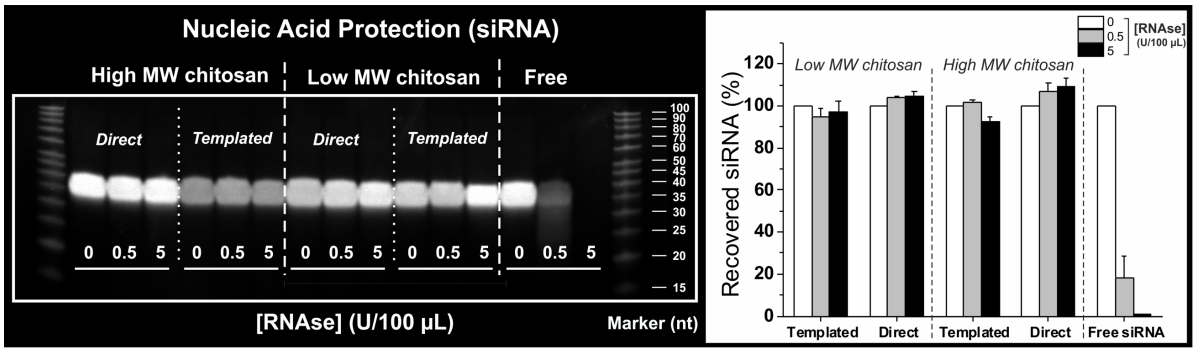

Figure 2—9. Protection of siRNA payload from enzymatic degradation. *Left:* PAGE analysis of entrapped siRNA after nanoparticle incubation with increasing concentrations of RNAse I, followed by chitosanase and heparin treatment after quenching of nucleases. Free, non-encapsulated siRNA was used as a control for RNAse I-mediated degradation. Please note that the siRNA content in the particles was 25%wt. in relation to chitosan. *Right:* Plot of the band intensities relative to the signal of the negative control (no RNAse I treatment) for each formulation. Error bars represent standard deviation (n=3). Please note that results are normalized against the amount of siRNA released from formulations incubated with no RNase I (non-degraded) to account for any dilution factor or lose of material during dialysis purification (direct nanoparticles), e.g. note the fainter bands detected for templated high $\overline{M}_v$ chitosan nanoparticles.

SI5. Total CD44 expression analysis (flow cytometry, direct staining)

Approximately 1 × 10^6 RAW264.7 or HCT-116 cells were harvested by gentle scraping in 100 µL FACS (Fluorescence-activated cell sorting) buffer (phosphate buffer solution (PBS) supplemented with 5% (v/v) FBS and 0.1% (m/v) NaN_3) per sample tube (1.5 mL Eppendorf tubes) and stained for 30 min at room temperature with Alexa Fluor® 594 anti-mouse/human CD44 Antibody, Clone IM7 (#103054, BioLegend, Cambridge, UK) as per manufacturer's instructions (< 0.25 µg antibody per million cells). To wash off any excess antibody, two serial steps of centrifugation were used and samples were suspended in a final volume of 400 µL PBS. The expression of CD44 was assessed on 10,000 live, individual cells using a BD LSRFortessa cytometer (BD Bioscience, San Jose CA, USA) equipped with the FACSDiva software (v8.0.1). Data were analyzed with FlowJo (vX.0.7, Tree Star, Ashland, OR, USA) after gating live cells in the FSC/SSC window and singlets in the FSC-H/FSC-A window, respectively. The median fluorescence intensity (MFI) of the isotype control (IgG2b, κ) was used as threshold to calculate the MFI of the marker of interest and number of positive cells.

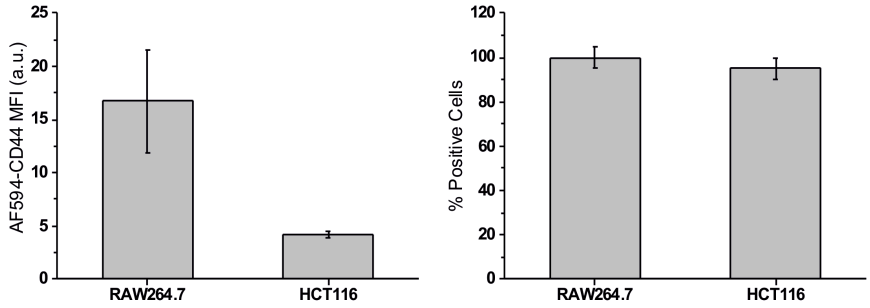

Figure 2—10. RAW264.7 and HCT-116 cells were analyzed for the expression of total CD44 using an anti-mouse/human CD44 antibody (Clone IM7) labelled with AlexaFluor594. Results are presented as average ± SD (n = 3).

Chapter 3 The CD44-Mediated Uptake of Hyaluronic Acid-Based Carriers in Macrophages

Julio M. Rios de la Rosa, Annalisa Tirella, Arianna Gennari, Ian J. Stratford and Nicola Tirelli[*]

North West Centre for Advanced Drug Delivery (NoWCADD), Division of Pharmacy & Optometry, School of Health Sciences, Faculty of Biology, Medicine and Health, Stopford building, Manchester, M13 9PT, United Kingdom

Adv. Healthcare Mater., **2017**, *6*, 1601012
DOI: 10.1002/adhm.201601012
Publication Date (Web): 19 December 2016

* to whom correspondence should be addressed:

Prof. Nicola Tirelli
NorthWest Centre for Advanced Drug Delivery (NoWCADD)
Division of Pharmacy and Optometry School of Health Sciences
University of Manchester Manchester, M13 9PT, UK
E-mail: nicola.tirelli@manchester.ac.uk
Tel.: +44 161 275 24 80.

3.1. Abstract

CD44 is a potentially rewarding target in cancer therapy, although its mechanisms of ligand binding and internalization are still poorly understood. In this study, we have established quantitative relationships between CD44 expression in differently polarized macrophages (M0, M1 and M2-polarized THP-1 human macrophages) and the uptake of hyaluronic acid (HA)-based materials, which are potentially usable for CD44 targeting. We have validated a robust method for macrophage polarization, which sequentially uses differentiating and polarizing factors, and allows to show that CD44 expression depends on polarization (M1>M0≥M2). It is noteworthy that THP-1-M2 expressed CD44v6, suggesting their suitability as a model of tumor-associated macrophages. In the uptake of HA, both as a soluble polymer and in the form of (siRNA-loaded) nanoparticles, CD44 expression correlated positively with binding, but negatively with internalization. Counterintuitively, it appears that a higher presence of CD44 (in M1) allows a more efficient capture of HA materials, but a lower expression (in M2) is conducive to better internalization. Although possibly cell-specific, this unexpected relationship indicates that the common paradigm "higher CD44 expression = better targetability" is too simplistic; mechanistic details of both receptor presentation and association still need to be elucidated for a predictable targeting behavior.

Keywords: CD44; nanoparticles; endocytosis; hyaluronan.

3.2. Introduction

The involvement of CD44 in tumorigenesis, acquisition of metastatic phenotype, and putatively as a cancer stem cell (CSC) marker [1-2] has made this receptor an interesting target in drug delivery [3-5]. Currently, two families of agents are used to target CD44:

A) Hyaluronic acid (HA)-based materials. HA is the most common natural ligand for CD44 [6] and has been used either directly as a carrier [7, 8], or as an active targeting ligand decorating nanocarriers such as lipo/polymersomes [9-11], or nanoparticles kept together by electrostatic interactions [12, 13], hydrophobic effect [14-16] or both [17]. The downsides of this approach are the competition with the host's own HA, and the moderate (from a few to hundreds of μM [18]) affinity of CD44 for HA, which is also affected by a number of complicating factors e.g. post-translational modifications [18] and in particular N-glycosylation [19, 20], which affect the HA-binding LINK module as well as flanking sequences [21], mechanical action [22], the presence of CD44 in a soluble form [23] and also the variable degree of clustering of this receptor.

B) Monoclonal antibodies. Their CD44 ligation contributes to both targeting and therapeutic effects [24] putatively ascribed to the disruption to CD44/HA interactions; for example, this is the proposed mechanism of action for the humanized recombinant RG7356 [25], which is likely the most widely used member of this family and has completed Phase I clinical trials [26]. A number of CD44 monoclonal antibodies are commercially available, some being specific to one variant isoform (e.g. the tumor-associated CD44v6 for VFF-7 [27], or CD44v10 for MEM-85 [28]), some having the non-variable region as the immunogen (e.g. RG7356). In a recent screening it has been shown that intermediate but not high affinity often correlates to high tumor uptake [29]. The drawbacks of antibodies are their potential immunogenicity, the possibly excessive specificity (which requires an appropriate patient stratification [30]), and the CD44 variability, as discussed for HA.

HA-based systems can be more easily combined with a variety of active pharmaceutical principles and have a lower cost, whereas antibodies have intrinsic therapeutic activity and higher targeting efficiency. For both classes, we still do not fully understand how CD44 expression affects binding (*strictu sensu* targeting), and how this relates to internalization; in this study we tackle these issues, using our experience with chitosan/HA (CS/HA) nanoparticles [31, 32] and soluble HA [33]. Here we use macrophages as a cellular model, because a) macrophages have a high CD44 expression and play a major role in HA uptake and degradation [34]; b) they should offer considerably less variability in CD44 structure and

behaviour than cancer cells, therefore they are an easier starting point; c) they are the prototypical off-target destination for any carrier-based therapy, therefore understanding their interactions with HA is important for the design of carriers with improved pharmacokinetics; d) they can be therapeutic targets themselves, if the tumor-associated macrophages (M2-like) are reprogrammed into a potentially tumoricidal (M1-like) phenotype [35, 36].

In terms of the macrophage model, we have have excluded primary human macrophages (difficult and invasive isolation, unable to proliferate in culture, significant donor-to-donor variations); murine cell lines such as RAW 264.7 have been extensively studied for CD44 functionality [37] and nanoparticle uptake [31, 32], and in a handful of cases their polarization has also been investigated [38, 39], but the human translatability of their classical or alternative activation is questionable. We have employed the human THP-1 cell line because: a) these premonocytes show commitment towards macrophage lineages [40-42], b) the differentiated cells resemble native monocyte-derived macrophages (MDM) in terms of morphology, antigen expression, and secretory products [40-42], c) their polarization has been studied rather extensively, and in particular the alternatively activated THP-1 cells are often regarded as a reasonable model of tumor-associated macrophages [43]. However, to date there is no consensus about the conditions for THP-1 *in vitro* polarization; for example, differentiating (phorbol 12-myristate-13-acetate, PMA) and polarizing (lipopolysaccharides, LPS, and IFN-γ for M1; IL-4 and IL-13 for M2) have been used in co-incubation [44] or in sequential treatments [43], nominally obtaining the same kind of activation, but without a quantitative comparison of the relevant phenotype markers. For this reason, we have first comparatively evaluated a set of protocols with the aim to maximize the morphological and biochemical differences between differently polarized THP-1 macrophages, and studied how macrophage polarization may affect the expression of CD44. Then, we have set out to establish a qualitative link between CD44 presence and the different phases of uptake (binding and internalization) of both soluble HA and HA-based nanoparticles.

3.3. Materials and Methods

3.3.1. General cell culture

The human monocyte cell line THP-1 (TIB-202™) was purchased from ATCC (Manassas, VA, USA) and cultured in RPMI 1640 medium (#42402-016, Lot. #1454711, Gibco®/Invitrogen, UK) supplemented with 10% (v/v) foetal bovine serum (FBS, F7524, Lot #123M3399), 2 mM L-Glutamine (G7513), 1% (v/v) antibiotic-antimycotic solution (A9909),

and 50 μM 2-mercaptoethanol (M3148), all of them purchased from Sigma-Aldrich (UK), in a humidified 5% (v/v) CO_2 air atmosphere at 37°C. Please note that all the materials were purchased from Sigma-Aldrich (UK). The medium above is hereafter referred to as complete medium. Cells were maintained at densities under 1×10^6 cells/mL, split every 2-3 days following the supplier's recommendations, and discarded upon reaching passage number 20.

Preparation of 2X concentrated RPMI 1640 medium. 10.39 g of RPMI 1640 powder (Gibco, UK) were dissolved in 350 mL of distilled water, followed by addition of 2 g of $NaHCO_3$ (*ReagentPlus*® ≥99.5%, powder, S8875, Sigma-Aldrich, UK) The pH was then adjusted to 7.1 by adding 1M HCl and the volume brought to 390 mL with distilled water. The resulting medium was filtered using Disposable Sterile Filter Systems 0.22 μm (Corning, UK) and supplemented accordingly (20% (v/v) FBS and 2% (v/v) antibiotic-antimycotic solution, referred to a final volume of 500 mL).

3.3.2. Differentiation protocols

PMA concentration. PMA (P1585, Sigma-Aldrich, UK) has been used at different concentrations, as high as 200 ng/mL (18h)[45] or 200 nM (≈120 ng/mL, 24h)[42], or as low as 25 nM (≈15 ng/mL, 48h)[46] or 5 ng/mL (48h)[47]; we have chosen an intermediate concentration (50 ng/mL) to avoid undesired gene upregulation seen with larger doses[47], but still provide a stable attachment of differentiated cells over the 24 hour period.

Cell density. It has been observed that more homogeneous THP-1 populations can be obtained using relatively low ($<1\times10^6$ cells/mL) premonocyte cell density [48]; in this study we have employed 5×10^5 cells/mL, corresponding to 1.25×10^5 cells/cm^2 in case of full attachment. All the cytokines mentioned before were purchased from Peprotech, Inc.

A) For premonocyte – M0 differentiation, the cells were incubated for 24 hours with 50 ng·mL^{-1} PMA in complete medium. Differentiated, adherent cells were washed twice with serum-free medium and then rested for a further 24 or 48 hours in PMA-free complete medium to obtain resting macrophages respectively defined as **M0$^{[24]}$** or **M0$^{[24]*}$**.

B) *For premonocyte – M1 differentiation/polarization*, in complete medium, the cells were treated **either** for 6 hours with 50 ng·mL^{-1} PMA, and then co-incubated with 100 ng·mL^{-1} Lipopolysaccharides (LPS) from *E. coli* O26:B6 (L8274, Lot. #032M4089V, Sigma-Aldrich, UK), 20 ng·mL^{-1} IFN-γ (#300-02, Lot #081427) and 50 ng·mL^{-1} PMA for the following 18 hours (followed by a 24h resting phase complete medium), **or** for 24 hours with 50 ng·mL^{-1}

PMA, and with 100 ng·mL^{-1} LPS and 20 ng·mL^{-1} IFN-γ (no PMA) for the following 24 hours, to obtain classically activated macrophages respectively defined as **M1$^{[6/18]}$** or **M1$^{[24/24]}$**.

C) For premonocyte – M2 differentiation/polarization, the cells were treated as in B) replacing LPS/IFN-γ with 20 ng·mL^{-1} IL-4 (#200-04, Lot #061314) and 20 ng·mL^{-1} IL-13 (#200-13, Lot #051023), obtaining alternatively activated macrophages defined as **M2$^{[6/18]}$** or **M2$^{[24/24]}$**.

3.3.3. Flow cytometry analysis

A) Direct staining: THP-1 premonocytes were differentiated and polarized on Nunc UpCell™ 12-well thermo-sensitive plates (Thermo-Scientific, UK), designed to promote cell detachment and subsequent suspension by cooling the plates at room temperature for 30 minutes. Approximately 0.5×10^6 cells were harvested in 100 µL FACS buffer (PBS supplemented with 2% (v/v) FBS and 0.1% (m/v) NaN_3) per sample tube (1.5 mL Eppendorf tubes), incubated for 20 minutes on ice with Fc-receptor blocking inhibitor (#14-9161, Affymetrix/eBioscience, UK) and then stained for 30 minutes at room temperature with primary-conjugated antibodies: i) mouse anti-human CD44:APC (1:20) (Clone MEM-263; Abcam, UK), ii) CD11c:PerCP/Cy5.5 (1:40) (Clone Bu15; BioLegend, UK), iii) CD14:FITC (1:10) (Clone MEM-18; AbD Serotec, UK), and iv) (1:10) CD206:PE (Clone 15-2; BioLegend, UK). To wash off any excess/unbound antibody, two serial steps of centrifugation were used. The expression of surface markers was assessed on 10,000 live, individual cells with a CyAn™ ADP analyzer using the Summit software (v4.3, Beckman Coulter, Inc.). Data were analyzed with FlowJo (vX.0.7, Tree Star, Ashland, OR, USA) after gating live and single events in the FSC/SSC and Pulse width/FSC windows, respectively. The median fluorescence intensity (MFI) of the isotype control (Mouse IgG1; AbD Serotec, UK) was used as threshold to calculate the MFI of the marker of interest. Shifts in the FSC and SSC signal along macrophage differentiation and polarization were also analyzed to evaluate phenotypical changes (cell size and inner cellular complexity). The same detachment procedure (without staining) was used to assess size and granularity for the morphological analysis.

B) Indirect staining: THP-1 premonocytes were differentiated to M0$^{[48]}$, M1$^{[24/24]}$ and M2$^{[24/24]}$ in Costar® polystyrene 6-well plates (3506, Corning, UK). Cells were detached using pre-warmed Cell Dissociation Buffer, Enzyme-Free, PBS (#13151-014, Gibco®/Invitrogen, UK). Approximately 0.5×10^6 cells were suspended in 100 µL FACS buffer per sample tube (1.5

mL Eppendorf tubes), incubated for 20 minutes on ice with Fc-receptor blocking inhibitor (#14-9161, Affymetrix/eBioscience, UK) and stained for 30 minutes at room temperature with the primary antibodies: i) mouse anti-human CD44 (1:100) (156-3C11, Cell Signaling), ii) mouse anti-human CD44v3 (1:20) (Clone #3G5, R&D Systems), iii) mouse anti-human CD44v4 (1:50) (MCA1728; AbD Serotec), iv) mouse anti-human CD44v6 (1:20) (Clone #2F10, R&D Systems), or v) IgG1/IgG2 control (1:10) (AbD Serotec). Excess antibody was removed by centrifugation and cells were incubated for further 30 minutes at room temperature with the secondary antibody: goat anti-mouse IgG H&L, AlexaFluor®647-conjugated (1:2000) (ab150115, Abcam). The expression of these markers was detected on 10,000 live, individual cells using a BD LSRFortessa cytometer (BD Bioscience, San Jose CA, USA) equipped with the FACSDiva software (v8.0.1). Data were analyzed with FlowJo (vX.0.7, Tree Star, Ashland, OR, USA) after gating live cells in the FSC/SSC window and singlets in the FSC-H/FSC-A window, respectively. The median fluorescence intensity (MFI) of the isotype control was used as threshold to calculate the MFI of the marker of interest.

3.3.4. Western blot analysis

THP-1 premonocytes were differentiated and polarized in Costar® 25cm² polystyrene angled neck flasks (3056, Corning, UK). Total cell extracts were prepared in ice-cold RIPA Buffer (R0278, Sigma-Aldrich, UK) supplemented with cOmpleteUltra Tablets, Mini, EDTA-free EASYpack (#05892791001, Roche, Germany) and stored at -80°C until use. Equal amounts of protein (cell lysates) in Laemmli buffer containing 5% (v/v) 2-mercaptoethanol (M3148, Sigma-Aldrich, UK) were separated by 7.5% acrylamide SDS-PAGE using a Criterion™ Cell (#165-6001; Run settings: 1 hour, 100V, 0.5 A) and transferred to a PVDF membrane (#162-0177 using a Criterion™ Blotter (#170-4070; Run settings: 30 minutes, 100 V, 0.5 A). Membranes were blocked by incubation with 5% (w/v) non-fat milk (#70166, Lot. #BCB68664V, Fluka, UK) in TBS-T (0.1% Tween-20 SigmaUltra - P7949, Sigma-Aldrich, UK - in 1X Tris-buffer - #170-6435) for 1 hour at room temperature. Membranes were then cut into two sections and incubated with 1:1000 dilution in TBS-T mouse anti-human CD44 (Clone 156-3C11, #170-5061; Cell Signaling Technology, UK) overnight at 4°C, or 1:5000 dilution in TBS-T rabbit anti-human β-actin (ab8227, Abcam, UK) for 1 hour at room temperature. After four washings in TBS-T (15 min/wash under gentle agitation), membranes were incubated for 1 hour at room temperature with goat anti-mouse IgG-peroxidase (A0168, Sigma-Aldrich, UK) or goat anti-rabbit IgG-peroxidase (A0545, Sigma-Aldrich, UK),

respectively. Bands were detected using Clarity Western enhanced chemiluminescence (ECL) substrate (#170-5061) with the aid of a ChemiDoc™ MP System (#170-8280). ImageJ software (v1.49p, http://rsb.info.nih.gov/ij) was used to perform a densitometry analysis of protein bands. Briefly, the relative expression of CD44 was determined by calculating the ratio of the band intensity for CD44 to that of the β-actin control (please note that actins are highly-conserved proteins and variations in band intensity are indicative of different protein loading between wells). Unless specified, all the products herein mention were purchased from Bio-Rad, UK.

3.3.5. Cytokine profiling

The Ready-SET-Go! ELISA kits for Human TNF-α (#88-7346-88), Human IL-1β (2nd Generation, #88-7261-88), Human IL-10 (#88-7106-88), Human TGF-β1 (2nd Generation, #88-8350-88), and Corning® Costar flat-bottom ELISA plates used in this study were all purchased from Affymetrix/eBioscience (UK) and used according to manufacturer's protocols.

3.3.6. Cell imaging

A) Light Microscopy. Phase contrast images of live THP-1 macrophages were acquired using a Leica DMI6000B inverted microscope (Leica Microsystems, UK) coupled with a 5.5 Neo sCMOS camera (Andor, UK). The *μManager* software (v.1.46, Vale Lab, UCSF, USA) was used to control both microscope and camera, as well as to capture images. For acquisitions, a dry 63X/0.7 PL Apo objective was used. Images were processed using ImageJ (v1.49p, http://rsb.info.nih.gov/ij).

B) Laser Scanning Confocal Microscopy (LSCM). An inverted SP5 laser confocal microscope (Leica TCS SP5 AOBS, Leica Microsystem, UK) was used to acquire volumetric datasets of resting and polarized THP-1 macrophages. Confocal acquisitions were performed using the immersion oil 63X/1.40 HCX PL Apo objective.

THP-1 morphology and CD44 staining. THP-1 macrophages were stained for F-actin and nuclei after each differentiation procedure. Briefly, cells were incubated for 10 min with 1 μg/mL Hoechst (Invitrogen, Thermo-Fisher, UK) solution in serum-free medium at 37°C and 5% (v/v) CO_2, cells were washed with PBS, fixed with 4% PFA solution for 10 min at room temperature, washed again with PBS, and then permeabilized with 0.1% (v/v) TritonX-100 solution in PBS (3 min incubation at room temperature). Cells were finally incubated for 20 min at room temperature with 1:200 Phalloidin-AlexaFluor488 (Invitrogen, Thermo-Fisher,

UK) in 1% BSA (w/v) PBS solution, then washed with PBS, and stored in the dark at 4°C in a 1 mg/mL ascorbic acid/PBS solution. Images of polarized THP-1 macrophages were acquired using an inverted confocal laser microscope (Leica SP5). Volumetric dataset of differentiated and polarized THP-1 with both [24]/[6/18] and [24]*/[24/24] protocols were analyzed using ImageJ (v1.49p, http://rsb.info.nih.gov/ij). The morphological analysis was performed considering the F-actin channel on volumetric datasets (n=2) analyzing about 10 cells per phenotype/method. Cell thickness was measured considering the difference between basal and the apical z-level. The measured difference was then multiplied by the z-size of the dataset voxel, obtaining the average thickness of each acquired cell. Cell surface area and solidity were measured using dataset maximum projections, Otsu threshold and watershed method were applied respectively to select cell bodies and to separate cell projections. Finally the surface area and the shape descriptors were determined using ImageJ plug-ins. Here, we present only solidity as the most representative descriptor to distinguish the macrophages phenotype/method.

For CD44 staining, after incubation with 1 μg/mL Hoechst solution cells were washed with cold PBS and placed on ice. A 1:200 dilution of anti-human CD44-Alexa594 conjugated antibody (#103054, Biolegend) in 1% (w/v) BSA/PBS was freshly prepared, incubating cells for 30 min on ice. Cells were then washed with PBS and fixed with 4% PFA solution by incubating 10 min on ice. After permeabilization with 0.1% (v/v) Triton X-100 solution in PBS (3 min incubation at room temperature), cells were incubated for 20 min at room temperature with a 1:200 Phalloidin-AlexaFluor488 (Invitrogen, Thermo-Fisher, UK) in 1% (w/v) BSA/PBS solution, washed with PBS and stored in the dark at 4°C in a 1 mg/mL ascorbic acid solution (PBS).

HA internalization. Sections and high-resolution (3D-HR) volumetric dataset were also acquired to precisely determine HA-Rho localization within the cell. For 3D-HR acquisitions, the confocal settings were set as follows: 1 Airy unit, scan speed 700 Hz, Average Line ×2, pixel size 117 nm, 0.4 μm z-step. To get rid of any possible cross talk between channels, images were collected with a sequential scan, using the following laser lines and mirror settings: 405(10%)/410-460 nm; 488(30%)/500-550 nm; 561(25%)/575-680 nm. Sections were then processed and analyzed using ImageJ, accordingly to the acquisition analysis. 3D rendering was performed using Imaris x64 (v7.7.2, Bitplane AG). Before acquisitions, the bottom and the top level were determined using the F-actin signal. At a post-processing level, the following morphological parameters were calculated:

- Approximated cell thickness, determined as the average basal vs. apical plane distance for each cell.
- Average surface area, determined with the maximum projection result of the volumetric dataset.
- Solidity of cell surface, determined after applying threshold method and calculating shape descriptors of the maximum projection (derived from volumetric dataset).

3.3.7. Preparation of fluorescently-labelled HA (HA-Rho)

Hyaluronic acid (HA; $\overline{M}_w$ = 180 kDa, assessed by GPC as described in Supporting Information, section SI5 and Table 3—1) was provided by Novozymes (Bagsvaerd, Denmark) and covalently conjugated to Lissamine™ Rhodamine B Ethylenediamine (Thermo Scientific, UK). All solutions were prepared in 100 mM HEPES buffer at pH = 7.4 unless stated otherwise. Briefly, 150 mg of HA (0.5 mmol of carboxylate) were dissolved in 15 mL by shaking overnight. After complete dissolution of HA, 3.75 mL of a solution containing 4.32 mg of Rhodamine were added followed by 3.75 mL of a 65 mM 4-(4,6-Dimethoxy-1,3,5-triazin-2-yl)-4-methylmorpholinium chloride (DMT-MM) solution (Sigma-Aldrich, UK). The reaction was stirred (at 300 rpm) for 24h at 25°C and then quenched and precipitated using a 20-fold volume excess of ethanol (96% v/v). The mixture was further incubated overnight at 4°C to ensure the complete precipitation of the labelled HA. The precipitate was collected after centrifugation (10 min at 4500 g), dissolved in 15 mL of deionized water, and purified by dialysis (MWCO = 20 kDa). Finally, the HA solution was freeze-dried. Mass recovery: 74%. Degree of derivatization: 0.7% mol (calculated by measuring the fluorescence of Rhodamine-conjugated HA (Ex: 540/25, Em: 620/40 nm) and comparing it to a calibration with free Rhodamine).

3.3.8. Preparation of HA-coated chitosan nanoparticles (CS/HA)

Chemicals. Middle viscosity chitosan (CS, average viscosimetric molecular weight $\overline{M_v}$= 656 kDa) and degree of deacetylation 85%) was purchased from Sigma (Sigma-Aldrich, UK). Chitosan with $\overline{M_v}$= 36 kDa was obtained by oxidative degradation of middle viscosity chitosan (1% wt. in 0.1 M HCl / 3 mM sodium nitrite). Chitosan samples were purified in-house prior to use as previously described [49].

Nanoparticle preparation. Nanoparticles were prepared by direct complexation of chitosan (CS) with HA and siRNA, following a single-step method recently adopted in our group;

please note that this is not the two-stage triphosphate (TPP)-mediated process previously employed by us [31, 32, 49]. This simplified approach encompasses first the preparation of a 0.069% wt. CS solution (36 or 656 kDa) in 4.6 mM HCl, the pH of the solution was then adjusted to 5 by adding 0.1 mM NaOH. The latter was further diluted 1:2 (v/v) with deionized water brought to pH = 5 using HCl 0.1 M; in the case of loaded nanoparticles, the CS solution was diluted with deionized nuclease-free water containing DY547-labelled siRNA (1.45%wt. in relation to CS) (Dharmacon, UK) and an initial complexation was carried under magnetic agitation (1,000 rpm) for 10 min at 25°C. The HA-coated nanoparticles (CS/HA) were obtained by addition of the resulting CS solution/suspension into an equal volume of a 1.5 mg/mL HA solution (HA-Rho for empty nanoparticles; non-labelled HA for the siRNA-loaded ones) in water at pH = 5 under vigorous stirring (1,000 rpm) for 30 min at 25°C. Please note that the preparation of nanoparticles was performed in a laminar flow hood with surfaces previously decontaminated using the RNaseZap® solution (Thermo Scientific, UK) when encapsulating siRNA payloads. Size and ζ potential of the particles are reported in Supporting Information, section SI5 and Table 3—1.

3.3.9. Study of macrophage-HA interactions

In the following paragraphs, we will refer to soluble HA or CS/HA nanoparticles as "treatment". Briefly, equal volumes of soluble HA or CS/HA nanoparticles (adjusted to 250 µg/mL with deionized water) were diluted with 2X concentrated RPMI 1640 medium to obtain a final concentration of 125 µg/mL in complete cell culture medium.

Please note that internalization studies (flow cytometry) of soluble HA were performed by tracking the HA-Rho signal, while those of CS/HA nanoparticles were performed by tracking an encapsulated fluorescently-labelled siRNA, respectively (see previous section for the preparation procedure).

A) Quantification of HA binding and uptake in cell lysates. THP-1 premonocytes were differentiated and polarized in Costar® polystyrene 12-well plates with flat bottom (3513; Corning, UK). Cells were incubated with the treatment at 37°C. After specified incubation times (0, 2, 4, 8, 16, and 24 h), cells were washed three times with pre-warmed PBS and lysed in 100 µL RIPA Buffer. The total uptake (comprising both membrane-bound and internalized macromolecules) was estimated from the measured fluorescence of the cell lysates, by using a calibration of HA-Rho or CS/HA nanoparticles in cell lysates at concentration range [0.12-125]µg/mL (Ex: 540/25, Em: 620/40 nm) Synergy2 Biotek plate reader using Gen5 software.

Sensitivity adjusted to the highest HA-Rho or CS/HA nanoparticles concentration of the calibration curve (125 μg/mL). Optical position: top 50%. Light source: Xenon flash) and normalized against the protein content in each well, as analyzed via the BCA assay kit (B9643, Sigma-Aldrich, UK). *B) Quantification of HA internalization via flow cytometry*. THP-1 premonocytes were differentiated and polarized in Costar® polystyrene 6-well plates (3513; Corning, UK). Cells were incubated with the treatment at 37°C. After specified incubation times (0, 2, 4, 8, 16, and 24 h), cells were washed three times with pre-warmed PBS to remove any excess. Macrophages were then detached using pre-warmed Cell Dissociation Buffer (#13151-014, Gibco®/Invitrogen, UK) with 15 minutes incubation at RT. The internalization was determined on 10,000 live, individual cells with a BD LSRFortessa cytometer (BD Bioscience, San Jose CA, USA) equipped with the FACSDiva software (v8.0.1). Data were analyzed with FlowJo (vX.0.7, Tree Star, Ashland, OR, USA) after gating live and single events in the FSC-A/FSC-H (singlets) and FSC/SSC (live) windows, respectively. Untreated cells were used as autofluorescence control in order to calculate the MFI for each time point, as well as the percentage of positive events.

C) *CD44 blocking*. THP-1 premonocytes were differentiated and polarized in Costar® polystyrene 12-well plates with flat bottom (3513; Corning, UK). Macrophages were pre-treated with RPMI 1640 medium containing either i) 20 μg/mL CD44 antibody (Clone HERMES-I; MA4400, Fischer Scientific UK), ii) 20 μg/mL Rat IgG2a antibody (MCA1212, Ad Serotec), iii) PBS for 1h at 37°C. Pre-treatment was followed by incubation with RPMI 1640 medium containing HA-Rho (125 μg/mL) together with either i) 10 μg/mL CD44 antibody, or ii) 10 μg/mL IgG2a, or iii) PBS for 2h at 37°C. Media were removed and cells were washed three times in pre-warmed PBS and lysed in 100 μL RIPA buffer. The total HA uptake (comprising both membrane-bound and internalized macromolecules) was estimated

D*) HA intracellular localization (via LSCM).* THP-1 premonocytes were differentiated and polarized in the μ-Slide 8-well slide (iBiDi, UK). Cells were incubated with a 125 μg/mL HA-Rho solution in complete RPMI 1640 at 37°C. After 16h incubation, cells were washed with PBS and fixed with a 4% PFA solution (5 min at RT). Cells were then washed with cold PBS (n=3), incubated for 10 min at RT with a 1% FBS solution in PBS, washed with PBS (n=3), incubated for 30 min at RT with 1:400 human anti-CD44 (156-3C11, Cell Signaling) in PBS, 1% (w/v) BSA, washed with PBS (n=3), and finally incubated for another 30 min at RT with anti-mouse IgG (whole molecule)–FITC antibody produced in goat (F0257, Sigma-Aldrich, UK) in PBS, 1% (w/v) BSA. Cells were incubated for 3 min at RT with a 1 μg/mL

DAPI solution in PBS, washed with PBS (n=3), and stored in the dark at 4°C in a 0.1 mg/mL ascorbic acid (A4403, Sigma-Aldrich, UK) solution in PBS.

3.3.10. Statistical analysis

The expression of markers and cytokines was compared using a two-way analysis of variance (Two-way ANOVA), setting the macrophage phenotype (i.e. M0, M1 or M2) as row factor and the differentiation/polarization method as column factor. In experiments related to CD44 isoforms and CD44-mediated uptake inhibition, we compared results between different phenotypes using one-way analysis of variance (One-way ANOVA). Differences between groups were considered significant at a *P* value of <0.05. Statistical analysis performed with GraphPad Prism 6.04 (GraphPad Software, Inc., San Diego, CA).

3.4 Results and discussion

3.4.1. The cellular model

We have used two different differentiation/polarization protocols (Figure 3—1A):

1) a 24h combined treatment (used e.g. by Tjiu *et al.* for M2 THP-1 [44]) referred to as ***[6/18]***; premonocytes (Mo) were first incubated with PMA (6h), then with PMA + polarizing factors (18h).

2) a 48h sequential treatment (similar to that used by Genin *et al*. to obtain M1 and M2 THP-1[43] or by Martinez *et al*. on primary cells [50]) referred to as ***[24/24]***, where premonocytes were first incubated with PMA alone (24h), then with polarizing factors alone (24h).

In order for all cells to experience the same overall treatment duration (48h), in some cases we have employed a final resting phase: ***[6/18]*** macrophages were cultured for additional 24h in full medium, and so were also M0 macrophages (24h PMA differentiaton, 24h resting: protocol **[24]**). Conversely, in the sequential ***[24/24]*** treatment the cells were not subjected to any resting time. Since the presence or absence of a resting time can be important (M1-like polarization arises in THP-1 after a 5-day resting following a 24h treatment with 200 nM≈120 ng/mL PMA) [42], we have also subjected M0 to a 48h recovery in a protocol is referred to as ***[24]****: any difference with ***[24]*** treatment will reflect the effect of a prolonged resting.

Cell viability. None of the treatments leading to M0 and M2 phenotypes affected cell viability, whereas a moderate reduction was observed for M1: about 20% of dead cells were

seen in live/dead assays, whereas MTS recorded a ≈30% decrease in average mitochondrial activity (see Supporting Information, Figure 3—5).

Cell morphology (Figure 3—1B and C). M0 and M2 macrophages exhibited almost identically round bodies (high solidity and thickness, low surface area; Figure 3—1B, *left*) and similar morphology (Figure 3—1B, *right*) on plastic, and also similar cellular size and granularity in suspension (Figure 3—1C, *right*; see the caption for parameter definitions), always without noticeable differences between the two polarization protocols. M1 were flatter and more spread, indicating a higher adhesion to the substrate, and were larger and more granular in suspension, with the M1 vs. M0 / M2 differences being more evident using the ***[24/24]*** protocol. Finally, the resting time (***[24]*** vs. ***[24]**** for M0) had no effect.

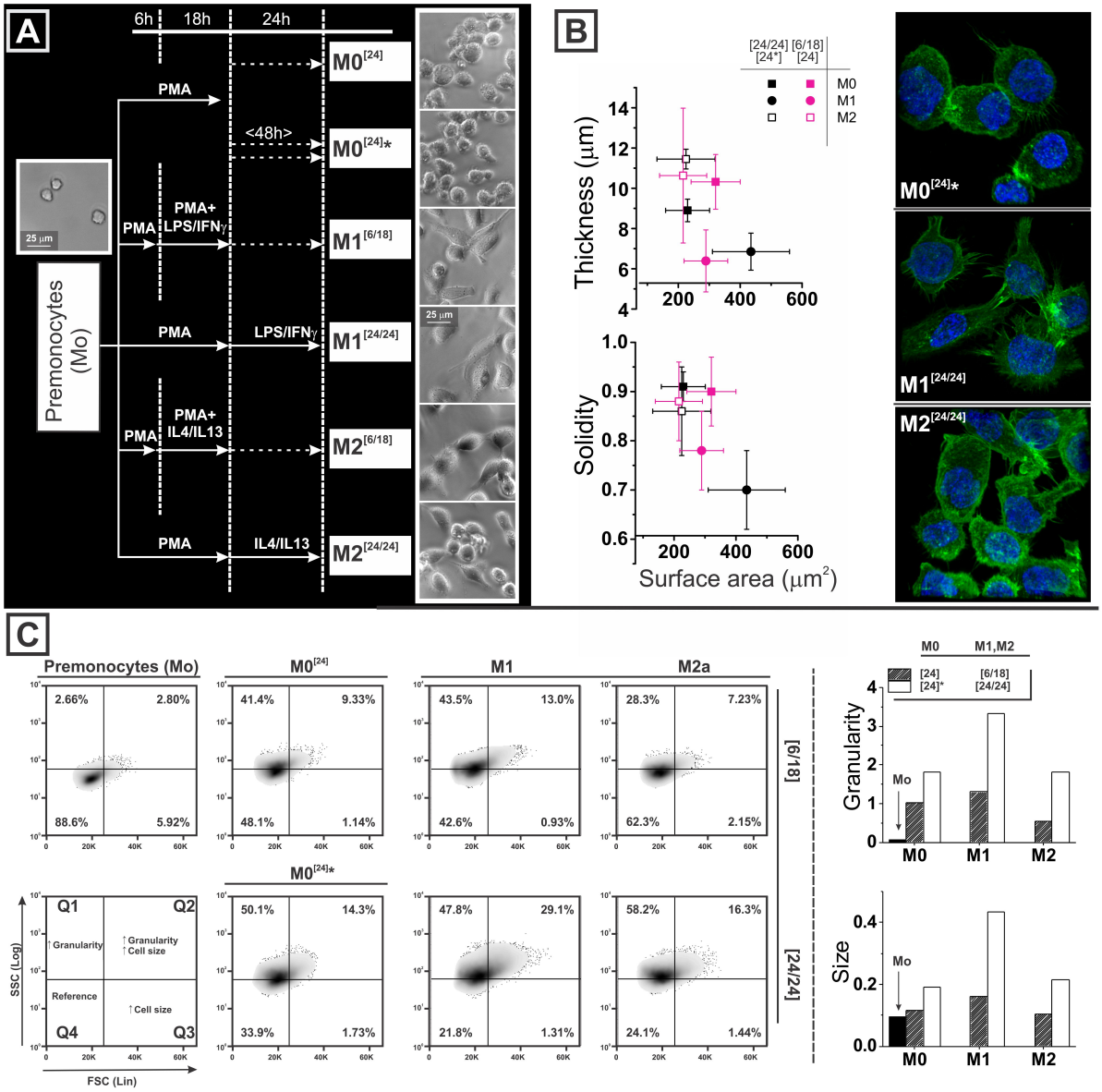

Figure 3—1. THP-1 differentiation/polarization protocols and their effect on morphological markers. ***A.*** Summary of the protocols used to differentiate premonocytic THP-1 cells into resting (M0; PMA), classically activated (M1; LPS+IFN-γ), and alternatively activated (M2; IL-4+IL-13) macrophages. Representative phase contrast images are shown for the different phenotypes (Scale bars: 25 µm). ***B.*** Morphological analysis. *Left:* Cell area, thickness, and solidity were employed as morphological descriptors; only M1 provided significantly different values, resp. vs. M2 in the ***[6/18]*** protocol, and vs. M2 and M0 in the ***[24/24]*** and ***[24]*** protocols. No significant difference was recorded between the two differentiation/polarization protocols. *Right:* Confocal images (Top view of volumetric reconstruction) of THP-1 macrophages representing nuclei (blue) and F-actin (green). A greater number of pseudopodia and flattened cells were observed in M1. M2 and M0 were very similar, with a slightly more developed F-actin network for M2 as the only visible difference ***C.*** Flow cytometry. *Left:* The contour plots show clear shifts in Forward Scattered Light (FSC) and Side Scattered Light (SSC) upon differentiation/polarization. The FSC/SSC plot for untreated premonocytes was used to define four arbitrary quadrants (Q1-Q4). *Right:* The results are summarized in histograms of granularity and size (top; granularity defined as (Q1+Q2)/(Q3+Q4)); and size (bottom; size defined as (Q2+Q3)/(Q1+Q4)). *n*=3.

Surface markers (Figure 3—2). In short, the three markers employed were all present in larger amounts under the ***[24/24]*** protocol.

A) CD14 (LPS co-receptor, Figure 3—2A) is a differentiation marker for the myelomonocytic stem cell line [51]; more specifically, its upregulation marks the THP-1 premonocyte-to-macrophage differentiation [42, 47, 52], although at low PMA doses this may not be observed e.g. in Aldo *et al.* [34]: same cell density as here, but ten times less PMA [48]. While the ***[24/24]*** protocol significantly upregulated CD14 with a predominantly $CD14^+$ cell population for both M1 and M2, under the ***[6/18]*** protocol its level was indistinguishable from that of the parent Mo cells. Since M0 **[24]*** macrophages (24 h additional resting time) showed a 3-fold higher CD14 than the M0 ***[24]*** ones, mechanistically we are inclined to ascribe the ***[24/24]*** better performance to its longer duration. It is also worth noting that CD14 was higher in the M1[53] than in the M2 state [54, 55].

B) CD11c (leukocyte integrin, Figure 3—2B) is a general marker of mononuclear phagocytes (particularly abundant in dendritic cells [56]); it is induced in macrophage maturation, and it is typically upregulated with PMA [57]. Our results confirmed both its presence in Mo and its upregulation as the result of maturation processes. The resting time did not seem to play a major role (similar levels in ***[24]*** and ***[24]**** M0), therefore the much larger CD11c expression in ***[24/24]*** vs. ***[6/18]*** is ascribed to a greater efficacy of the sequential stimulation. Last, it is noteworthy that the very large CD11c presence observed in the ***[24/24]*** M2 polarization appears to mirror what reported in the M2a induction from primary cells [58], which suggests the identification of the ***[24/24]*** M2 cells as M2a.

C) CD206 (macrophage mannose receptor, Figure 3—2C) is considered to be an alternative activation marker [59], and it was upregulated with the ***[24/24]*** protocol, whereas the ***[6/18]*** was completely ineffective. Similar to what is seen for CD14, the longer duration of the latter protocol may play a major role, since a similar upregulation can be seen when comparing the ***[24]*** and ***[24]**** protocols. Importantly, with most treatments except M0 ***[24]**** a majority of cells did not appear to be CD206 positive, nor M2 showed a significantly higher expression, suggesting differences between THP-1 and primary macrophages, as already highlighted elsewhere [42].

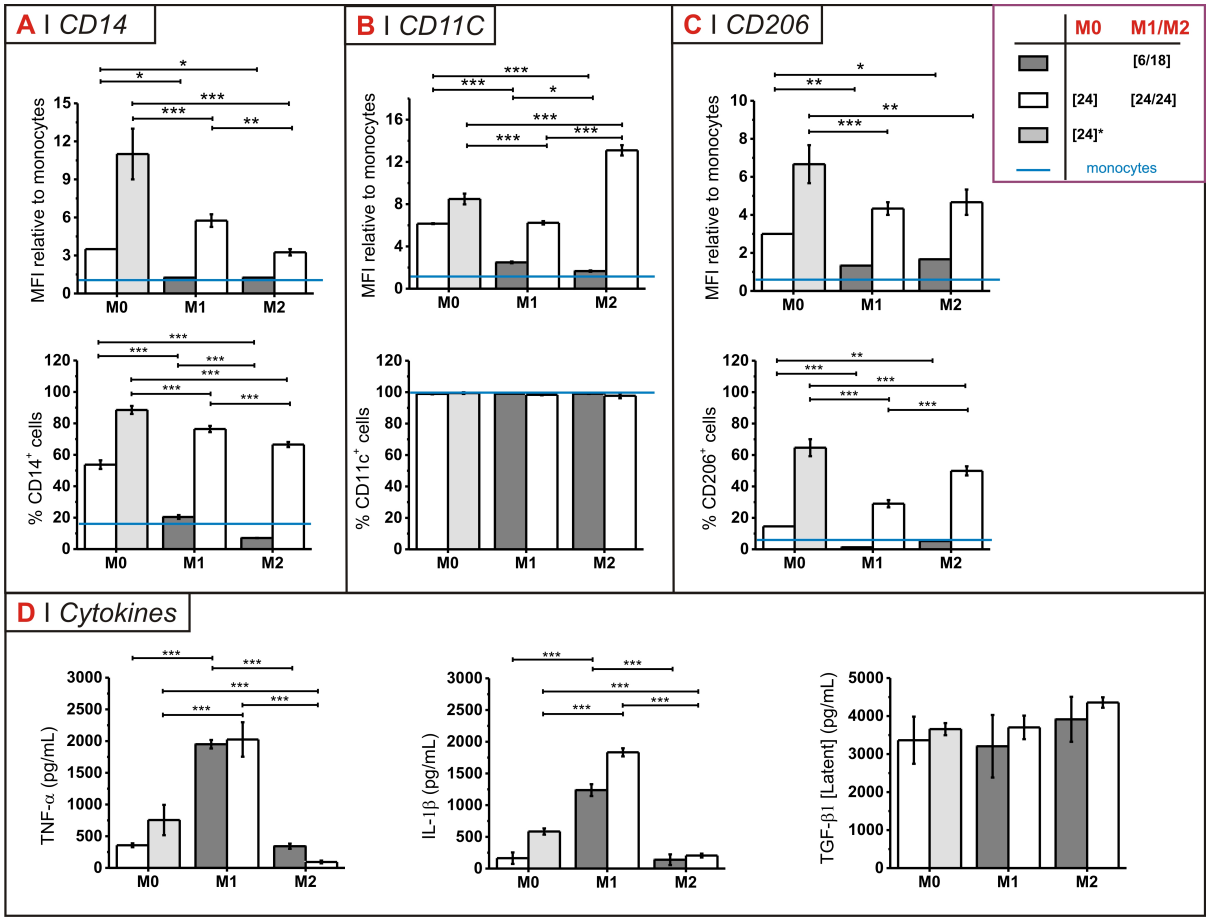

Figure 3—2. THP-1 macrophage markers; please note that thermosensitive substrates were employed in order to avoid degradation and/or removal of surface proteins. ***A to C.*** The expression of CD14 **(*A*)**, CD11c **(*B*)**, and CD206 **(*C*)** on THP-1 was evaluated via flow cytometry using primary antibodies. The Median Fluorescence Intensity (MFI) for PMA-treated (M0), LPS+IFN-γ-treated (M1), and IL-4+IL-13-treated (M2) cells is expressed in relation to that of their parent, untreated monocytes (blue horizontal bar). ***D.*** The levels of TNF-α, IL-1β and TGF-β1 were measured via ELISA. Notice that the differences in terms of both marker expression and release of cytokines were not affected by differences in cell viability for the two experimental protocols (see Supporting Information, section SI2 and Figure 3—5). Data are presented as average ± SD of n=3 experiments (flow cytometry) and of n=4 experiments (ELISA). The statistical analysis refers to the comparison of receptor expression in different polarizations: ***$P<0.001$, **$P<0.01$, *$P<0.05$ (Two-way ANOVA).

Cytokine profiling. Three cytokines (TNF-α, IL-1β and TGF-β1, Figure 3—2D) were analyzed for a final assessment of the polarization into pro-inflammatory and anti-inflammatory subtypes; a fourth marker, IL-10, was under the detection limit for the three macrophagic polarizations (data not shown), which may be a peculiarity of THP-1 [60] (in addition to what is seen for CD206). In short, the two polarization protocols were largely similar. Not surprisingly, the highest levels of pro-inflammatory cytokines (TNF-α and IL-1β) were detected for the M1 phenotype, while being lower for M0 and lowest for M2 macrophages. M2 macrophages showed the highest levels of (latent) TGF-β1.

On the grounds of the increased upregulation of all differentiation markers, the ***[24/24]*** protocol was chosen for all further polarization experiments, using the analogous ***[24]*** protocol for M0 polarization.

3.4.2. Expression of CD44 and of its isoforms

CD44 was already present in Mo, but its expression increased upon their differentiation (see Supporting Information, Figure 3—6; compare to see literature reports [61], also with regards to HA affinity [62]).

CD44 exhibited a punctuated fluorescence preferentially localized at or close to the cell surface, without any noticeable difference for the three macrophage polarizations (red in Figure 3—3A); qualitatively, CD44 appeared to be present in larger amounts in M1, and this was then quantitatively confirmed via various techniques: 1) Western blotting (Figure 3—3B) indicated CD44 expression in the order M1 > M0 > M2 ≥ Mo. In comparison to Mo premonocytes, M0 showed a 3.5-fold increase, M1 a 5.5-fold increase, and M2 a 1.25-fold increase. 2) Direct staining flow cytometry (Figure 3—3C) and 3) indirect staining flow cytometry (Figure 3—3D) provided a similar picture, with the only difference that CD44 expression in M0 and M2 is statistically indistinguishable, confirming literature reports that it remains largely unaffected by alternative activation [63].

In terms of CD44 splice variants, the absence of intense secondary bands in the Western blots (Figure 3—3B) already suggests standard CD44 (~85-90 kDa) to be the predominant isoform. We have confirmed this by assessing the presence of some CD44 variants (CD44v3, v4 and v6, among the most relevant in cancer [64-66]) in relation to the total CD44 (Figure 3—3D). These isoforms appeared to be marginally present in Mo, and substantially absent in M1 and M2, with one notable exception: at least 60% of the M2 population was positive for CD44v6, showing peripheral/membrane localization virtually identical to that of the standard variant (Figure 3—3E). Although never clearly associated to M2, the scarce evidence about the expression of CD44v6 in macrophages aligns with our finding: this variant (in a soluble form) was found to be produced in monocytes undergoing macrophagic differentiation [67], while it has been shown that infiltrating (most likely M1) leukocytes in skin are completely devoid of CD44v6 [68]. Besides the possible use of CD44v6 as a marker of THP-1 M2 polarization, it is tempting to think about its utility for M2 macrophage targeting.

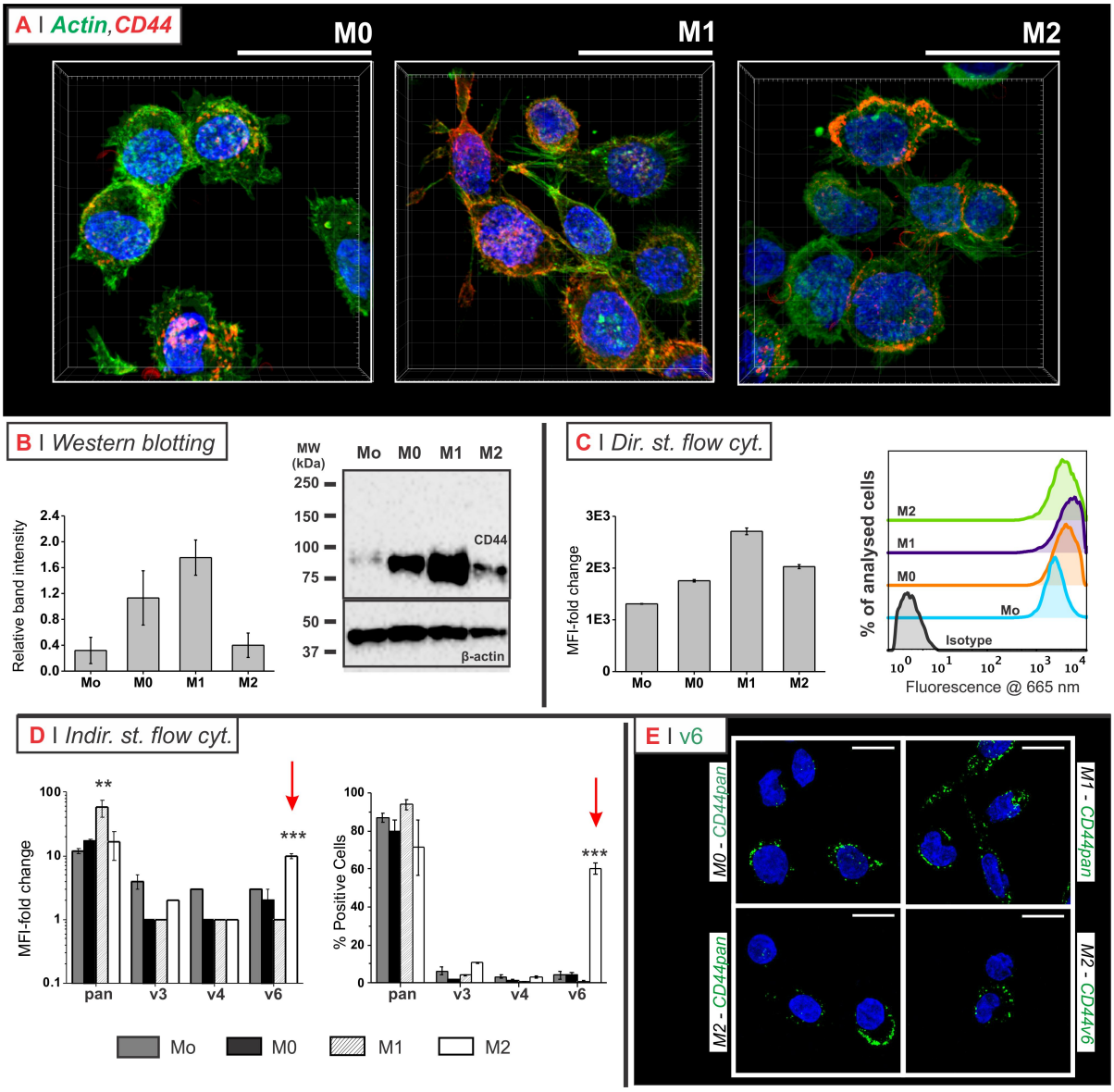

Figure 3—3. CD44 expression in THP-1 cells. ***A.*** Confocal Microscopy: volume rendering of THP-1 showing nuclei (blue), F-actin (green) and CD44 (red) (experimental protocol: see Experimental Section, section 4.6). ***B.*** Representative CD44 Western blot (right) of untreated (Mo), M0[24], M1[24/24] and M2[24/24] cells. β-actin was used as loading control. Average ± SD (*n*=3) is reported in the left panel. ***C.*** Expression of CD44 obtained via direct staining flow cytometry (APC-labelled anti-CD44 mAb). Incidentally, these data are analogous to the expression recorded using ***[6/18]*** and ***[24]**** protocols (see Supporting Information, Figure 4—6). Average ± SD (*n*=3). ***D.*** Expression of total CD44 (CD44pan; same stain as for Western blotting) and CD44 variants (CD44v3, CD44v4, and CD44v6) by flow cytometry after indirect staining with AlexaFluor®647 (AF647). The cells were detached using an enzyme-free protocol, which provided quantitative cell recovery while maintaining full viability (see Supporting Information, section SI3 and Figure 3—7). Histogram of n-fold change in median fluorescence intensity (MFI) over isotype control (*left*), and percentage of positive cells for the various cell populations (*right*) are expressed as average ± SD (*n*=3). For more complete data, see Supporting Information, Figure S4. For the statistical comparison between the three highlighted peaks and the isoform presence in other polarizations: ****P<0.001*, ***P<0.01* (One-way ANOVA). ***E:*** Confocal images of CD44 indirect staining of THP-1 with anti-mouse IgG (whole molecule)–FITC; all images were acquired with sequential scans with keeping constant the following settings Ex(power)/Em[adjusted mirrors]: a) DAPI Ex/Em 405(10%)/[410-460]nm, b) CD44tot/CD44v6 488(30%)/[500-550]nm. Merge of fluorescent acquisition of the first 5 µm from cellular basal layer are here showed (scale bars: 15 µm).

3.4.3. Complex relationship between uptake of HA materials and CD44 expression

We have prepared rhodamine-labelled HA (HA-Rho; $\overline{M}_w$ = 180 kDa, 0.7% mol functionalization), and used it as such as a soluble ligand, or in the form of chitosan/HA (CS/HA) nanoparticles. The latter were produced via direct polyelectrolyte complexation employing CS with two different molecular weights, and were loaded with a DY547-labelled siRNA in order to provide a generic model for HA-decorated nanocarriers. Please note that they differ from soluble HA both in size and in surface density of CD44-binding groups (HA is more condensed when bound to CS).

We have followed the uptake kinetics of both soluble HA and of CS/HA nanoparticles by monitoring their fluorescence in cell lysates and via flow cytometry after trypsinization. The fluorescence of cell lysates accounts for both surface bound and internalized material; on the contrary, due to the trypsin-mediated degradation of CD44 [69] and the ensuing removal of membrane-bound HA [70], we assume that flow cytometry predominantly refers to internalized material. This assumption is confirmed by the negligible effect of an extracellular fluorescence quencher (trypan blue, data not shown) in flow cytometry experiments.

For all the three macrophage polarizations, the fluorescence of cell lysates (black symbols in all panels of Figure 3—4A) reached a plateau already at 2 h for soluble HA and at 4 h for nanoparticles, with virtually all cells being positive for internalized material.

This indicates a rapid binding and saturation of the HA receptor(s), which we predominantly identify as CD44, due to the significant inhibition obtained with the Hermes-1 antibody, specifically for M1 and M2 (2 h, HA-Rho fluorescence in cell lysates; Figure 3—4D).

Flow cytometry showed the internalization kinetics to proceed much more slowly (purple symbols in all panels of Figure 3—4A). Since the 2 h internalization appeared to be almost negligible, we have considered the 2 h cell lysate data as an indication of the capacity of the three macrophage polarizations to bind free HA or CS/HA nanoparticles. On the other hand, we have used the 16 h flow cytometry MFI as a measure of their internalization efficiency. We have then cross-correlated for each macrophage phenotype these binding and internalization data with the expression of CD44, as quantified via Western blotting and direct and indirect stain flow cytometry, for the three macrophage phenotypes (Figure 3—4B).

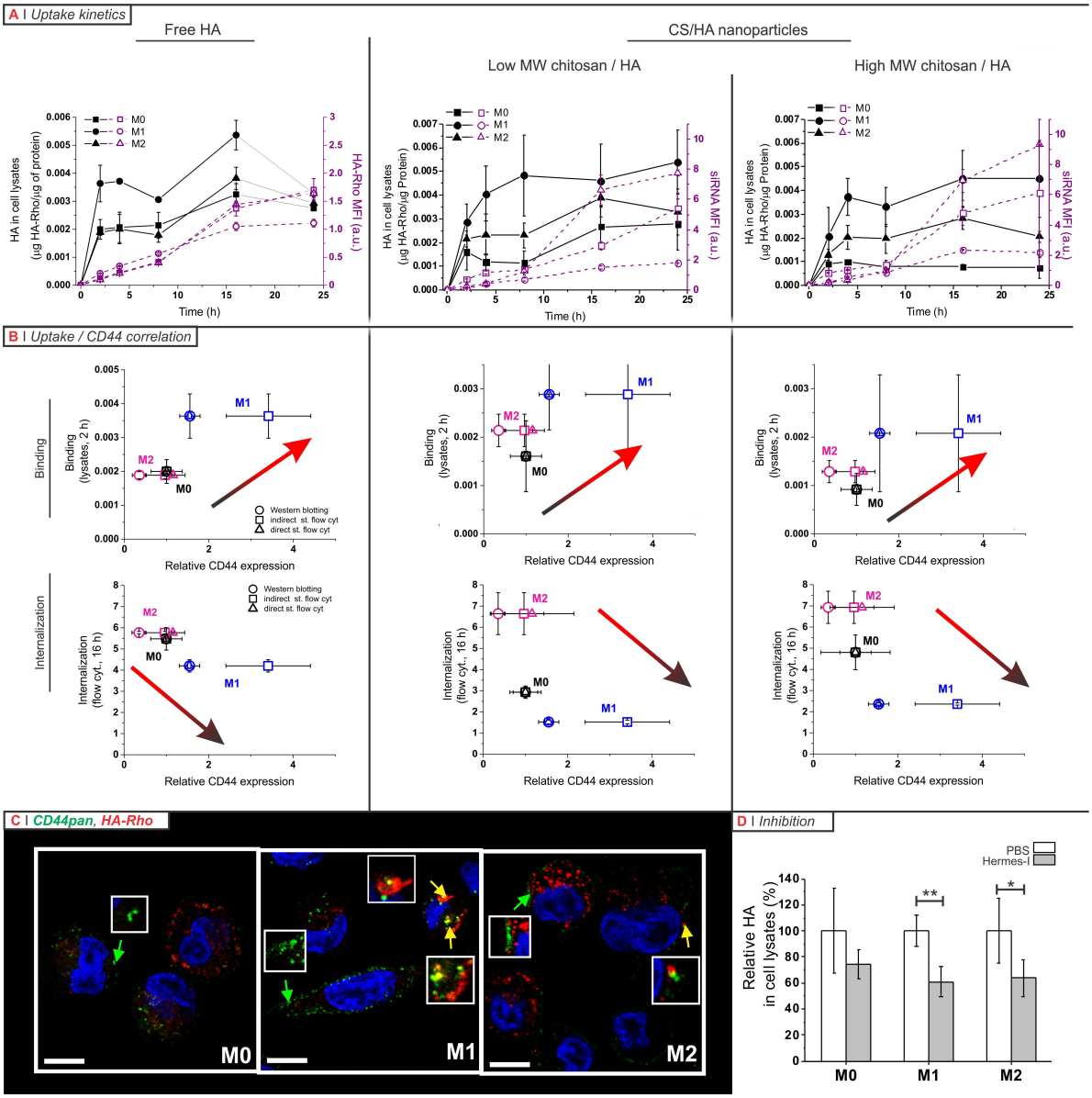

Figure 3—4. ***A:*** Uptake of HA-Rho (*left*) and of CS/HA nanoparticles (*center and right*) followed by flow cytometry (*purple*) and fluorimetry of cell lysates (black; the lysate data are normalized against the protein content). Please note that the flow cytometry data of CS/HA nanoparticles are obtained by monitoring the fluorescence of the nanoparticle cargo i.e. DY547-labelled siRNA (*purple*). ***B:*** Cross-correlation between the expression of CD44 (CD44pan; measured through Western blotting and both direct and indirect stain. flow cytometry) and HA or CS/HA binding (cell lysate at 2h, *top*) and internalization (flow cytometry at 16h, *bottom*). Please note that the CD44 expression is normalized against M0 independently for each analytical technique. The indirect flow cytometry CD44 expression data for M0 macrophages (Figure 3—3D) was used as a reference to determine X-axis values. ***C:*** Confocal microscopy acquisitions of fixed THP-1 macrophages after incubation with HA-Rho for 16h and counter-staining with anti-CD44pan mAb. Scale bars: 10 µm. ***D:*** Effect of CD44 antibody treatment on the uptake of HA-Rho. THP-1 macrophages were pre-treated with 20 µg/mL Hermes-I antibody followed by a 2h incubation with medium containing both 10 µg/mL antibody and 125 µg/mL HA-Rho (n=3). Statistical analysis: M1, **P=0.0005; M2, *P=0.00039 (Two-way ANOVA). The only partial inhibition is not a concern: a max 50% inhibition is common for Hermes-1, which is nevertheless one of the best means to reduce HA internalization in human cells [71]. Please note that only few anti-CD44 antibodies bind close enough to the LINK module to reduce HA uptake [72].

CD44 expression and HA binding showed a positive correlation (both M1>M0≥M2), more clearly for HA in a soluble form than when on the nanoparticles surface. In literature, the higher HA binding for TNF-α (M1) than for IL-4 (M2)-treated macrophages has been ascribed only to differences in CD44 post-translational modification [73], but our data show also a link to its actual level of expression.

Surprisingly, we have recorded a negative correlation between HA internalization and CD44 expression for all the three HA systems studied i.e. the amount of internalized HA material appeared to reduce with increasing levels of CD44. This unexpected phenomenon could be due to HA internalization being mediated by receptors other than CD44; the transfer of HA to these putative internalization receptors would require its de-complexation from CD44, which is likely to be slowed down by a larger CD44 expression. A different level of clustering with different CD44 expression can also be invoked. Indeed, confocal microscopy showed that the co-localization between internalized HA and CD44 was rather limited (Figure 3—4C), and it appeared to be higher for M1, which showed both the highest CD44 expression and the slowest internalization.

3.5. Conclusion

In this study, we have validated a robust polarization method for THP-1 cells, and used them as an *in vitro* model to study the role of human macrophage polarization in the CD44-mediated uptake of HA-based systems. We have shown that the expression of CD44 is polarization-dependent; not only CD44v6 (normally associated with tumors) was found exclusively in M2 macrophages, but also the overall CD44 amount scaled as M1 > M0 ≥ M2. Intriguingly, the same order was found in the capacity of macrophages to bind soluble HA and two kinds of HA-displaying nanoparticles, but their internalization appeared to follow an inverse order. This may profoundly affect the efficiency of a delivery approach: paradoxically, cells with the highest CD44 expression and potentially the best ‘binders’ may turn out to be the most difficult to e.g. transfect with a nucleic acid payload, because of the slower/more difficult internalization of the HA carrier structure.

3.6. Acknowledgements

Novozymes Biopharma (Krogshoejvej 36, 2880 36, 2880 Bagsvaerd, Denmark) is gratefully acknowledged for the provision of hyaluronic acid. The authors also want to thank Prof. Tony Day (University of Manchester) for the helpful discussions.

This study was supported by EPSRC (PhD studentship for Mr. Rios de la Rosa as part of the North-West Nanoscience (NoWNano) Doctoral Training Centre, EPSRC grant EP/G03737X/1). The Bioimaging Facility of the Faculty of Life Sciences (University of Manchester) is maintained with grants from BBSRC, Wellcome Trust, and the University of Manchester Strategic Fund.

The research leading to these results has received funding from the European Community's Seventh Framework Programme (FP7/2007-2013) under grant agreement n° 601738, and from AstraZeneca for the establishment of the NorthWest Centre of Advanced Drug Delivery.

3.7. References

[1] K. Williams, K. Motiani, P.V. Giridhar, S. Kasper, CD44 integrates signaling in normal stem cell, cancer stem cell and (pre)metastatic niches, Exp Biol Med 238(3) (2013) 324-338.

[2] M. Zoller, CD44: can a cancer-initiating cell profit from an abundantly expressed molecule?, Nat Rev Cancer 11(4) (2011) 254-267.

[3] A.R. Jordan, R.R. Racine, M.J.P. Hennig, V.B. Lokeshwar, The role of CD44 in disease pathophysiology and targeted treatment, Front Immunol 6 (2015).

[4] V. Orian-Rousseau, CD44, a therapeutic target for metastasising tumours, Eur J Cancer 46(7) (2010) 1271-1277.

[5] S. Misra, V.C. Hascall, R.R. Markwald, S. Ghatak, Interactions between hyaluronan and its receptors (CD44, RHAMM) regulate the activities of inflammation and cancer, Front Immunol 6 (2015).

[6] A. Aruffo, I. Stamenkovic, M. Melnick, C.B. Underhill, B. Seed, CD44 Is the principal cell-surface receptor for hyaluronate, Cell 61(7) (1990) 1303-1313.

[7] E. Auzenne, S.C. Ghosh, M. Khodadadian, B. Rivera, D. Farquhar, R.E. Price, M. Ravoori, V. Kundra, R.S. Freedman, J. Klostergaard, Hyaluronic acid-paclitaxel: Antitumor efficacy against CD44(+) human ovarian carcinoma xenografts, Neoplasia 9(6) (2007) 479-486.

[8] Y. Luo, M.R. Ziebell, G.D. Prestwich, A hyaluronic acid-taxol antitumor bioconjugate targeted to cancer cells, Biomacromolecules 1(2) (2000) 208-18.

[9] R.E. Eliaz, F.C. Szoka, Liposome-encapsulated doxorubicin targeted to CD44: A strategy to kill CD44-overexpressing tumor cells, Cancer Res 61(6) (2001) 2592-2601.

[10] S.L. Hayward, C.L. Wilson, S. Kidambi, Hyaluronic acid-conjugated liposome nanoparticles for targeted delivery to CD44 overexpressing glioblastoma cells, Oncotarget 7(23) (2016) 34158-34171.

[11] K.K. Upadhyay, A.N. Bhatt, A.K. Mishra, B.S. Dwarakanath, S. Jain, C. Schatz, J.F. Le Meins, A. Farooque, G. Chandraiah, A.K. Jain, A. Misra, S. Lecommandoux, The intracellular drug delivery and anti tumor activity of doxorubicin loaded poly(gamma-benzyl L-glutamate)-b-hyaluronan polymersomes, Biomaterials 31(10) (2010) 2882-2892.

[12] M. de la Fuente, B. Seijo, M.J. Alonso, Bioadhesive hyaluronan-chitosan nanoparticles can transport genes across the ocular mucosa and transfect ocular tissue, Gene Therapy 15(9) (2008) 668-676.

[13] A. Nasti, N.M. Zaki, P. de Leonardis, S. Ungphaiboon, P. Sansongsak, M.G. Rimoli, N. Tirelli, Chitosan/TPP and Chitosan/TPP-hyaluronic Acid Nanoparticles: Systematic Optimisation of the Preparative Process and Preliminary Biological Evaluation, Pharm Res 26(8) (2009) 1918-1930.

[14] H.J. Cho, H.Y. Yoon, H. Koo, S.H. Ko, J.S. Shim, J.H. Lee, K. Kim, I.C. Kwon, D.D. Kim, Self-assembled nanoparticles based on hyaluronic acid-ceramide (HA-CE) and Pluronic (R) for tumor-targeted delivery of docetaxel, Biomaterials 32(29) (2011) 7181-7190.

[15] K.Y. Choi, K.H. Min, J.H. Na, K. Choi, K. Kim, J.H. Park, I.C. Kwon, S.Y. Jeong, Self-assembled hyaluronic acid nanoparticles as a potential drug carrier for cancer therapy: synthesis, characterization, and in vivo biodistribution, J Mater Chem 19(24) (2009) 4102-4107.

[16] E. Montanari, S. Capece, C. Di Meo, M. Meringolo, T. Coviello, E. Agostinelli, P. Matricardi, Hyaluronic Acid Nanohydrogels as a Useful Tool for BSAO Immobilization in the Treatment of Melanoma Cancer Cells, Macromol Biosci 13(9) (2013) 1185-1194.

[17] S. Ganesh, A.K. Iyer, D.V. Morrissey, M.M. Amiji, Hyaluronic acid based self-assembling nanosystems for CD44 target mediated siRNA delivery to solid tumors, Biomaterials 34(13) (2013) 3489-3502.

[18] T.P. Skelton, C.X. Zeng, A. Nocks, I. Stamenkovic, Glycosylation provides both stimulatory and inhibitory effects on cell surface and soluble CD44 binding to hyaluronan, J Cell Biol 140(2) (1998) 431-446.

[19] N.M. English, J.F. Lesley, R. Hyman, Site-specific de-N-glycosylation of CD44 can activate hyaluronan binding, and CD44 activation states show distinct threshold densities for hyaluronan binding, Cancer Res 58(16) (1998) 3736-3742.

[20] O. Guvench, Revealing the mechanisms of protein disorder and N-glycosylation in CD44-hyaluronan binding using molecular simulation, Front Immunol 6 (2015) 1-9.

[21] P. Teriete, S. Banerji, M. Noble, C.D. Blundell, A.J. Wright, A.R. Pickford, E. Lowe, D.J. Mahoney, M.I. Tammi, J.D. Kahmann, I.D. Campbell, A.J. Day, D.G. Jackson, Structure of

the regulatory hyaluronan binding domain in the inflammatory leukocyte homing receptor CD44, Mol. Cell 13(4) (2004) 483-496.
[22] T. Suzuki, M. Suzuki, S. Ogino, R. Umemoto, N. Nishida, I. Shimada, Mechanical force effect on the two-state equilibrium of the hyaluronan-binding domain of CD44 in cell rolling, Proc. Natl. Acad. Sci. U. S. A. 112(22) (2015) 6991-6996.
[23] J. Cichy, E. Pure, The liberation of CD44, J Cell Biol 161(5) (2003) 839-843.
[24] J.N. Liu, G.S. Jiang, CD44 and Hematologic Malignancies, Cell. Mol. Immunol. 3(5) (2006) 359-365.
[25] S.P. Zhang, C.C.N. Wu, J.F. Fecteau, B. Cui, L.G. Chen, L. Zhang, R.R. Wu, L. Rassenti, F. Lao, S. Weigand, T.J. Kipps, Targeting chronic lymphocytic leukemia cells with a humanized monoclonal antibody specific for CD44, Proc. Natl. Acad. Sci. U. S. A. 110(15) (2013) 6127-6132.
[26] N. Vey, J. Delaunay, G. Martinelli, W. Fiedler, E. Raffoux, T. Prebet, C. Gomez-Roca, C. Papayannidis, M. Kebenko, P. Paschka, R. Christen, E. Guarin, A.M. Broske, M. Baehner, M. Brewster, A.C. Walz, F. Michielin, V. Runza, V. Meresse, C. Recher, Phase I clinical study of RG7356, an anti-CD44 humanized antibody, in patients with acute myeloid leukemia, Oncotarget 7(22) (2016) 32532-32542.
[27] P. Carbognani, L. Spaggiari, A. Romani, P. Solli, A. Corradi, A.M. Cantoni, P.G. Petronini, A.F. Borghetti, M. Rusca, P. Bobbio, Expression of human CD44v6 in non-small-cell lung cancer, Eur. Surg. Res. 30(6) (1998) 403-408.
[28] J. Skerlova, V. Kral, M. Kachala, M. Fabry, L. Bumba, D.I. Svergun, Z. Tosner, V. Veverka, P. Rezacova, Molecular mechanism for the action of the anti-CD44 monoclonal antibody MEM-85, J Struct Biol 191(2) (2015) 214-223.
[29] D.M. Glatt, D.R.B. Vera, M.C. Parrott, J.C. Luft, S.R. Benhabbour, R.J. Mumper, The Interplay of Antigen Affinity, Internalization, and Pharmacokinetics on CD44-Positive Tumor Targeting of Monoclonal Antibodies, Mol. Pharm. 13(6) (2016) 1894-1903.
[30] F. Birzele, E. Voss, A. Nopora, K. Honold, F. Heil, S. Lohmann, H. Verheul, C. Le Tourneau, J.P. Delord, C. van Herpen, D. Mahalingam, A.L. Coveler, V. Meresse, S. Weigand, V. Runza, M. Cannarile, CD44 Isoform Status Predicts Response to Treatment with Anti-CD44 Antibody in Cancer Patients, Clin Cancer Res 21(12) (2015) 2753-2762.
[31] A. Almalik, P.J. Day, N. Tirelli, HA-Coated Chitosan Nanoparticles for CD44-Mediated Nucleic Acid Delivery, Macromol Biosci 13(12) (2013) 1671-1680.

[32] A. Almalik, S. Karimi, S. Ouasti, R. Donno, C. Wandrey, P.J. Day, N. Tirelli, Hyaluronic acid (HA) presentation as a tool to modulate and control the receptor-mediated uptake of HA-coated nanoparticles, Biomaterials 34(21) (2013) 5369-5380.
[33] S. Ouasti, P.J. Kingham, G. Terenghi, N. Tirelli, The CD44/integrins interplay and the significance of receptor binding and re-presentation in the uptake of RGD-functionalized hyaluronic acid, Biomaterials 33(4) (2012) 1120-1134.
[34] M. Culty, H.A. Nguyen, C.B. Underhill, The hyaluronan receptor (CD44) participates in the uptake and degradation of hyaluronan, J Cell Biol 116(4) (1992) 1055-1062.
[35] T.L. Rogers, I. Holen, Tumour macrophages as potential targets of bisphosphonates, J Transl Med 9 (2011).
[36] A. Sica, T. Schioppa, A. Mantovani, P. Allavena, Tumour-associated macrophages are a distinct M2 polarised population promoting tumour progression: Potential targets of anti-cancer therapy, Eur J Cancer 42(6) (2006) 717-727.
[37] E. Vachon, R. Martin, J. Plumb, V. Kwok, R.W. Vandivier, M. Glogauer, A. Kapus, X.M. Wang, C.W. Chow, S. Grinstein, G.P. Downey, CD44 is a phagocytic receptor, Blood 107(10) (2006) 4149-4158.
[38] B. Koscso, B. Csoka, E. Kokai, Z.H. Nemeth, P. Pacher, L. Virag, S.J. Leibovich, G. Hasko, Adenosine augments IL-10-induced STAT3 signaling in M2c macrophages, J Leukocyte Biol 94(6) (2013) 1309-1315.
[39] B. Tao, W. Jin, J. Xu, Z. Liang, J. Yao, Y. Zhang, K. Wang, H. Cheng, X. Zhang, Y. Ke, Myeloid-specific disruption of tyrosine phosphatase Shp2 promotes alternative activation of macrophages and predisposes mice to pulmonary fibrosis, J Immunol 193(6) (2014) 2801-2811.
[40] J. Auwerx, The human leukemia-cell line, THP-1 - a multifaceted model for the study of monocyte-macrophage differentiation, Experientia 47(1) (1991) 22-31.
[41] S. Tsuchiya, Y. Kobayashi, Y. Goto, H. Okumura, S. Nakae, T. Konno, K. Tada, Induction of maturation in cultured human monocytic leukemia-cells by a phorbol diester, Cancer Res 42(4) (1982) 1530-1536.
[42] M. Daigneault, J.A. Preston, H.M. Marriott, M.K.B. Whyte, D.H. Dockrell, The identification of markers of macrophage differentiation in PMA-stimulated THP-1 cells and monocyte-derived macrophages, Plos One 5(1) (2010).
[43] M. Genin, F. Clement, A. Fattaccioli, M. Raes, C. Michiels, M1 and M2 macrophages derived from THP-1 cells differentially modulate the response of cancer cells to etoposide, Bmc Cancer 15 (2015).

[44] J.W. Tjiu, J.S. Chen, C.T. Shun, S.J. Lin, Y.H. Liao, C.Y. Chu, T.F. Tsai, H.C. Chiu, Y.S. Dai, H. Inoue, P.C. Yang, M.L. Kuo, S.H. Jee, Tumor-Associated Macrophage-Induced Invasion and Angiogenesis of Human Basal Cell Carcinoma Cells by Cyclooxygenase-2 Induction, J Invest Dermatol 129(4) (2009) 1016-1025.

[45] C.B. Aarons, O. Bajenova, C. Andrews, S. Heydrick, K.N. Bushell, K.L. Reed, P. Thomas, J.M. Becker, A.F. Stucchi, Carcinoembryonic antigen-stimulated THP-1 macrophages activate endothelial cells and increase cell-cell adhesion of colorectal cancer cells, Clin. Exp. Metastasis 24(3) (2007) 201-209.

[46] M.E. Lund, J. To, B.A. O'Brien, S. Donnelly, The choice of phorbol 12-myristate 13-acetate differentiation protocol influences the response of THP-1 macrophages to a pro-inflammatory stimulus, J. Immunol. Methods 430 (2016) 64-70.

[47] E.K. Park, H.S. Jung, H.I. Yang, M.C. Yoo, C. Kim, K.S. Kim, Optimized THP-1 differentiation is required for the detection of responses to weak stimuli, Inflamm Res 56(1) (2007) 45-50.

[48] P.B. Aldo, V. Craveiro, S. Guller, G. Mor, Effect of Culture Conditions on the Phenotype of THP-1 Monocyte Cell Line, Am J Reprod Immunol 70(1) (2013) 80-86.

[49] A. Gennari, M. Pelliccia, R. Donno, I. Kimber, N. Tirelli, Mannosylation Allows for Synergic (CD44/C-Type Lectin) Uptake of Hyaluronic Acid Nanoparticles in Dendritic Cells, but Only upon Correct Ligand Presentation, Adv. Healthc. Mater. 5(8) (2016) 966-976.

[50] F.O. Martinez, S. Gordon, M. Locati, A. Mantovani, Transcriptional profiling of the human monocyte-to-macrophage differentiation and polarization: New molecules and patterns of gene expression, J Immunol 177(10) (2006) 7303-7311.

[51] H.W.L. Zieglerheitbrock, R.J. Ulevitch, CD14 - Cell-surface receptor and differentiation marker Immunol. Today 14(3) (1993) 121-125.

[52] G.L. Zhang, H.Z. Zhang, Y.W. Liu, Y.Q. He, W.J. Wang, Y. Du, C.X. Yang, F. Gao, CD44 clustering is involved in monocyte differentiation, Acta Bioch Bioph Sin 46(7) (2014) 540-547.

[53] F. Rey-Giraud, M. Hafner, C.H. Ries, In vitro generation of monocyte-derived macrophages under serum-free conditions improves their tumor promoting functions, Plos One 7(8) (2012).

[54] F.O. Martinez, A. Sica, A. Mantovani, M. Locati, Macrophage activation and polarization, Front Biosci-Landmrk 13 (2008) 453-461.

[55] S. Becker, E.G. Daniel, Antagonistic and additive effects of Il-4 and interferon-gamma on human monocytes and macrophages - effects on Fc-receptors, Hla-D antigens, and superoxide production, Cell Immunol 129(2) (1990) 351-362.
[56] D.A. Hume, Differentiation and heterogeneity in the mononuclear phagocyte system, Mucosal Immunol. 1(6) (2008) 432-441.
[57] J. Prieto, A. Eklund, M. Patarroyo, Regulated expression of integrins and other adhesion molecules during differentiation of monocytes into macrophages, Cell Immunol 156(1) (1994) 191-211.
[58] J. Bai, G. Adriani, T.M. Dang, T.Y. Tu, H.X.L. Penny, S.C. Wong, R.D. Kamm, J.P. Thiery, Contact-dependent carcinoma aggregate dispersion by M2a macrophages via ICAM-1 and beta 2 integrin interactions, Oncotarget 6(28) (2015) 25295-25307.
[59] F. Porcheray, S. Viaud, A.C. Rimaniol, C. Leone, B. Samah, N. Dereuddre-Bosquet, D. Dormont, G. Gras, Macrophage activation switching: an asset for the resolution of inflammation, Clin. Exp. Immunol. 142(3) (2005) 481-489.
[60] A. Schildberger, E. Rossmanith, T. Eichhorn, K. Strassl, V. Weber, Monocytes, peripheral blood mononuclear cells, and THP-1 cells exhibit different cytokine expression patterns following stimulation with lipopolysaccharide, Mediat Inflamm (2013).
[61] R.V. Sionov, D. Naor, Calcium- and calmodulin-dependent PMA-activation of the CD44 adhesion molecule, Cell Adhes Commun 6(6) (1998) 503-523.
[62] M.C. Levesque, B.F. Haynes, Cytokine induction of the ability of human monocyte CD44 to bind hyaluronan is mediated primarily by TNF-alpha and is inhibited by IL-4 and IL-13, J Immunol 159(12) (1997) 6184-6194.
[63] B. Ruffell, G.F.T. Poon, S.S.M. Lee, K.L. Brown, S.L. Tjew, J. Cooper, P. Johnson, Differential Use of Chondroitin Sulfate to Regulate Hyaluronan Binding by Receptor CD44 in Inflammatory and Interleukin 4-activated Macrophages, J Biol Chem 286(22) (2011) 19179-19190.
[64] S.J. Wang, G. Wong, A.M. de Heer, W.L. Xia, L.Y.W. Bourguignon, CD44 variant isoforms in head and neck squamous cell carcinoma progression, Laryngoscope 119(8) (2009) 1518-1530.
[65] S.J. Wang, V.B. Wreesmann, L.Y.W. Bourguignon, Association of CD44 v3-containing isoforms with tumor cell growth, migration, matrix metalloproteinase expression, and lymph node metastasis in head and neck cancer, Head Neck-J Sci Spec 29(6) (2007) 550-558.

[66] J. Ni, P.J. Cozzi, J.L. Hao, J. Beretov, L. Chang, W. Duan, S. Shigdar, W.J. Delprado, P.H. Graham, J. Bucci, J.H. Kearsley, Y. Li, CD44 variant 6 is associated with prostate cancer metastasis and chemo-/radioresistance, Prostate 74(6) (2014) 602-617.
[67] H. Braumuller, S. Gansauge, M. Ramadani, F. Gansauge, CD44v6 cell surface expression is a common feature of macrophages and macrophage-like cells - implication for a natural macrophage extravasation mechanism mimicked by tumor cells, Febs Lett 476(3) (2000) 240-247.
[68] S. Seiter, D. Schadendorf, W. Tilgen, M. Zoller, CD44 variant isoform expression in a variety of skin-associated autoimmune diseases, Clin. Immunol. Immunopathol. 89(1) (1998) 79-93.
[69] A. Biddle, L. Gammon, B. Fazil, I.C. Mackenzie, CD44 Staining of Cancer Stem-Like Cells Is Influenced by Down-Regulation of CD44 Variant Isoforms and Up-Regulation of the Standard CD44 Isoform in the Population of Cells That Have Undergone Epithelial-to-Mesenchymal Transition, Plos One 8(2) (2013).
[70] C.B. Knudson, K.T. Rousche, R.S. Peterson, G. Chow, W. Knudson, CD44 and cartilage matrix stabilization, in: V.C. Hascall, K.E. Kuettner (Eds.), Many Faces of Osteoarthritis, Birkhäuser2002, pp. 219-230.
[71] M. Culty, K. Miyake, P.W. Kincade, E. Silorski, E.C. Butcher, C. Underhill, The hyaluronate receptor is a member of the CD44 (H-CAM) familt of cell-surface glycoproteins, J Cell Biol 111(6) (1990) 2765-2774.
[72] H.X. Liao, D.M. Lee, M.C. Levesque, B.F. Haynes, N-terminal and central regions of the human CD44 extracellular domain participate in cell-surface hyaluronan-binding, J Immunol 155(8) (1995) 3938-3945.
[73] M.C. Levesque, B.F. Haynes, TNF alpha and IL-4 regulation of hyaluronan binding to monocyte CD44 involves posttranslational modification of CD44, Cell Immunol 193(2) (1999) 209-218.

3.8. Supporting Information

SI1. Shape descriptors comparison between two experimental differentiation/polarization protocols

Methods. Image acquisition and analysis of THP-1 macrophages: THP-1 macrophages were stained for F-actin and nuclei after each differentiation procedure. Briefly, cells were incubated for 10 min with 1 μg/mL Hoechst (Invitrogen, Thermo-Fisher, UK) solution in serum-free medium at 37°C and 5% (v/v) CO_2, cells were washed with PSB, fixed with 4%

PFA solution for 10 min at room temperature, washed again with PBS, and then permeabilized with 0.1% (v/v) TritonX-100 solution in PBS (3 min incubation at room temperature). Cells were finally incubated for 20 min at room temperature with 1:200 Phalloidin-AlexaFluor488 (Invitrogen, Thermo-Fisher, UK) in 1% BSA (w/v) PBS solution, then washed with PBS, and stored in the dark at 4°C in a 1 mg/mL ascorbic acid solution in PBS. Images of polarized THP-1 macrophages were acquired using an inverted confocal laser microscope (Leica SP5). Volumetric dataset of differentiated and polarized THP-1 with both [24]/[6/18] and [24]*/[24/24] protocols were analyzed using ImageJ (v1.49p, http://rsb.info.nih.gov/ij). The morphological analysis was performed considering the F-actin channel on volumetric datasets (n=2) observing about 10 cells per phenotype/method. Cell thickness was measured considering the difference between basal and the apical z-level. The measured difference was then multiplied by the z-size of the dataset voxel, obtaining the average thickness of each acquired cells. Cell surface area and solidity were measured using dataset maximum projections, Otsu threshold and watershed method were applied respectively to select cell bodies and to separate cell projections. Finally, the surface area and the shape descriptors were determined using ImageJ plug-in. Herein, we include only the solidity descriptor as the most representative parameter to distinguish the macrophages phenotype/method.

Results. No significant difference was recorded between the two differentiation/polarization protocols used in the study.

SI2. Viability of THP-1 macrophages after differentiation/polarization.

Cell culture. THP-1 premonocytes (1.25×10^5 cells/cm^2) were differentiated/polarized following the [24]/[6/18] and [24]*/[24/24] protocols: cell viability was measured immediately after to assess any potential variation between experimental protocols using both cell proliferation and live/dead assays.

Methods. Cell culture medium was removed and cells were washed twice with 1 mL of PBS. Cell viability was determined using the CellTiter 96® AQ_{ueous} One Solution Cell Proliferation Assay (MTS). Briefly, cells were washed with PBS and incubated for one hour at 37°C in serum- and phenol-red-free RPMI-1640 containing MTS 5% (v/v). Cell viability was measured by reading the absorbance values at 490nm (Synergy2 Biotek plate reader, Gen5 software). Cell viability measurements were normalized by the amount of total protein content in each well using the BCA kit. We compared the resulting cell viability using two-

way analysis of variance (ANOVA), setting the macrophage phenotype as row factor and the differentiation/polarization method as column factor. Differences between groups were considered to be significant at a P value of <0.05. Statistical analyses were performed with GraphPad Prism 6.04 (GraphPad Software, Inc., San Diego, CA).

In parallel, cells differentiated/polarized following the longer protocol ([24]*/[24/24]) in µ-slide 8 well (iBidi, Planegg, Germany) and stained with the Live/Dead Assay (ab11347, Abcam, UK) following the manufacturer instructions (cell incubation in 5X Live/Dead Dye (PBS) for 10 minutes at room temperature). Images were acquired on a Leica DMI6000 B inverted microscope (Live: $Em_{(max)}$=495nm, $Ex_{(max)}$=515nm; Dead: $Em_{(max)}$=528nm, $Ex_{(max)}$=617nm) and analyzed with ImageJ. Each channel was thresholded and the fluorescent area was measured. The analysis was performed on images with an area of (832×702)µm^2. Note that the analysis was performed on at least n=6 images, observing the live/dead status of a total number of about 5000 cells.

Results. A significant reduction in cell viability (~40%) following polarization into pro-inflammatory phenotypes (M1) was recorded, with no significant differences between the two differentiation/polarization methods (Figure 3—5A). These results were also confirmed by the Live/Dead assay (Figure 3—5B).

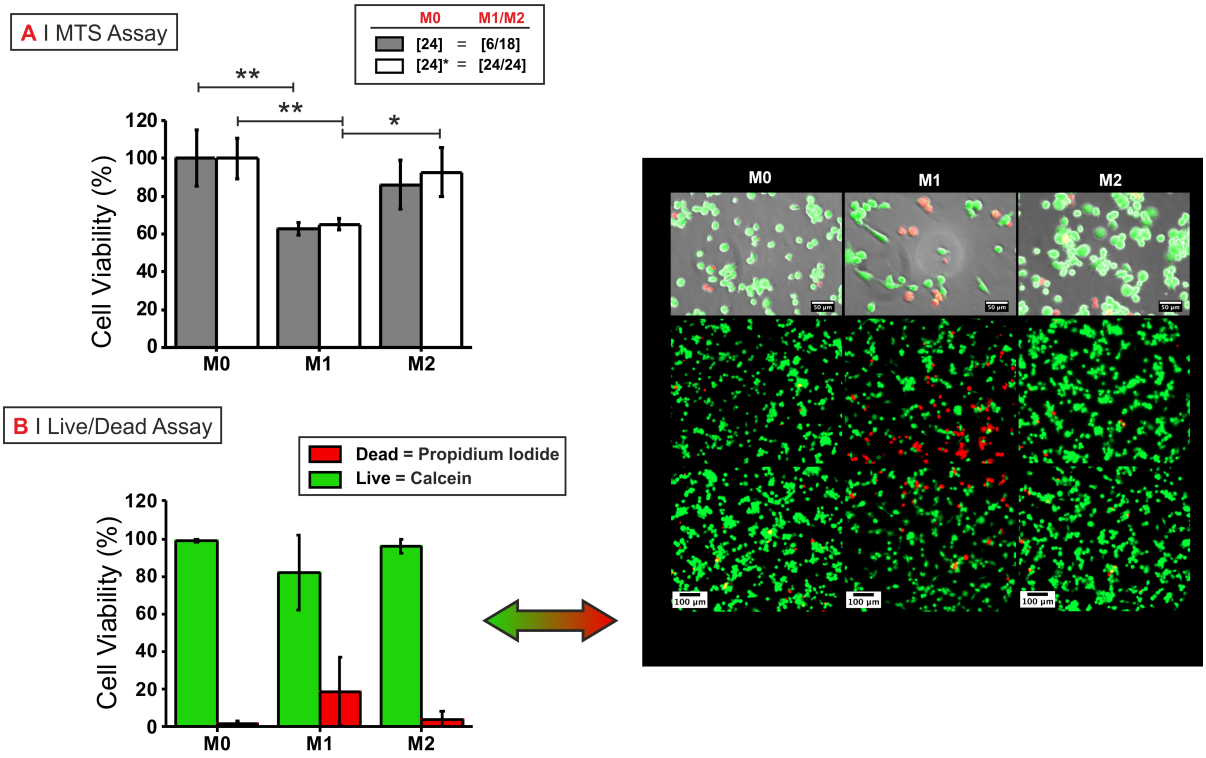

Figure 3—5. Cell viability after differentiation/polarization. ***A.*** Viability of THP-1 macrophages assessed via the MTS assay (normalized against the protein content measured via BCA assay) upon exposure to polarizing agents. Data represented as relative percentage of cell viability with respect to resting macrophages (M0); average ± SD, n=3. For statistical analysis: $^{**}P<0.01$, $^{*}P<0.05$ (Two-way ANOVA). ***B.*** representative pictures of Live/Dead staining (calcein-AM/green: live; propidium iodide/red: dead) for THP-1 macrophages incubated with 100 ng·mL^{-1} LPS and 20 ng·mL^{-1} IFN-γ (M1), 20 ng·mL^{-1} IL-4 and IL-13 (M2), or medium (M0) (protocol [24]*/[24/24]).

SI3. Immunofluorescence of membrane-bound CD44

THP-1 macrophages were stained for F-actin and nuclei after [24]*/[24/24] differentiation/ polarization procedure. Briefly cells were incubated for 10 min with 1 µg/mL Hoechst (Invitrogen, Thermo-Fisher, UK) solution in serum-free medium at 37°C and 5% (v/v) CO_2, and then cells were washed with cold PBS and placed on ice. A 1:200 dilution of anti-human CD44-Alexa594 conjugated antibody (#103054, Biolegend) in 1% (w/v) BSA/PBS was freshly prepared, incubating cells for 30 minutes on ice. Cells were then washed with PBS and fixed with 4% PFA solution incubating 10 minutes on ice. After permeabilization with 0.1% (v/v) Triton X-100 solution in PBS (3 min incubation at room temperature), cells were finally incubated for 20 min at room temperature with a 1:200 Phalloidin-AlexaFluor488 (Invitrogen, Thermo-Fisher, UK) in 1% (w/v) BSA/PBS solution, washed with PBS and stored in the dark at 4°C in a 1 mg/mL ascorbic acid solution (PBS).

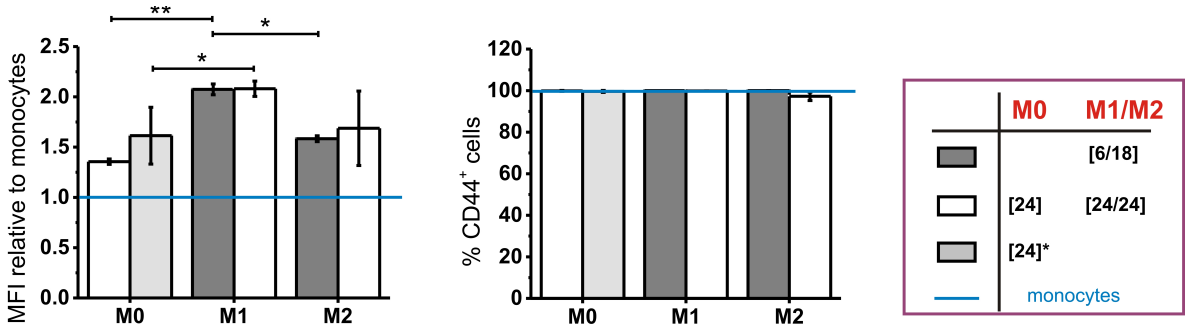

Figure 3—6. CD44 expression as a function of the various differentiation/polarization protocols.

SI4. Detachment of THP-1 macrophages via enzymatic and non-enzymatic methods

Cell culture. THP-1 premonocytes (1.25×10^5 cells/cm^2 in 24-well flat-bottomed plates) were differentiated into THP-1 macrophages for 24 hours by incubation in 0.5 mL of complete medium containing 50 ng·mL^{-1} PMA. After differentiation, PMA medium was removed; cells were washed once with 1 mL of serum-free RPMI 1640 and rested for a further 24 hours in 0.5 mL of PMA-free complete medium.

Methods. Cell culture medium was removed and cells were washed twice with 1 mL of PBS. Cells were then incubated for 15 minutes at RT with 0.5 mL of i) trypsin-EDTA solution (0.05% trypsin, 0.02% EDTA) (59417C; Sigma Aldrich, UK), ii) Accutase I (A6964; Sigma Aldrich, UK), or iii) pre-warmed Cell Dissociation Buffer, Enzyme-Free, PBS (#13151-014, Gibco®/Invitrogen, UK). The supernatant was collected and cells were counted with a Scepter 2.0 Handheld Automated Cell Counter with 60 µm Scepter Sensors (EMD-Milipore). In parallel, cell viability was determined using the dye exclusion test - Trypan Blue Solution 0.4% (Thermo Scientific, UK).

Results. Cell viability remained unchanged regardless of the detachment procedure. A high number of cells were recovered by using the enzyme-free solution, showing feasibility of using this approach for cell harvesting and posterior cell surface marker analysis.

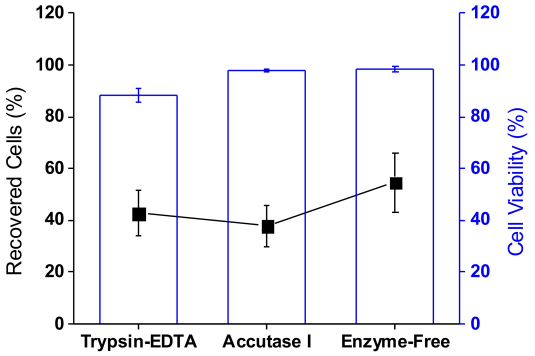

Figure 3—7. Effect of the detachment procedure on the recovery and viability of THP-1 macrophages. Percentage of recovered cells with respect to number of seeded cells (left y-axis), cell viability measured by the dye exclusion test (right y-axis). Values represented as average ± SD, *n*=3 individual experiments.

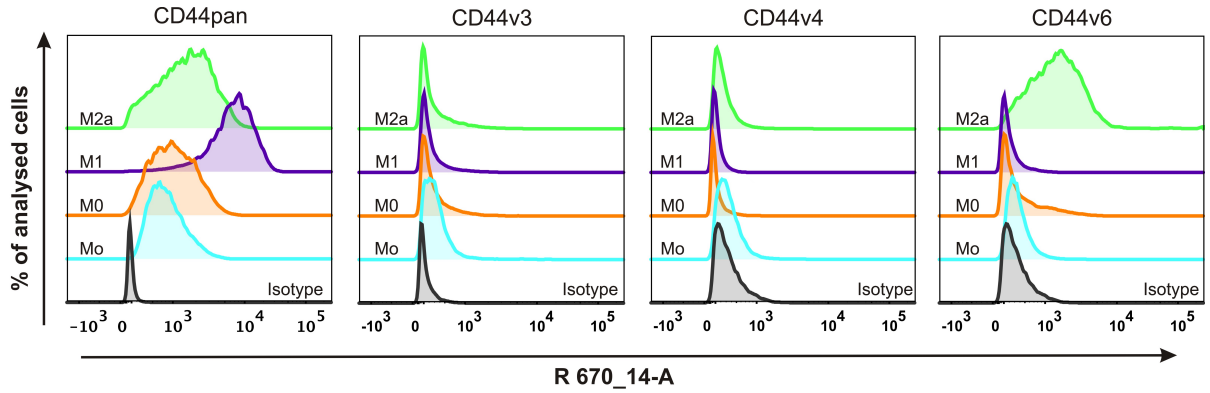

Figure 3—8. Flow cytometry data for the expression of CD44 and some of its most important isoforms. Overlay comparison of untreated (Mo), PMA-treated (M0), LPS+IFN-γ-treated (M1), and IL-4+IL-13-treated (M2a) cells.

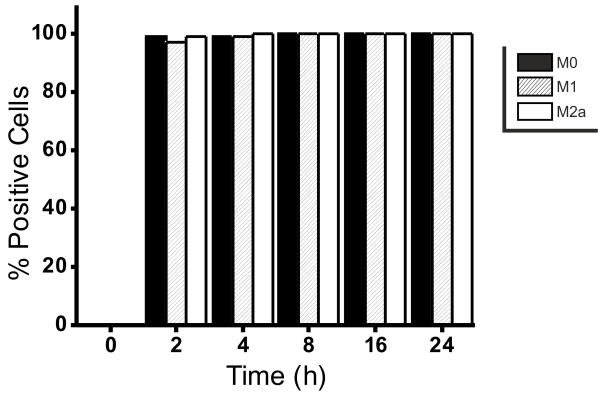

Figure 3—9. Flow cytometry data for the uptake of fluorescently-labelled hyaluronic acid (HA-Rho) over time. Percentage of positive cells for HA-Rho measured at each time point. Positivity was calculated by using the autofluorescence of untreated cells (i.e. *t*=0h) as threshold.

SI5. Polymer and nanoparticle characterization

Table 3—1. Physical characteristics of soluble HA and CS/HA nanoparticles prepared with 36 and 656 kDa chitosan. Please note that the loading of siRNA did not affect size or charge of the nanoparticles.

Soluble HA		
$\overline{d_{H_w}}$ (kDa)	180	
Đ	1.56	
$\overline{d_{H_w}}$[a] (nm)	40	
HA nanoparticles		
	CS36/HA	CS656/HA
Z-average size (nm)	170 ± 5	230 ± 13
PDI	0.21 ± 0.06	0.19 ± 0.02
ζ potential (mV)	-37 ± 2	-37 ± 1

[a] $\overline{d_{H_w}}$: weight-average hydrodynamic diameter.

Gel Permeation Chromatography (GPC). Molecular weight distribution, intrinsic viscosity, hydrodynamic diameter (d_H) and radius of gyration (R_g) for native HA were determined by GPC using an isocratic pump (PN1130, Postnova Analytics, Landsberg, Germany), two CLM3021-A6000M columns (Malvern Instruments, Malvern, UK) and the following online detectors: MALLS (Viscotek SEC-MALS20, Malvern Instruments), refractive index (Optilab T-rEX, Wyatt Technology, Dernbach, Germany) and viscometer (Viscotek 270 Dual Detector, Malvern Instruments). 50 µL of a 3 mg/mL solution of HA were injected and eluted at 0.7 mL/min in 10 mM phosphate buffer supplemented with 100 mM sodium nitrate and 0.02 % w/v sodium azide at pH = 7.4. Signals were analyzed using OmniSEC 5.0 software (Malvern). The HA dn/dc at 25 °C dissolved in the eluent was determined prior GPC analysis and was then used for the calculations (dn/dc = 0.132).

Dynamic Light Scattering (DLS). DLS analysis of the hydrodynamic diameter (reported as Z-average size), size polydispersity (PDI), and ζ potential of the particles after preparation was performed on three independent samples at a temperature of 25 °C using a Zetasizer Nano ZS instrument (Model ZEN3600, Malvern Instruments Ltd., UK) equipped with a solid state HeNe laser (λ=633 nm) at a scattering angle of 173°. Size measurement data were analyzed by using the General urpose algorithm. The electrophoretic mobility of the samples was converted in ζ potential by using the Smoluchowski equation.

Chapter 4 Chitosan/hyaluronic acid nanoparticles: rational design revisited for RNA delivery

Enrique Lallana[1§], Julio M. Rios de la Rosa[1§], Annalisa Tirella[1], Maria Pelliccia[1], Arianna Gennari[1], Ian J. Stratford[1], Sanyogitta Puri[2], Marianne Ashford[2], Nicola Tirelli[1]*

[§] The two authors contributed equally to the study.

[1] North West Centre for Advanced Drug Delivery (NoWCADD), Division of Pharmacy & Optometry, School of Health Sciences, Faculty of Biology, Medicine and Health, Stopford building, Manchester, M13 9PT, United Kingdom

[2] Innovative Medicines-Pharmaceutical Sciences, AstraZeneca, Silk Road Business Park, Macclesfield, SK10 2NA, United Kingdom

Mol. Pharmaceutics, **2017**, *14* (7), pp 2422–2436
DOI: 10.1021/acs.molpharmaceut.7b00320
Publication Date (Web): June 9, 2017

* to whom correspondence should be addressed:

Prof. Nicola Tirelli
NorthWest Centre for Advanced Drug Delivery (NoWCADD)
Division of Pharmacy and Optometry School of Health Sciences
University of Manchester Manchester, M13 9PT, UK
E-mail: nicola.tirelli@manchester.ac.uk
Tel.: +44 161 275 24 80.

4.1. Abstract

Chitosan/hyaluronic acid (HA) nanoparticles can be used to deliver a RNA/DNA cargo to cells overexpressing HA receptors such as CD44. For these systems, unequivocal links have not been established yet between chitosan macromolecular (molecular weight; degree of deacetylation, i.e. charge density) and nanoparticle variables (complexation strength, i.e. stability; nucleic acid protection; internalization rate) on one hand, and transfection efficiency on the other hand.

In this chapter, we have focused on the role of avidity on transfection efficiency using the CD44-expressing HCT-116 as a cellular model; we have employed two differently sized payloads (a large luciferase-encoding mRNA and a much smaller anti-luc siRNA), and a small library of chitosans (variable molecular weight and degree of deacetylation). The RNA avidity for chitosan showed – as expected – an inverse relationship: higher avidity – higher polyplex stability – lower transfection efficiency. The avidity of chitosan for RNA appears to lead to opposite effects: higher avidity – higher polyplex stability but also higher transfection efficiency. Surprisingly, the best transfecting particles were those with the lowest propensity for RNA release, although this might be a misleading relationship: for example, the same macromolecular parameters that increase avidity can also boost chitosan's endosomolytic activity, with a strong enhancement in transfection. The performance of these non-viral vectors appears therefore difficult to predict simply on the basis of carrier- or payload-related variables and a more holistic consideration of the journey of the nanoparticle, from cell uptake to cytosolic bioavailability of payload, is needed.

It is also noteworthy that the nanoparticles used in this study showed optimal performance under slightly acidic conditions (pH 6.4), which is promising for applications in a tumoral extracellular environment. It is also worth pointing out that under these conditions we have for the first time successfully delivered mRNA with chitosan/HA nanoparticles.

Keywords: hyaluronan; RNA; chitosan; targeting; gene delivery; HCT-116.

4.2. Introduction

Chitosan is popularly employed in the production of polyplexes for the delivery of nucleic acids [1, 2]; such structures can be binary complexes, or may include also other polyelectrolytes, e.g. hyaluronic acid (HA), in a ternary complex. The coexistence of chitosan and HA is attractive in that it combines the low toxicity of the former with the receptor-mediated internalization of the latter, thus allowing for a targeted delivery in cells overexpressing HA receptors such as CD44, which is upregulated in a number of tumors [3, 4]. It is worth mentioning that HA can also act as a platform for the presentation of additional ligands, and therefore allow for synergic targeting capabilities, as we have demonstrated in the case of mannose receptors [5] or integrins [6].

In the use of polyplexes for nucleic acid delivery, (macro)molecular properties play a crucial but sometimes unclear role in controlling stability of the complex, endosomal escape and ultimately transfection efficacy [7-9]. Differently from lipoplexes where ordered structures can be found and characterized [10], in such polyplexes the components are likely to be disordered and therefore it is reasonable to assume that the carrier performance can be tuned solely by controlling chitosan/nucleic acids interactions through affinity (e.g. via steric hindrance on protonated amines) or avidity (proximity between cations regulated through degree of protonation, or chitosan molecular weight). This, however, ushers a more complex and delicate balance of beneficial and detrimental effects: for example, stronger interactions supposedly increase the stability of nanocarriers (desirable) and at the same time make the release phase more difficult (detrimental); the same molecular variables also control other interactions such as those with cell membranes leading to endosomal escape, which heavily contribute to the efficacy of the delivery system. Unsurprisingly, literature is rife with conflicting evidence about the influence of chitosan's macromolecular variables on transfection efficiency: for instance, in comparative studies a better silencing/transfection is reported with carriers prepared from chitosans of high [11-13], of intermediate [14, 15] or even low molecular weight [16-21]. A number of other variables further complicate the landscape, such as differences in the preparative methods or cell-specific issues (for instance, influence of chitosan/nucleic acid charge ratio on DNA transfection on ARPE-19 and HEK-293 cells [19]).

Here, we have specifically tackled the role of avidity in the polyplex partners employed in chitosan/HA nanoparticles. To do so, we have designed a small library of nanoparticles with variable chitosan-nucleic acid reciprocal avidity (Scheme 4—1). From the polycation side, we

have employed five chitosans differing in molecular weight and density of cationizable groups (amines, hereafter expressed as the deacetylation degree, DD); they were produced from a commercially available precursor (viscosity average molecular weight ($\bar{M}_v$ = 685 kDa, DD = 84%) via nitrous acid-mediated oxidative depolymerization [22] and/or reacetylation with acetic anhydride [23]. The chitosan samples were named after their size (High, Low or UltraLow molecular weight) and DD, e.g. H84 refers to the high molecular weight, DD=84%. As nucleic acids, we have employed siRNA (21 bases, double-stranded) payload and a ≈2000-base mRNA respectively as a low- and high- avidity payload. While siRNA/chitosan binary complexes have been extensively studied [2, 11, 24], only a few papers have focused on ternary complexes (+ HA [11, 25, 26]) and, to the best of our knowledge, this is the first study dealing with the use of the latter to deliver mRNA. Chitosan/HA nanoparticles prepared from the above materials were evaluated in terms of ability to encapsulate, protect (against nuclease degradation) and release RNA, and their internalization and transfection efficiency; we specifically focused on their behavior under slightly acidic conditions (using pH 6.4) as representative of the extracellular environment of a number of pathologies in inflammation [27] and cancer [28, 29].

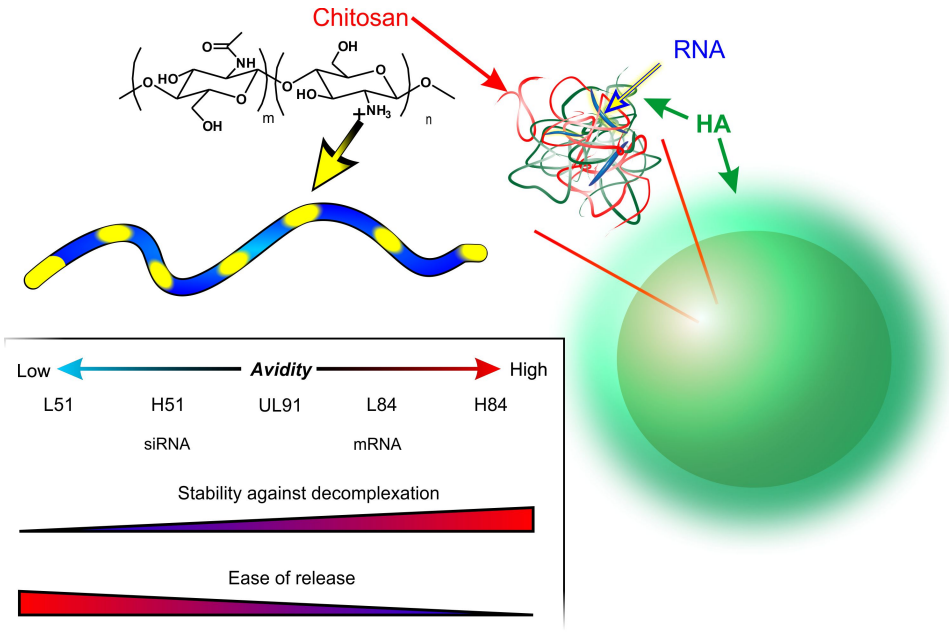

Scheme 4—1. Chitosan/HA nanoparticles feature HA (green) on the surface and a core where the two polymers produce a ternary complex with RNA (blue). In this study, we have used five chitosans and two RNAs with different avidity, which is expected to influence with opposite effects the stability of the particles and the ease of the RNA release.

4.3. Materials and Methods

4.3.1. Materials

The list of the chemicals and nucleic acids is provided in the Supporting Information, Section SI1. Materials.

4.3.2. Physico-chemical characterization

Nuclear Magnetic Resonance (NMR). ^{1}H NMR spectra were recorded on 1.0 – 0.1% wt. polymer solutions (in 2% DCl in D_2O) using a Bruker Avance 400 MHz spectrometer. The DD of the different chitosans was calculated from the integration of the resonances of the N-acetyl group (1.80 – 2.20 ppm, 3H, GluNAc units) and the H2-H6 protons (2.80 – 4.20 ppm, 6H, GluN and GluNAc units).

Dynamic Light Scattering (DLS). Hydrodynamic diameter (Z-average size), size polydispersity (PDI) and ζ potential were measured at 25 °C (pre-equilibration for 2 min; 1 mg/mL) using a Zetasizer Nano ZS (Model ZEN3600, Malvern Instruments Ltd., UK) equipped with a solid state HeNe laser ($\lambda = 633$ nm) at a scattering angle of 173°. Size distributions were calculated by applying the General Purpose algorithm and are presented as the average of the Z-average values of three independent samples.

Viscosimetry. Viscosity measurements were performed with a falling ball automated microviscometer (Anton Parr, Graz, Austria) equipped with a 1.6 mm internal diameter capillary tube set at an inclination angle of 30° and a temperature of 25 °C. The polymers were dissolved overnight in 0.25 M AcOH/0.25 M AcONa at concentrations in the range 20-0.3 mg/mL. The intrinsic viscosity ($[\eta]$) was calculated by means of the Huggins and Kraemer plots (extrapolation to 0 concentration), and used to calculate $\overline{M}_v$ from the Mark–Houwink equation $[\eta] = K \cdot \overline{M}_v^a$, assuming $K = 1.57 \times 10^{-5}$ L g^{-1} and $a = 0.79$ for all chitosans [30].

4.3.3. Preparative operations

1) Oxidative depolymerization of chitosan. Chitosans of lower molecular weight (L84 and UL91) were prepared by oxidative depolymerization of H84 at 25 °C using sodium nitrite/HCl following slightly modified procedures reported in the literature [31]. Briefly, 100 mL of a solution of H84 (1% wt 0.1M HCl (aq), dissolved overnight) were transferred into a 250 mL reaction vessel of a Tornado reactor (Radleys, UK) and mechanically stirred (1,000 rpm). For the preparation of L84, sodium nitrite was added to a final concentration of 3 mM (dropwise from a 3 M stock solution) and the solution was stirred for 12 h. For the

preparation of UL91, a second equal portion of sodium nitrate solution was sequentially added after the first 12 h, and the solution was stirred for additional 12 h. Afterwards, the chitosans were precipitated by addition of 0.1 M NaOH (aq) until pH 10 was reached, and isolated and purified by several cycles of centrifugation (4500 rpm, 5-10 min) and thorough re-suspension in MilliQ water. Finally, the suspensions containing L84 and UL91 were freeze-dried to recover the chitosans as dry solids (850 and 450 mg, respectively).

2) Re-acetylation of chitosan. CSs of lower DD were prepared through re-acetylation of H84 and L84 with acetic anhydride (Ac_2O) at 25 °C following a general procedure reported by the group of Domard [23]. After confirming the general applicability of the procedure (see Supporting Information, Section SI2. Acetylation of chitosan, and Figure 4—9, which reports the degree of acetylation as a function of the amount of acetic anhydride), H84 and L84 were reacted using an Ac_2O:NH_2 molar ratio of 0.4 (total reaction volume: 50 mL; final chitosan concentration of a 5 mg/mL final chitosan reaction solution; in a Tornado reactor vessel under mechanical agitation, 1,000 rpm). After completion of reaction, the re-acetylated chitosans were purified by extensive dialysis (MWCO of 100 and 2 KDa for H51 and L51, respectively) against 1 mM HCl (aq), 5.5 mM NH_4OH (aq) and MilliQ water, and finally recovered after freeze-drying (225 and 195 mg for H84 and L84, respectively).

3) Labelling of chitosan with Alexa Fluor 405. 8.0 mg of chitosan (H84 and L84) were dissolved overnight in 1.45 mL of 4.6 mM HCl (aq), then adding 145 µL of 1 M MES buffer (pH 5.5) were. Alexa Fluor 405 NHS ester (equivalent to 1.3% mol of Glu units) was then dissolved in 75 µL of DMSO and added to the reaction vessel. The reaction mixture was stirred overnight at 25 °C in the dark. The resulting solution was purified via centrifugal ultrafiltration using an Amicon Ultra-4 (MWCO: 100 and 10 KDa for H84/H51 and L84, respectively) against MilliQ water. The purified products were recovered by freeze-drying (6-7 mg). The degree of functionalization was determined by measuring the fluorescence intensity the products, using an Alexa Fluor 405 NHS ester dye to link the emission to the molar concentrations of the fluorophore (please note that this is later transformed in a molar ratio between functionalized and non-functionalized units in the polymer). Typical degree of derivatization: 0.1-0.3% mol of Glu units.

4) Preparation of chitosan/hyaluronic acid nanoparticles. All materials used for the handling of RNA solutions were nuclease-free or sequentially washed with RNaseZap solution (Thermo Scientific, UK), 70% v/v EtOH in water, and nuclease-free water prior to use. Chitosan solutions were prepared by dissolving it overnight at a concentration of 0.069 wt.% in 4.6 mM HCl (aq) in nuclease-free water, then adjusting pH to 5 by adding 0.1 M NaOH

(aq). Hyaluronic acid (HA) was dissolved overnight in nuclease-free water at a concentration of 1.5 mg/mL, and then the pH was adjusted to 5 by adding 0.1 M HCl (aq). RNA solutions were prepared at the desired concentration by diluting stock solutions in nuclease-free water. Chitosan and HA solutions were filtered respectively through 0.45 and 0.22 μm pore size filters prior to use. In a typical procedure, a given volume of RNA solution (concentration depending on the targeted wt.% loading i.e. the nitrogen-to-phosporous (A/P) ratio, calculated from the molar ratio between amine groups in chitosan and phosphate groups in RNA) was added slowly over the same volume of the 0.69 wt.% chitosan solution under magnetic stirring (1,000 rpm, 25 °C, 2 mL Eppendorf tubes). After 10 minutes, the chitosan/RNA dispersion would be added to the same volume of a solution of 1.5 mg/mL HA. The final mixture was stirred for 30 min under the same conditions, which rendered nanoparticle formulations at a concentration of ca. 1 mg/mL for all RNA loadings (calculated from the nanoparticle polyelectrolytes feed ratio). The Encapsulation Efficiency (EE) was determined by measuring the amount of non-complexed RNA remaining in solution. Briefly, after nanoparticle sedimentation via centrifugation (13,000 rpm, 60 min), the amount of nucleic acid in solution was quantified fluorimetrically (Synergy2 Biotek plate reader using Gen5 software) using the RiboGreen reagent as specified by the manufacturer. EE values (%) were calculated by the formula: $EE = (A - B)/A \times 100$, where A is the amount of RNA in the nanoparticle feed, and B is the amount of RNA in the supernatant.

4.3.4. Functional characterization

Heparin displacement assay. 7 μL of a heparin solution (0.8, 8, and 80 mg/mL in RNAse free water; corresponding approximately to a sulfate/phosphate charge molar ratio of 2.5, 25 and 250, respectively, were added to 50 μL of 10% wt. RNA-loaded nanoparticles (pH 5.0) previously diluted with 63 μL of nuclease-free water. The resulting suspension was incubated overnight at 25 °C. Afterwards, the solution was centrifuged (12,000 rpm, 60 min) and the amount of nucleic acid released in solution was quantified using the RiboGreen assay.

Protection assay: chitosanase/heparin-mediated nucleic acid release. 44 μL of 10% wt. loaded RNA-loaded nanoparticles were incubated with 22 μL of a solution of RNase I (15 mM Tris buffer, 0.3 M NaCl, pH 7.0) at a concentration of 0, 0.33 and 3.33 U (corresponding to 0, 0.5, and 5 U of enzymes per 100 μL of final reaction volume, respectively). Samples were incubated at 37 °C for 30 min. The nuclease reaction was then quenched with the addition of 7.6 μL of 1.0% SDS (aq). Afterwards, 3 μL of chitosanase (0.084 units/μL, 50 mM acetate buffer, pH 5.0) were added to the mixture, and the enzymatic reaction was

allowed to occur for 3 h at 37 °C. Finally, 4.7 µL of a solution of heparin (80 mg/mL in RNase-free water; corresponding approximately to a negative/positive charge molar ratio of of 250) were added. The resulting mixture was incubated overnight at 25 °C. After centrifugation (13,000 rpm, 30 min), the nucleic acid released in solution was quantified using agarose gel electrophoresis (for mRNA; GelRed-loaded 1.3 wt.% agarose gels, 60 min, 100 mA) or polyacrylamide gel electrophoresis (for siRNA; 18-well/30µL, 15% CriterionTM TBE-Urea Gel, Biorad; 70 min, 120V).

4.3.5. Cell-based experiments

1) General cell culture. Unless otherwise stated all products were purchased from Sigma-Aldrich (Gillingham, UK). The human colorectal carcinoma cell line HCT-116 (CCL-247™) was purchased from ATCC (VA, USA). Cells were cultured in a humidified 5% (v/v) CO_2 air atmosphere at 37°C in complete medium: McCoy's 5A medium (M8403) supplemented with 10% (v/v) foetal bovine serum (FBS, F7524), 2 mM L-Glutamine (G7513), and 1% (v/v) penicilin-streptomycin (P4333). Complete medium refers to bicarbonate-buffered medium at pH 7.4, unless otherwise specified. HEPES-buffered (25 mM) McCoy's 5A medium was prepared from powder medium (M4892) and supplemented appropriately. Cells were passaged every 3-4 days following the supplier's recommendations, and discarded upon reaching passage number 30. Medium was replaced every 2 days. For the preparation of concentrated media and nanoparticle suspensions to be used in cell culture experiments, please refer to Supporting Information, section 1SI: Preparation of media for cell culture.

2) CD44 expression via flow cytometry (indirect staining). HCT-116 cells were detached using cell dissociation buffer, enzyme-free, PBS (#13151-014, Gibco/Invitrogen, UK) to avoid any influence of enzymatic treatments on the integrity of CD44. Approximately $0.5x10^6$ cells were suspended in 100 µL of FACS buffer (PBS, 0.1% NaN_3, 5% FBS) per sample tube (1.5 mL Eppendorf tubes) and separately stained for 30 min at room temperature with the following primary antibodies: i) mouse anti-human CD44 (1:100) (156-3C11, Cell Signaling), ii) mouse anti-human CD44v3 (1:20) (Clone #3G5, R&D Systems), iii) mouse anti-human CD44v4 (1:50) (MCA1728; AbD Serotec), iv) mouse anti-human CD44v6 (1:20) (Clone #2F10, R&D Systems), or v) IgG1/IgG2 control (1:10) (AbD Serotec). Excess primary antibody was removed by centrifugation and cells were incubated for a further 30 min at room temperature with the secondary antibody Alexa Fluor 647-conjugated goat anti-mouse IgG H&L (1:2000) (ab150115, Abcam). The expression of CD44 isoforms was analyzed on

10,000 live, individual cells using a BD LSRFortessa cytometer (BD Bioscience, San Jose CA, USA) equipped with the FACSDiva software (v8.0.1). Data were analyzed with FlowJo (vX.0.7, Tree Star, Ashland, OR, USA) after gating live cells in the FSC/SSC window and singlets in the FSC-H/FSC-A window, respectively. The median fluorescence intensity (MFI) of the isotype control was used as threshold to calculate the MFI of the marker of interest.

3) CD44(pan) immunofluorescence. HCT-116 cells in complete McCoy's 5A medium were seeded in an Ibidi µ-Slide VI0.4 (ibiTreat 80606, Ibidi, Germany) at a concentration of 1×10^4 cells/cm^2 and allowed to attach and proliferate overnight under standard sterile conditions for cell culture (5% CO_2, 37 °C). Immunostaining of membrane-bound CD44(pan) was performed on live cells. Briefly, cells were firstly washed with cold PBS and then incubated for 20 min at room temperature with 5% (w/w) BSA solution in PBS. Cells were then washed with PBS three times, placed on ice and incubated for 30 min with mouse anti-human CD44 (1:400) (156-3C11, Cell Signaling, US) diluted in 1% (w/w) BSA solution in PBS according to the manufacturer's instructions. Cells were washed with cold PBS three times, and then incubated for 30 min on ice with a goat anti-mouse IgG H&L AlexaFluor488-conjugate (1:500) (ab150113, Abcam, UK) in 1% BSA (w/w) solution in PBS according to the manufacturer's instructions. Finally, cells were washed with PBS three times and then fixed with 4% PFA (10 min on ice), washed again with PBS, and stored in 1 mg/mL ascorbic acid solution in PBS.

Images were acquired using the inverted microscopy (Leica DMI6000) equipped with a 63X immersion oil objective, using the I3 filter cube (BP 450/490 nm). Background removal of acquired images was performed using ImageJ software (v1.51.h, http://rsb.info.nih.gov/ij).

4) Nanoparticle internalization via flow cytometry. HCT-116 cells in complete McCoy's 5A medium were seeded in 12 well plates (2×10^4 cells/cm^2) and allowed to attach and proliferate overnight under standard sterile conditions for cell culture (5% CO_2, 37 °C). Cells were then incubated with LTX or 125 µg/mL of chitosan/HA nanoparticles loaded either with siRNA:DY547 or mRNA:Cy5 (RNA loading: 2.43% wt.% for all chitosans) in complete HEPES-buffered McCoy's 5A medium (pH 6.4 or 7.4) at 37°C for 4 h. Then, cells were washed three times with PBS, detached using trypsin-EDTA Solution (59417C, Sigma-Aldrich, UK) for 10 min at room temperature, thoroughly fixed 1% paraformaldehyde on ice for 20 min, centrifuged and finally suspended in 100 µL of PBS. The uptake of siRNA or mRNA was determined on 5,000 individual cells with an Amnis ImageStream®^{X} Mark II Imaging Flow Cytometer (Merck Millipore) equipped with the Amnis INSPIRE™ software (v200.1.388.0) using the 595/642 or 642/745 nm detectors in the case of siRNA:DY547 or

mRNA:Cy5, respectively. The results were analyzed using the Amnis IDEAS® software (v6.2.64.0) after gating single cells using the features *area* and *aspect ratio* of the bright-field image. Untreated cells were used as auto-fluorescence control and as percentage of positive events.

5) CD44 blocking experiments. HCT-116 cells in complete McCoy's 5A medium were seeded in 12 well plates (2×10^4 cells/cm^2) and allowed to attach and proliferate overnight under standard conditions (5% CO_2, 37 °C). Cells were pre-treated for 1 h with McCoy's 5A medium (HEPES, pH = 7.4) containing either (i) an excess of soluble HA ($\overline{M_w}$ = 680 KDa, 1.5 mg mL^{-1}, corresponding to a ~24-fold excess compared to an HA content in the nanoparticle of about 50% wt., i.e. 125 µg mL^{-1} chitosan/HA nanoparticles correspond to 62.5 µg mL^{-1} of HA) [Please note that the effect of this blocking on CD44(pan) surface expression (Figure 4—4E) was first determined by flow cytometry using a primary staining with mouse anti-human CD44:APC (1:20) (Clone MEM-263; Abcam, UK) for 30 min in a final volume of 100 µL per sample, after detachment of cells using Cell Dissociation Buffer, Enzyme-Free, PBS (#13151-014, Gibco®/Invitrogen, UK)], (ii) 20 µg mL^{-1} CD44 antibody (Clone HERMES-I; MA4400, Fischer Scientific UK), (iii) 20 µg mL^{-1} CD44v6 antibody (Clone #2F10, R&D Systems), or (iv) PBS for 1 h at 37 °C. Following pre-treatment and through washing steps (PBS), cells were exposed to DY-547 siRNA-loaded (2.43% wt.) chitosan/HA nanoparticles (125 µg mL^{-1}) for 4 h at 37 °C (full medium). Finally, media was removed, and cells washed with PBS, trypsinized, and finally resuspended in a final volume of 400 µL FACS buffer per sample. The internalization of siRNA was determined on 10,000 live, individual cells with a BD LSRFortessa cytometer (BD Bioscience, San Jose CA, USA) equipped with the FACSDiva software (v8.0.1). Data were analyzed with FlowJo (vX.0.7, Tree Star, Ashland, OR, USA) after gating live and single events in the FSC-A/FSC-H (singlets) and FSC/SSC (live) windows, respectively. Untreated cells (negative control) were used during acquisition as autofluorescence control as well as to threshold the percentage of positive events. Data were finally normalized to the positive control (cells treated with siRNA-loaded chitosan/HA nanoparticles after pre-treatment with PBS). Statistical analysis (T-test, Two-tailed) was performed using GraphPad Prism software (v7.00).

6) Transfection and silencing experiments. HCT-116 cells were seeded into 48-well plates at a density of 2×10^4 cells/cm^2 using 0.25 mL of complete McCoy's 5A medium under standard sterile conditions for cell culture (5% CO_2, 37 °C). Cells were allowed to adhere and

proliferated for 24 h. The culture medium was then discarded and the wells were washed with PBS.

For mRNA transfection experiments, 0.25 mL of complete medium (bicarbonate or HEPES buffer at pH 7.4 or 6.4) containing 0.67 μg of FLuc mRNA (3.9 nM) encapsulated in nanoparticles at different amine-to-phosphorous (A/P) ratios (9-50; with nanoparticle concentration therefore ranging from 72 to 785 μg/mL) were added to each well. 0.67 μg of FLuc mRNA complexed with LTX with plus reagent were used as a positive control following manufacturer's recommended conditions (0.7 μL LTX and 0.7 μL of plus reagent in 40 μL of serum free Opti-MEM I medium added over 0.25 mL of the same complete buffer). For transfection experiments at different mRNA concentrations: Anti-Luc siRNA-1-loaded H84-based nanoparticles of A/P ratio 50 in HEPES-buffered medium at pH 6.4 were used (21, 42, 84, 168, 335 and 670 ng RNA per well; nanoparticle concentration range 12 to 380 μg/mL). Cells were incubated with the nanoparticle solutions for 4 h. Then, the culture medium was discarded, the cells washed with PBS, and incubated with 0.25 mL of fresh bicarbonate-buffered complete medium (pH 7.4) for 24 h. Finally, the medium was discarded, cells were washed with PBS, and first analyzed for metabolic activity (MTS assay). Then cells were lysed with Glo lysis buffer (10 min, 25 °C). The luciferase activity was measured after cell lysate centrifugation (4,500 rpm, 2 min) as reported above and normalized against the total protein content (BCA) of cell lysates.

For siRNA silencing experiments, cells were pre-transfected for 4 h with 0.25 μg of pGL3 vector encapsulated in LTX (i.e., 0.7 μL LTX and 0.3 μL of plus reagent in 40 μL of serum free Opti-MEM I medium). Afterwards, the medium was removed and the cells gently washed with PBS. For silencing experiments at different A/P ratios: 0.25 mL of complete medium (bicarbonate or HEPES buffer at pH 7.4 or 6.4) containing 0.67 μg of anti-Luc siRNA-1 (200 nM) encapsulated in nanoparticles at different A/P ratios (9-50; with nanoparticle concentration range of 72 to 785 μg/mL μg/mL) were added to each well. Anti-Luc siRNA-1:LTX complex encapsulating 0.67 μg of siRNA was used as a positive control. For silencing experiments at different RNA concentrations: Anti-Luc siRNA-1-loaded H84-based nanoparticles of A/P ratio 50 in HEPES-buffered medium at pH 6.4 were used (21, 42, 84, 168, 335 and 670 ng RNA per well; nanoparticle concentration range 12 to 380 μg/mL). After incubation of the above formulations for 4 h, the medium was discarded and cells were washed with PBS and incubated with 0.25 mL of complete medium (bicarbonate, pH 7.4) for 24 h. Finally, the medium was discarded, cells were washed with PBS, and then analyzed for

metabolic activity (MTS assay), luciferase activity and total protein content (BCA) of cell lysates as described above for transfection experiments.

7) Confocal microscopy on transfected cells. HCT-116 cells in complete medium were seeded at a concentration of 10,000 cells/cm^2 in an Ibidi µ-Slide VI0.4 (ibiTreat 80606, Ibidi, Germany) and left to attach and proliferate overnight under standard sterile conditions for cell culture (5% CO_2, 37 °C). Cells were then incubated with 250 µg/mL of mRNA:Cy5-loaded chitosan/HA nanoparticles (Alexa Fluor 405-labelled chitosans H84 or L84, both A/P ratio 50) in HEPES-buffered medium (pH 7.4 or 6.4); this nanoparticle concentration was designed to provide both a good nanoparticle uptake and high transfection readings under the conditions used for this experiment. Cells were incubated with the nanoparticle formulations for 4 h plus an additional 24 h of resting (in complete medium) after nanoparticle removal and washing of cells with PBS. Afterwards, cells were washed with PBS, fixed with 4% PFA (5 min, RT), washed twice with PBS, and then stored in a 1 mg/mL ascorbic acid solution in PBS (dark, 4 °C). Finally, the localization of chitosan and mRNA was determined through confocal acquisitions. Untreated cells were used as auto-fluorescence control. Images were processed using ImageJ software (v1.51h).

Confocal images were recorded with an inverted SP5 laser confocal microscope (Leica TCS SP5 AOBS, Leica Microsystem, UK) using an immersion oil 63X/1.40 HCX PL Apo objective. Z-sections were acquired to precisely determine chitosan and mRNA localization within the cell. The confocal settings for image acquisitions were set as follows: pinhole 1 a.u. (equivalent section thickness 772 nm), scan speed 400 Hz, pixel size 126 nm. Sections of the entire cell thickness were acquired to precisely determine chitosan and mRNA localization using a z-step of 126 nm. To reduce possible cross talk between channels, images were collected with a sequential scan, using the following laser lines and mirror settings: 405(20%)/415-490 nm; 633(35%)/640-760 nm. Please note that the same gain and offset on the detectors were kept constant for all the acquisitions. Images were processed using ImageJ software (v1.51h). Acquisitions with a large field of view (176 µm × 176 µm, comprising 10-14 cells per image) were used to quantify the area percentages with internalized mRNA and chitosan. Briefly, a maximum projection for each channel was obtained, then Otsu threshold applied, and finally the area for each compound selected and measured (n=3 images, averaging 40-50 cells per formulation treatment).

4.4. Results and Discussion

4.4.1. Effect of macromolecular variables (molecular weight; deacetylation degree) on nanoparticle properties

Preparation of chitosans. Starting from H84, we have produced chitosans with $\overline{M}_v$ in the order of 30 kDa ('L' samples) and lower (12 kDa) ('UL' sample), with high (H84, L84, UL91) and medium (H51 and L51) deacetylation degrees (DDs). Chitosans with DD≈20% were also prepared (the DD is easily adjustable through the Ac_2O/amine molar ratio, see Supporting Information, section SI2, Figure 4—9), but their lower aqueous solubility after freeze-drying made them unsuitable for nanoparticle preparation and were not further employed. The DD and molecular weight of these polymers were respectively determined via ^{1}H NMR (Figure 4—1A, Table 4—1) and viscosity (Table 4—1) measurements. Interestingly, H51 and L51 showed essentially the same size as their precursors [32], but it is worth pointing out that the corresponding $\overline{M}_v$ are semi-quantitative estimates, as the use of the same Mark–Houwink parameters (*K* and *a*) for all chitosans neglects the influence of the DD on the coil expansion (lower degree of aggregation [33] and loss of crystallinity [34]).

Preparation of nanoparticles. RNA-loaded chitosan/HA nanoparticles were produced from the above five chitosans using a two-step process (initial RNA/chitosan complexation, followed by addition to HA). Nanoparticles with Z-average size predominantly between 200 and 300 nm (Table 4—1) were obtained. All formulations showed a similarly negative ζ potential (in the region of -40 mV) that confirms the surface presence of HA. However, due to the large excess of positive charges (A/P ratio) in the first complexation step, HA chains may also be integrated within the bulk of nanoparticle structure.

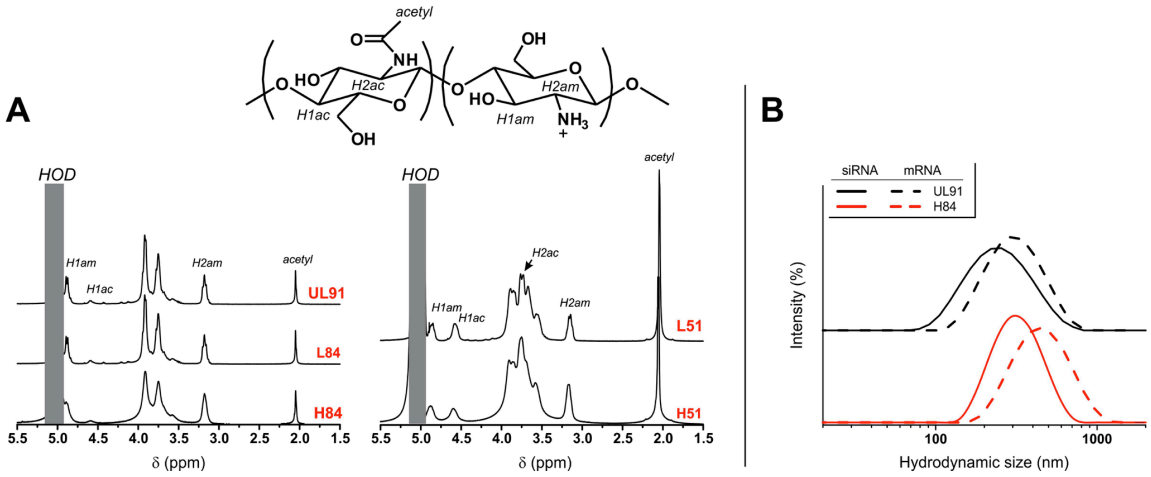

Figure 4—1. ***A.*** ^{1}H NMR spectra for the chitosans with a high DD (left) and around 50% de-acetylation (right); the content of acetyl groups is easily monitored not only through their resonance at 2.1 ppm, but also through the different signals of the H1 (anomeric position) and H2 (amine/amide) protons. ***B.*** Intensity size distribution of nanoparticles obtained using UL91 (black lines) and H84 (red lines) chitosan in the presence of siRNA (solid lines) or mRNA (dashed lines).

Table 4—1. Physico-chemical characterization of different chitosans and of their nanoparticles obtained through complexation with nucleic acids and HA.

Chitosan[a]	DD [b] (mol %)	$\bar{M}_v$ [c] (kDa)	CS/HA nanop.s + siRNA [d]			CS/HA nanop.s + mRNA [d]		
			Z-average size [e] (nm)	ζ potential [e] (mV)	EE [f] (%)	Z-average size [e] (nm)	ζ potential [e] (mV)	EE [f] (%)
H84	16	685	230 ± 5	-39 ± 1	>99	350 ± 10	-41 ± 1	>99
H51	49	645	250 ± 5	-39 ± 1	>99	320 ± 30	-38 ± 1	>99
L84	16	30	195 ± 5	-37 ± 1	>99	260 ± 30	-44 ± 4	>99
L51	49	30	260 ± 5	-39 ± 1	97	280 ± 5	-38 ± 1	>99
UL91	9	12	195 ± 5	-36 ± 1	>99	265 ± 5	-37 ± 1	>99

[a] H stands for high, L for low and UL for ultra-low molecular weight. The numbers refer to the molar percentage of deacetylated (glucosamine) units.
[b] Calculated from the integration of the resonances of the N-acetyl group (1.80 – 2.20 ppm, 3H, GluNAc units) and the H2-H6 protons (2.80 – 4.20 ppm, 6H, GluN and GluNAc units).
[c] Calculated from viscosity measurements in 0.25 M AcOH/0.25 M AcONa at 25°C, extrapolating the intrinsic visocity from Huggins and Kraemer plots, using the Mark–Houwink equation and assuming $K = 1.57\times10^{-5}\,L\,g^{-1}$ and a = 0.79 for all chitosans [30].
[d] The RNA loading is always 10% wt. in comparison to chitosan, and this corresponds to an A/P molar ratio (protonatable amines/phosphates) of 18 for H84 and L84, 10 for H51 and L51, and 20 for UL91.
[e] From DLS and electrophoretic mobility measurements.
[f] Calculated as the amount of non-complexed nucleic acid (positive to RiboGreen assay) relative to the total amount of nucleic acid used in the experiments.

Both RNAs were quantitatively entrapped (encapsulation efficiencies, EE >95%), and their amount did not appreciably affect the nanoparticle characteristics up to a loading of 20% wt. in relation to chitosan (see Supporting Information, Section SI3, Figure 4—10). On the other hand, the molecular size of the payload heavily affected the nanoparticle size, with siRNA consistently providing smaller nanoparticles than mRNA; this is likely due to a less efficient polyelectrolyte complexation with increasing polymer size: the enthalpic gain of electrostatic

interactions is countered by the entropy penalty of un-coiling that increases much more than linearly with the macromolecular size [35]. The less efficient positive/negative pairing may determine both higher probability of aggregation during nanoparticle formation and a lower volumetric cross-link density, hence resulting in a higher swelling in the final products.

RNA complexation strength. The complex formed by RNA and chitosan (and HA) should be sufficiently stable to allow quantitative encapsulation (as seen in Table 4—1), but yet show reversibility and allow the payload release. We have assessed the strength of RNA encapsulation through a displacement assay using a polyanion with a higher charge density than RNA (Figure 4—2A); due to the high density of sulfate groups, heparin has been frequently used for this purpose [16, 36-38].

Importantly, this assay evaluates the ease of decomplexation of the polyplexes, but does not estimate the amount of actually releasable payload, due to the likely very significant differences between these experiments and endosomal or cytosolic environments in terms of pH, ionic strength, concentration and nature of competing polyanions. Therefore, our data must not be interpreted as a quantitative prediction of the nanoparticle's ability to release RNA intracellularly, but rather as a relative ranking of the internal cohesion and stability of the different nanoparticles (please note that instability may be caused by a number of other factors and may lead to agglomeration instead of release of individual components).

It is also worth pointing out that the presence of HA will affect chitosan/RNA interactions, possibly weakening them, as already shown for siRNA [25]; for example, the reportedly lower long-term stability of ternary chitosan/HA/pDNA polyplexes in comparison to that of binary chitosan/pDNA ones could indeed be ascribed to this effect [39]. However, here we will ascribe any effect directly to differences in the chitosan structure affecting its interactions with RNA, and neglect any second-order effects mediated by the HA/chitosan interactions for the sake of simplicity.

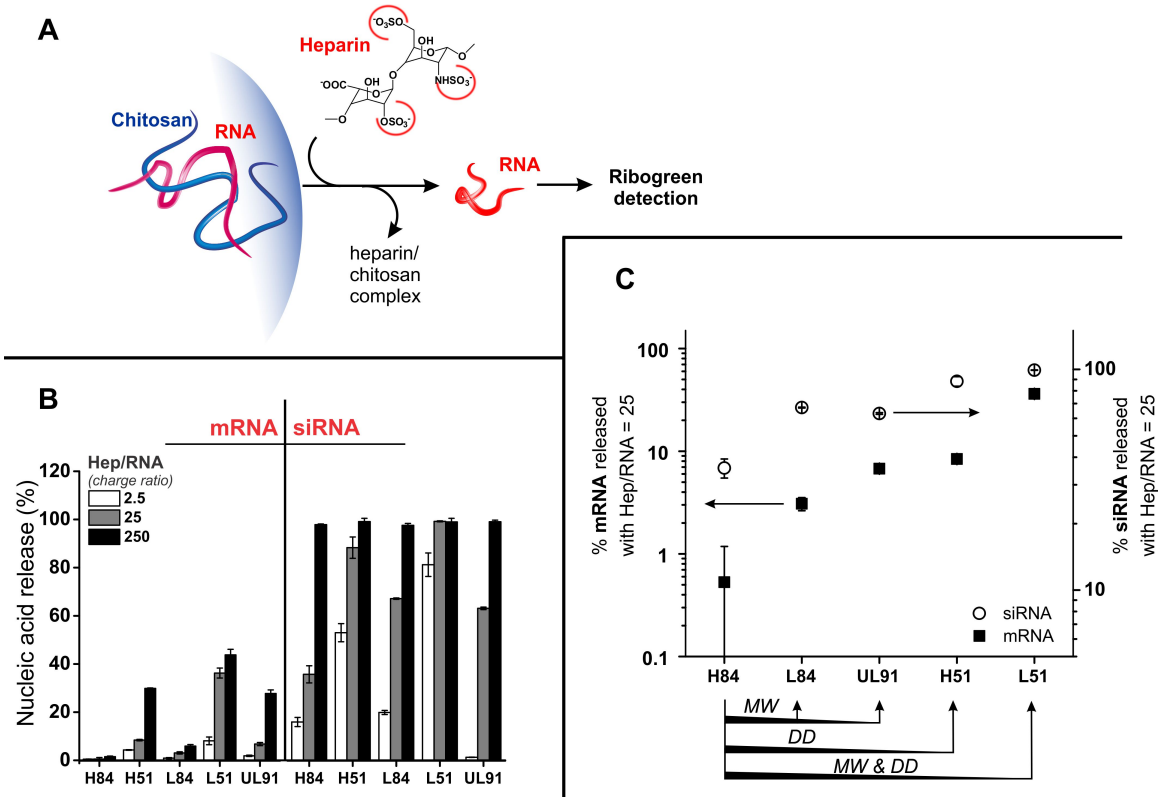

Figure 4—2. ***A.*** Sketch of the heparin displacement assay: chitosan/HA nanoparticles containing either siRNA or mRNA were incubated with heparin in order to release the nucleic acid in a soluble form analyzable by Ribogreen; it is noteworthy that in such assays heparin is always used in large excesses to achieve decomplexation, whereas low charge ratios (e.g. around 1) are known to be ineffective [40]. ***B.*** Amount of RNA released as a function of the heparin/RNA charge ratio (sulfate/phosphate molar ratio) from chitosan/HA nanoparticles based on different chitosans; 10% wt. RNA loading. ***C.*** The amount of released RNA at a charge ratio = 25 spanned from virtually 0 (H84/mRNA) to almost 100% (L51/siRNA), and therefore best separates the effect of chitosans on the complex stability. Please note the different vertical scales in the graph.

We have quantified the amount of released RNA using three different phosphate (RNA)/sulfate (heparin) molar ratios, hereafter referred to as charge ratios. Firstly, it is apparent that siRNA complexes were much more easily reversed than those with mRNA (Figure 4—2B): siRNA was always quantitatively decomplexed at a charge ratio = 250, and to an extent comprised between 40 and 100% at a charge ratio = 25, whereas under the same conditions the much higher avidity of mRNA prevented its quantitative release. Please note that the enhanced retention of mRNA results from a high number of cross-links per molecule (which is due to the high molecular weight); this does not contradict our prediction of its low number of cross-links per volume unit (or per repeating group in each chain, e.g. per phosphate).

Despite the amount of released siRNA and mRNA being numerically different, the two nucleic acids showed the same dependency on the parameters determining chitosan's avidity (Figure 4—2C); for example, both high molecular weight (H84 vs H51) and high DD (H84 vs

L84) led to a smaller RNA displacement. Further, it would appear that the differences in amine density affect the complexation of both payloads to a greater extent than the differences in size, in agreement with previous works, e.g. on chitosan/plasmid DNA interactions [40].

RNA protection. RNA-loaded chitosan/HA nanoparticles were first exposed to RNase I, and the protective effect of each formulation was evaluated by monitoring the integrity of the RNA chains liberated after a successive treatment with chitosanase and heparin. This treatment allowed for a quantitative retrieval of intact siRNA (Figure 4—3A); no difference could be seen among the different chitosans despite their largely different complexation strength and previous reports of a higher protection with higher chitosan molecular weight and DD in chitosan/siRNA nanoparticles [12].

On the other hand, mRNA could not be retrieved quantitatively from any of the formulations, which is broadly in agreement with its more difficult decomplexation, as seen in the heparin displacement assay. It is worth mentioning that, due to the incomplete recovery, the mRNA protection assay should be therefore considered as qualitative, but nevertheless it appears to exclude any significant nuclease-mediated depolymerisation: RNA fragments should be released more easily than the intact molecule because of their lower avidity for chitosan, but even with 5 U RNase/100 μL none could be detected (Figure 4—3B).

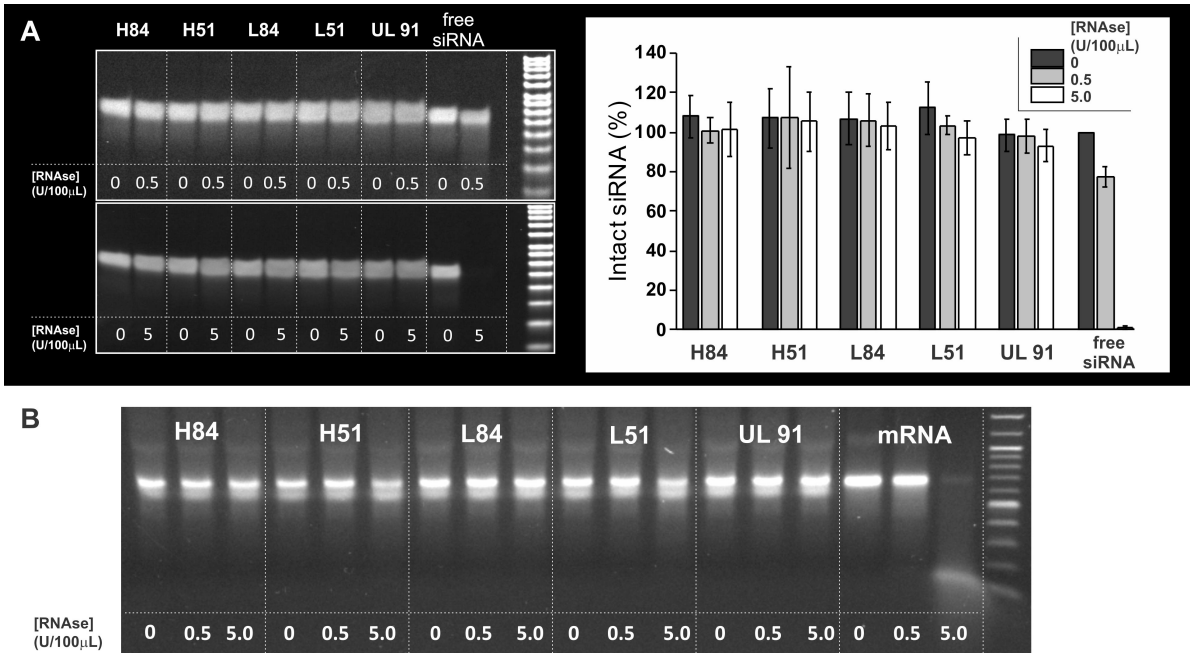

Figure 4—3. ***A.*** PAGE analysis of encapsulated siRNA after nanoparticle incubation first with RNase I, and then with chitosanase and heparin after RNase I quenching (left), and plot of the band intensities (right). 10% wt. RNA loading. ***B.*** PAGE analysis of encapsulated mRNA after incubation as described in A. Please note that the free mRNA bands are typically more intense than those of mRNA from particles, despite using the same amount of nucleic acids, because of its incomplete extraction during the two-stage incubation process (chitosanase and heparin). For both encapsulated siRNA and mRNA a secondary band is apparent (not a smear, which would indicate degradation; secondary bands can also be seen in literature reports [41]), which we interpret as due to RNA still complexed to and condensed onto chitosan fragments.

4.4.2. RNA transfection

Cellular model. We have used the human colorectal carcinoma HCT-116 (CCL-247™) cell line, whose suitability as target for HA-based carriers has been demonstrated in several studies [42-46]. HCT-116 show very high levels of total CD44(pan) expression, with a high abundance of the tumor-associated CD44 variant isoforms v3 and v6 (Figure 4—4), confirming previous reports that depicted them as key drivers of metastasis during colorectal cancer progression [47]. In particular, CD44v6 has been related to a poor clinical outcome of patients with colorectal cancer due to its functional role in the upregulation of the mesenchymal phenotype [48].

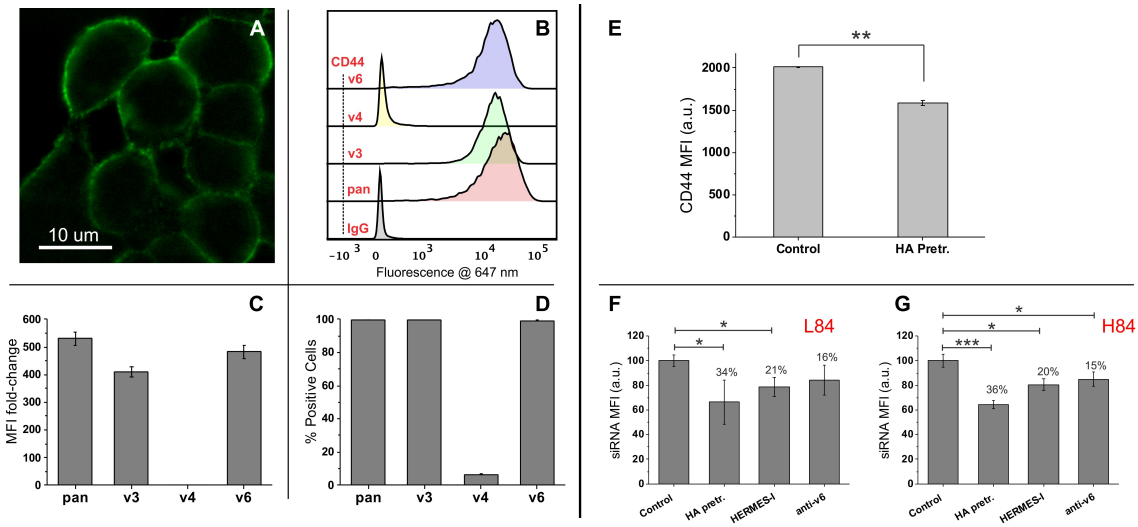

Figure 4—4. Expression of total CD44(pan) and some of its variants in HCT-116. ***A.*** CD44(pan) immunofluorescence images. ***B-D.*** Flow cytometry (B: histograms, C: Median Fluorescence Intensity fold-change, D: percentage of positive cells). *E.* Reduction of CD44(pan) surface presence on HCT-116 after 1 h pre-treatment with 1.5 mg/mL HA. Statistical analysis (T-test, Two-tailed): **HA pretr. = 0.0028. *F, G*. The relative nanoparticle (L84 in F, H84 in G) uptake after 4 h incubation was significantly reduced after pre-treatment with (i) 1.5 mg/mL soluble HA, (ii) 20 µg/mL HERMES-I anti-CD44(pan), or (iii) 20 µg/mL anti-CD44v6 for 1 h; the uptake is expressed as the median fluorescence intensity of the cells arising from DY-547 siRNA-loaded nanoparticles. Statistical analysis (T-test, Two-tailed): L84 - *HA pretr. = 0.0334, *HERMES-I = 0.0144; H84 - ***HA pretr. = 0.0006, *HERMES-I = 0.0262, *anti-v6 = 0.0283.

In HCT-116 CD44 is involved in HA internalization: treatment of cells with soluble HA led to a significant reduction of the CD44 surface presence (Figure 4—4E). When HCT-116 were pre-treated with HA before exposure to nanoparticles, this CD44 reduction led to a corresponding decrease in chitosan/HA (H84- and L84-based siRNA-loaded) nanoparticle uptake (Figures 4—4F and G). Similarly, although to a lower extent, the reduced uptake was separately confirmed using antibodies for CD44(pan) and for CD44v6. Therefore, these combined findings validate HCT-116 as a model for CD44-mediated internalization.

Transfection experiments. We have studied the effects of amine-to-phosphate ratio (A/P, ranging from 9 to 50) and of pH on the expression of firefly luciferase (FLuc) used as a model reporter protein. In terms of pH, experiments were conducted at pH = 7.4 and 6.4, respectively representative of healthy and pathologic (e.g. inflammation [27] and cancer [28, 29]) extracellular environments; this can also provide information about which routes of administration are more suitability for these systems.

It is important to note as well that we have systematically employed HEPES-buffered media, even at pH = 6.4 [49, 50], where in principle it has a low buffering capacity; nevertheless, we have recorded variation < 0.1 pH units after incubation of cells with nanoparticles for up to 4 h.

siRNA (Figure 4—5, left)*:* anti-Luc siRNA-loaded chitosan/HA nanoparticles (4 h exposure, followed by 24 h resting) prepared from low DD chitosans (H51 and L51) failed to produce appreciable silencing at any pH and A/P ratio. The more highly charged H84, L84 and UL91 at pH 6.4 silenced FLuc comparably to or even better (H84 and high A/P ratio) than LTX, which was used as positive control (80-60% reduction in protein expression); on the contrary, only H84 exhibited a high level of silencing at pH 7.4.

mRNA (Figure 4—5, right)*:* The direct mRNA delivery (4 h exposure, followed by 24 h resting) provided negligible FLuc expression at physiological pH with any of the formulations, independently of the A/P ratio, whereas nanoparticles based on H84, L84 and UL91 induced luciferase expression at pH 6.4, with the highest levels for H84 at A/P = 50.

We here analyze separately the different variables:

A) pH: we observed better silencing and protein expression at pH 6.4. Our observations match well the existing literature, although reports slightly vary in terms of the optimal pH values for transfection: it has been reported to be 7.0 for low molecular weight (40 or 84 kDa) chitosan nanoparticles (GFP pDNA) on SOJ cells [14], 6.5 for UltraLow molecular weight (10 kDa) chitosan nanoparticles (EGFP pDNA) on HEK 293 cells [20], 6.4-6.8 for UltraLow molecular weight chitosan (<10 kDa)/64 kDa HA nanoparticles (EGFP pDNA) on HEK 293T cells [51], 6.6-7.0 for high DD, low molecular weight chitosan (50kDa)/160 kDa HA nanoparticles (EGFP pDNA) on primary chondrocytes [15].

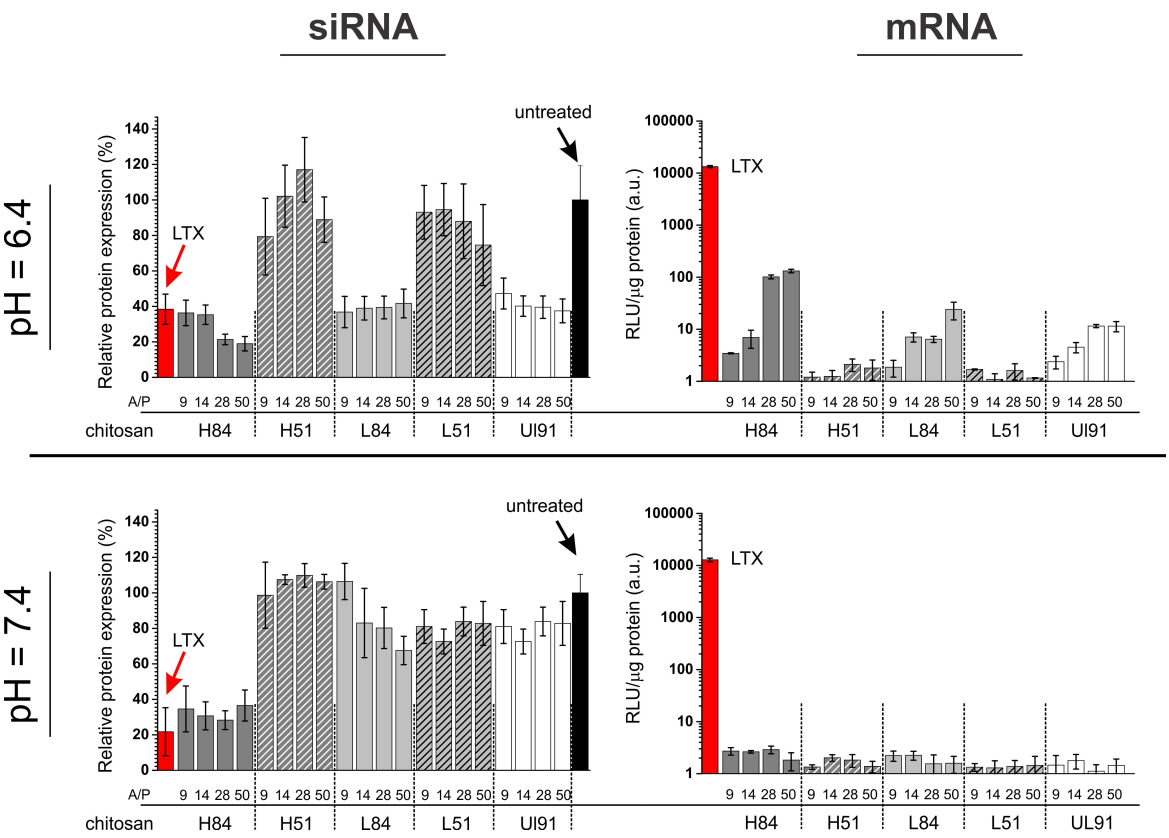

Figure 4—5. Transfection of HCT-116 cells with chitosan/HA nanoparticles loaded with firefly luciferase (FLuc)-encoding mRNA (right) and silencing of the same cells (pre-transfected with FLuc pGL3 plasmid) with chitosan/HA nanoparticles loaded with anti-Luc siRNA-1 (left). The experiments were performed in media based on HEPES buffer at pH = 6.4 (*top*) or 7.4 (bottom). The results are expressed as normalized FLuc expression (silencing) or relative light units (RLU) (transfection), both relative to the total protein content. Experiments were performed as follows: 4 h incubation with nanoparticle formulations at a concentration of [siRNA] and [mRNA] = 0.67 mg/well (pH 6.4 or 7.4) followed by 24 h of resting time (pH 7.4 for both RNAs); this concentration maximizes the RNA delivery effects while producing no significant change in cell viability (see Supporting Information, Section SI4 and Figure 4—11). Silencing results are relative to the signal intensity of untreated cells (in black). LTX (low toxicity lipofectamine) was used as a positive control in all experiments (in red). The A/P ratio is calculated as the molar ratio of glucosamine units in chitosan and phosphate units in RNA in the nanoparticle feed.

These effects may be related to poor physical stability at pH 7.4, since nanoparticles undergo some aggregation in full medium at that pH (see Supporting Information, section SI5 and Figure 4—12). Importantly, this does not preclude the perspective use of the particles, since in routes such as intra- peritumoral [52-54], or nasal administration [55, 56] the particles typically would not experience pH>6.9. Confocal microscopy supports the poor stability at pH 7.4 (Figure 4—6): at pH 6.4, chitosan in part is colocalized with mRNA, while the latter also had a cytoplasmic presence in a free form (respectively showing intact nanoparticles intracellularly, and suggesting endolysosomal escape and decomplexation). On the contrary, at pH 7.4 chitosan was present as large featureless aggregates with minimal co-localization with mRNA, which on its turn had a lower cytoplasmic presence (suggesting destabilization

and extracellular release). The detrimental effect of high pH was even more evident when also our best performing nanoparticles showed no silencing activity in bicarbonate buffer (see Supporting Information, section SI6 and Figure 4—14): the pH can drift to basic values (pH>8) upon prolonged exposure of the nanoparticle containing media to non-CO_2-enriched air (out of incubators, during nanoparticle handling) and the nanoparticle stability decreases due to the negligible chitosan protonation at even slightly basic pH [57], ultimately leading to aggregation visible to the naked eye.

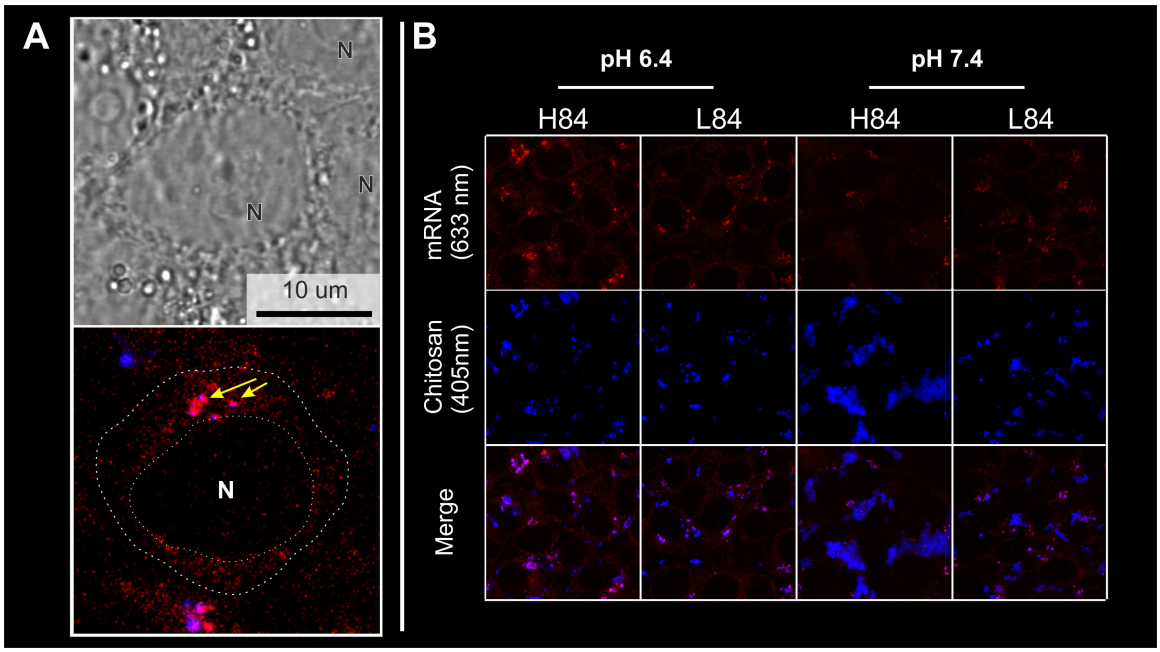

Figure 4—6. HCT-116 treated with chitosan/HA nanoparticles (A/P ratio 50; chitosan labelled with Alexa Fluor 405 (blue), mRNA labelled with Cy5 (red)) in full medium at pH 6.4 and 7.4, after 4 h incubation with nanoparticles followed by a 24 h resting time (pH 7.4). *A*. High magnification bright field (top) and confocal fluorescence microscopy (bottom) images after treatment with H84/HA nanoparticles at pH 6.4. In the bottom picture, the yellow arrows highlight areas of chitosan/mRNA co-localization, i.e. still intact nanoparticles; the nuclei (N) are easily recognizable as darker areas, whereas a diffused, punctuated red fluorescence is seen throughout the cytoplasm. *B.* Comparison of confocal microscopy pictures of H84 and L84 nanoparticles at both pH values, clearly showing the different chitosan (blue) morphology. The increasing amount of intracellular mRNA in the order H84/7.4 ≈ L84/7.4 < L84/6.4 < H84/6.4 correlates with the functional readings reported in Figure 4—5.

B) chitosan DD: the use of low DD chitosans produced negligible transfection at any pH, which also in this case confirms the existing literature on highly acetylated chitosans [20, 41]. Interestingly, low DD would allow an easier RNA release, therefore this effect must be ascribed to either reduced nanoparticle uptake or impaired endolysosomal escape.

C) chitosan molecular weight: we observed better mRNA transfection with larger chitosans (H84>L84>UL91 for most A/P ratios), whereas no clear influence of molecular weight could be seen on siRNA activity. The influence of molecular weight is highly debatable in literature.

For example, for siRNA-loaded nanoparticles, better silencing [11, 12] and higher transfection [13] have been shown with increasing chitosan molecular weight. However, in other reports pDNA delivery was shown to be highest with low molecular chitosan both in binary (40 kDa vs. 1 and 84 kDa) [14] and in ternary complexes with HA (50-100 kDa chitosans performing best in the 5-900 kDa range) [15]. Some other sources have reported highest transfection efficiency with UltraLow molecular weight chitosan/oligomers (in the range 5-15 kDa) in binary [16-20] and ternary (with HA) [21] nanoparticles. These apparently contradictory results suggest that chitosan molecular weight may command a number of other associated effects whose balance determines an overall positive or negative influence on the nanocarrier performance. For example, in our case mRNA experiences a more difficult release from larger chitosans, but yet they achieve a better transfection, which possibly suggests a more efficient endosomal escape.

D) A/P ratio: we observed better transfection at high A/P ratios, whereas silencing did not appear to show any clear dependency on it. This parameter has also been much debated in literature. A trend towards better effects at high ratios has been separately reported for various pDNA [16] and siRNA (binary and ternary) [25] chitosan complexes. However, in some other cases, using the same nanoparticle formulations on different cell lines, opposite effects [19] or no apparent correlation [58] have also been reported. Interestingly, the performance of the polyelectrolyte complex is highly dependent on this parameter; for example, intermediate A/P ratios may lead to formulations with optimal transfection levels [14, 15, 59], whereas low A/P ratios may lead to easy decomplexation and large ones to poor release due to too high stability.

E) Payload size / comparison to control systems: At pH 6.4, the siRNA activity of high DD chitosan formulations (H84, L84, UL91) favorably compared to that of our positive reference LTX (low toxicity lipofectamine), whereas the mRNA transfection efficiency was at best almost two orders of magnitude lower than LTX. We ascribe this effect to the comparably much higher avidity of mRNA for polycations than for lower molecular weight lipids such as LTX (compare left and right part of Figure 4—2), which reduces the likelihood of its delivery in a free form; indeed, it is still possible to see chitosan and mRNA still substantially co-localized 24 h after HCT-116 were exposed to nanoparticles (Figure 4—6A).

4.4.3. Nanoparticle internalization

We analyzed cells after a 4 h incubation with nanoparticles, followed by trypsinization; this treatment degrades CD44 [60], thereby also removing any CD44-bound material on the cell

surface. These flow cytometry data (Figure 4—7) therefore do not reflect the total uptake of transfecting nanoparticles, which would also comprise those membrane-bound at 4 h that are later internalized during the 24 h 'resting' phase (as in transfection experiments). They rather assess an internalization rate, as recently discussed by us in human macrophage models [61]. Firstly, it is noticeable that particles from low DD chitosans (H51 and L51) were very poorly internalized at both pH 6.4 and 7.4 (note the negligible number of positive cells, Figure 4—7B). Their very low transfection efficiency should therefore be ascribed to low uptake, which is likely due to their low complexation strength (Figure 4—2C) leading to extracellular RNA release. All the high DD chitosan-nanoparticles (H84, L84 and UL91; high stability) showed a high uptake rate (Figure 4—7A) with virtually complete transfection of the cell populations (Figure 4—7B). Further, their uptake rate was always higher than that of LTX, at both pH and for both cargos, which rules out a clear link between transfection efficiency and kinetics of nanoparticle internalization. On the contrary, we can ascribe to a more difficult nucleic acid decomplexation both the lower transfection for mRNA vs. siRNA for all systems, and that of mRNA-loaded nanoparticles vs. LTX.

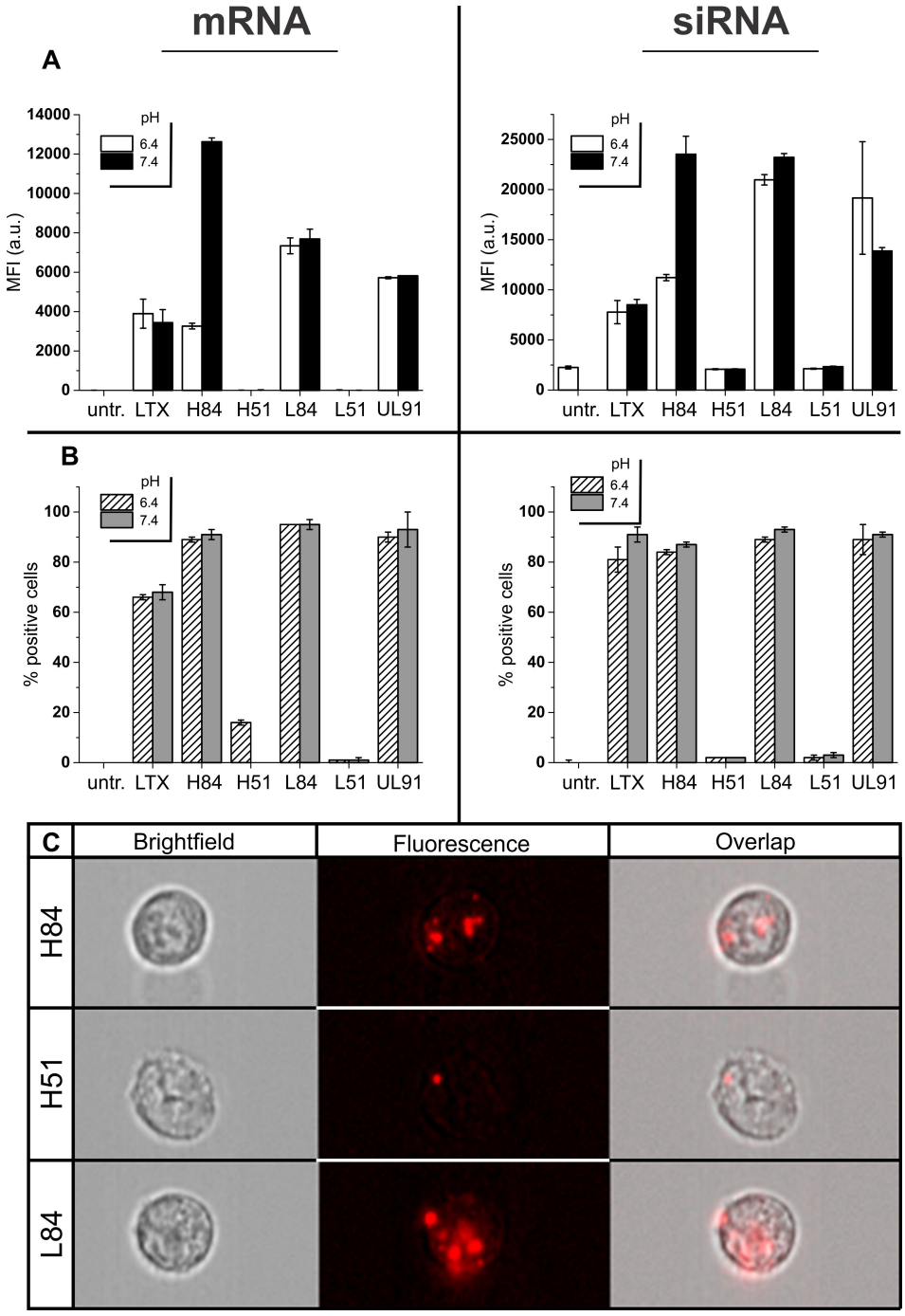

Figure 4—7. ***A.*** Median fluorescence intensity (MFI) obtained through flow cytometry analysis of HCT-116 cells after a 4 h exposure to various chitosan/HA nanoparticles at pH 6.4 (white bars) or 7.4 (black bars) in HEPES-buffered McCoy's 5A medium (A/P ratio 50). Please note that the cells were trypsinized before analysis, which results in CD44 degradation and detachment of any surface bound particles. Please also note that only the nucleic acids are labelled, and that the MFI therefore is likely to be directly proportional to the internalization of intact particles, although the MFI of siRNA- and that of mRNA-containing particles are not directly comparable because of the different chromophores used (Cy5-labelled mRNA and DY547-labelled siRNA). ***B.*** Percentage of cells positive for loaded nanoparticles in the experiments described in A. ***C.*** Representative images of HCT-116 cells treated with chitosan/HA nanoparticles (pH 6.4) during flow analysis. This picture confirms that the different uptake of particles containing high molecular weight/high amine content (H84), high molecular weight/low amine content (H51) and low molecular weight/high amine content (L84) chitosan is indeed related to a different level of nanoparticle internalization.

Secondly, it is apparent that pH had a mixed influence. On one hand, it did not affect the amount of internalized L84 and UL91-based particles, whereas the higher pH showed a dramatically reduced transfection efficiency (Figure 4—5). We interpret this as a result of pH-induced nanoparticle destabilization, which must occur in an endolysosomal environment, possibly early enough to allow an effective nucleic acid degradation prior to endolysosomal disruption (had it occurred extracellularly, the amount of internalizable material would have decreased). On the other hand, whatever the cargo, H84 nanoparticles were internalized more rapidly at pH 7.4 than at 6.4. Mechanistically, we currently lack a sound explanation for this H84 peculiarity, which may be behind its reduced but still significant silencing activity at pH 7.4. Nevertheless, two hypotheses are worth postulating: Firstly, the larger size of H84 nanoparticles: chitosan solubility at neutral pH decreases with molecular weight, and the resulting self-association is the likely cause of H84-containing particles aggregating more than the other systems (see Supporting Information, Figure 4—13, and Figure 4—6B); the larger the particles the more likely they are to be internalized through a size-sensitive uptake mechanism such as phagocytosis (or macropinocytosis). Secondly, influence of HA presentation: the lower chitosan protonation at pH 7.4 should lead to a less cross-linked/more porous matrix; we have shown in RAW 264.7 macrophages that a more porous matrix leads to a lower HA exposure, and this increases nanoparticle uptake likely due to a lower number of receptors per particle [62, 63].

4.4.4. The avidity conundrum

In an attempt to further rationalize the functional readings (transfection at pH 6.4) we have separately cross-correlated them with the uptake rate (pH 6.4) and complexation stability for each nanoparticle formulation (Figure 4—8). For the uptake rate (Figure 4—8A) neither the most rapidly internalizing particles, nor the slowest were the best in transfection; clearly, no meaningful correlation can be drafted with the number of cells internalizing the particles (Figure 4—7B). The absence of a clear correlation between internalization rate and transfection efficiency has already been observed for chitosan/RNA complexes (no HA); for instance, for nanoparticles prepared from chitosans of different molecular weights and pDNA (SOJ cells) [14], from completely deacetylated chitosans of different molecular weights and pDNA (HEK293) [37], and siRNA-loaded nanoparticles from chitosans of different molecular weight and DD (HepG2) [64].

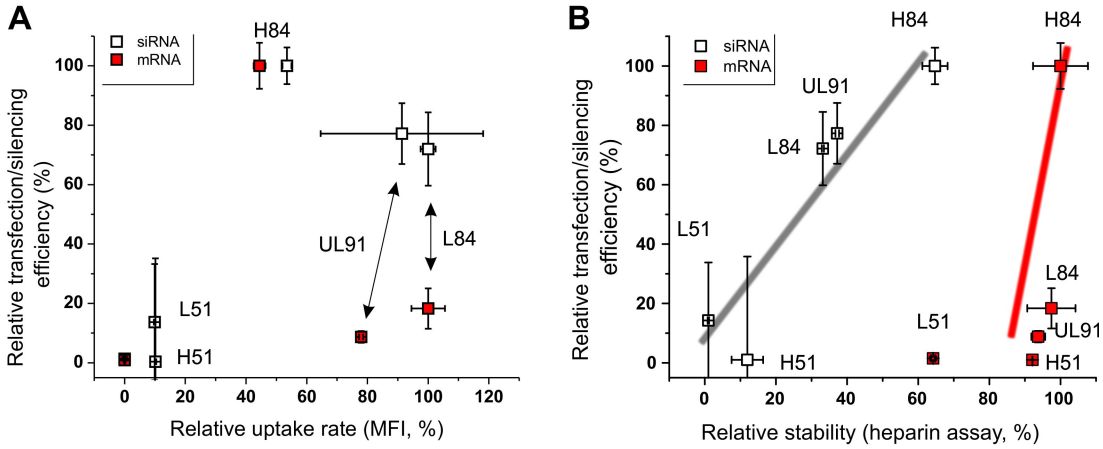

Figure 4—8. Cross-correlations between RNA delivery efficiency (vertical axes; silencing – empty symbols; mRNA translation – red symbols) and uptake rate (horizontal axis in ***A***) or complexation stability (horizontal axis in ***B***) for chitosan/HA formulations at pH 6.4 and A/P ratio 50. The 4 h uptake rate (from the median fluorescence intensity in flow cytometry experiments in Figure 7A), and the luciferase silencing/expression data (in Figure 4—5, top graphs) are normalized to 100 for the highest values, independently for siRNA and mRNA; the relative stability (proportional to the percentage of nucleic acid concentrations not released at heparin/RNA charge ratio = 25 in Figure 4—2C) data are normalized assigning 100% to the H84/mRNA system. Please note that the grey and red lines are just guides for eyes.

On the contrary, a link between complexation strength and transfection efficiency would appear at the same time obvious (although quantitatively different for mRNA- and for siRNA-containing particles; see grey and red lines in Figure 4—8B) and puzzling: i) chitosan avidity (large size, high DD) would seem to be beneficial for transfection; see larger transfection values for H84 than for L84 (unexpected), (ii) but detrimental for decomplexation; for instance, see higher RNA retention for H84 than for L84 (expected); (iii) at the same time, RNA avidity is detrimental for both transfection and decomplexation (expected for both), see the different nucleic acid release (Figure 4—8B) and functional readings for siRNA- and mRNA-loaded formulations with respect to their LTX controls (Figure 4—5).

We explain this apparent contradiction through two points: A) higher chitosan avidity increases both protection to the cargo and hindrance to its release; higher RNA avidity only the latter. Therefore, the better efficiency with larger chitosans but not with larger RNAs may entail a better protection of the cargo. B) The endosomal escape would logically increase with both chitosan molecular weight and DD, be it due to either proton sponge effect (higher concentration of 'free' counterions) or membrane poration (higher membrane damage, which also causes higher chitosan cytotoxicity [65]). Larger endosomolytic activity has been reported for small chitosans (in chitosan/pDNA complexes, A/P = 5 [66]), but we believe this to be due to the larger chitosans being more difficult to liberate from binary polyplexes at low A/P ratio, and therefore being comparatively less available for membrane poration. Since the

present study used ternary polyplexes (HA presence likely facilitating decomplexation) and high A/P ratios (≥9), the chitosan in our nanoparticles is likely to increase its endosomolytic activity with both molecular weight and DD, i.e. when it is also a better RNA binder. Under this assumption, the avidity/efficiency correlation in Figure 4—8B may be a case of 'red herring', i.e. a false correlation masking the real controlling mechanism, which is likely to be the endosomolytic activity.

4.5. Conclusion

We have studied the CD44-targeted delivery of RNAs through chitosan/HA nanoparticles, including what to our knowledge is the first example of mRNA delivery with such carriers. In particular, we have evaluated the transfection efficiency effects of (macro)molecular parameters such as chitosan molecular weight and DD, producing nanoparticles that differed both in RNA binding strength (avidity) and in their rate of internalization in HCT-116. These particles presented a pH-dependent behavior with better transfection at pH 6.4; since this is a reflection of an insufficient stability at neutral pH, it seems logical that these systems would be better suited for intra- or peritumoral administration. In terms of the rational design of nanocarriers, firstly we have observed that low chitosan DD has detrimental effects on stability, internalization and ultimately in RNA delivery, as similarly reported in literature for chitosan/nucleic acid binary nanoparticles. Secondly, we have shown that the increase in chitosan molecular weight is detrimental for the reversibility of the RNA complexes, has a complex influence on internalization rate, but above all proves a very positive factor for transfection efficiency. We are inclined to ascribe the latter to a combination of increased protection and above all better endosomolytic activity; this points out the necessity of a better understanding of the nanoparticle/endosomal environment interactions for a more accurate prediction of the nanoparticle behavior.

4.6. Acknowledgments

Dr. Roberto Donno is gratefully acknowledged for both discussions and experimental help. The Bioimaging Facility of the Faculty of Life Sciences (University of Manchester) is maintained with grants from BBSRC, Wellcome Trust, and the University of Manchester Strategic Fund. This work was supported by AstraZeneca through the establishment of the NorthWest Centre of Advanced Drug Delivery (NoWCADD) at the University of Manchester. J.M.R. is indebted to EPSRC for a PhD studentship (part of the North-West Nanoscience

(NoWNano) Doctoral Training Centre, EPSRC Grant EP/G03737X/1). A.T. was funded through the Innovate UK Project No. 101710. A.G. and M.P. gratefully acknowledges financial support from the EU FP7 project UniVax (Grant No. 601738).

4.7. References

[1] M.D. Buschmann, A. Merzouki, M. Lavertu, M. Thibault, M. Jean, V. Darras, Chitosans for delivery of nucleic acids, Adv. Drug Deliv. Rev. 65(9) (2013) 1234-1270.

[2] S. Mao, W. Sun, T. Kissel, Chitosan-based formulations for delivery of DNA and siRNA, Adv. Drug Deliv. Rev. 62(1) (2010) 12-27.

[3] D. Naor, S. Nedvetzki, I. Golan, L. Melnik, Y. Faitelson, CD44 in cancer, Crit. Rev. Cl. Lab. Sci. 39(6) (2002) 527-579.

[4] S. Goodison, V. Urquidi, D. Tarin, CD44 cell adhesion molecules, Mol. Pathol. 52(4) (1999) 189-196.

[5] A. Gennari, M. Pelliccia, R. Donno, I. Kimber, N. Tirelli, Mannosylation Allows for Synergic (CD44/C-Type Lectin) Uptake of Hyaluronic Acid Nanoparticles in Dendritic Cells, but Only upon Correct Ligand Presentation, Adv. Healthc. Mater. 5(8) (2016) 966-976.

[6] S. Ouasti, P.J. Kingham, G. Terenghi, N. Tirelli, The CD44/integrins interplay and the significance of receptor binding and re-presentation in the uptake of RGD-functionalized hyaluronic acid, Biomaterials 33(4) (2012) 1120-1134.

[7] H. Hillaireau, P. Couvreur, Nanocarriers' entry into the cell: relevance to drug delivery, Cell. Mol. Life Sci. 66(17) (2009) 2873-2896.

[8] A. Akinc, G. Battaglia, Exploiting Endocytosis for Nanomedicines, Cold Spring Harbor Perspect. Biol. 5(11) (2013) a016980.

[9] J.H. Jeong, S.W. Kim, T.G. Park, Molecular design of functional polymers for gene therapy, Prog. Polym. Sci. 32(11) (2007) 1239-1274.

[10] B. Angelov, A. Angelova, M. Drechsler, V.M. Garamus, R. Mutafchieva, S. Lesieur, Identification of large channels in cationic PEGylated cubosome nanoparticles by synchrotron radiation SAXS and Cryo-TEM imaging, Soft Matter 11(18) (2015) 3686-3692.

[11] H. Ragelle, R. Riva, G. Vandermeulen, B. Naeye, V. Pourcelle, C.S. Le Duff, C. D'Haese, B. Nysten, K. Braeckmans, S.C. De Smedt, C. Jerome, V. Preat, Chitosan nanoparticles for siRNA delivery: Optimizing formulation to increase stability and efficiency, J. Control Release 176 (2014) 54-63.

[12] X. Liu, K.A. Howard, M. Dong, M.Ø. Andersen, U.L. Rahbek, M.G. Johnsen, O.C. Hansen, F. Besenbacher, J. Kjems, The influence of polymeric properties on chitosan/siRNA nanoparticle formulation and gene silencing, Biomaterials 28(6) (2007) 1280-1288.
[13] Y. Yuan, J. Tan, Y. Wang, C. Qian, M. Zhang, Chitosan nanoparticles as non-viral gene delivery vehicles based on atomic force microscopy study, Acta Biochim. Biophys. Sin. 41 (2009) 515-525.
[14] T. Ishii, Y. Okahata, T. Sato, Mechanism of cell transfection with plasmid/chitosan complexes, Biochim. Biophys. Acta, Biomembr. 1514(1) (2001) 51-64.
[15] H.-D. Lu, H.-Q. Zhao, K. Wang, L.-L. Lv, Novel hyaluronic acid–chitosan nanoparticles as non-viral gene delivery vectors targeting osteoarthritis, Int. J. Pharm. 420(2) (2011) 358-365.
[16] M. Koping-Hoggard, K.M. Varum, M. Issa, S. Danielsen, B.E. Christensen, B.T. Stokke, P. Artursson, Improved chitosan-mediated gene delivery based on easily dissociated chitosan polyplexes of highly defined chitosan oligomers, Gene Ther 11(19) (2004) 1441-1452.
[17] T. Sato, T. Ishii, Y. Okahata, In vitro gene delivery mediated by chitosan. Effect of pH, serum, and molecular mass of chitosan on the transfection efficiency, Biomaterials 22(15) (2001) 2075-2080.
[18] N. Csaba, M. Köping-Höggård, M.J. Alonso, Ionically crosslinked chitosan/tripolyphosphate nanoparticles for oligonucleotide and plasmid DNA delivery, Int. J. Pharm. 382(1–2) (2009) 205-214.
[19] G. Puras, J. Zarate, M. Aceves, A. Murua, A.R. Díaz, M. Avilés-Triguero, E. Fernández, J.L. Pedraz, Low molecular weight oligochitosans for non-viral retinal gene therapy, Eur. J. Biomed. Pharm. Sci. 83(2) (2013) 131-140.
[20] M. Lavertu, S. Méthot, N. Tran-Khanh, M.D. Buschmann, High efficiency gene transfer using chitosan/DNA nanoparticles with specific combinations of molecular weight and degree of deacetylation, Biomaterials 27(27) (2006) 4815-4824.
[21] M. de la Fuente, B. Seijo, M.J. Alonso, Design of novel polysaccharidic nanostructures for gene delivery, Nanotechnol. 19(7) (2008) 1.
[22] G.G. Allan, M. Peyron, Molecular weight manipulation of chitosan I: kinetics of depolymerization by nitrous acid, Carbohydr. Res. 277(2) (1995) 257-272.
[23] L. Vachoud, N. Zydowicz, A. Domard, Formation and characterisation of a physical chitin gel, Carbohydr. Res. 302(3) (1997) 169-177.
[24] H. Ragelle, G. Vandermeulen, V. Preat, Chitosan-based siRNA delivery systems, J. Control Release 172(1) (2013) 207-218.

[25] S. Al-Qadi, M. Alatorre-Meda, E.M. Zaghloul, P. Taboada, C. Remunán-López, Chitosan–hyaluronic acid nanoparticles for gene silencing: The role of hyaluronic acid on the nanoparticles' formation and activity, Colloids Surf., B 103 (2013) 615-623.
[26] A. Almalik, P.J. Day, N. Tirelli, HA-Coated Chitosan Nanoparticles for CD44-Mediated Nucleic Acid Delivery, Macromol Biosci 13(12) (2013) 1671-1680.
[27] S.E. Andersson, K. Lexmüller, A. Johansson, G.M. Ekström, Tissue and intracellular pH in normal periarticular soft tissue and during different phases of antigen induced arthritis in the rat, J. Rheumatol. 26(9) (2016) 2018-2024.
[28] P. Vaupel, F. Kallinowski, P. Okunieff, Blood Flow, Oxygen and Nutrient Supply, and Metabolic Microenvironment of Human Tumors: A Review, Cancer Res. 49(23) (1989) 6449-6465.
[29] Y. Kato, S. Ozawa, C. Miyamoto, Y. Maehata, A. Suzuki, T. Maeda, Y. Baba, Acidic extracellular microenvironment and cancer, Cancer Cell Int. 13 (2013).
[30] M.R. Kasaai, J. Arul, G. Charlet, Intrinsic viscosity–molecular weight relationship for chitosan, J. Polym. Sci., Part B: Polym. Phys. 38(19) (2000) 2591-2598.
[31] S. Mao, X. Shuai, F. Unger, M. Simon, D. Bi, T. Kissel, The depolymerization of chitosan: effects on physicochemical and biological properties, Int. J. Pharm. 281(1–2) (2004) 45-54.
[32] M. Huang, E. Khor, L.-Y. Lim, Uptake and Cytotoxicity of Chitosan Molecules and Nanoparticles: Effects of Molecular Weight and Degree of Deacetylation, Pharm. Res. 21(2) (2004) 344-353.
[33] R. Novoa-Carballal, R. Riguera, E. Fernandez-Megia, Chitosan hydrophobic domains are favoured at low degree of acetylation and molecular weight, Polymer 54(8) (2013) 2081-2087.
[34] I.A. Sogias, V.V. Khutoryanskiy, A.C. Williams, Exploring the Factors Affecting the Solubility of Chitosan in Water, Macromol. Chem. Phys. 211(4) (2010) 426-433.
[35] V.A. Bloomfield, DNA condensation by multivalent cations, Biopolymers 44(3) (1997) 269-282.
[36] S. Danielsen, S. Strand, C. de Lange Davies, B.T. Stokke, Glycosaminoglycan destabilization of DNA–chitosan polyplexes for gene delivery depends on chitosan chain length and GAG properties, Biochim. Biophys. Acta, Gen. Subj. 1721(1–3) (2005) 44-54.
[37] S.P. Strand, S. Lelu, N.K. Reitan, C. de Lange Davies, P. Artursson, K.M. Vårum, Molecular design of chitosan gene delivery systems with an optimized balance between polyplex stability and polyplex unpacking, Biomaterials 31(5) (2010) 975-987.

[38] L. Han, C. Tang, C. Yin, Effect of binding affinity for siRNA on the in vivo antitumor efficacy of polyplexes, Biomaterials 34(21) (2013) 5317-5327.
[39] A.V. Oliveira, D.B. Bitoque, G.A. Silva, Combining Hyaluronic Acid with Chitosan Enhances Gene Delivery, J. Nanomater. 2014 (2014) 9.
[40] S. Danielsen, K.M. Vårum, B.T. Stokke, Structural Analysis of Chitosan Mediated DNA Condensation by AFM: Influence of Chitosan Molecular Parameters, Biomacromolecules 5(3) (2004) 928-936.
[41] M. Huang, C.-W. Fong, E. Khor, L.-Y. Lim, Transfection efficiency of chitosan vectors: Effect of polymer molecular weight and degree of deacetylation, J. Control Release 106(3) (2005) 391-406.
[42] Y. Yamada, M. Hashida, H. Harashima, Hyaluronic acid controls the uptake pathway and intracellular trafficking of an octaarginine-modified gene vector in CD44 positive- and CD44 negative-cells, Biomaterials 52 (2015) 189-198.
[43] K. Liang, K.H. Bae, F. Lee, K.F. Xu, J.E. Chung, S.J. Gao, M. Kurisawa, Self-assembled ternary complexes stabilized with hyaluronic acid-green tea catechin conjugates for targeted gene delivery, J. Control Release 226 (2016) 205-216.
[44] K.Y. Choi, O.F. Silvestre, X. Huang, N. Hida, G. Liu, D.N. Ho, S. Lee, S.W. Lee, J.I. Hong, X. Chen, A nanoparticle formula for delivering siRNA or miRNAs to tumor cells in cell culture and in vivo, Nat Protoc 9(8) (2014) 1900-15.
[45] O.P. Oommen, C. Duehrkop, B. Nilsson, J. Hilborn, O.P. Varghese, Multifunctional Hyaluronic Acid and Chondroitin Sulfate Nanoparticles: Impact of Glycosaminoglycan Presentation on Receptor Mediated Cellular Uptake and Immune Activation, ACS Appl. Mater. Interfaces 8(32) (2016) 20614-24.
[46] X.Y. Yang, Y.X. Li, M. Li, L. Zhang, L.X. Feng, N. Zhang, Hyaluronic acid-coated nanostructured lipid carriers for targeting paclitaxel to cancer, Cancer Lett 334(2) (2013) 338-45.
[47] B. Banky, L. Raso-Barnett, T. Barbai, J. Timar, P. Becsagh, E. Raso, Characteristics of CD44 alternative splice pattern in the course of human colorectal adenocarcinoma progression, Mol Cancer 11 (2012).
[48] S. Saito, H. Okabe, M. Watanabe, T. Ishimoto, M. Iwatsuki, Y. Baba, Y. Tanaka, J. Kurashige, Y. Miyamoto, H. Baba, CD44v6 expression is related to mesenchymal phenotype and poor prognosis in patients with colorectal cancer, Oncol. Rep. 29(4) (2013) 1570-1578.

[49] H. Endo, C. Matsuda, Y. Kagawa, Exclusion of an alternatively spliced exon in human ATP synthase gamma-subunit pre-mRNA requires de novo protein synthesis, J. Biol. Chem. 269(17) (1994) 12488-93.

[50] C. Cavelier, P.M. Ohnsorg, L. Rohrer, A. von Eckardstein, The β-Chain of Cell Surface F_0F_1 ATPase Modulates ApoA-I and HDL Transcytosis Through Aortic Endothelial Cells, Arterioscler., Thromb., Vasc. Biol. 32(1) (2012) 131-139.

[51] N. Duceppe, M. Tabrizian, Factors influencing the transfection efficiency of ultra low molecular weight chitosan/hyaluronic acid nanoparticles, Biomaterials 30(13) (2009) 2625-2631.

[52] M. Stubbs, P.M.J. McSheehy, J.R. Griffiths, C.L. Bashford, Causes and consequences of tumour acidity and implications for treatment, Mol. Med. Today 6(1) (2000) 15-19.

[53] V. Estrella, T.A. Chen, M. Lloyd, J. Wojtkowiak, H.H. Cornnell, A. Ibrahim-Hashim, K. Bailey, Y. Balagurunathan, J.M. Rothberg, B.F. Sloane, J. Johnson, R.A. Gatenby, R.J. Gillies, Acidity Generated by the Tumor Microenvironment Drives Local Invasion, Cancer Res. 73(5) (2013) 1524-1535.

[54] I.F. Robey, B.K. Baggett, N.D. Kirkpatrick, D.J. Roe, J. Dosescu, B.F. Sloane, A.I. Hashim, D.L. Morse, N. Raghunand, R.A. Gatenby, R.J. Gillies, Bicarbonate Increases Tumor pH and Inhibits Spontaneous Metastases, Cancer Res. 69(6) (2009) 2260-2268.

[55] N. Washington, R.J.C. Steele, S.J. Jackson, D. Bush, J. Mason, D.A. Gill, K. Pitt, D.A. Rawlins, Determination of baseline human nasal pH and the effect of intranasally administered buffers, Int. J. Pharm. 198(2) (2000) 139-146.

[56] R.J.A. England, J.J. Homer, L.C. Knight, S.R. Ell, Nasal pH measurement: a reliable and repeatable parameter, Clin. Otolaryngol. 24(1) (1999) 67-68.

[57] Q.Z. Wang, X.G. Chen, N. Liu, S.X. Wang, C.S. Liu, X.H. Meng, C.G. Liu, Protonation constants of chitosan with different molecular weight and degree of deacetylation, Carbohydr. Polym. 65(2) (2006) 194-201.

[58] O. Germershaus, S. Mao, J. Sitterberg, U. Bakowsky, T. Kissel, Gene delivery using chitosan, trimethyl chitosan or polyethylenglycol-graft-trimethyl chitosan block copolymers: Establishment of structure–activity relationships in vitro, J. Control Release 125(2) (2008) 145-154.

[59] K. Romøren, S. Pedersen, G. Smistad, Ø. Evensen, B.J. Thu, The influence of formulation variables on in vitro transfection efficiency and physicochemical properties of chitosan-based polyplexes, Int. J. Pharm. 261(1–2) (2003) 115-127.

[60] C.B. Knudson, K.T. Rousche, R.S. Peterson, G. Chow, W. Knudson, CD44 and cartilage matrix stabilization, in: V.C. Hascall, K.E. Kuettner (Eds.), The Many Faces of Osteoarthritis, Birkhäuser Basel, Basel, 2002, pp. 219-230.
[61] J.M.R. de la Rosa, A. Tirella, A. Gennari, I.J. Stratford, N. Tirelli, The CD44-Mediated Uptake of Hyaluronic Acid-Based Carriers in Macrophages, Adv. Healthc. Mater. 6(4) (2017) 2192-2659.
[62] A. Almalik, R. Donno, C.J. Cadman, F. Cellesi, P.J. Day, N. Tirelli, Hyaluronic acid-coated chitosan nanoparticles: Molecular weight-dependent effects on morphology and hyaluronic acid presentation, J. Control Release 172(3) (2013) 1142-1150.
[63] A. Almalik, S. Karimi, S. Ouasti, R. Donno, C. Wandrey, P.J. Day, N. Tirelli, Hyaluronic acid (HA) presentation as a tool to modulate and control the receptor-mediated uptake of HA-coated nanoparticles, Biomaterials 34(21) (2013) 5369-5380.
[64] M. Jean, M. Alameh, D. De Jesus, M. Thibault, M. Lavertu, V. Darras, M. Nelea, M.D. Buschmann, A. Merzouki, Chitosan-based therapeutic nanoparticles for combination gene therapy and gene silencing of in vitro cell lines relevant to type 2 diabetes, Eur. J. Pharm. Sci. 45(1–2) (2012) 138-149.
[65] S. Ungphaiboon, D. Attia, G.G. d'Ayala, P. Sansongsak, F. Cellesi, N. Tirelli, Materials for microencapsulation: what toroidal particles ("doughnuts") can do better than spherical beads, Soft Matter 6(17) (2010) 4070-4083.
[66] M. Thibault, M. Lavertu, M. Astolfi, M.D. Buschmann, Structure Dependence of Lysosomal Transit of Chitosan-Based Polyplexes for Gene Delivery, Mol. Biotechnol. 58(10) (2016) 648-656.

4.8. Supporting Information

SI1. Materials

1) Chemicals. Middle viscosity chitosan with viscosity average molecular weight ($\overline{M}_v$) of 685 kDa and degree of de-acetylation (DD) of 84%, hereafter referred to as H84, was purchased from Sigma Aldrich (Gillingham, UK) and purified prior to use as previously described [1]. H84 was used to produce chitosans of lower molecular weight (by its oxidative degradation with sodium nitrite) and higher DD (amine acylation with acetic anhydride) as described below. Hyaluronic acid (HA; $\overline{M}_w$ = 180 kDa) was kindly donated by Novozymes (Bagsvaerd, Denmark). 1 M HCl (aq), 1 M NaOH (aq), sodium bicarbonate ($NaHCO_3$), 4-(4,6-dimethoxy-1,3,5-triazin-2-yl)-4-methylmorpholinium chloride (DMTMM), DMSO,

acetic anhydride (Ac_2O), 1,2-propanol, 4-(2-hydroxyethyl)-1-piperazineethanesulfonic acid (HEPES), heparin sodium salt (from porcine intestinal mucosa), sodium nitrate and bicinchoninic acid (BCA) kit were obtained from Sigma Aldrich (Gillingham, UK). Chitosanase from *Streptomyces sp.* N174 (220477-10U; 0.084 units/μL) was purchased from from Merck (Nottingham, UK). RNase I (cloned) 100 U/μL (AM2294) was bought from Thermo Fisher Scientific (Paisley, UK). Glacial acetic acid (AcOH) and sodium acetate (AcONa) were purchased from VWR BDH Chemicals (Poole, UK). GelRed nucleic acid gel stain and Quant-iT RiboGreen RNA assay kit reagent were from Biotium (CA, USA) and Molecular Probes (OR, USA), respectively. UltraPure™ DNase/RNase-free distilled water, Alexa Fluor 405 NHS ester, and Lipofectamine LTX (hereafter LTX alone) with plus reagent were purchased from Invitrogen (Paisley, UK). 10 mM phosphate buffered saline (PBS) was prepared from appropriate tablets (Basingtoke, UK). ONE-Glo luciferase assay and MTS assay were bought from Promega (WN, USA). SpectraPor dialysis membranes were obtained from Spectrum Laboratories Inc. (CA, USA). MilliQ water (18.2 $M\Omega.cm^{-1}$) was used for experiments not requiring nuclease-free water.

2) Nucleic Acids. A) Amplification and purification of pDNA: Firefly luciferase pGL3-control vector (E1741; Promega, WN, USA) was amplified in E. coli DHT5α as previously described [2]. Briefly, bacteria were transformed with pGL3 by the heat shock method (42 °C, 90 s). LB Agar bacterial growth medium (Sigma–Aldrich, MO, USA) was dissolved in deionized water and autoclaved prior to use. pGL3 transformed bacteria were then streaked on a solid agar plate and incubated overnight at 37 °C. A single bacteria colony was collected using a sterile inoculation loop, transferred to LB medium containing 10 μg mL^{-1} ampicillin (for selection of pGL3 transformed E. coli) and cultured for 12–16 h at 37 °C. pDNA was then extracted and purified using an EndoFree Plasmid Maxi Kit (Qiagen, CA, USA) following manufacturer's recommended conditions. The quantity and quality (absence of protein contaminants) of the purified pDNA (in nuclease free water) was assessed spectrophotometrically at 260 and 280 nm using a NanoDrop 1000 Spectrophotometer (Thermo Fisher Scientific).

B) mRNA: Firefly Luciferase (FLuc) mRNA and cyanine 5 (Cy5)-labelled FLuc mRNA (5meC, Psi; 1929 nucleotides; 040L-6107 and 040L-6401, respectively) both in 10 mM Tris buffer (pH 7.5) were purchased from TebuBio (Le Perray-en-Yvelines Cedex, France); buffer salts were removed prior to nanoparticle preparation using an Amicon Ultra-4 centrifugal filter (MWCO of 10 kDa) from VWR (Leicestershire, UK) against nuclease-free water. mRNA concentration after purification was measured spectrophotometrically at 260 nm using

a NanoDrop 1000 Spectrophotometer. Aliquots were frozen and stored at -80 °C.

C) siRNA: Anti-Luc siRNA-1 (D-002050-01-05) with target sequence 5'-GAT TAT GTC CGG TTA TGT ATT -3' was purchased from Dharmacon Inc. (IL, USA) and resuspended in nuclease free water. Aliquots were frozen and stored at -20 °C. Dy547-labelled siGENOME Cyclophilin B Control siRNA (D-001136-01-20) with target sequence 5'-GGA AAG ACU GUU CCA AAA A-3' was purchased from Dharmacon Inc. (IL, USA) and resuspended in nuclease free water. Aliquots were frozen and stored at -20 °C.

Preparation of concentrated media: 500 mL of 2X concentrated McCoy's 5A complete medium were prepared as follows: 11.9 g of McCoy's 5A powder were dissolved in 350 mL of nuclease-free water, followed by addition 2.2 g of $NaHCO_3$ (or 6.0 g of HEPES). The pH was then adjusted (to 7.1 for bicarbonate- or 7.4 and 6.4 for HEPES-buffered media) by adding adequate volumes of HCl 0.1 M, and then nuclease-free water was added to reach the required volume. The resulting solutions were sterile filtered using disposable sterile filter systems 0.22 μm (Corning, UK) and supplemented accordingly (20% (v/v) FBS and 2% (v/v) antibiotic-antimycotic solution). The pH of the media was checked after addition of supplements. Similarly, 5X concentrated McCoy's 5A complete medium was prepared from 29.8 g of McCoy's 5A powder, nuclease-free water, 5.5 g of $NaHCO_3$ (or 15.0 g of HEPES), and supplemented accordingly (50% (v/v) FBS and 5% (v/v) antibiotic-antimycotic solution). For antibiotic-free experiments, media without antibiotic-antimycotic solution were similarly prepared.

Preparation of nanoparticles in media: Nanoparticles in complete medium (bicarbonate or HEPES) were prepared by the addition of an equal volume of 2X McCoy's 5A complete medium (as prepared above) to a two-fold concentrated nanoparticle dispersions. Nanoparticle formulations at high A/P ratios and/or concentrations required the use of appropriate volumes of 5X McCoy's 5A complete medium. Experiments with LTX and toxicity experiments were both performed under antibiotic-antimycotic free conditions.

SI2. Acetylation of chitosan

H84 was dissolved overnight in 0.5% wt. AcOH (aq) at a concentration of 1% wt. Then, 1,2-propanol (80 mL per 100 mL of chitosan solution) was added slowly while stirring vigorously. After overnight stirring, 4.5 mL of this solution were transferred to a reaction vessel of a Carousel 12 parallel reactor (Radleys, UK) and 0.5 mL of 1,2-propanol containing an adequate amount of acetic anhydride (Ac_2O), corresponding to an Ac_2O:NH_2 ratio of 1.2, 1.0,

0.8, 0.6, 0.4 and 0.2, were then added. The reaction mixture was magnetically stirred (300 rpm) for 3 h. The re-acetylated chitosans were purified by centrifugal ultrafiltration using an Amicon Ultra-4 (MWCO: 100 KDa) against MilliQ water, 4.6 mM HCl (aq) and again MilliQ water, and finally, washed (once) with and diluted in 2% DCl in D_2O to allow direct ^1H NMR analysis without polymer isolation. The results are shown in Figure 4—9.

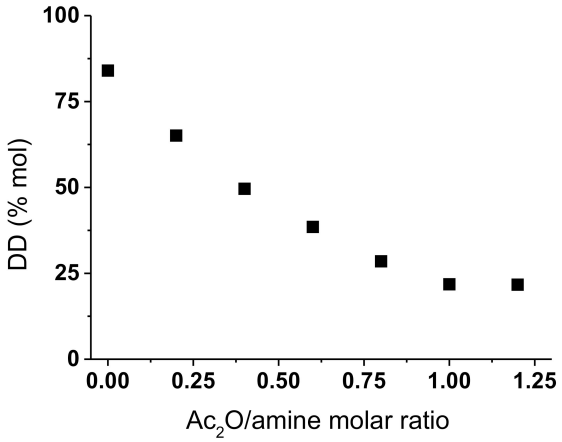

Figure 4—9. Degree of chitosan deacetylation (DD) as a function of the molar ratio between acetic anhydride and chitosan amines.

SI3. Effect of cargo loading on size and ζ potential of nanoparticles

mRNA-loaded CS/HA nanoparticles prepared from H84 and L84 were used to investigate the effect of cargo loading on the size and ζ potential of nanoparticles. Nanoparticles with increasing concentrations of mRNA (5 – 25% wt. compared to chitosan, corresponding to A/P ratios of 7 to 35) were obtained using the preparative procedure described in the section *Preparation of chitosan/hyaluronic acid nanoparticles* in Materials and Methods. Hydrodynamic diameters (Z-average size) and ζ potential were measured as described previously.

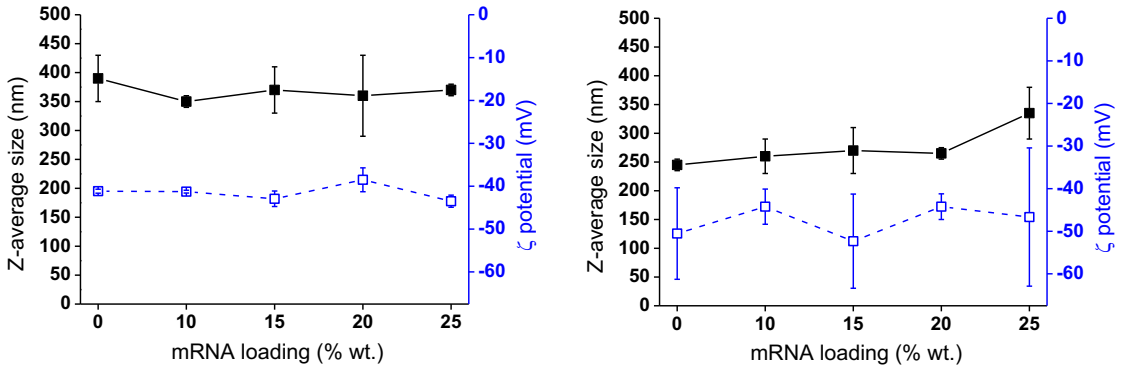

Figure 4—10. Z-average size and ζ potential of H84 (left) and L84 (right) nanoparticles and loaded with different amounts of mRNA; the latter are expressed as %wt in relation to chitosan and correspond to an amine/phosphate (A/P) molar ratio ranging between 35 and 9.

SI4. Cell viability (MTS) and concentration dependency of RNA delivery

HCT-116 were transfected with RNA-loaded CS/HA H84 nanoparticles at pH 6.4, and luciferase, MTS and BCA assays were performed as described in the section *Transfection and silencing experiments* in Materials and Methods.

For both mRNA transfection and siRNA silencing the maximum effects were reported at a concentration of 0.67 mg RNA/well (corresponding to a nanoparticle concentration close to 400 μg/mL).

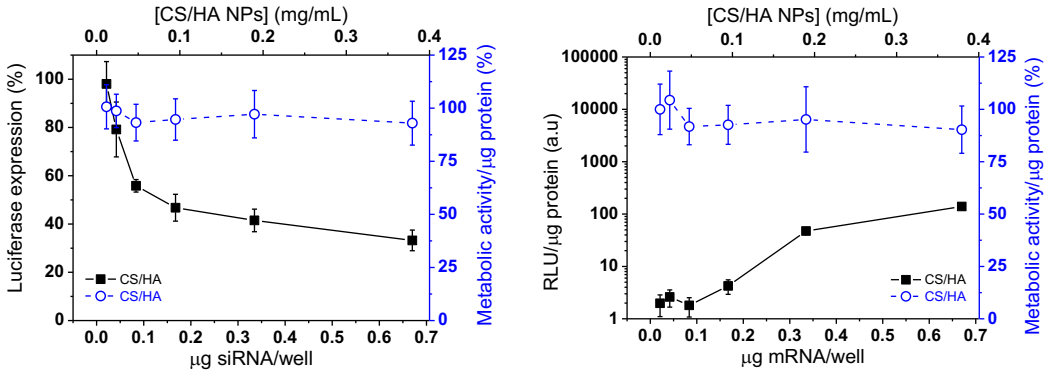

Figure 4—11. Blue symbols report the cytotoxicity (blue: metabolic activity measured via MTS assay and normalized against the protein content) and black symbols the mRNA transfection (left) or siRNA silencing (right) efficiency of H84/HA nanoparticles produced with A/P = 50 (corresponding to a 3.53%wt. loading of RNA compared to chitosan) at pH 6.4 (HEPES).

SI5. size of nanoparticles in cell culture media

RNA-loaded CS/HA nanoparticles (A/P ratio 50) prepared from H84 and L84 were used to show the effect of cell media and pH on their size. Nanoparticles were diluted with 2X HEPES-buffered McCoy's 5A complete medium (pH 6.4 or 7.4) prior to DLS measurement (25 °C).

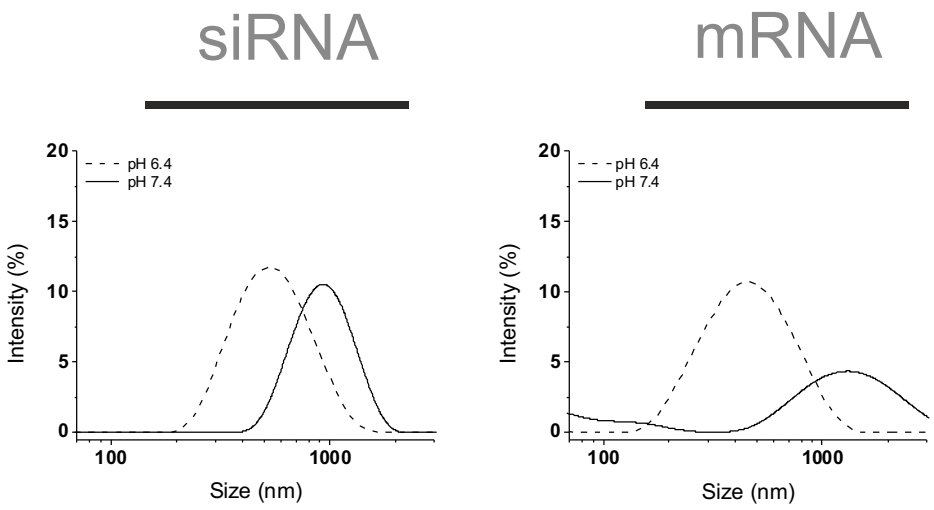

Figure 4—12. Size distributions via DLS for H84/HA nanoparticles loaded with siRNA (left) or mRNA (right) in HEPES buffer-containing complete medium.

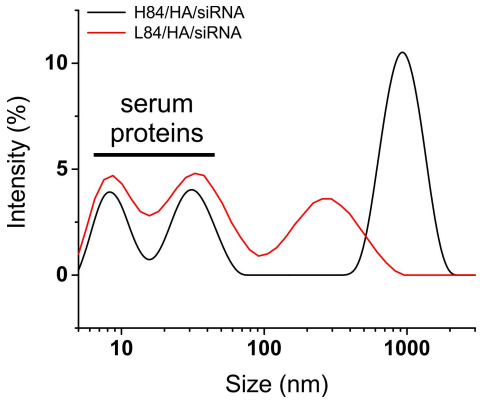

Figure 4—13. Comparison of the size distributions (DLS) of H84/HA/siRNA and L84/HA/siRNA nanoparticles in HEPES buffer-containing complete medium.

SI6. Comparison of silencing in HEPES and bicarbonate buffers

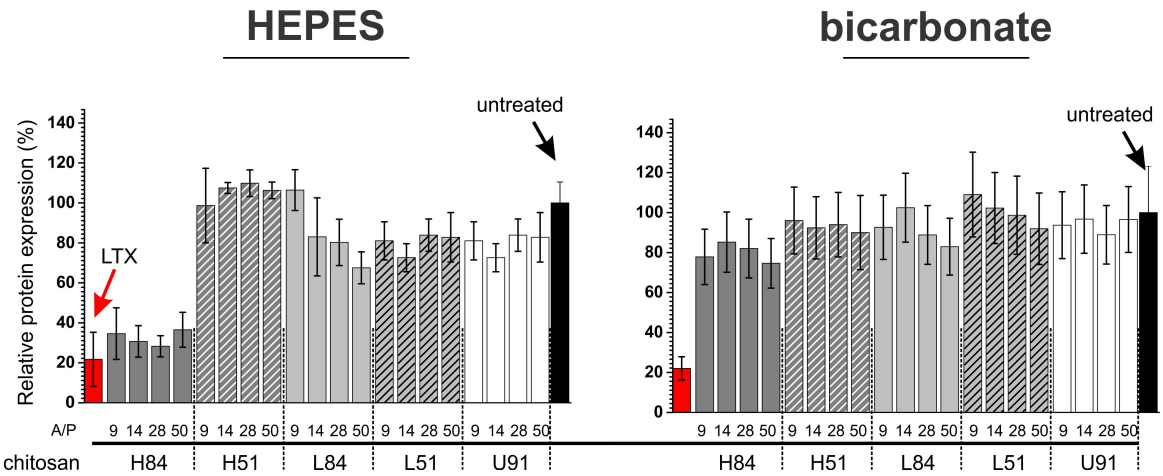

Figure 4—14. HCT-116 cells were pre-transfected with FLuc pGL3 plasmid and treated with siRNA-loaded CS/HA nanoparticles at pH 7.4 (see also Figure 4—5 in the main text) in HEPES (left) or bicarbonate (right) buffer-based media. Typically, due to the large number of samples, the systems would be exposed to non-CO_2-enriched environment for about 30 minutes, during which in the case of bicarbonate buffer the media would experience a pH drift to well above pH 8.

SI7. References

[1] A. Gennari, M. Pelliccia, R. Donno, I. Kimber, N. Tirelli, Mannosylation Allows for Synergic (CD44/C-Type Lectin) Uptake of Hyaluronic Acid Nanoparticles in Dendritic Cells, but Only upon Correct Ligand Presentation, Adv. Healthc. Mater. 5(8) (2016) 966-976.

[2] A. Almalik, P.J. Day, N. Tirelli, HA-Coated Chitosan Nanoparticles for CD44-Mediated Nucleic Acid Delivery, Macromolecular Bioscience 13(12) (2013) 1671-1680.

Chapter 5 Target Specificity of Chitosan/HA Nanoparticles for siRNA Therapeutics: An *In Vitro* Study

*Julio M. Rios de la Rosa, Annalisa Tirella, Alice Spadea, Maria Pelliccia, Ponpawee Pingrajai, Enrique Lallana, Arianna Gennari, Ian J. Stratford, and Nicola Tirelli**

North West Centre for Advanced Drug Delivery (NoWCADD), Division of Pharmacy & Optometry, School of Health Sciences, Faculty of Biology, Medicine and Health, Stopford building, Manchester, M13 9PT, United Kingdom

Manuscript in preparation.

* to whom correspondence should be addressed:

Prof. Nicola Tirelli
NorthWest Centre for Advanced Drug Delivery (NoWCADD)
Division of Pharmacy and Optometry School of Health Sciences
University of Manchester Manchester, M13 9PT, UK
E-mail: nicola.tirelli@manchester.ac.uk
Tel.: +44 161 275 24 80.

5.1. Abstract

CD44 is the main receptor of hyaluronic acid (HA) on mammalian cell membranes, and its diverse biological activity is reflected in the pathology of a plethora of diseases, most remarkably in cancer. The overexpression of CD44 in a number of solid tumors, particularly in the cancer stem cell subpopulation, represents a golden opportunity in cancer therapy for the use of HA-based platforms for the selective and controlled delivery of nucleic acids (e.g. siRNA). However, an array of challenges has arisen in the potential exploitation of HA-based targeting strategies to treat CD44-expressing cells: not only is this receptor ubiquitous in the human body, being present in virtually all cellular types, but also CD44-HA interactions seem to depend heavily on the cell type as well as their developmental stage. As a result, the possible off-target destination of candidate CD44-targeted therapies remains a major cause for concern and must be investigated. Here, using various normal and cancer cell types, we explore the correlation between the expression of CD44 and of its variant isoforms and the uptake and further biological efficacy of a model HA-based drug carrier. In particular, we focus on the different phases of the uptake process (i.e. binding and internalization) and the gene silencing capabilities of HA-based nanoparticles across a panel of pancreatic and colorectal cell lines, as well as of normal cell models including macrophages, endothelial cells, and fibroblasts. The latter cell group is considered as the most likely off-target destination in a tumor microenvironment scenario. Interestingly, although both cancer and normal cell types were able to bind these particles, only the metastatic AsPC-1 (pancreatic) and HCT-116 (colorectal) cancer cell models were highly active in their internalization, which positively correlated with a high gene silencing efficiency. In striking contrast, HT-29 cells were inefficient in the uptake of the particles despite a very high level of CD44 expression. Our study therefore suggests that the activation state of CD44 i.e. their internalization capabilities, rather than their overall expression levels, should be a major focus in the design and evaluation of HA-based carriers in targeted cancer therapy.

Keywords: CD44 targeting; hyaluronic acid; siRNA; macrophages; tumor microenvironment; off-target.

5.2. Introduction

The glycosaminoglycan hyaluronic acid (HA), a major component of extracellular matrices, has emerged as a promising biomaterial in the formulation of novel drug conjugates [1-6] and drug carriers [6-11] owing to its favorable physicochemical and biological characteristics, including its anionic character and extraordinary hydrophilicity [12], receptor-mediated internalization [13], and inherent cell targeting capabilities [14-16]. Although a number of HA-binding proteins and receptors have been identified to date [13, 17-19], only two of them stand out as suitable therapeutic targets because of their overexpression in tumoral tissues and pivotal role in cancer initiation and progression [20]: Receptor for Hyaluronic Acid Mediated Motility (RHAMM) and CD44. While the blocking of HA interactions with RHAMM [21, 22] and CD44 [23] has been extensively exploited in peptide-based strategies (e.g. to switch off survival pathways activated upon HA binding [23]), the development of HA-based carriers in drug delivery has focused exclusively on CD44-mediated drug delivery [14, 20]. The markedly different targeting exploitation of both receptors most likely stems from the soluble nature of RHAMM (hence its difficult cellular targeting) and the wide acceptance of CD44 as a cancer stem cell (CSC) marker [24, 25]. Additionally, the experimental demonstration of the 'superselective' binding of HA to cell surface CD44 (i.e. the ability of HA to sharply discriminate between different CD44 receptor densities and hence to target a desired density of binding sites has reinforced its suitability as a targetable receptor in nanomedicine [26].

However, two main caveats in the targeting of drugs to CD44-expressing cells and translational advances of such therapies have been exposed so far [16, 27-30]. The first one is the general lack of understanding and consensus on the mechanism of CD44-HA interaction, which has been suggested to dependent on the cell type and developmental stage [31-33]. In this context, we have recently unveiled the complex relationship between the uptake of HA-based materials and the expression of CD44 in differently polarized THP-1 macrophages [34]. The second caveat is the ubiquitous expression of HA receptors in the body, which needs to be addressed from two different perspectives: liver toxicity and reduced targeting efficiency. Due to the abundant expression of Hyaluronic Acid Receptor for Endocytosis (HARE) by endothelial cells in the liver and spleen, it is hypothesized the *a priori* saturation of this receptor would be required in order to reduce side effects, e.g. by pre-administration of soluble HA [29] or chondroitin sulfate, the latter being in principle more adequate due to its high HARE affinity and very low CD44 affinity [1, 35]. On the other hand, the widespread physiological expression and function of CD44 in the human body raises concerns about the

reduction in the efficiency of a tumor targeting strategy based on HA-CD44 interactions. The presence of CD44 in healthy tissue accounts as off-target (and undesired) destination of HA-based carriers, thereby reducing the amount of drugs delivered into CD44-expressing tumor cells.

Despite all the above-mentioned issues, there is a consensus that the success of CD44-targeted drug delivery relies not only on the overexpression of CD44 (in particular of variant isoforms) in malignant cells [36-39], but more importantly on the pronounced differences of CD44 activation state in normal *versus* cancer cells [31]. The activation state of CD44 determines both the HA binding and internalization capabilities of the receptor [40-42], and three strictly regulated and cell specific HA-binding states have been reported [43]: inactive, constitutively active, or inducible upon binding of HA or other factors e.g. phorbol myristate acetate [44, 45].

Adding another level of complexity, the binding and receptor-mediated internalization of HA are not necessarily concomitant processes, and noteworthy some cell specific factors may play a key role in enabling HA endocytosis. For example, the acylation of the CD44 cytoplasmic tail may render the receptor inactive for the endocytosis of HA, but not for its binding [46]. In summary, the successful targeting of drugs to CD44 would require of a differential receptor expression and HA-internalization behavior, ideally depicted as the overexpression of CD44 with increased HA-endocytic activity in cancer cells in comparison to normal cells.

The tumor microenvironment comprises not only malignant cells but also CD44-expressing stromal cells that support this environment, being identified as fibroblasts, macrophages, and endothelial cells (the latter form blood vessels that provide nourishment to the tumor [47]). Unfortunately, most of the published literature fails to provide a detailed study about the differential uptake of HA-based platforms by cancer and normal cells. In our view, this would provide the first step to assess the potential off-targeting effects of HA-based drug delivery carriers, and hence to allow the structural tailoring of the system in order to maximize the efficiency of a targeted treatment; for instance, the incorporation of additional targeting moieties has proven useful in facilitating preferential uptake of HA-based carriers by specific cell populations [11, 48, 49].

In this paper, we aimed to assess the feasibility of using HA-based carriers to preferentially deliver a functional siRNA payload to CD44-expressing cancer cells. Employing chitosan/HA nanoparticles as a generic model of HA-based carrier [34], we have analyzed the binding and internalization kinetics of the nanoparticles in a panel of *target/disease* (pancreatic and

colorectal cancer cell lines) and *off-target/normal* (macrophages, fibroblasts and endothelial cells) cellular models. We have then cross-correlated the expression of CD44 with both the nanoparticle uptake and their silencing efficiency.

5.3. Materials and Methods

5.3.1. General Cell Culture

THP-1 (TIB-202™), AsPC-1 (CRL-1682™), PANC-1 (CRL-1469™), HT-29 (HTB-28™), and HCT-116 (CCL-247™) cell lines were purchased from ATCC (Manassas, VA, USA). Human Dermal Fibroblasts, adult (HDF) (#C0135C) were purchased from Thermo Fisher Scientific, UK. Human Umbilical Vein Endothelial Cells (HUVEC) (#C12255, HUVEC-p pre-screened) were purchased from Promocell, UK. Cells were routinely cultured following the manufacturer's instructions as indicated in Table 5—1. The RPMI 1640 cell culture growth medium (#42402-016) was purchased from Gibco®/Invitrogen, UK, Endothelial Cell Medium with Supplement Mix (C-39215) was purchased from Promega, UK, McCoy's 5A (M8403) and DMEM (D5671) media were purchased from Sigma-Aldrich, UK. All cell culture growth media were supplemented with 10% (v/v) Foetal Bovine Serum (FBS, F7524), 2 mM L-Glutamine (G7513), and 1% (v/v) Penicilin-Streptomycin (P4333), all purchased from Sigma-Aldrich, UK. Cells were grown in a humidified 5% (v/v) CO_2 air atmosphere at 37°C, regularly tested for mycoplasma, and used at passage numbers below 20.

Table 5—1. General information about the immortalized human cells used in this study.

Name	Tissue/Disease	Growth Medium
THP-1	Peripheral blood/Acute monocytic leukemia	RPMI 1640
HDF, adult	Dermal/Normal	DMEM
HUVEC	Umbilical, vascular endothelium/Normal	Endothelial Cell Medium
PANC-1	Pancreas, duct/Epithelioid carcinoma	DMEM
AsPC-1	Pancreas, metastatic site/Adenocarcinoma	RPMI 1640
HT-29	Colon/Adenocarcinoma	McCoy's 5A
HCT-116	Colon/Carcinoma	McCoy's 5A

1) THP-1 macrophage differentiation and polarization. THP-1 premonocytes were differentiated into resting macrophages (M0) and further activated either classically (M1) or

alternatively (M2) as we recently described [34]. Briefly, THP-1 premonocytes ($1.25x10^5$ cells/cm^2) were incubated for 24 h with medium containing 50 ng/mL phorbol 12-myristate-13-acetate (PMA) (P1585, Sigma-Aldrich, UK), followed by thorough rinsing with serum free medium, to obtain:

-M0 macrophages, cells were rested in PMA-free complete medium for a further 24 h,

-M1-like macrophages, treated for further 24 h with PMA-free medium supplemented with 100 ng/mL lipopolysaccharides (LPS) from *Escherichia coli* O26:B6 (L8274, Lot. #032M4089V, Sigma-Aldrich, UK) and 20 ng/mL IFN-γ (#300-02, Lot #081427, Prepotech, Inc., USA),

-M2-like macrophages, treated for further 24 h with PMA-free medium supplemented with 20 ng/mL IL-4 (#200-04, Lot #061314) and 20 ng/mL IL-13 (#200-13, Lot #051023).

5.3.2. CD44 expression analysis

1) Flow cytometry - indirect staining. Cells were grown in T-75 flasks until reaching ~70% confluency and harvested using pre-warmed Enzyme-Free, Phosphate Buffer solution (PBS)-based Cell Dissociation Buffer (#13151-014, Gibco®/Invitrogen, UK). Individual cell samples were prepared in 1.5 mL Eppendorf tubes by suspending approximately $5x10^5$ viable cells in 100 µL Fluorescence-Activated Cell Sorting (FACS) buffer (PBS, 5% (v/v) FBS, 0.1% (m/v) NaN_3) and stained for 30 min at room temperature with one the following primary antibodies according to manufacturer's instructions: i) mouse anti-human CD44 (1:100) (156-3C11, Cell Signaling Technology, UK), ii) mouse anti-human CD44v3 (1:20) (Clone #3G5, R&D Systems, UK), iii) mouse anti-human CD44v4 (1:50) (MCA1728; AbD Serotec), iv) mouse anti-human CD44v6 (1:20) (Clone #2F10, R&D Systems, UK), or v) IgG1/IgG2 control (1:10) (AbD Serotec, UK). In the case of THP-1 macrophages, a blocking step prior to staining was performed by incubating cells with Fc-receptor blocking inhibitor (#14-9161, Affymetrix/eBioscience, UK) on ice for 20 min. Excess primary antibody was removed by centrifugation and cells were incubated for further 30 min at room temperature with the secondary antibody: goat anti-mouse IgG H&L, AlexaFluor®647-conjugated (1:2000) (ab150115, Abcam, UK). The expression of total CD44 (CD44pan) and CD44 variant isoforms spanning variant exons 3, 4, or 6 (CD44v3, CD44v4, or CD44v6) was recorded for 10,000 live, individual cells using a BD LSRFortessa cytometer (BD Bioscience, San Jose CA, USA) equipped with the FACSDiva software (v8.0.1). Data were analyzed with FlowJo (vX.0.7, Tree Star, Ashland, OR, USA) after gating live cells in the FSC/SSC window and

cell singlets in the FSC-H/FSC-A window, respectively. The median fluorescence intensity (MFI) of the isotype control for each cell line was used to calculate the MFI fold change for each marker.

2) Western blotting. Total cell lysates were prepared in ice-cold RIPA Buffer (R0278, Sigma-Aldrich, UK) supplemented with Protease Inhibitor (cOmpleteUltra Tablets, Mini, EDTA-free, EASYpack, #05892791001, Roche, Germany) and stored at -80°C until use. Equal amounts of protein (20 μg), quantified using the BCA assay kit (B9643, Sigma-Aldrich, UK), were diluted with Laemmli buffer (#161-0737) containing 5% (v/v) 2-mercaptoethanol (M3148, Sigma-Aldrich, UK), incubated at 95°C for 5 min, and placed on ice until loading. Proteins were then separated by polyacrylamide electrophoresis (SDS-PAGE) using a Criterion™ Cell (#165-6001; Run settings: 1 h, 100V, 0.5 A) and transferred to a PVDF membrane (#162-0177 using a Criterion™ Blotter (#170-4070; Run settings: 1 h, 100 V, 0.5 A). Membranes were blocked by incubation with 5% (w/v) non-fat milk (#70166, Lot. #BCB68664V, Fluka, UK) in TBS-T (0.1% Tween-20 SigmaUltra - P7949, Sigma-Aldrich, UK - in 1X Tris-buffer - #170-6435) for 1 h at room temperature. Membranes were then cut into two sections. The upper section of the membrane, corresponding to the high molecular weight bands, was incubated with 1:200 dilution in TBS-T mouse anti-human CD44v6 (Clone #2F10, R&D Systems) overnight at 4°C. The lower section of the membrane, corresponding to the low molecular weight protein bands, was incubated with 1:5000 dilution in TBS-T mouse anti-human β-actin (ab6276, Abcam, UK) for 1 h at room temperature. Following four washings in TBS-T (15 min/wash under gentle agitation), membranes were incubated for 1 h at room temperature with goat anti-mouse IgG-peroxidase (A0168, Sigma-Aldrich, UK). Bands were detected using Clarity Western enhanced chemiluminescence (ECL) substrate (#170-5061) with the aid of a ChemiDoc™ MP System (#170-8280). ImageJ software (v1.49p, http://rsb.info.nih.gov/ij) was used to perform a densitometry analysis of protein bands. Briefly, the relative expression of CD44v6 was determined by calculating the ratio of the band intensity for CD44v6 to that of the β-actin control (please note that actins are highly-conserved proteins and variations in band intensity are indicative of different protein loading between wells). Please note that, unless specified, all the products herein mention were purchased from Bio-Rad, UK.

5.3.3. Preparative operations

1) Labeling of HA with Rhodamine B (HA-Rho). Hyaluronic acid (HA; $\overline{M}_w$ = 180 kDa) was kindly provided by Kyowa (Milan, Italy) and covalently conjugated to Lissamine™ Rhodamine B Ethylenediamine (L2424, Thermo Scientific, UK) via DMTMM (4-(4,6-Dimethoxy-1,3,5-triazin-2-yl)-4-methylmorpholinium chloride) (Sigma-Aldrich, UK) mediated acylation. Briefly, 100 mg of HA (0.25 mmol of carboxylate units) were dissolved in 10 mL of HEPES buffer 100 mM pH = 7.4 under mild stirring overnight. Then, 2 mg of lissamine rhodamine B ethylenediamine dye (0.00325 mmol, targeted degree of carboxylate substitution = 1%, 1.3 eq.) dissolved in 2.5 mL of HEPES buffer were added followed by addition of 2.5 mL of a 65 mM solution of 4-(4,6-Dimethoxy-1,3,5-triazin-2-yl)-4-methylmorpholinium chloride (DMTMM, Sigma-Aldrich, UK) (0.1625 mmol, 0.65 eq.) in HEPES buffer. The reaction mixture was stirred (300 rpm) for 24 h at 25°C, then quenched and precipitated by addition of a 20-fold volume excess of cold ethanol 96% (v/v). The resulting dispersion was left overnight at 4°C to allow complete precipitation of the polymer. The precipitate was isolated by centrifugation (10 min at 4500 g), dissolved in 10 mL of deionized water, and purified by dialysis (MWCO = 20 kDa) against deionized water. Finally, the solution containing HA-rhodamine (HA-Rho) conjugate was freeze-dried (mass recovery: 70%). The degree of functionalization was calculated by measuring the fluorescence intensity of the fluorescently-labeled HA (Ex: 540/25, Em: 620/40 nm; Synergy2 Biotek plate reader equipped with Gen5 software) using Lissamine Rhodamine B Ethylenediamine dye to calculate the emission to the molar concentrations of the fluorophore. Please note that the degree of functionalization is later transformed and reported in a molar ratio between the dye-functionalized and non-functionalized monomer units in the polymer. Typical degree of derivatization: 0.7-1.0 % mol of carboxylate units.

2) Preparation and characterization of chitosan/HA nanoparticles. All the materials used while handling of siRNA were nuclease-free - or previously treated with the following procedure: washed with RNaseZap solution (Thermo Scientific, UK), 70% (v/v) ethanol in water, and nuclease-free water (Thermo Scientific, UK) prior to use. Middle viscosity chitosan, average viscosimetric molecular weight ($\overline{M}_v$) = 656 kDa and degree of deacetylation 85% was purchased from Sigma-Aldrich, UK. Chitosan with $\overline{M}_v$ = 36 kDa was obtained by oxidative degradation of middle viscosity chitosan (1% wt. in 0.1 M HCl / 3 mM sodium nitrite). Chitosan samples were purified in-house prior to use as previously described [11]. Nanoparticles were prepared by direct polyelectrolyte complexation of chitosan with HA and

siRNA in aqueous medium. This preparative method encompasses first the preparation of a 0.069% wt. chitosan solution — low ($\overline{M}_v$ = 36 kDa) or high ($\overline{M}_v$ = 656 kDa) molecular weight chitosan — by dissolving it overnight in 4.6 mM HCl (aq), and then adjusting the pH to 5 by adding 0.1 M NaOH (aq). HA was dissolved overnight in nuclease-free water (room temperature) at a concentration of 1.5 mg/mL, and the pH was adjusted to 5 by adding 0.1 M HCl (aq). The siRNA solutions were prepared at the desired concentration by diluting the 100 μM stock with nuclease-free water and stored at -20°C. The chitosan and HA solutions were sterile filtered through 0.45 and 0.22 μm pore size filters (Merck Millipore, UK), respectively. For the preparation of empty nanoparticles, the chitosan solution was further diluted 1:2 (v/v) with sterile nuclease-free water. For the preparation of siRNA-loaded nanoparticles, the chitosan solution was diluted with nuclease-free water containing siRNA (concentration depending on the targeted %wt. loading) and an initial complexation step was carried in 2.0 mL round-bottom Eppendorf tubes under magnetic agitation (1000 rpm) for 10 min at 25°C. HA-coated nanoparticles (chitosan/HA) were finally obtained by addition of the chitosan solution or chitosan/siRNA suspension into an equal volume of 1.5 mg/mL HA under the same stirring conditions for additional 30 min at room temperature.

Dynamic light scattering (DLS) analysis of the hydrodynamic size, ζ-potential, and polydispersity index (PDI) of chitosan/HA nanoparticles was performed on three independent samples at 25 °C using a Zetasizer Nano ZS instrument (Model ZEN3600, Malvern Instruments Ltd., UK) equipped with a solid state HeNe laser (λ=633 nm, scattering angle of 173°). The size measurement data were analyzed by using the General Purpose algorithm provided in the Malvern software; the electrophoretic mobility of the samples was converted into ζ-potential by using the Smoluchowski equation.

The encapsulation efficiency (EE) of siRNA was determined by measuring the amount of non-complexed nucleic acid remaining in solution. Briefly, chitosan/HA nanoparticles were sedimented via centrifugation (13,000 rpm for 60 min at 4°C), and the amount of siRNA in solution was quantified via fluorimetry (Synergy2 Biotek plate reader equipped with Gen5 software) using the Quant-iT RiboGreen RNA Assay Kit (Thermo Scientific, UK) as specified by the manufacturer. EE values (%) were calculated as follows: $EE = (A - B)/A \times 100$, where A is the amount of siRNA in the nanoparticle feed, and B is the amount of free siRNA in the supernatant.

5.3.4. Study of chitosan/HA nanoparticle binding and internalization

Nanoparticle dispersions for cell experiments were prepared in complete cell growth medium at a final working concentration of 125 μg/mL by addition of an equal volume of two-fold medium (prepared as described in Supporting Information, section SI2) to a two-fold concentrated nanoparticle aqueous dispersion (i.e. 250 μg/mL). Please note that nanoparticle binding and internalization studies were performed using respectively HA-Rho or DY547-labeled siRNA (siGLO Cyclophilin B Control, sequence: 5'-GGA AAG ACU GUU CCA AAAA-3'; #D-001610-01-05, Dharmacon, UK) as fluorescent reporter.

1) Quantification of nanoparticle binding and uptake (cell lysates). Cells were plated in Costar polystyrene 12-well plates with flat bottom (#3513, Corning, UK) and incubated with chitosan/Rho-HA nanoparticles for specific time points (2, 4, 8, 16, and 24 h) in a humidified 5% (v/v) CO_2 air atmosphere at 37°C. Untreated cells were also used as a control. After each incubation time, nanoparticle-containing medium was removed, cells were washed three times with PBS, and finally lysed in 100 μL RIPA buffer. The total uptake, comprising both membrane-bound and internalized materials, was estimated from the fluorescence intensity of cell lysates by using a calibration of chitosan/HA-Rho nanoparticles suspension in cell lysates at a concentration range 0.12-125 μg/mL using a Synergy2 Biotek plate reader (Ex: 540/25, Em: 620/40 nm) equipped with Gen5 software (sensitivity of the instrument adjusted to wells with the highest nanoparticle concentration of the calibration curve, optical position: top 50%, light source: Xenon flash). The number of cells for each well was estimated by using a standard curve that correlates the number of cells (Scepter cell counter) *versus* protein content (BCA) for each individual cell line. Finally, the nanoparticle concentration values were normalized against the number of cells per well.

2) Quantification of nanoparticle internalization (flow cytometry). Cells were plated in Costar polystyrene 12-well plates with flat bottom (#3513, Corning, UK) and incubated with chitosan/HA nanoparticles loaded with DY547-labeled siRNA (1.45%wt. loading with respect to chitosan content) for specific time points (2, 4, 8, 16, and 24 h) in a humidified 5% (v/v) CO_2 air atmosphere at 37°C. Untreated cells were also used as a control. After each incubation time, nanoparticle-containing medium was removed, cells were washed three times with PBS, and detached using Trypsin-EDTA solution (#59417C, Sigma-Aldrich, UK) for 10 min at room temperature. Cells were pelleted (1000 rpm, 5 min, 25ºC) and resuspended in 400 μL PBS. The internalization of DY547-labeled siRNA was determined on 10,000 live, individual cells with a BD LSRFortessa cytometer (BD Bioscience, San Jose CA, USA)

equipped with the FACSDiva software (v8.0.1). Data were analyzed with FlowJo (vX.0.7, Tree Star, Ashland, OR, USA) after gating single and live events in the FSC-A/FSC-H and FSC/SSC windows, respectively. Untreated cells were used as autofluorescence control in order to calculate the median fluorescence intensity (MFI) fold change over time, as well as the percentage of positive events for each cell line.

5.3.5. Immunofluorescence staining

PANC-1 cells were plated in Ibidi µ-slide (prod.no. 80826, Ibidi®, Germany) at a cell density of $2.5x10^4$ cells/cm^2, left to adhere overnight (37°C, 5%CO_2), and then stained for panCD44 and nuclei while alive to detect membrane bound panCD44 only. Briefly, cells were washed with PBS, incubated with 1 µg/mL Hoechst solution in PBS (5 min, 37°C, 5%CO_2), washed again with PBS (n=3) and placed on ice. A 1:200 dilution of anti-human CD44-Alexa594 conjugated antibody (prod. No. 103054, Biolegend, UK) in 1% (w/v) BSA/PBS was prepared and cells were incubated for 30 min on ice. Cells were then washed with PBS (n=3) and fixed with 4% PFA solution (10 min, on ice). Cells were finally washed again with PBS (n=3) and stored in a 1 mg/mL ascorbic acid solution in PBS.

5.3.6. Laser Scanning Confocal Microscope

An inverted SP5 laser confocal microscope (Leica TSC SP5 AOBS, Leica Microsystem, UK) was used to acquire volumetric datasets of stained cells. Acquisitions were performed using the immersion oil 63X/1.40 HCX PL Apo objective. Images were acquired with sequential scan with the following settings Ex(power)/Em[adjusted mirrors]: Hoechst 405(5%)/[410-460]nm, and panCD44 594(30%)/[605-650]nm. During acquisitions: 1) pixel size was adjusted to 165 nm, 2) pinhole was kept with 1 airy unit aperture, and 3) 6x averaged line setting (to remove background).

5.3.7. Silencing experiments

For functional silencing experiments, nanoparticles loaded with siGENOME Cyclophilin B Control siRNA (12.45%wt. with respect to chitosan or A/P ratio = 14) (Sequence: 5'-GGA AAG ACU GUU CCA AAAA-3', #D-001136-01-20; Dharmacon, UK) were brought to a final working concentration of 125 µg/mL in complete cell growth medium based on HEPES buffer (pH = 6.4) by the addition of an equal volume of two-fold medium to a two-fold

concentrated nanoparticle aqueous dispersion (i.e. 250 μg/mL). Note that these conditions are equivalent to a siRNA concentration of 200 nM per well (or 0.67 μg of siRNA/well).

1) Knockdown at the mRNA level (qPCR). Cells were plated in Costar polystyrene 12-well plates with flat bottom (#3513, Corning, UK) and incubated in media based on HEPES buffer at pH = 6.4 containing siRNA-loaded chitosan/HA nanoparticles for 24 h in a humidified 5% (v/v) CO_2 air atmosphere at 37°C. Nanoparticle-containing media were removed and cells were lysed with trypsin-EDTA solution after thorough rinsing with PBS. The total RNA was extracted using PureLink® RNA mini kits (Applied Biosystems™, UK), purified via sequential elution with RNAse-free water, and stored at -80ºC for long term use. The total RNA concentration and purity were measured via spectrophotometry (NanoDrop® ND-1000; Thermo Fisher Scientific, UK). Samples with a 260/280 nm absorbance ratio in the range 1.80-2.0 were used for reverse transcription using the High Capacity cDNA Reverse Transcription Kits (Applied Biosystems™, UK). Reverse transcription was performed using the Peltier Thermal Cycler PTC-200 (MJ Research, Waltham, Massachusetts, USA) to yield cDNA for downstream TaqMan® gene expression analysis. The TaqMan® Gene Expression Master Mix (Life Technologies, UK) was used alongside Human Cyclophilin B (PPIB) (Hs00168719_m1) and Human Glyceraldehyde-3-Phosphate Dehydrogenase (GAPDH) (Hs02758991_g1), the latter utilized as an endogenous control (house-keeping gene). The real-time polymerase chain reactions (qPCR) were carried out in MicroAmp® Fast Optical 96-Well Reaction Plates (Applied Biosciences, UK) on a StepOnePlus™ (Life Technologies, UK) equipped with StepOne software. All reactions were carried out for a total of 40 thermal cycles. Results were run against the house-keeping gene in a ΔΔCT quantitative evaluation method and all results were expressed as fold change in gene expression relative to negative control samples (i.e. cells not exposed to siRNA against Cyclophilin B). All qPCR experiments were run on 3 different wells (technical replicates) and each experiment was repeated 3 times (biological replicates).

5.3.8. Statistical analysis

Differences between chitosan $\overline{M}_v$ and transfection efficiency were considered to be significant at a *P* value of <0.05 (T-test, Two-tailed). Statistical analyses were performed with GraphPad Prism 7.0 (GraphPad Software, Inc., San Diego, CA).

5.4. Results and Discussion

5.4.1. CD44 expression in cancer and healthy cellular models

In this study, we have first analyzed the expression of total CD44 (CD44pan) and also of its most common variant isoforms (CD44v3, CD44v4, and CD44v6) in a panel of cell lines. The CD44 fingerprint of cancer cells was compared with that of three normal cell line controls, screening pancreatic (AsPC-1 and PANC-1) and colorectal (HCT-116 and HT-29) human cancer cell lines, fibroblasts (HDF), endothelial cells (HUVEC), and macrophages (THP-1). The CD44 expression was measured by flow cytometry and Western blotting, the two techniques were used to minimize differences in the relative protein quantification. Please note that both analyses were performed using the same primary antibodies. Although both techniques are based on a two-step immunolabeling procedure, a major difference exists between them: in flow cytometry, the detected signal depends on antibody binding to cell surface proteins, while in Western blotting it relies on recognition and binding to soluble proteins recovered in cell extracts, whose structured might be considerably modified [34]. The two experimental techniques revealed remarkable differences between cancer and normal cellular models (Figure 5—1).

A) Flow cytometry: as expected from the ubiquitous nature of this receptor, all cell populations stained positive for CD44pan (Figure 5—1A, greater than 80% positive cells). Indirect staining for CD44pan revealed a high protein expression in colorectal cancer cell lines [50, 51] and a moderate to high expression in the pancreatic ones [52, 53], the latter comparable to that seen in fibroblasts [54] and endothelial cells [55]. Macrophages had an overall low expression of total CD44 [56], with significantly higher levels for the M1 subtype and indistinguishable amounts for M0 and M2. The expression of CD44 isoforms containing variant exons v3 (CD44v3) and v6 (CD44v6) was also confirmed in all the cancer models, also present albeit in lower amounts in AsPC-1 and PANC-1 [53], while absent in normal cell models (with the exception of the tumor-associated M2 macrophages, with ~60% of cells expressing low levels of CD44v6 [56]). CD44 isoforms containing exon v4 (CD44v4) were not detected, except for a marginal expression in PANC-1 cells [57] (with ~20% of cells expressing low level of CD44v4).

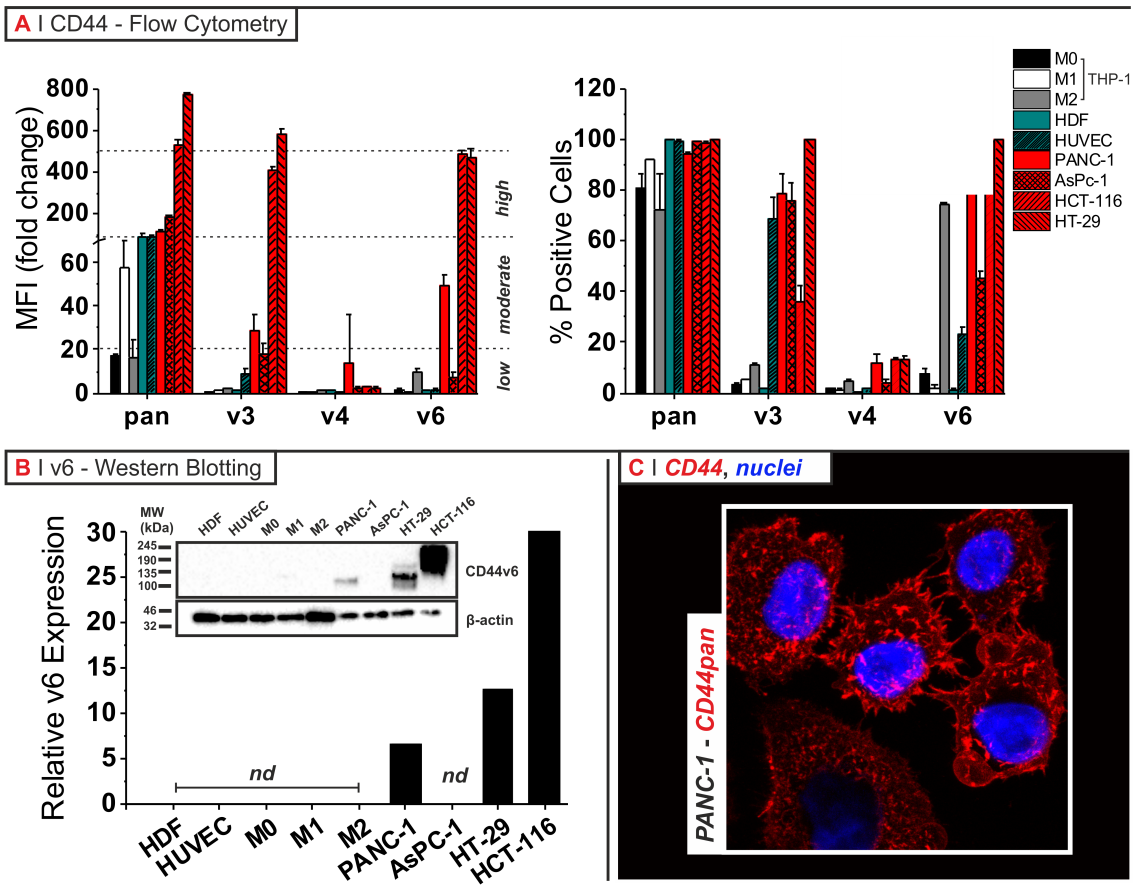

Figure 5—1. CD44 expression in cancer (colorectal and pancreatic cell lines) and healthy (fibroblasts, macrophages, and endothelial cells) *in vitro* cellular models. *A.* Expression of total CD44 (CD44pan) and CD44 variants (CD44v3, CD44v4, and CD44v6) measured by flow cytometry after indirect staining with AlexaFluor647-labeled antibody. Histogram of n-fold change in median fluorescence intensity (MFI) relative to the intensity of the isotype control (left), and percentage of positive cells for the various cell populations (right) are expressed as average ± SD (n = 3). ***B.*** Representative Western blot analysis of CD44v6 detected using anti-CD44v6 (2F10) under reducing conditions. For semi-quantification purposes, β-actin was used as loading control. *Nd* = non-detected. ***C.*** Confocal Microscopy: volume rendering of PANC-1 showing nuclei (blue) and the distribution of CD44pan (red). All data are represented as the average ± SD (n = 3).

B) Western blotting: using anti-CD44pan as a probe (Supporting Information SI1 and Figure 5—6), this technique revealed intense protein bands at ≈85-90 kDa for HDF [58, 59], HUVEC [60], and THP-1 [52, 56], which suggests the predominant expression of CD44 standard isoform (CD44s). Moreover, a prevalent expression of CD44s was also evidenced for the pancreatic cell lines AsPC-1 and PANC-1 [52, 53], the later showing additional higher molecular weight, low intensity bands at longer exposure times. The colorectal cancer lines HT-29 and HCT-116 showed exclusively high molecular weight bands (≈140-200 kDa), suggesting the predominant expression of variant isoforms (CD44v) [52, 61]. In fact, Western blotting against CD44v6 (Figure 5—1B) revealed a faint high molecular weight band for PANC-1 (~100 kDa), moderate to high intensity bands for HT-29 (~140 kDa), and remarkably higher intensity bands for HCT-116 (~140-245 kDa). No bands for v6 were

detected, however, for AsPC-1 and M2 macrophages, most likely due to the experimental detection limit (as suggested from the overall low expression of this isoform in flow cytometry data). Western blotting against variant exons v3 and v4 did not reveal any further bands (data not shown).

Taking into account these results, and based solely on the amounts of CD44 expressed by cancer and normal cell models, we hypothesized HCT-116 and HT-29 to be *a priory* the best candidates for the *in vitro* screening of a CD44-targeted therapy. Complementarily, our results depict HDF and HUVEC cell models as the most likely off-target to compete with cancer cells for the uptake of HA-based materials in the tumor microenvironment.

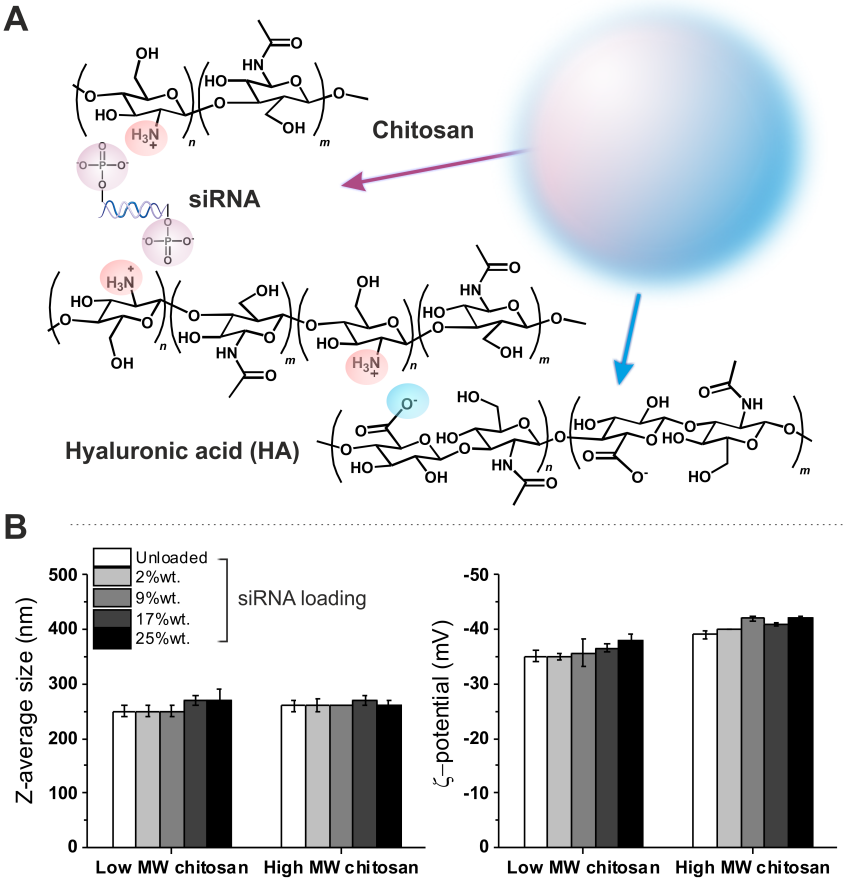

Figure 5—2. ***A.*** Sketch of siRNA-loaded chitosan/HA nanoparticles. The nucleic acid cargo is present in the bulk of the nanoparticles complexed with the positive charges of the chitosan chains. The negatively charged HA then binds chitosan on the surface of the nanoparticles. ***B.*** Physico-chemical characterization of chitosan/HA nanoparticles as a function of siRNA loading. All data are represented as the average ± SD (n = 3).

5.4.2. HA binding and internalization capabilities

Following initial quantification of CD44 expression, we aimed to evaluate the existing relationship between the uptake of HA-decorated nanocarriers and the expression of this receptor across cancer and normal cell line models. In particular, we wanted to test the assumption that the overexpression of CD44 in cancer cells necessarily correlates with a highly endocytic / active internalization state upon binding of HA materials, i.e. high expression = high activity / internalization. To this end, we have used chitosan/HA nanoparticles as a model of HA-decorated carrier, prepared by simple direct polyelectrolyte complexation of chitosan with siRNA and HA (Figure 5—2A). Please note that chitosan/HA nanoparticles differ from soluble HA both in size and in surface charge density (due to a greater condensation of HA when bound to chitosan), and this should be reflected on a different interaction with CD44-binding groups on cell membrane. Moreover, we have varied the chitosan $\overline{M}_v$ to produce nanoparticles that differed in siRNA and HA binding strength. Both low and high $\overline{M}_v$ chitosan/HA nanoparticles have an average hydrodynamic size of approximately 250 nm, a negative ζ potential (evidencing the surface exposure of HA), and provide quantitative siRNA entrapping with encapsulation efficiency (EE) > 99%. Please also note that the complexation of the siRNA payload does not have any significant effect on the nanoparticle characteristics up to a loading of 25%wt. in relation to chitosan (Figure 5—2B).

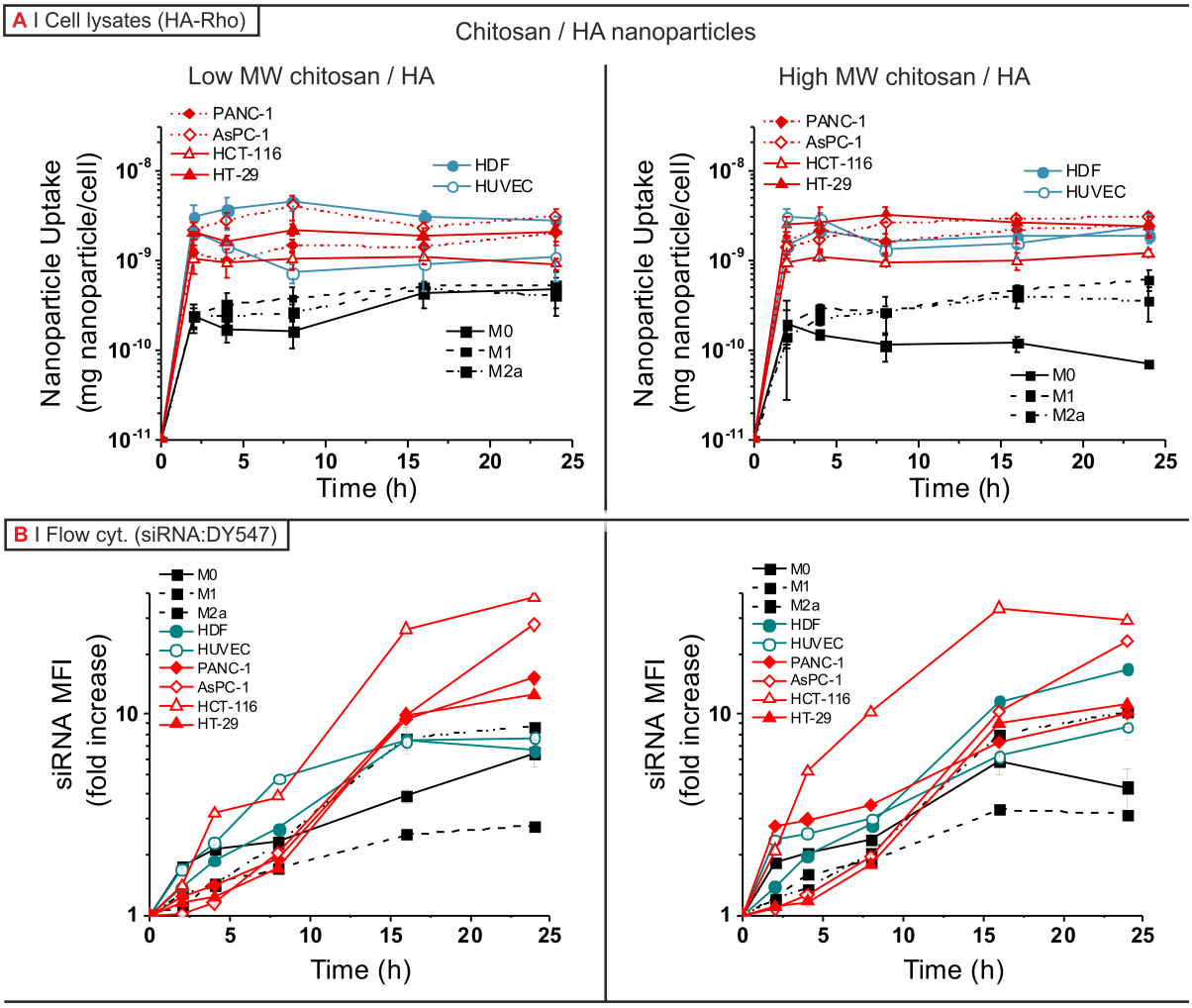

Figure 5—3. ***A.*** Binding and uptake of chitosan/HA nanoparticles (left and right column graphs, respectively) measured by fluorimetry of cell lysates, monitoring the fluorescence of HA-Rho (lysate data are normalized against the cell number, estimated from the protein content for each cell type). ***B.*** Internalization kinetics of low and high $\overline{M}_v$ chitosan/HA nanoparticles measured by flow cytometry on live cells, monitoring the fluorescence of the nanoparticle cargo i.e. DY547-labeled siRNA (the MFI-fold relative to untreated control is directly proportional to the internalization of intact particles). Please note that the cells were trypsinized and thoroughly washed before flow cytometry analysis, which results in CD44 degradation and detachment of surface bound nanoparticles. All data are represented as the average ± SD (n = 3).

We then focused on the study of the capacity of different cell types to take up these carriers (analyzing both bound and internalized materials) by monitoring the time course increase of the fluorescence of Rhodamine-conjugated HA in cell lysates. Separately, we analyzed their capacity to internalize these particles via flow cytometry on trypsinized cells (DY547-labeled siRNA cargo) [56]. Please note that the trypsinization step results in the degradation of surface CD44 and concomitant detachment of CD44-bound material on the cell surface [62]; therefore, the kinetics measured relate exclusively to internalized nanoparticles.

As reported in Figure 5—3A, plateau values in cell lysates are reached after 4 h for all cellular models, suggesting a rapid binding and saturation of HA-receptor(s). On the other

hand, the internalization of these nanoparticles – as expected - proceeded much more slowly (Figure 5—3B), reaching plateau values after ~20 h with virtually complete transfection of all cell populations (see Figure 5—7 in Supporting Information).

In order to test the targeting behavior of HA, we investigated whether the expression of CD44pan correlated with the capacity of the different cells to bind and to internalize chitosan/HA nanoparticles (Figure 5—4). We have used the 4 h cell lysate time point as representative of a cell type's ability to bind these particles due to the much faster kinetics of binding compared to internalization at early time points (for this aspect, please note the relatively low number of positive events in flow cytometry at 4 h, see Figure 5—7 in Supporting Information). We recently reported that the expression of CD44pan possesses a positive correlation with HA binding for differently-polarized THP-1 macrophages [34]. We found that this correlation was also true across normal and cancer cell line models, with the exception of the high CD44 expressing colorectal cell lines HCT-116 and HT-29 (Figure 5—4A). This seemingly erratic behavior may be associated with a different glycosylation pattern, which has been reported to have either stimulatory or inhibitory effects via the alteration of the intrinsic CD44 affinity for HA or the CD44-mediated HA avidity [63].

The internalization experiments (flow cytometry, 24 h time point), on the other hand, suggested a possible correlation between the nanoparticle internalization efficiency and CD44pan expression, with the exception of HT-29 cells (Figure 5—4B). In this context, it is important to remark that although HT-29 cells express high amounts of CD44v6 isoforms, these mostly associate into protein complexes with c-Met and HGF [64]. Therefore, we hypothesize that the participation of CD44 in such multimeric complexes may favor its role as a signaling molecule to the detriment of its endocytic activity. Moreover, the seemingly counterintuitive behavior exhibited by HT-29 mirrors the results we have previously reported for THP-1 macrophages [56], i.e. a higher CD44 expression results in a poorer internalization of HA-based materials. Another highlight derived from the flow cytometry screening was the identification of AsPC-1 and HCT-116 as potentially the most efficient chitosan/HA nanoparticle 'internalizers'. AsPC-1 cells internalized about two times more nanoparticles than PANC-1, HT-29, M2 macrophages and HDF, and about three times more particles than M0 macrophages and HUVEC. HCT-116 cells internalized circa three times more nanoparticles than PANC-1, HT-29, M2 macrophages and HDF, about four times more particles than HUVEC, and about six times more than M0 macrophages. Both cell types showed a 10-fold increase in the internalization of the particles compared to M1 macrophages. Incidentally, AsPC-1 and HCT-116 cell lines happen to be widely accepted as metastatic

pancreatic [65] and metastatic colorectal [66] models, respectively. Thus, it may be tempting to speculate that the metastatic potential of a cell type might correlate with an increased CD44 endocytic activity/activation state, which in turn opens up a number of opportunities for targeting and treating highly invasive cells, e.g. CSCs.

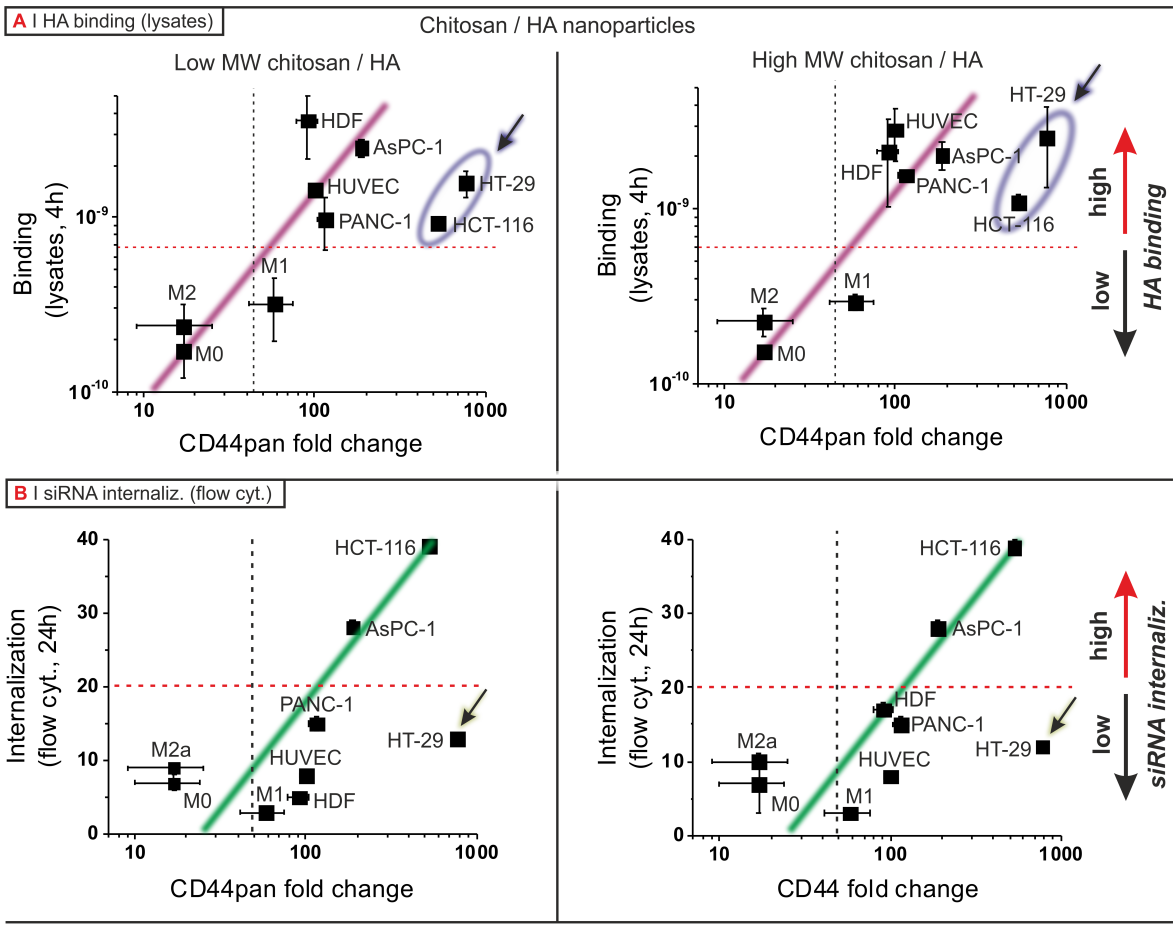

Figure 5—4. Cross-correlation between the expression of total membrane-bound CD44 (CD44pan; measured through indirect staining flow cytometry) and *A.* nanoparticle uptake / binding (HA-Rho, cell lysate at 4 h), *B.* siRNA median fluorescence intensity (MFI) fold change / internalization (DY547-labeled siRNA, flow cytometry at 24 h) of low and high $\overline{M}_v$ chitosan/HA nanoparticles (left and right column graphs, respectively). Data are represented as the average ± SD (n = 3). Please note that the violet circle, purple and green lines are just guides for eyes, and the dotted black and red lines represent arbitrary low and high quadrants on both axes.

5.4.3. Effect of nanoparticle internalization on gene silencing

Finally, we assessed the silencing capabilities of chitosan/HA nanoparticles for the different cellular models so as to be able to relate the above binding and internalization data with the therapeutic efficacy of chitosan/HA nanoparticles. To this end, we targeted the cyclophilin B (PPIB) gene, not only due to its abundant expression across most cell lines, but more importantly because it is a non-essential gene i.e. its knockdown does not compromise cell viability [67]. In order to determine the optimal siRNA concentration to be used for

transfection experiments, we performed an initial titration experiment using HCT-116 cells as model and Lipofectamine LTX (low toxicity) as a transfection positive control (see Figure 5—8 in the Supporting Information). Whereas no significant effect was found at the low nM siRNA concentration range, relatively high silencing values were achieved at concentrations of 100-200 nM siRNA per well. As a consequence of these results, all further experiments were performed formulating chitosan/HA nanoparticles to obtain a concentration of 200 nM siRNA (highest PPIB silencing values recorded). Please note the apparent lack of off-target silencing effects (see scramble siRNA control, Figure 5—8), and the fact that this relatively high siRNA concentration is often used to transfect primary human macrophages [68] and in other studies dealing with chitosan-based delivery systems [69-71].

All cell types mentioned above were incubated for 24 h with anti-PPIB siRNA-loaded chitosan/HA nanoparticles, prepared from both low and high $\overline{M}_v$ chitosan. This treatment failed to produce any silencing at the mRNA level in M1-like macrophages, and produced a rather variable low silencing in M0/M2 macrophages, endothelial cells, and fibroblasts. On the contrary, a consistent silencing was achieved for all tested cancer models, measuring a high silencing efficiency with HCT-116 cells (~70-80% reduction in mRNA levels), a moderate one in AsPC-1 and PANC-1 (~50-60% reduction), and a rather low in HT-29 cells (~30-40% reduction). No significant differences were found between particles prepared from different $\overline{M}_v$ chitosan under these experimental conditions (Figure 5—5A).

Finally, and in order to investigate the relationship between the amounts of siRNA delivered in the cells (i.e. intracellular concentration) and PPIB gene silencing efficiency (i.e. its biological effect), we cross-correlated the internalization data (flow cytometry tracking the cargo – D547 labeled siRNA) with the qPCR knockdown data. Scatter plots were curve-fitted assuming the simplest drug binding model i.e. the biological response is a graded effect (Figure 5—5B). A similar relationship between gene silencing efficiency and cellular uptake has also been depicted for solid lipid nanoparticles [72]. This trend also suggests the presence of a threshold level of siRNA needed for a stable PPIB silencing (reduced variability between experimental replicates).

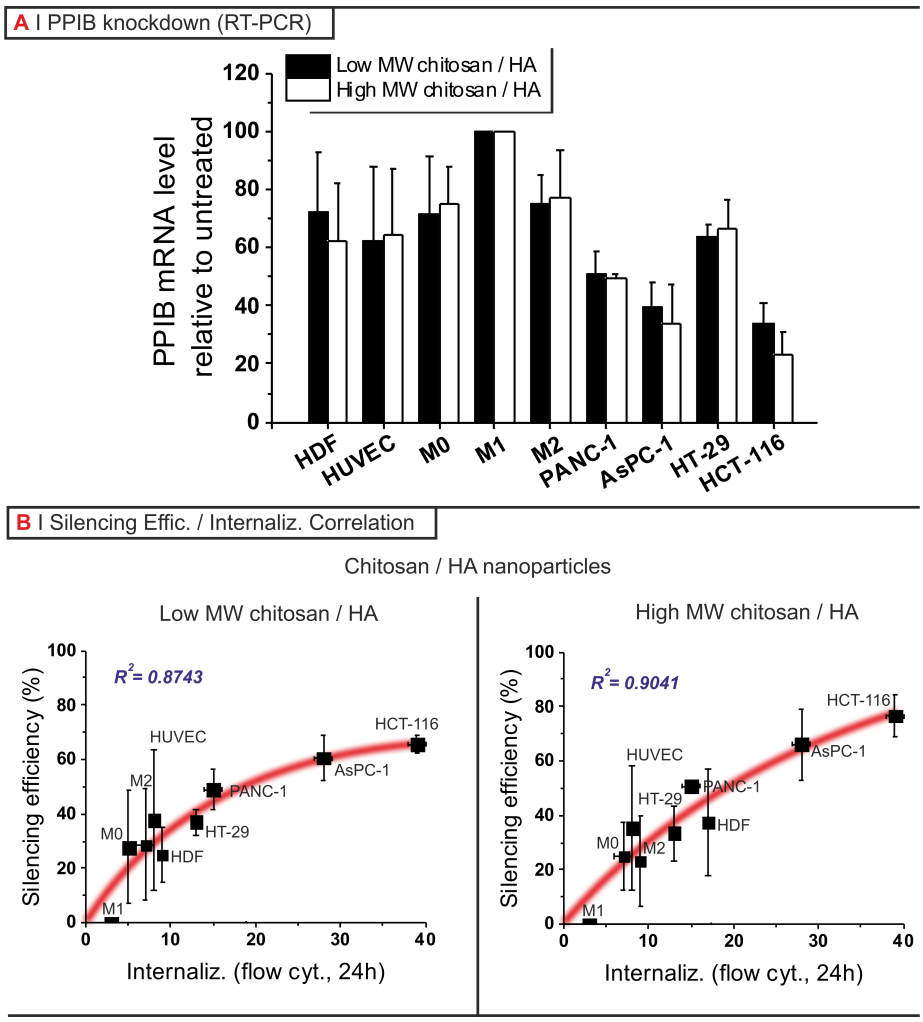

Figure 5—5. ***A.*** Knockdown of PPIB transcription (measured by RT-PCR) upon treatment with low and high $\overline{M}_v$ chitosan/HA nanoparticles loaded with anti-PPIB siRNA (12.45% wt. with respect to chitosan). ***B.*** Cross-correlations between siRNA delivery efficiency (PPIB gene silencing) and the amount of internalized siRNA (MFI-fold over untreated control). Scatter plots were curved-fitted (red line) assuming the simplest drug-response graded mode, i.e. as the dose of drug increases, so it does its biological effect. All data are represented as the average ± SD (n = 3). Statistical analysis (T-test, Two-tailed) showed no significant differences between low and high $\overline{M}_v$ chitosan particles.

5.5. Conclusion

A wide diversity of expression profiles of hyaluronic acid (HA)-binding CD44 receptor exists across cancer and normal cells: colorectal cancer cells express very high amounts of this receptor, while pancreatic cancer cells present a moderate expression level, similar to that seen in fibroblasts and endothelial cells, but significantly higher to that of macrophages. In terms of variant isoforms, we confirmed the overexpression of CD44v in colorectal cell lines and the preferential appearance of CD44s in pancreatic cell lines and other relevant normal cell models. Based solely on these expression profiles, it seems that colorectal cell lines are a priori the most suitable cell models for CD44-targeting cancer therapy, with fibroblasts and

endothelial cells being the most likely off-target destination of HA materials in a more complex, multicellular tumor microenvironment. The obtained results of HA uptake confirm this hypothesis.

Targeted delivery of siRNA through HA-exposing nanoparticles to a panel of CD44-expressing cancer and normal cellular models showed the lack of an apparent correlation between CD44 expression and nanoparticle binding in the two colorectal cell lines assayed, and also revealed an absence of correlation with nanoparticle internalization for CD44-high expressing cells i.e. HT-29. The unexpected behavior of this cell line is a wake-up call for researchers in the field to stress the role of the activation state of CD44 rather than simply predicting the success of a delivery strategy and its positive therapeutic outcome based solely on CD44 overexpression.

Interestingly, and as opposed to normal cellular models, high siRNA internalization and gene silencing efficiencies were observed in widely approved metastatic cellular models HCT-116 (high CD44 expression) and AsPC-1 (moderate CD44 expression). This behavior could be indicative of an increased CD44 endocytic activity in cells with a high metastatic potential, such as CSCs, emphasizing the suitability of CD44 as a therapeutic target.

5.6. Acknowledgements

Mr. Rios de la Rosa is indebted to EPSRC for a PhD studentship as part of the North-West Nanoscience (NoWNano) Doctoral Training Centre (EPSRC grant EP/G03737X/1). Dr. Tirella was funded through the Innovate UK project number 101710. Dr. Pelliccia and Dr. Gennari gratefully acknowledges financial support from the EU FP7 project UniVax (grant number 601738). Kyowa (Milan, Italy) is gratefully acknowledged for the provision of hyaluronic acid.

5.7. References

[1] Y. Luo, M.R. Ziebell, G.D. Prestwich, A hyaluronic acid-taxol antitumor bioconjugate targeted to cancer cells, Biomacromolecules 1(2) (2000) 208-18.

[2] X. Wei, T.H. Senanayake, G. Warren, S.V. Vinogradov, Hyaluronic acid-based nanogel-drug conjugates with enhanced anticancer activity designed for the targeting of CD44-positive and drug-resistant tumors, Bioconjug Chem 24(4) (2013) 658-68.

[3] H.Q. Zhang, S.L. Huang, X.Y. Yang, G.X. Zhai, Current research on hyaluronic acid-drug bioconjugates, Eur J Med Chem 86 (2014) 310-317.
[4] A. Gennari, C. Gujral, E. Hohn, E. Lallana, F. Cellesi, N. Tirelli, Revisiting Boronate/Diol Complexation as a Double Stimulus-Responsive Bioconjugation, Bioconjugate Chemistry (2017).
[5] B. Chen, R.J. Miller, P.K. Dhal, Hyaluronic acid-based drug conjugates: state-of-the-art and perspectives, Journal of biomedical nanotechnology 10(1) (2014) 4-16.
[6] V.M. Platt, F.C. Szoka, Jr., Anticancer therapeutics: targeting macromolecules and nanocarriers to hyaluronan or CD44, a hyaluronan receptor, Mol Pharm 5(4) (2008) 474-86.
[7] M. de la Fuente, B. Seijo, M.J. Alonso, Novel hyaluronic acid-chitosan nanoparticles for ocular gene therapy, Invest Ophth Vis Sci 49(5) (2008) 2016-2024.
[8] E.C. Dreaden, S.W. Morton, K.E. Shopsowitz, J.H. Choi, Z.J. Deng, N.J. Cho, P.T. Hammond, Bimodal Tumor-Targeting from Microenvironment Responsive Hyaluronan Layer-by-Layer (LbL) Nanoparticles, Acs Nano 8(8) (2014) 8374-8382.
[9] A. Mero, M. Campisi, M. Caputo, C. Cuppari, A. Rosato, O. Schiavon, G. Pasut, Hyaluronic Acid as a Protein Polymeric Carrier: An Overview and a Report on Human Growth Hormone, Curr Drug Targets 16(13) (2015) 1503-1511.
[10] A. Almalik, P.J. Day, N. Tirelli, HA-Coated Chitosan Nanoparticles for CD44-Mediated Nucleic Acid Delivery, Macromol Biosci 13(12) (2013) 1671-1680.
[11] A. Gennari, M. Pelliccia, R. Donno, I. Kimber, N. Tirelli, Mannosylation Allows for Synergic (CD44/C-Type Lectin) Uptake of Hyaluronic Acid Nanoparticles in Dendritic Cells, but Only upon Correct Ligand Presentation, Adv. Healthc. Mater. 5(8) (2016) 966-976.
[12] J. Necas, L. Bartosikova, P. Brauner, J. Kolar, Hyaluronic acid (hyaluronan): a review, Vet Med-Czech 53(8) (2008) 397-411.
[13] R. Racine, M.E. Mummert, Hyaluronan Endocytosis: Mechanisms of Uptake and Biological Functions, Molecular Regulation of Endocytosis (2012) 377-390.
[14] A. Cadete, M.J. Alonso, Targeting cancer with hyaluronic acid-based nanocarriers: recent advances and translational perspectives, Nanomedicine-Uk 11(17) (2016) 2341-2357.
[15] S. Arpicco, P. Milla, B. Stella, F. Dosio, Hyaluronic Acid Conjugates as Vectors for the Active Targeting of Drugs, Genes and Nanocomposites in Cancer Treatment, Molecules 19(3) (2014) 3193-3230.
[16] S. Misra, P. Heldin, V.C. Hascall, N.K. Karamanos, S.S. Skandalis, R.R. Markwald, S. Ghatak, Hyaluronan-CD44 interactions as potential targets for cancer therapy, Febs J 278(9) (2011) 1429-1443.

[17] M. Litwiniuk, A. Krejner, T. Grzela, Hyaluronic Acid in Inflammation and Tissue Regeneration, Wounds 28(3) (2016) 78-88.
[18] A.J. Day, G.D. Prestwich, Hyaluronan-binding proteins: Tying up the giant, J. Biol. Chem. 277(7) (2002) 4585-4588.
[19] D.H. Jiang, J.R. Liang, P.W. Noble, Hyaluronan as an Immune Regulator in Human Diseases, Physiol Rev 91(1) (2011) 221-264.
[20] S. Misra, V.C. Hascall, R.R. Markwald, S. Ghatak, Interactions between hyaluronan and its receptors (CD44, RHAMM) regulate the activities of inflammation and cancer, Front Immunol 6 (2015).
[21] J. Greiner, A. Schmitt, K. Giannopoulos, M.T. Rojewski, M. Gotz, I. Funk, M. Ringhoffer, D. Bunjes, S. Hofmann, G. Ritter, H. Dohner, M. Schmitt, High-dose RHAMM-R3 peptide vaccination for patients with acute myeloid leukemia, myelodysplastic syndrome and multiple myeloma, Haematol-Hematol J 95(7) (2010) 1191-1197.
[22] M. Schmitt, A. Schmitt, M.T. Rojewski, J.F. Chen, K. Giannopoulos, F. Fei, Y.Z. Yu, M. Gotz, M. Heyduk, G. Ritter, D.E. Speiser, S. Gnjatic, P. Guillaume, M. Ringhoffer, R.F. Schlenk, P. Liebisch, D. Bunjes, H. Shiku, H. Dohner, J. Greiner, RHAMM-R3 peptide vaccination in patients with acute myeloid leukemia, myelodysplastic syndrome, and multiple myeloma elicits immunologic and clinical responses, Blood 111(3) (2008) 1357-1365.
[23] M. Finlayson, Modulation of CD44 activity by A6-peptide, Front Immunol 6 (2015) 1-8.
[24] M. Zoller, CD44: can a cancer-initiating cell profit from an abundantly expressed molecule?, Nat Rev Cancer 11(4) (2011) 254-267.
[25] K. Williams, K. Motiani, P.V. Giridhar, S. Kasper, CD44 integrates signaling in normal stem cell, cancer stem cell and (pre)metastatic niches, Exp Biol Med 238(3) (2013) 324-338.
[26] G.V. Dubacheva, T. Curk, R. Auzely-Velty, D. Frenkel, R.P. Richter, Designing multivalent probes for tunable superselective targeting, P Natl Acad Sci USA 112(18) (2015) 5579-5584.
[27] A. Almalik, S. Karimi, S. Ouasti, R. Donno, C. Wandrey, P.J. Day, N. Tirelli, Hyaluronic acid (HA) presentation as a tool to modulate and control the receptor-mediated uptake of HA-coated nanoparticles, Biomaterials 34(21) (2013) 5369-5380.
[28] B.P. Toole, Hyaluronan-CD44 Interactions in Cancer: Paradoxes and Possibilities, Clin Cancer Res 15(24) (2009) 7462-7468.
[29] F.A. Venning, L. Wullkopf, J.T. Erler, Targeting ECM disrupts cancer progression, Front Oncol 5 (2015).

[30] R. Thapa, G.D. Wilson, The Importance of CD44 as a Stem Cell Biomarker and Therapeutic Target in Cancer, Stem Cells Int (2016).
[31] J. Lesley, R. Hyman, N. English, J.B. Catterall, G.A. Turner, CD44 in inflammation and metastasis, Glycoconjugate J 14(5) (1997) 611-622.
[32] H.J. Greyner, T. Wiraszka, L.S. Zhang, W.M. Petroll, M.E. Mummert, Inducible macropinocytosis of hyaluronan in B16-F10 melanoma cells, Matrix Biol 29(6) (2010) 503-510.
[33] A.J. Day, The structure and regulation of hyaluronan-binding proteins, Biochem Soc T 27(2) (1999) 115-121.
[34] J.M.R. de la Rosa, A. Tirella, A. Gennari, I.J. Stratford, N. Tirelli, The CD44-Mediated Uptake of Hyaluronic Acid-Based Carriers in Macrophages, Adv. Healthc. Mater. 6(4) (2017).
[35] E.N. Harris, S.V. Kyosseva, J.A. Weigel, P.H. Weigel, Expression, processing, and glycosaminoglycan binding activity of the recombinant human 315-kDa hyaluronic acid receptor for endocytosis (HARE), The Journal of biological chemistry 282(5) (2007) 2785-97.
[36] S. Hiscox, B. Baruha, C. Smith, R. Bellerby, L. Goddard, N. Jordan, Z. Poghosyan, R.I. Nicholson, P. Barrett-Lee, J. Gee, Overexpression of CD44 accompanies acquired tamoxifen resistance in MCF7 cells and augments their sensitivity to the stromal factors, heregulin and hyaluronan, Bmc Cancer 12 (2012).
[37] H.J. Wei, T. Yin, Z. Zhu, P.F. Shi, Y. Tian, C.Y. Wang, Expression of CD44, CD24 and ESA in pancreatic adenocarcinoma cell lines varies with local microenvironment, Hepatob Pancreat Dis 10(4) (2011) 428-434.
[38] D. Naor, S.B. Wallach-Dayan, M.A. Zahalka, R.V. Sionov, Involvement of CD44, a molecule with a thousand faces, in cancer dissemination, Semin Cancer Biol 18(4) (2008) 260-267.
[39] N.M. Resnick, M.R. Clarke, J.M. Siegfried, R. Landreneau, D.C. Asman, L.S. Ge, L.S. Kierstead, G.D. Dougherty, D.L. Cooper, Expression of the cell adhesion molecule CD44 in human lung tumors and cell lines, Mol Diagn 3(2) (1998) 93-103.
[40] J. Lesley, R. Hyman, Cd44 Can Be Activated to Function as an Hyaluronic-Acid Receptor in Normal Murine T-Cells, Eur J Immunol 22(10) (1992) 2719-2723.
[41] J. Cichy, E. Pure, The liberation of CD44, J Cell Biol 161(5) (2003) 839-843.
[42] N.M. English, J.F. Lesley, R. Hyman, Site-specific de-N-glycosylation of CD44 can activate hyaluronan binding, and CD44 activation states show distinct threshold densities for hyaluronan binding, Cancer Res. 58(16) (1998) 3736-3742.

[43] J. Lesley, V.C. Hascall, M. Tammi, R. Hyman, Hyaluronan binding by cell surface CD44, The Journal of biological chemistry 275(35) (2000) 26967-75.
[44] R.V. Sionov, D. Naor, Calcium- and calmodulin-dependent PMA-activation of the CD44 adhesion molecule, Cell Adhes Commun 6(6) (1998) 503-523.
[45] D.C. Liu, M.S. Sy, Phorbol myristate acetate stimulates the dimerization of CD44 involving a cysteine in the transmembrane domain, Journal of immunology 159(6) (1997) 2702-2711.
[46] S.P. Thankamony, W. Knudson, Acylation of CD44 and its association with lipid rafts are required for receptor and hyaluronan endocytosis, J. Biol. Chem. 281(45) (2006) 34601-34609.
[47] I.M. Adjei, S. Blanka, Modulation of the Tumor Microenvironment for Cancer Treatment: A Biomaterials Approach, Journal of Functional Biomaterials 6(1) (2015) 81-103.
[48] S.P. Qiao, Y.F. Zhao, S. Geng, Y. Li, X.L. Hou, Y. Liu, F.H. Lin, L.F. Yao, W.M. Tian, A novel double-targeted nondrug delivery system for targeting cancer stem cells, Int J Nanomed 11 (2016) 6667-6678.
[49] X.B. Zhao, X. Jia, L. Liu, J. Zeng, K. Tian, T.T. Zhou, P. Liu, Double-Cross-Linked Hyaluronic Acid Nanoparticles with pH/Reduction Dual-Responsive Triggered Release and pH-Modulated Fluorescence for Folate-Receptor-Mediated Targeting Visualized Chemotherapy, Biomacromolecules 17(4) (2016) 1496-1505.
[50] T. Ishimoto, O. Nagano, T. Yae, M. Tamada, T. Motohara, H. Oshima, M. Oshima, T. Ikeda, R. Asaba, H. Yagi, T. Masuko, T. Shimizu, T. Ishikawa, K. Kai, E. Takahashi, Y. Imamura, Y. Baba, M. Ohmura, M. Suematsu, H. Baba, H. Saya, CD44 Variant Regulates Redox Status in Cancer Cells by Stabilizing the xCT Subunit of System xc(-) and Thereby Promotes Tumor Growth, Cancer Cell 19(3) (2011) 387-400.
[51] P. Zhang, C.L. Fu, H.Y. Bai, E.Q. Song, Y. Song, CD44 variant, but not standard CD44 isoforms, mediate disassembly of endothelial VE-cadherin junction on metastatic melanoma cells, Febs Lett 588(24) (2014) 4573-4582.
[52] F. Birzele, E. Voss, A. Nopora, K. Honold, F. Heil, S. Lohmann, H. Verheul, C. Le Tourneau, J.P. Delord, C. van Herpen, D. Mahalingam, A.L. Coveler, V. Meresse, S. Weigand, V. Runza, M. Cannarile, CD44 Isoform Status Predicts Response to Treatment with Anti-CD44 Antibody in Cancer Patients, Clin Cancer Res 21(12) (2015) 2753-2762.
[53] S. Zhao, C. Chen, K. Chang, A. Karnad, J. Jagirdar, A.P. Kumar, J.W. Freeman, CD44 Expression Level and Isoform Contributes to Pancreatic Cancer Cell Plasticity, Invasiveness, and Response to Therapy, Clin Cancer Res 22(22) (2016) 5592-5604.

[54] M.A. Croce, F. Boraldi, D. Quaglino, R. Tiozzo, I. Pasquali-Ronchetti, Hyaluronan uptake by adult human skin fibroblasts in vitro, Eur J Histochem 47(1) (2003) 63-73.
[55] R.C. Savani, G.Y. Cao, P.M. Pooler, A. Zaman, Z. Zhou, H.M. DeLisser, Differential involvement of the hyaluronan (HA) receptors CD44 and receptor for HA-mediated motility in endothelial cell function and angiogenesis, J Biol Chem 276(39) (2001) 36770-36778.
[56] J.M. Rios de la Rosa, A. Tirella, A. Gennari, I.J. Stratford, N. Tirelli, The CD44-Mediated Uptake of Hyaluronic Acid-Based Carriers in Macrophages, Advanced Healthcare Materials 6(4) (2017) 1601012-n/a.
[57] J. Ringel, R. Jesnowski, C. Schmidt, J. Ringel, H.J. Kohler, J. Rychly, S.K. Batra, M. Lohr, CD44 in normal human pancreas and pancreatic carcinoma cell lines, Teratogen Carcin Mut 21(1) (2001) 97-106.
[58] L. Vistejnova, B. Safrankova, K. Nesporova, R. Slavkovsky, M. Hermannova, P. Hosek, V. Velebny, L. Kubala, Low molecular weight hyaluronan mediated CD44 dependent induction of IL-6 and chemokines in human dermal fibroblasts potentiates innate immune response, Cytokine 70(2) (2014) 97-103.
[59] G.M. Campo, A. Avenoso, A. D'Ascola, V. Prestipino, M. Scuruchi, G. Nastasi, A. Calatroni, S. Campo, 4-Mer Hyaluronan Oligosaccharides Stimulate Inflammation Response in Synovial Fibroblasts in Part via TAK-1 and in Part via p38-MAPK, Curr Med Chem 20(9) (2013) 1162-1172.
[60] G.I. Mun, Y.C. Boo, Identification of CD44 as a senescence-induced cell adhesion gene responsible for the enhanced monocyte recruitment to senescent endothelial cells, Am J Physiol-Heart C 298(6) (2010) H2102-H2111.
[61] B. Banky, L. Raso-Barnett, T. Barbai, J. Timar, P. Becsagh, E. Raso, Characteristics of CD44 alternative splice pattern in the course of human colorectal adenocarcinoma progression, Mol. Cancer 11 (2012).
[62] C.B. Knudson, K.T. Rousche, R.S. Peterson, G. Chow, W. Knudson, CD44 and cartilage matrix stabilization, in: V.C. Hascall, K.E. Kuettner (Eds.), The Many Faces of Osteoarthritis, Birkhäuser Basel, Basel, 2002, pp. 219-230.
[63] T.P. Skelton, C.X. Zeng, A. Nocks, I. Stamenkovic, Glycosylation provides both stimulatory and inhibitory effects on cell surface and soluble CD44 binding to hyaluronan, J Cell Biol 140(2) (1998) 431-446.
[64] V. Orian-Rousseau, L.F. Chen, J.P. Sleeman, P. Herrlich, H. Ponta, CD44 is required for two consecutive steps in HGF/c-Met signaling, Gene Dev 16(23) (2002) 3074-3086.

[65] Z.H. Li, K. Chen, P. Jiang, X. Zhang, X.W. Li, Z.H. Li, CD44v/CD44s expression patterns are associated with the survival of pancreatic carcinoma patients, Diagn Pathol 9 (2014).
[66] I.L. Botchkina, R.A. Rowehl, D.E. Rivadeneira, M.S. Karpeh, Jr., H. Crawford, A. Dufour, J. Ju, Y. Wang, Y. Leyfman, G.I. Botchkina, Phenotypic subpopulations of metastatic colon cancer stem cells: genomic analysis, Cancer genomics & proteomics 6(1) (2009) 19-29.
[67] T.L. Cuellar, D. Barnes, C. Nelson, J. Tanguay, S.F. Yu, X. Wen, S.J. Scales, J. Gesch, D. Davis, A. van Brabant Smith, D. Leake, R. Vandlen, C.W. Siebel, Systematic evaluation of antibody-mediated siRNA delivery using an industrial platform of THIOMAB-siRNA conjugates, Nucleic Acids Res 43(2) (2015) 1189-203.
[68] A. Troegeler, C. Lastrucci, C. Duval, A. Tanne, C. Cougoule, I. Maridonneau-Parini, O. Neyrolles, G. Lugo-Villarino, An efficient siRNA-mediated gene silencing in primary human monocytes, dendritic cells and macrophages, Immunol Cell Biol 92(8) (2014) 699-708.
[69] H. Ragelle, R. Riva, G. Vandermeulen, B. Naeye, V. Pourcelle, C.S. Le Duff, C. D'Haese, B. Nysten, K. Braeckmans, S.C. De Smedt, C. Jerome, V. Preat, Chitosan nanoparticles for siRNA delivery: Optimizing formulation to increase stability and efficiency, J. Control Release 176 (2014) 54-63.
[70] K. Wan, J. Li, D. Li, J.H. Ge, Y.L. Wang, X.X. Li, Y.F. Guo, J.J. Guo, M. Leng, P. Wang, Y. An, Novel hydroxybutyl chitosan nanoparticles for siRNA delivery targeting tissue factor inhibits proliferation and induces apoptosis in human vascular smooth muscle cells, Mol Med Rep 12(6) (2015) 7957-7962.
[71] K.A. Howard, U.L. Rahbek, X.D. Liu, C.K. Damgaard, S.Z. Glud, M.O. Andersen, M.B. Hovgaard, A. Schmitz, J.R. Nyengaard, F. Besenbacher, J. Kjems, RNA interference in vitro and in vivo using a chitosan/siRNA nanoparticle system, Mol Ther 14(4) (2006) 476-484.
[72] T. Nakamura, M. Kuroi, Y. Fujiwara, S. Warashina, Y. Sato, H. Harashima, Small-sized, stable lipid nanoparticle for the efficient delivery of siRNA to human immune cell lines, Sci Rep-Uk 6 (2016).

5.8. Supporting information

SI1. Western blotting - CD44pan

Methods. Total cell lysates were prepared in ice-cold RIPA Buffer (R0278, Sigma-Aldrich, UK) supplemented with cOmpleteUltra Tablets, Mini, EDTA-free, EASYpack (#05892791001, Roche, Germany) and stored at -80°C until use. Equal amounts of protein,

quantified using the BCA assay kit (B9643, Sigma-Aldrich, UK) were diluted with Laemmli buffer (#161-0737) containing 5% (v/v) 2-mercaptoethanol (M3148, Sigma-Aldrich, UK), incubated at 95°C for 5 min, and placed on ice until loading. Proteins were then separated by polyacrylamide electrophoresis (SDS-PAGE) using a Criterion™ Cell (#165-6001; Run settings: 1 h, 100V, 0.5 A) and transferred to a PVDF membrane (#162-0177 using a Criterion™ Blotter (#170-4070; Run settings: 1 h, 100 V, 0.5 A). Membranes were blocked by incubation with 5% (w/v) non-fat milk (#70166, Lot. #BCB68664V, Fluka, UK) in TBS-T (0.1% Tween-20 SigmaUltra - P7949, Sigma-Aldrich, UK - in 1X Tris-buffer - #170-6435) for 1 h at room temperature. Membranes were then cut into two sections. The upper section of the membrane, corresponding to the high molecular weight bands, was incubated with 1:1000 dilution in TBS-T mouse anti-human CD44pan (Clone 156-3C11, #170-5061; Cell Signaling Technology, UK) overnight at 4°C. The lower section of the membrane, corresponding to the low molecular weight protein bands, was incubated with 1:5000 dilution in TBS-T mouse anti-human β-actin (ab6276, Abcam, UK) for 1 h at room temperature. Following four washings in TBS-T (15 min/wash under gentle agitation), membranes were incubated for 1 h at room temperature with goat anti-mouse IgG-peroxidase (A0168, Sigma-Aldrich, UK). Bands were detected using Clarity Western enhanced chemiluminescence (ECL) substrate (#170-5061) with the aid of a ChemiDoc™ MP System (#170-8280). ImageJ software (v1.49p, http://rsb.info.nih.gov/ij) was used to perform a densitometry analysis of protein bands. Briefly, the relative expression of CD44 was determined by calculating the ratio of the band intensity for CD44 to that of the β-actin control (please note that actins are highly-conserved proteins and variations in band intensity are indicative of different protein loading between wells). Unless specified, all the products herein mention were purchased from Bio-Rad, UK.

Results and discussion. Western blotting against CD44pan proved challenging due to remarkable differences in band intensities. For the sake of accuracy, two different exposure times were used to develop clear bands for all cell types: a low exposure time (i.e. 1 s) for PANC-1, HT-29, HUVEC, and HDF, and a high exposure time (i.e. 40 s) for HCT-116, AsPC-1, and THP-1 macrophages.

In order to compare the expression of CD44pan detected by Western blotting and flow cytometry, we have normalized the Western blotting data (CD44pan/β-actin band intensity ratio) for each cell type with respect to M1 macrophages as these cells show clear bands both at shorter and longer exposure times. Following normalization of flow cytometry data to M1 macrophages, we observed an excellent match between both techniques for THP-1

macrophages, HDF, HUVEC, and PANC-1, a rather poor correlation for AsPC-1, and a very bad correlation for HCT-116 and HT-29 cells. The particularly bad correlation seen for colorectal cell lines could be easily explained assuming the 156-3C11 anti-CD44pan to have a high affinity for CD44s and a low affinity for CD44v, just as described for the IM7 antibody by Birzele *et al.* [1]. This assumption matches well the result obtained in the v6 blot, which reveals higher intensity molecular weight bands, indicative of CD44v expression, in HT-29 and particularly in HCT-116 (main text, Figure 5—11). However, the same rationale cannot be applied to AsPC-1 cells, which show a preferential expression of CD44s. In this case, we are tempted to invoke the possible influence of the denaturation process or the presence of additional post-translational modifications that might change affinity of the antibody toward its epitope.

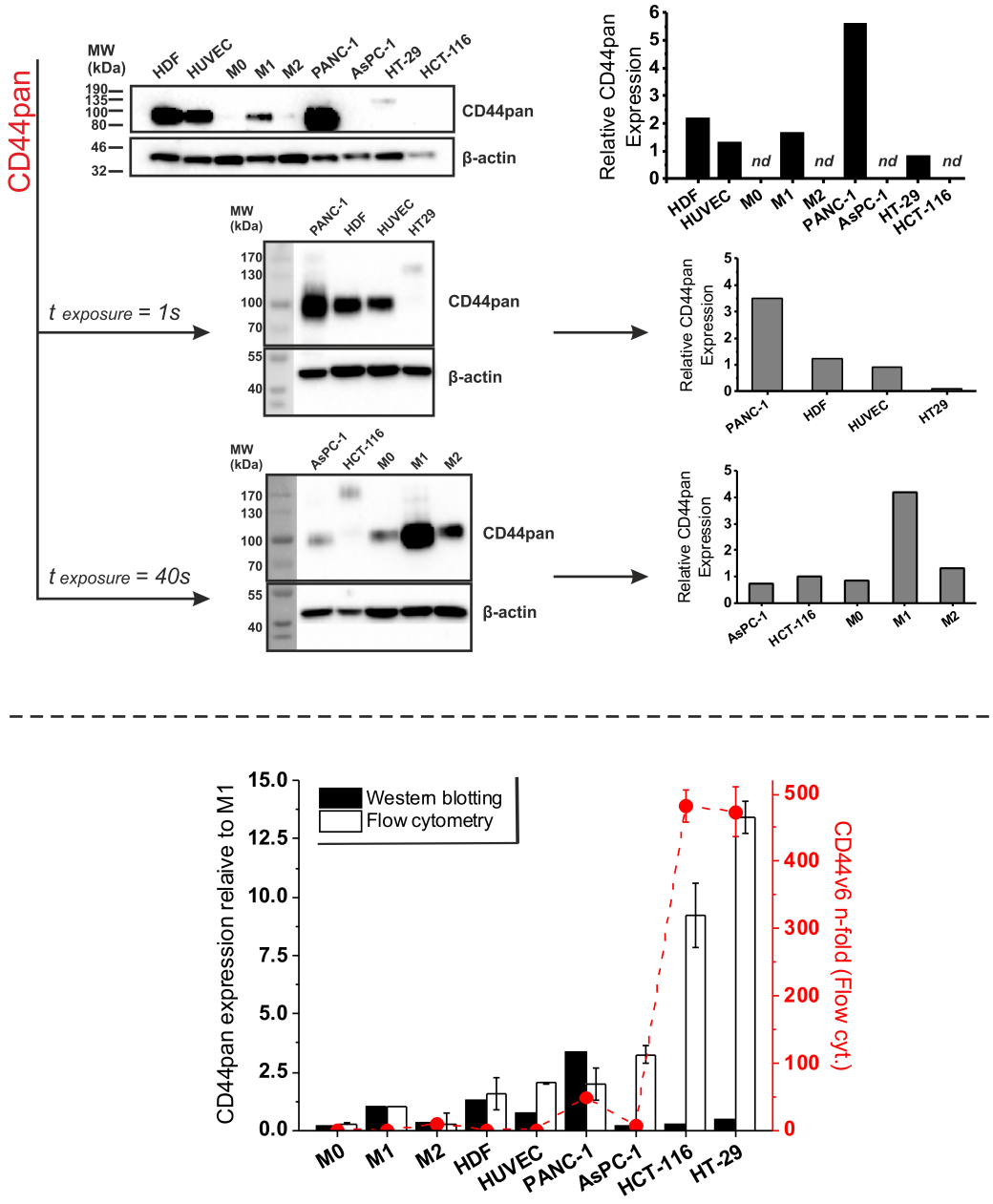

Figure 5—6. CD44 expression in target (colorectal and pancreatic cell lines) and off-target (fibroblasts, macrophages, endothelial cells) *in vitro* cellular models. ***Top:*** Representative Western blot analysis of CD44pan, detected using anti-CD44 (156-3C11) under reducing conditions and adjusting the sensitivity of the instrument to high intensity bands in order to avoid signal saturation. Please note that different exposure times were subsequently used in two separate blots to develop bands for all cellular models. For semi-quantification purposes, β-actin was used as loading control. ***Bottom:*** detection of CD44pan by Western blotting (black bars) compared to flow cytometry on live cells (white bars). The red dashed line represents the expression of CD44v6 detected via flow cytometry.

SI2. Preparation of two-fold concentrated (2X) cell culture growth media

In order to prepare 250 mL of two-fold concentrated (2X) media from powder, the following amounts were dissolved in 175 mL nuclease-free water:

- 5.95 g of McCoy's 5A powder (31800-089, Gibco®/Invitrogen, UK) - HT-29, HCT-116
- 6.75 g DMEM powder – high glucose (D777, Sigma-Aldrich, UK) - PANC-1, HDF
- 5.2 g RPMI powder (M4892, Sigma-Aldrich, UK) - AsPC-1, THP-1
- 6.8 g Opti-MEM® I powder (22600-134, Gibco®/Invitrogen, UK) - HUVEC

Upon dissolution of media powder, 3 g of HEPES (H4034, Sigma-Aldrich, UK) were added to each preparation. The pH was then adjusted to 6.4 by adding adequate volumes of HCl 0.1 M, and then nuclease-free water was added to make up to 195 mL. The resulting preparations were sterile filtered using disposable sterile filter systems 0.22 µm (Corning, UK) and supplemented accordingly (50 mL / 20% (v/v) FBS and 5 mL / 2% (v/v) antibiotic-antimycotic solution).

SI3. Internalization of siRNA-loaded nanoparticles (Flow cytometry)

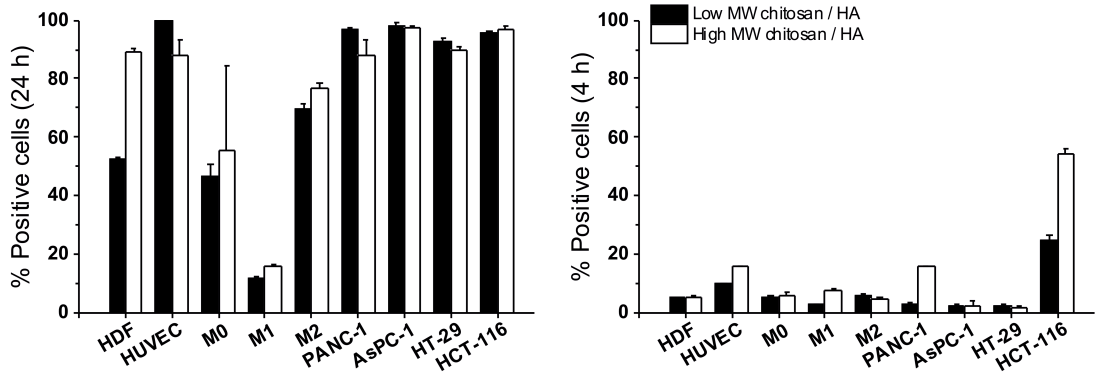

Figure 5—7. Percentage of cells positive for loaded nanoparticles upon treatment for 24 h (left) or 4 h (right). Data represented as average ± SD (n = 3).

SI4. Anti-PPIB siRNA titration on HCT-116 cells (Western blotting)

Methods. HCT-116 ($2x10^4$ cells/cm^2) were plated in Costar polystyrene 12-well plates with flat bottom (#3513, Corning, UK) and left to adhere and grow overnight Lipofectamine LTX complexed with increasing amounts of anti-PPIB siRNA in order to achieve final concentrations ranging from 10-200 nM per well. Cells were then incubated with LTX/siRNA complexes for 24 h in a humidified 5% (v/v) CO_2 air atmosphere at 37°C. LTX-containing media were aspirated, replaced with fresh complete media, and cells were allowed to rest a further 24 h. After this resting time, cells were thoroughly rinsed with PBS and lysed in 100 µL RIPA buffer supplemented with cOmpleteUltra Tablets and stored at -80°C until use. As previously described, equal amounts of protein were loaded and separated by SDS-PAGE

using a Criterion™ Cell (Run settings: 1 h, 100V, 0.5 A) and transferred to a PVDF membrane at 4ºC using a Criterion™ Blotter (Run settings: 1 h, 100 V, 0.5 A). Membranes were blocked by incubation with 5% (w/v) non-fat milk in TBS-T for 1 h at room temperature. Membranes were then cut into two sections and incubated with 1:1000 dilution in TBS-T mouse anti-human Cyclophilin B (ab74173, Abcam, UK) overnight at 4°C, or 1:5000 dilution in TBS-T mouse anti-human β-actin (ab6276, Abcam, UK) for 1 h at room temperature. Following four washings in TBS-T (15 min/wash under gentle agitation), membranes were incubated for 1 h at room temperature with goat anti-mouse IgG-peroxidase (A0168, Sigma-Aldrich, UK). Bands were detected using Clarity Western enhanced chemiluminescence (ECL) substrate with the aid of a ChemiDoc™ MP System. ImageJ software (v1.49p, http://rsb.info.nih.gov/ij) was used to perform a densitometry analysis of protein bands. Briefly, the relative expression of PPIB was determined by calculating the ratio of the band intensity for PPIB to that of the β-actin control (please note that actins are highly-conserved proteins and variations in band intensity are indicative of different protein loading between wells). Unless specified, all the products herein mention were purchased from Bio-Rad, UK.

Results and discussion. No significant effect was found at low concentrations (10-20 nM per well), while relatively high silencing values were achieved at higher concentrations (100-200 nM per well).

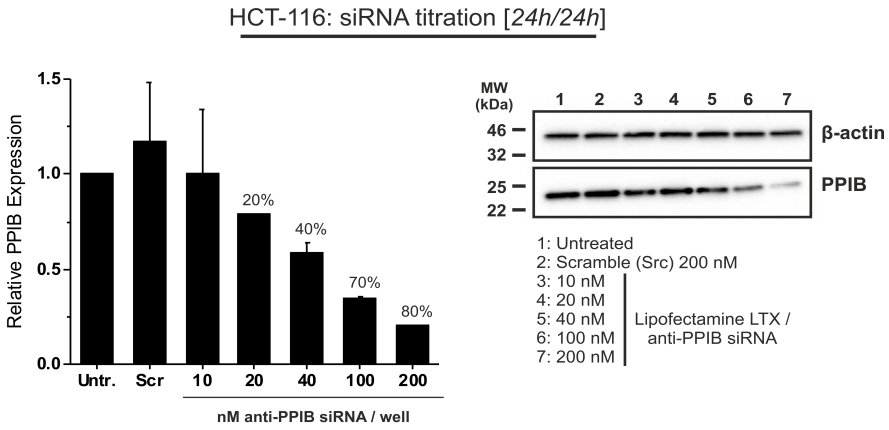

Figure 5—8. Western blot analysis of PPIB expression in HCT-116 cells at 48 h post-transfection with Lipofectamine LTX/siRNA complexes (24 h treatment, followed by 24 h resting). The intensity of PPIB protein band decreases as the amount of siRNA per well increases (10 – 200 nM). For the scramble control, 200 nM siRNA/well were used. β-actin was used as loading control. Data represented as average ± SD (n = 2).

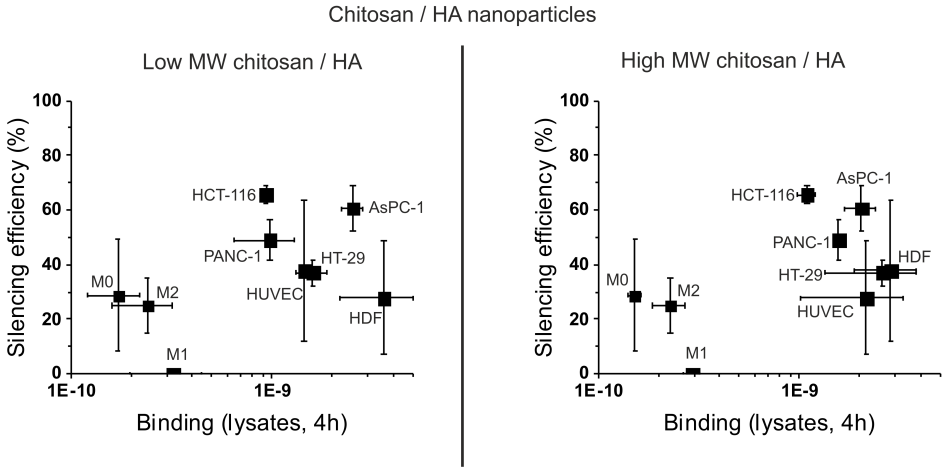

Figure 5—9. ***A.*** Cross-correlations between PPIB gene silencing and the amount of nanoparticles taken up by each cell type (cell lysates data, spanning both bound and internalized materials). All data are represented as the average ± SD (n = 3).

SI4. References

[1] F. Birzele, E. Voss, A. Nopora, K. Honold, F. Heil, S. Lohmann, H. Verheul, C. Le Tourneau, J.P. Delord, C. van Herpen, D. Mahalingam, A.L. Coveler, V. Meresse, S. Weigand, V. Runza, M. Cannarile, CD44 Isoform Status Predicts Response to Treatment with Anti-CD44 Antibody in Cancer Patients, Clin Cancer Res 21(12) (2015) 2753-2762.

Conclusion

The advent of nanoparticle-based therapies is envisioned to have a great impact on healthcare as they can confer the ability to effectively deliver new generation biologicals and preferentially target disease over healthy tissue. HA has been extensively investigated as a nanoparticle component due to its excellent biocompatibility, anionic character, tunable chemical groups, and inherent targeting capabilities.

The aim of this thesis was to optimize the preparation of chitosan/HA nanoparticles and to assess their potential as CD44-targeted RNA delivery vehicles in cancer therapy. The work presented herein addresses three key themes regarding the challenges that arise in the development of any generic HA-based carrier: (1) the clinical translatability of the nanoparticle preparation, (2) the rational selection of the carrier variables to improve nucleic acid delivery, and (3) the off-target destination of HA materials in the body. The research questions that address these themes were selected on the basis of the limited number of studies in literature dealing with the detailed study of HA nanoparticles-cell interactions and the extremely complex relationship between the expression of HA receptors (mainly CD44) in different cell types and the uptake of HA materials (i.e. how CD44 expression affects HA binding, and ultimately how binding relates to internalization). Each research question is systematically addressed in Chapters 2-5 and specifically focus on one of the three outlined themes, trying to marry these with the biological challenges of a putative CD44-targeting strategy previously raised in the literature review in Chapter 1.

(1) Clinical translatability of chitosan/HA nanoparticles

In this framework, we investigated the viability of alternative preparative methods to the mainstream multi-step chitosan/HA ionotropic gelation. In Chapter 2, we have illustrated a simplified protocol based on the direct polyelectrolyte complexation of chitosan with HA (and RNA) in water. The advantages of this preparative method are as follows:

A) it does not require the use of TPP, thus reducing the number of user-dependent operations and improving the reproducible scale up of the formulation.

B) it yields polyplexes with virtually identical physicochemical properties and biological behavior, however improving RNA cargo protection over time.

Therefore, we believe our new preparative method proves a solid and facile alternative to what has been reported in literature. This easy and scalable preparation improves

experimental reproducibility, promoting the potential use of this formulation in clinical trials in a way that guarantees the stability of the fragile RNA cargo (sterile and nuclease-free manufacturing). Nonetheless, the main limitation of this platform remains the only partial protonation of the chitosan bulk at physiological pH, which may compromise the stability of nanoparticles leading to agglomeration phenomena that dramatically reduce nanoparticle transfection efficiency, as demonstrated in Chapter 4.

Another finding derived from Chapter 2 was the strong influence of the cell type on the clustering behavior of CD44 and hence on the uptake of different $\overline{M}_v$ chitosan/HA nanoparticles. Here we have presented an update on the current knowledge of the relationship between HA exposure in drug carriers and their uptake, to which our group has greatly contributed over the past years. However, the current lack of solid experimental tools to establish quantitative links for the cell-specific clustering of CD44/protein partners around these nanoparticles limits the accurate prediction of the CD44-mediated character of these carriers in target cells.

(2) Rational design of chitosan/HA nanoparticles for RNA delivery

In Chapter 4, we have looked at the influence of the carrier and RNA payload characteristics on the nanoparticle transfection efficiency. First, we showed that a bigger RNA payload with a higher avidity for chitosan forms very stable polyplexes and relates to lower transfection efficiencies. In terms of the carrier, we found that a low chitosan DD has detrimental effects on nanoparticle stability and RNA delivery, and that a higher chitosan $\overline{M}_v$ proves beneficial to the nanoparticle transfection efficiency despite a lowest propensity for RNA release. These results complement the few studies in literature dealing with ternary chitosan nanoparticles (i.e. chitosan-RNA/HA) and in fact improve the current knowledge about the behavior of these systems as we have considered both the cargo and carrier characteristics to study their effect on the stability of the polyplexes, cargo protection, and most importantly their internalization rate (often not considered for the interpretation of nanoparticle transfection data). Nevertheless, our study is not without limitations. For example, we have not established yet a clear correlation between the carrier properties and its endosome disrupting capabilities in a manner that unequivocally marries all our findings in order to achieve an optimal carrier design.

An additional contribution of this thesis to the field is that it describes for the first time the delivery of mRNA into cancer cells using chitosan/HA nanoparticles. Although the

transfection efficiencies recorded were very low compared to those seen for Lipofectamine, these preliminary results are encouraging and invite researchers in the drug delivery field to explore the possibilities offered by these materials for further translational studies.

Last, we have also demonstrated an improved CD44-mediated delivery of RNAs at pH 6.4, which suggests suitability of these particles for intra- or peritumoral injection and overall their ability to target a physical characteristic of solid tumors. This nanoparticle behavior can be easily rationalized due to the increased protonation of the amino groups in chitosan at acidic pH; however, the deprotonation of these groups at physiological pH may indeed be the Achilles' heel of this platform, leading to aggregation phenomena that may subsequently limit their use *in vivo* (e.g. their intravenous injection).

(3) Off-target destination of HA-based carriers

The third and last key theme of this thesis is tackled through the research questions posed in Chapter 3 and Chapter 5, dealing with the inherent targeting behavior of HA materials.

On the one hand, the big question raised in Chapter 3 was whether human macrophage polarization has an effect on CD44 expression and on the different phases of HA uptake. We found an answer to this question and in fact we have reported an upregulation of CD44 in M1 macrophages and the expression of CD44v6 exclusively in M2 macrophages, pointing at its potential use as a therapeutic target. Counterintuitively, we have found that a higher CD44 expression in M1 macrophages does correlate with a higher capture, but a lower internalization of HA materials. Although we currently lack sufficient experimental evidence, another avenue study of this thesis reveals that THP-1 macrophages produce large extracellular vesicles (micron-size, putative oncosomes), which in confocal microscopy pictures appear to be much more enriched in CD44 in comparison to cell membranes. In principle, full length CD44 embedded in vesicles could either compete with cells for the binding to HA-based carriers or indeed change (even improve) the presentation of these carriers to cell membrane-anchored CD44, similarly to the hyaladherin TSG-6. In collaboration with Dr Stefano Pluchino from the University of Cambridge, we have commenced work to characterize vesicular bodies (exosomes, oncosomes) produced by differently-polarized THP-1 macrophages, with a focus on their CD44 content and putative role in the tumor microenvironment. Further understanding of the nature and role of these vesicles may open the way to the design of more efficacious CD44-targeting strategies.

On the other hand, Chapter 5 tried to investigate whether a differential expression of CD44 isoforms exists in cancer cells with respect to macrophages and stromal cells, and if this

differential expression correlates with an improved uptake of (siRNA-loaded) chitosan/HA nanoparticles. In response to this question, we have illustrated a remarkable overexpression of CD44v in colorectal cancer cells, and have predicted fibroblasts and endothelial cells to be the most likely off-target destination based on their high CD44s expression (compared to the low CD44s expression in macrophages). Intriguingly, we have found a lack of correlation between the high CD44v expression seen in HT-29 colorectal cells and the nanoparticle binding, internalization, and consequently silencing efficiency; but a very good correlation for widely approved metastatic cellular models with a rather moderate CD44 expression, such as AsPC-1 pancreatic cells, was observed. These results exemplify the biological complexity of CD44s/CD44v as described in the literature review in Chapter 1.

The contribution of these two studies to the drug delivery field are possibly the most relevant out of the whole thesis. First, we have developed an experimental protocol to study the main processes governing the uptake of HA materials (i.e. binding and internalization) based on the use of trypsin, which readily degrades surface-bound HA. This methodology accounts for a better understanding of the behavior of HA materials. For instance, it can help to differentiate whether a poor therapeutic outcome derives from a poor HA exposure on the surface of a carrier, from a poor colloidal stability leading to agglomeration, or even from the expression of CD44 isoforms inactive for the internalization of HA (e.g. due to post-translational modifications). At the same time, we have thrown a clear message that should echo in the community: the assumption that a greater CD44 expression is conducive to an increased efficacy of an HA-based therapy is too simplistic and maybe erratic. The behavior shown herein for M1 macrophages and HT-29 colorectal cells clearly supports this message; in fact, these unexpected results make us wonder whether patient stratification may be necessary in order to guarantee the success of a CD44-targeted intervention. The limitations of these studies, however, are evident: they are both based on cell lines. Whereas the use of these cellular models is justified in terms of experimental reproducibility and practicality, the verification of these phenomena requires the use of more complex cellular models (e.g. primary cells, co-culture systems, 3D culture, dynamic cell culture) and, in the last instance, the multicellular *in vivo* scenario.

Future Research

Chitosan/HA nanoparticles show great promise as carriers that may use their interactions with HA receptors (chiefly CD44) to preferentially deliver RNA payloads into cancer cells.
The results presented in this thesis should be complemented by a number of additional experiments to improve the colloidal stability of the system and to better understand the complex relationship between CD44 expression and its clustering with the capture and internalization of HA before moving on to *in vivo* experiments:

A) For the chitosan/HA platform, it would be necessary to assess feasibility of chemically or physically modifying the structure of chitosan in order to achieve an improved nanoparticle stability at physiological pH (7.4). This is possibly the most urgent action required as we have shown (in agreement with literature) that the low buffering capacity of chitosan has a negative impact on the transfection efficiency for most formulations studied.

B) For the RNA delivery, it would be required to show whether CD44 clustering around chitosan/HA nanoparticles could influence the nature of the endosomal environment (e.g. its acidity) and to determine the influence of the chitosan macromolecular variables (e.g. chitosan $\bar{M}_v$) on the kinetics of endosomal disruption; in other words, the endosomolytic activity of the nanoparticles as a function of the chitosan bulk. In the specific case of mRNA, an in-depth study regarding the selection of further chitosan variables and/or chemical modification of these polymers needs to be explored.

C) For the uptake of HA materials in human macrophages, we cannot completely rule out a THP-1 cell line-specific behavior in terms of the CD44 expression across macrophage polarization states and the subsequent effect on the uptake of HA materials. Therefore, it would be beneficial to confirm the results reported in Chapter 3 using more relevant/complex human cell models (e.g. primary macrophages, iPS-cell derived macrophages). Additionally, the mechanistic details of CD44 clustering and protein partners should be at least qualitatively understood in order to more accurately predict a targeting behavior. Last, the characterization of macrophage-derived extracellular vesicles in terms of their polarization-dependent production and amount of embedded full-length CD44 receptors proves key to understanding a potentially novel off-target destination of HA-based therapies in the body. It also opens the

door to the decoration of these vesicles with CD44-binding ligands (in particular with HA) in the search for novel, highly efficient drug delivery vehicles.

D) For the complex internalization state of CD44v, further experiments should be conducted in HT-29 and other colorectal cancer cell lines in order to elucidate the putative role of post-translational modifications (e.g. palmitoylation) in the nanoparticle internalization efficiency. Once depicted, their validation would require once again the use of more complex/physiologically relevant cancer cell models to rule out any cell line-specific phenomenon.

Chapter 6 Nanomanufacturing through microfluidic-assisted nanoprecipitation: advanced analytics and structure-activity relationships

Roberto Donno[1], Arianna Gennari[1], Enrique Lallana [1], Julio M. Rios De La Rosa[1], Richard d'Arcy[1], Kevin Treacher [3], Kathryn Hill[2], Marianne Ashford[2], Nicola Tirelli[1]

[1]North West Centre for Advanced Drug Delivery (NoWCADD), Division of Pharmacy & Optometry, School of Health Sciences, Faculty of Biology, Medicine and Health, Stopford building, Manchester, M13 9PT, United Kingdom

[2]Pharmaceutical Sciences, Innovative Medicines and Early Development, AstraZeneca, Macclesfield, SK10 2NA, United Kingdom

[3]Pharmaceutical Technology & Development, AstraZeneca, Macclesfield, SK10 2NA, United Kingdom

Manuscript accepted.

* to whom correspondence should be addressed:

Prof. Nicola Tirelli
NorthWest Centre for Advanced Drug Delivery (NoWCADD)
Division of Pharmacy and Optometry School of Health Sciences
University of Manchester Manchester, M13 9PT, UK
E-mail: nicola.tirelli@manchester.ac.uk
Tel.: +44 161 275 24 80.

6.1. Abstract

We have used microfluidics (cross-shaped chip) for the preparation of drug-loaded poly(lactic acid-co-glycolic acid) (PLGA) nanoparticles. The polymer precipitates from an acetone solution upon its controlled laminar mixing (flow focusing) with an aqueous solution of a surfactant, allowing for an operator-independent, up-scalable and reproducible preparative process of nanoformulations.

Firstly, using PEGylated surfactants we have compared batch and microfluidic processes, and showed the superior reproducibility of the latter and its strong dependency on the acetone/water ratio (flow rate ratio). We have then focused on the issue of purification from free surfactant, and employed advanced characterization techniques such as flow-through dynamic light scattering as the in-line quality control technique, and field flow fractionation (FFF) with dynamic and static light scattering detection, which allowed the detection of surfactant micelles in mixture with nanoparticles (hardly possible with stand-alone dynamic light scattering). Finally, we have shown that the choice of polymer and surfactant affects the release behaviour of a model drug (paclitaxel), with high molecular weight PLGA (RG756) and low molecular weight surfactant (tocopheryl poly(ethylene glycol) 1000 succinate, TPGS) apparently showing higher burst and accelerated release.

Keywords: asymmetric flow field flow fractionation; nanoprecipitation; microfluidics; drug delivery; Pluronic®.

6.2. Introduction

Nanoprecipitation is a common preparative method for polymer nanoparticles [1, 2]. Either this process is performed in batch or flow, an organic phase is prepared by dissolving a hydrophobic polymer in a water-miscible solvent (best results with theta solvents to approach the so-called 'Ouzo' region [3]), which is then injected into the water solution of a surfactant. By adsorbing onto the polymer aggregates, the surfactant limits the size of the particles (most commonly within hundreds of nanometres) and determines their surface chemistry. When block copolymers such as poly(ethylene glycol-*bl*-poly(lactic acid-*co*-glycolic acid)) (PEG-PLGA) are employed, no surfactant is necessary due to the inherent amphiphilicity of their structure. Finally, active pharmaceutical principles are often co-dissolved with the polymer, which upon nanoparticle formation will entrap and control their release.

In nanoprecipitation, controlling fluid dynamics is critical to achieve homogeneous (e.g. narrow size distribution) products in a reproducible fashion: the flow regime (turbulent/transition/laminar) or the lateral mixing between polymer solution and non-solvent (typically water) strongly affect the kinetics of phase separation, of particle nucleation and growth, and potentially aggregation.

Batch processes, although attractive because of lower costs and simpler set-up, can suffer from significant limitations in the uniformity and reproducibility of mixing. For example, the flow regime can be heavily dependent on factors such as the size and shape of the available agitator: the Reynolds number is proportional to the mixing length scale, which in a turbulent or transition regime is linked to the size of large energy-containing eddies and thus to the diameter of a stirrer [4-6]. Other variables are important for its effects on mixing kinetics, but often neglected; they include the rate at which the organic solution is injected into the non-solvent, and the composition of the medium during addition, which is constant in microfluidics and changes in batch.

In contrast, flow processes are considerably more reproducible, as the geometry of mixing is fixed and the flow regime is more controlled. After the pioneering work in the late 2000s from the group of Farokhzad [7, 8], microfluidic-assisted flow processes have become increasingly investigated in nanoparticle research. In addition to the more reproducible flow, other advantages of microfluidic-assisted nanoprecipitation are: 1) its operator-independent and scalable nature, 2) its rapidity, which allows to potentially screen large nanoparticle libraries [9]; 3) a significant degree of control over particle size which is chiefly using the flow rate ratio between solvent and non-solvent at the mixing point, as has been shown

extensively for PEG-PLGA precipitated in water from acetonitrile [7], for PMMA from THF [10], or for hyaluronic acid precipitated in isopropyl alcohol from water [11]. In the case of PEG-PLGA, it has been shown that also polymer concentration plays a role, with more diluted solutions yielding smaller particles [12, 13], and the magnitude of the effect depending on the solvent used [14].

PLGA nanoparticles are popular drug delivery vehicles, and are typically prepared through batch processes [15-17]. However, PLGA itself has been the subject of relatively few studies using microfluidic nanoprecipitation (e.g. from mixtures of solvents with PVA as a stabilizer [18, 19], or for in-droplet nanoprecipitation [20]), which is surprising in the light of the attention paid to PEG-PLGA. These two systems (PLGA+surfactant and PEG-PLGA) have pros and cons: the block copolymer is better suited to obtain smaller nanoparticles, while the PLGA/surfactant combination allows for easier tuning of surface chemistry without affecting the composition of the bulk. The reactive terminal groups of PEG-PLGA can allow for selective surface decoration [8], but this approach is rather laborious, since it requires both block copolymer synthesis and particle derivatization, and the latter may affect colloidal stability.

In this study, we have addressed the processability of PLGA in microfluidic-assisted nanoprecipitation, comparing commercially available (Evonik) PLGAs with different molecular weight and two surfactants (Scheme 2), studying their effect on particle size and on process variables such as the presence of free surfactant or the possibility of sterile filtration, and on the release kinetics of a model hydrophobic drug (paclitaxel, PXT).

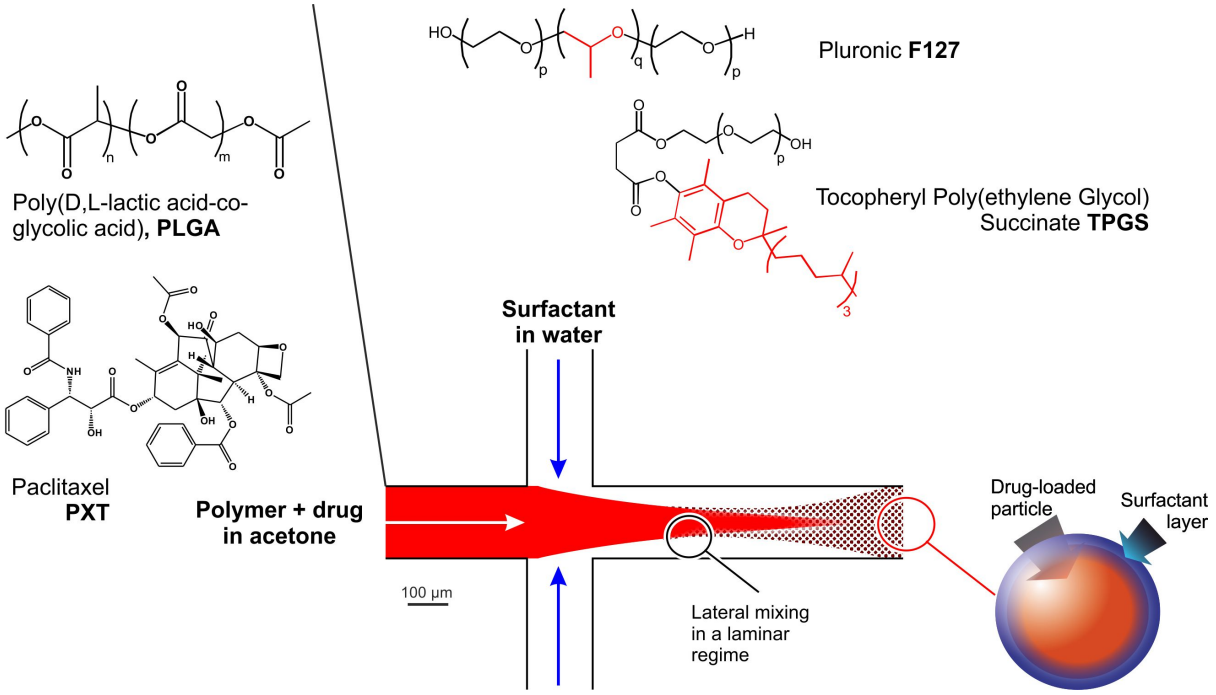

Scheme 6—1. Sketch of the process used in this study: a 3-input cross-shaped microfluidic chip was used, adding the water phase of Pluronic® or TPGS through two counter-flowing channels (blue arrows), which are perpendicular to the flow of the organic phase. The structures of PLGA and PXT (in the organic phase) and of the two surfactants (in the water phase; in red, their hydrophobic groups are shown.

Here, we have employed a cross-shaped microfluidic chip, which allows for (2D) flow focusing. Although T-shaped chips have been used for nanoparticle preparations [19], the improved drug encapsulation [18] and reduced polydispersity [7] afforded by flow focusing have popularized the cross-shaped geometry, which, with some variations is currently employed for a variety of systems [11, 13, 18].

6.3. Materials & Methods

6.3.1. Materials

RG502, RG505 and RG756S poly(D,L-lactide-*co*-glycolide) (PLGA, Resomer®, see Supporting Information, Table 1SI) were obtained from Evonik (Wembley, UK). Paclitaxel (PXT) was purchased from Apollo Scientific (Manchester, UK). Pluronic® F127 and d-α-tocopheryl poly(ethylene glycol) 1000 succinate (TPGS), Cremophor® EL, QuantiPro™ BCA assay kit, Triton X-100 and phosphate buffered saline solution (PBS, 10 mM PO_4^{3-}, pH = 7.4, D8537) were purchased from Sigma-Aldrich (Gillingham, UK). *d*6-dimethylsulfoxide (d6-DMSO) was purchased from VWR (Lutterworth, UK). Dichloromethane (DCM) and acetonitrile (HPLC grade) were purchased from Fisher Scientific (Loughborough, UK). CellTiter 96® Aqueous One Solution Cell Proliferation Assay (MTS) was provided by

Promega (Southampton, UK). Human colorectal carcinoma cell line HCT-116 (CCL-247^{TM}) was purchased from ATCC (Manassas, USA). Cells were cultured in McCoy's 5A medium supplemented with 10 % (v/v) foetal bovine serum (FBS), 2 mM L-glutamine and 1% (v/v) penicillin-streptomycin (Sigma-Aldrich) at 37˚C in a humidified 5% CO_2 air atmosphere.

6.3.2. Physico-chemical characterization

Dynamic Light Scattering (DLS): Z-average size and size polydispersity of nanoparticles were obtained by dynamic light scattering at 25˚C using a Zetasizer Nano ZS (Malvern Instrument, UK). ζ-potential of the different samples was measured with a Zetasizer Nano ZS at 25˚C. Experimental values are presented as the mean and standard deviation (n = 3). When the Zetasizer Nano ZS was used as an in-line detector connected to the microfluidic Asia 320 system (Syrris, Royston UK), the measurements were performed using a quartz flow cell (ZEN0023, Malvern Instrument, UK).

Asymmetric Flow Field-Flow Fractionation (AF4): The AF2000 TM AF4 system (Postnova Analytics, Landsberg, Germany) was coupled to UV/VIS (S3210 working at 220 nm; Laserchrom, Rochester, UK), MALLS (Viscotek SEC-MALS20; Malvern Instruments, Worcestershire, UK), refractive index (Optilab T-rEX; Wyatt Technology, Dernbach, Germany) and DLS (Zetasizer Nano SZ; Malvern) detectors in the given order. The AF4 channel was equipped with a 350 µm spacer, and a 10 kDa MWCO membrane of regenerated cellulose as the accumulation wall. A 0.02% wt. NaN_3 solution filtered through a 0.1 µm was used as eluent. In a typical experiment, the detector flow rate was set at 0.5 mL/min and 50 µL of samples were injected over 5 minutes at 0.2 mL/min with a cross flow of 1.0 mL/min and a focusing flow of 1.3 mL/min (focusing step). For the elution step, the cross flow was maintained constant at 1.0 mL/min for 0.2 min and then exponentially (exponent = 0.20) decreased to 0.1 mL/min over 40 minutes and subsequently kept at 0.1 mL/min for an additional 20 minutes, followed by a 2 min rinse step (i.e. cross flow at 0 mL/min and purge valve on). The UV/VIS, MALS and refractive index data were analysed with AF2000 software (Postnova Analytics) and fitted with a sphere model to obtain the radius of gyration distributions. The data collected by the DLS were exported by using the Zetasizer Nano software and analysed with OriginPro 8.5.1 in order to obtain the hydrodynamic radius distributions measured in flow.

Scanning Electron Microscopy (SEM): 15 µL of nanoparticle dispersions were deposited on a clean mica surface and left to dry overnight at 30°C, then sputter-coated with gold/palladium

in a Quorum SC7620 Sputter Coater (Quorum Technologies) and analysed with a FEI Quanta 250 FEG SEM. ImageJ (Wayne Rasband National Institutes of Health, USA) was employed for image analysis.

Atomic Force Microscopy (AFM): 15 μL of nanoparticle dispersions were deposited on a clean mica surface and left to dry overnight at 30°C. A Molecular Force Probe 3D AFM (MFP-3D, Asylum Research, Oxford Instruments, Abingdon, UK) equipped with an OTESPA-R3 cantilever (Bruker, Camarillo, CA, USA) was used to acquire the images in air at room temperature in tapping mode.

6.3.3. Nanoparticle preparation

Batch: the preparation of nanoparticles was carried out in 2 mL round-bottom Eppendorf tubes. 330 μL of a 0.31 % wt. RG502 acetone solution were added to 1670 μL of 0.015 % wt. F127 water solution under magnetic stirring (1000 rpm using 6 mm x 3 mm stirring bars, corresponding to a linear velocity of 0.314 m/s). The addition of the organic phase was performed using a Hamilton® glass syringes placed at different heights in the Eppendorf tube ('Top', 'Middle', 'Bottom', as described in Figure 1A); the suspension, where polymer and surfactant had a final concentration of, respectively, 0.052 % wt. and 0.013 % wt., was left under stirring for 20 min at room temperature.

Microfluidics: The automated microfluidic Asia 320 system (Syrris, Royston UK) was used for all preparations. A 5, 0.5, 0.12, 0.025 or 0.015 % wt. surfactant aqueous solution (F127 or TPGS) was mixed with a 0.31 % wt. PLGA (RG502, RG505, RG756 or a 1:1-RG502/RG505 blend) acetone solution in an Asia 1000 μL 3-input reaction chip (Syrris part number: 2100146); for drug-loaded particles, the acetone solution contained 0.015 % wt. of PXT. The flow rates were controlled to have an acetone/water flow rate ratio of 0.1, 0.2 and 0.5 and a total flow of 2 mL/min, 3 mL/min and 4 mL/min (see Table 1 for details).

For both processes, the acetone was evaporated by keeping 50 mL (for microfluidics) or 2mL (for batch) of nanoparticle suspensions under continuous agitation at 30˚C for 0.5 hours in an orbital shaker (Heidolph Incubator 1000). MilliQ water was then added in amounts equal to the volume loss, in order to maintain the initial nanoparticle concentration.

Filtration and centrifugation. Filtration was performed with 0.22 μm PES filters at room temperature. Centrifugation was typically performed on 1 mL aliquots of each suspension (8000 g for 15 mins at 4˚C, Centrifuge: accuSpin^{TM} Micro R, Fisher Scientific); the supernatant was discarded, re-suspending the pellets in 1.0 mL of MilliQ water by vortexing

for 1 min at 4˚C. The composition of the freeze-dried material was obtained via ^{1}H NMR (Bruker Avance 400 MHz, in *d*6-DMSO) using the resonances of the PPO block methyl groups at δ = 1.15-0.95 ppm (Pluronic®) and that of LA methyl groups at δ = 1.55-1.35 ppm (PLGA), and those of the PEG block at δ = 3.62-3.30 ppm (TPGS) and that of GA methylene group at δ = 5.00-4.70 ppm (PLGA), respectively for Pluronic® and TPGS-based formulations. The individual mass recovery for PLGA and surfactant was calculated from the total amount of mass recovered after freeze-drying weighted against the composition ratio obtained from the NMR analysis.

Table 6—1. Summary of the conditions used in nanoparticle preparations.

Entry	PLGA[a]	Feed conc. (% wt.)		Flow rates			Final conc. (% wt.)	
		PLGA[b]	Surf[c]	Total (μL/min)	PLGA/Surf flow ratio	PLGA (μL/min)	PLGA	Surf
1	RG502	0.31	5	2000	0.2	333	0.052	4.167
2	RG502	0.31	0.5	2000	0.2	333	0.052	0.417
3	RG502	0.31	0.12	2000	0.2	333	0.052	0.100
4	RG502	0.31	0.025	2000	0.2	333	0.052	0.021
5	RG502	0.31	0.015	2000	0.1	182	0.028	0.014
6	RG502	0.31	0.015	2000	0.2	333	0.052	0.013
7	RG502	0.31	0.015	2000	0.5	667	0.103	0.010
8	RG505	0.31	0.015	2000	0.1	182	0.028	0.014
9	RG505	0.31	0.015	2000	0.2	333	0.052	0.013
10	RG505	0.31	0.015	2000	0.5	667	0.103	0.010
11	RG756	0.31	0.015	2000	0.1	182	0.028	0.014
12	RG756	0.31	0.015	2000	0.2	333	0.052	0.013
13	RG756	0.31	0.015	2000	0.5	667	0.103	0.010
14	RG502/505	0.31	0.015	2000	0.1	182	0.028	0.014
15	RG502/505	0.31	0.015	2000	0.2	333	0.052	0.013
16	RG502/505	0.31	0.015	2000	0.5	667	0.103	0.010
17	RG502	0.31	0.015	3000	0.1	273	0.028	0.014
18	RG502	0.31	0.015	3000	0.2	500	0.052	0.013
19	RG502	0.31	0.015	3000	0.5	1000	0.103	0.010
20	RG505	0.31	0.015	3000	0.1	273	0.028	0.014
21	RG505	0.31	0.015	3000	0.2	500	0.052	0.013
22	RG505	0.31	0.015	3000	0.5	1000	0.103	0.010
23	RG756	0.31	0.015	3000	0.1	273	0.028	0.014
24	RG756	0.31	0.015	3000	0.2	500	0.052	0.013
25	RG756	0.31	0.015	3000	0.5	1000	0.103	0.010
26	RG502/505	0.31	0.015	3000	0.1	273	0.028	0.014
27	RG502/505	0.31	0.015	3000	0.2	500	0.052	0.013
28	RG502/505	0.31	0.015	3000	0.5	1000	0.103	0.010
29	RG502	0.31	0.015	4000	0.1	364	0.028	0.014
30	RG502	0.31	0.015	4000	0.2	667	0.052	0.013
31	RG502	0.31	0.015	4000	0.5	1333	0.103	0.010
32	RG505	0.31	0.015	4000	0.1	364	0.028	0.014
33	RG505	0.31	0.015	4000	0.2	667	0.052	0.013
34	RG505	0.31	0.015	4000	0.5	1333	0.103	0.010
35	RG756	0.31	0.015	4000	0.1	364	0.028	0.014
36	RG756	0.31	0.015	4000	0.2	667	0.052	0.013
37	RG756	0.31	0.015	4000	0.5	1333	0.103	0.010

38	RG502/505	0.31	0.015	4000	0.1	364	0.028	0.014
39	RG502/505	0.31	0.015	4000	0.2	667	0.052	0.013
40	RG502/505	0.31	0.015	4000	0.5	1333	0.103	0.010

[a] As reported in Supporting Information, Table 1SI, according to the supplier's information RG502 has a molecular weight in the range 7-17 kDa, RG505 54-69 kDa, RG756 76-116 kDa; RG502/505 is the 1:1 in weight blend of RG502 and RG505. RG756 has also a 75% content of lactides.
[b] Higher concentrations increased significantly both size (as also reported by Farokhzad [21]) and size dispersity to the limit of macroscopic precipitation, which e.g. occurred in 1 minute for 1.25 % wt. PLGA / 0.015% wt. Pluronic® (total flow rate = 2 mL/min, flow rate ratio = 0.2).
[c] Surfactant: F127 or TPGS

Drug loading and encapsulation efficiency. Freeze dried samples (from 2 mL of 0.22 μm-filtered suspensions) were dissolved in 100 μL acetone and vortexed to obtain a clear solution. An Agilent 1100 Series HPLC equipped with a Zorbax Eclipse XDB-C18 4.5 x 150mm 5μm column and an UV detector (UV 1575, Jasco) was used to determine the drug content [22-24]. Samples were eluted in acetonitrile – MilliQ water (50:50 v/v), with flow rate, injection volume and detection wavelength set at 1.0 mL/min, 10 μL and 260 nm, respectively. The Agilent Chemstation software (Rev.B.04.03 (16)) was used for data analysis. 10-800 μg/mL PXT solutions in acetone (retention time = 7.45 minutes) were used to build a calibration curve (linear in this concentration range (R^2 = 0.9993). The drug loading (%) was expressed as the mass of drug loaded/the total weighted mass of the freeze-dried samples x100. The encapsulation efficiency (%) was expressed as the amount of drug encapsulated/total drug added x100; the latter was not the theoretical amount, but was measured by freeze drying the samples as prepared.

6.3.4. Drug release and cell experiment

Drug release. 1 mL of 0.5 mg/mL PXT-loaded nanoparticles (corresponding to a PXT concentration in the range 16-18 μg/mL) was diluted in a Falcon tube with PBS to obtain a total final volume of 48 mL (therefore corresponding to a PXT concentration ≈ 0.3 μg/mL. PTX solubility = 0.3 μg/mL in water [25] and 0.45 μg/mL in PBS [26]) and placed in a temperature-controlled orbital shaker (Heidolph Incubator 1000) at 37°C and 150 rpm. The whole sample was used to determine the drug release at each time point (2.5, 5, 12, 24, 48, 72, 120 and 240 h), dividing it in 2 mL aliquots, centrifuging them (8000g for 15 mins at 4°C, Centrifuge: accuSpin™ Micro R, Fisher Scientific) and discarding the supernatant. The combined pellets were dissolved in 1.2 mL of acetone, dried and re-dissolved in 40 μL of acetone to provide a PXT concentration suitable for HPLC.

Cytotoxicity. HCT-116 in 200 μL of supplemented medium were seeded in 96-well plates (Corning Inc., NY, USA) at a density of $2x10^3$ cell/well. Cell viability was measured via MTS

assay and normalised against total protein content/well (BCA assay) after 24 h, 48 h, 72 h and 96 h incubation with 0.5 mg/mL PXT-loaded nanoparticles, Paclitaxel in vehicle (similar to Taxol®) and separately its vehicle Cremophor® EL/ethanol as positive controls and untreated cells as negative control. At each time point, cells were washed with PBS, adding 120 µL/well of MTS solution (prepared following manufacturer's instruction) and recording the absorbance at 490 nm after 1.5 h at 37°C (Synergy2 Biotek plate reader, Gen5 software). Cells were then washed three times with PBS and incubated for 15 min in 100 µL of lysis buffer (0.5 % Triton X-100 in PBS). 100 µL of Quantipro BCA solution (prepared following manufacturer's instruction) were added, recording the absorbance at 562 nm after 3 h of incubation at 37°C. Bovine serum albumin was used for calibration.

6.4. Results and discussion

6.4.1. Batch vs. flow nanoprecitation methods

We have compared the size and breadth of size distribution (polydispersity) of nanoparticles produced from nanoprecipitation experiments conducted in a batch process (Figure 6—1A) and in flow conditions using a cross-shaped microfluidic chip (Figure 6—1B). The geometry of this commercially available glass chip is similar to that used by Karnick *et al.* [7] and Knight *et al.* [27] for hydrodynamic flow focusing experiments, although the size of our channel is considerably larger (width ≈ 160 µm vs. respectively 20 or 10 µm).

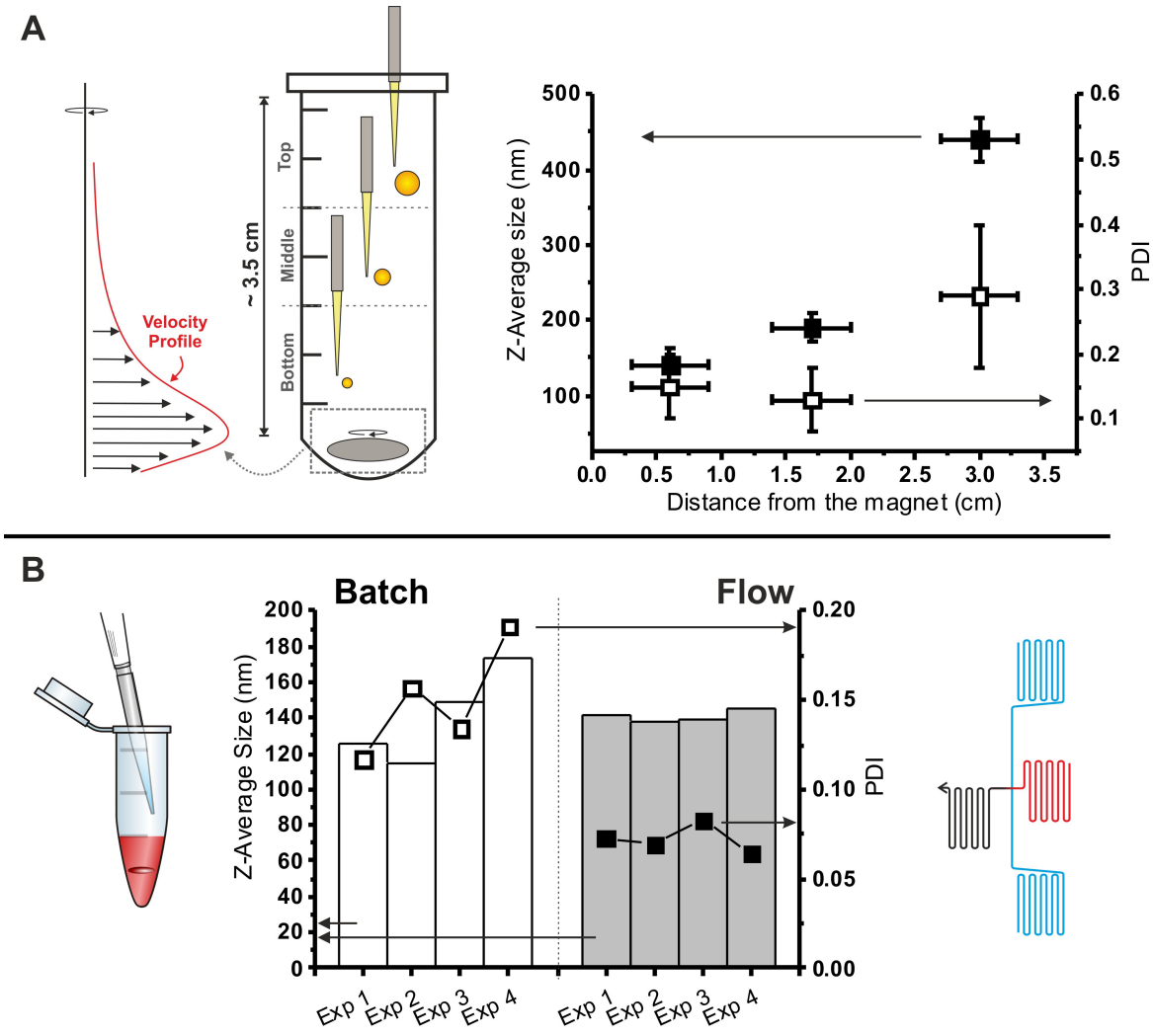

Figure 6—1. ***A.*** Sketch of the process (left) and nanoparticles characteristics (right) when the organic phase was injected in a 2 mL-round-bottom Eppendorf tube where the aqueous phase was kept under stirring by a magnet. The injection was performed at different distances from the magnet (bottom: 0.3 – 0.9 cm from the magnet; middle: 1.4 – 2.0 cm; top: 2.7 – 3.3 cm), but always within the water phase to avoid splashes at the water surface. Please note that the velocity profile (left) is just an example [4]. ***B.*** Reproducibility of size (bars) and polydispersity (symbols) of batch (left) and flow (right) nanoparticle preparations performed by the same operator on the same day under identical conditions (flow rate ratio: 0.2) using 0.052 % wt. RG502 and 0.013% wt. Pluronic® F127. Please note that in the batch method the organic phase was always injected at the constant distance of 1 cm from the magnet.

The batch process is poorly reproducible, because of the poorly controlled fluidodynamic environment. For example, when the organic phase is injected from within the water phase, the distance of the point of injection from the stirring magnet is critical and often an overlooked variable (Figure 6—1A). At the bottom of the vessel, taking into account the geometry of the magnet (d = $6x10^{-3}$ m), the kinematic viscosity of water (θ = $0.892x10^{-6}$ m^2/s) and the velocity of the stirrer (v = 0.314 m/s), one obtains Reynolds numbers ($Re = \frac{v_\theta(z)\, d}{\theta}$) of around 2100, which suggests turbulent flow [28]. If the organic solution is injected at some

distance from the magnet, the mixing process occurs under a less turbulent or possibly completely laminar regime; the lowest Re is probably that of the organic solution flowing out the injector, which is likely to be in the region of 1400. Nanoparticles formed in these regions showed both larger size (from ≈ 140 nm to ≈ 450 nm) and broader size dispersity (PDI from ≈ 0.15 to ≈ 0.3) (Figure 6—1A). This heterogeneity, however, is neither a direct effect of the decreasing Re (indeed the influence of Re on size is still debated [29]), nor the associated transition to a laminar flow regime, but rather by a poorly reproducible (and slow) precipitation due to the variable flow conditions and poor control over the lateral dimension of the organic phase during mixing. In contrast, in microfluidic channels the flow is purely laminar (Re values are most likely < 700) [7], but nevertheless the lateral mixing of a thin, focused fluid jet of the organic phase occurs rapidly. For example, using the approach of Karnik et al [7] ($\tau_{mix} \approx \frac{w^2}{9D\ (1+\frac{1}{R^2})}$, where D ≈ 10^{-9} m^2/sec is the diffusivity of water, w = 160 μm is the internal diameter of the channel in our system and R = 0.2 is the flow rate ratio), we estimate the mixing time for the systems in Figure 6—1B, *right*, to be in the order of 100 ms, which was sufficiently rapid to yield very homogeneous nanoparticles., This can be further reduced with techniques of 3D flow focusing [13]. It is noteworthy that the variable injector height is not the sole contributor to the poorly reproducible mixing of batch processes: even when it was kept constant, the variability in nanoparticle size was not entirely eliminated (Figure 6—1B, *left*).

6.4.2. Optimization of the preparative parameters

We have evaluated the influence of a number of process variables on nanoparticle size (Figure 6—2); all experiments are described in Table 6—1. In detail, we have always kept the PLGA concentration in the organic phase (0.31% wt.; larger values led to macroscopic aggregation and irregular flow) constant; we have then varied the PLGA molecular weight (RG502 < RG505 < RG756, see note *a* to Table 1; the 1:1 RG502/RG505 blend was used to obtain a broader molecular weight dispersity), the type of surfactant (Pluronic® F127, HLB ≈ 22, critical micellar concentration (CMC) = 0.725 % wt. (25 °C) [30, 31]; TPGS, HLB ≈ 13, CMC = 0.02 % wt. (37 °C) [32, 33]), the total flow rate (from 2 to 4 mL/min) and the organic/water flow rate ratio (from 0.1 to 0.5).

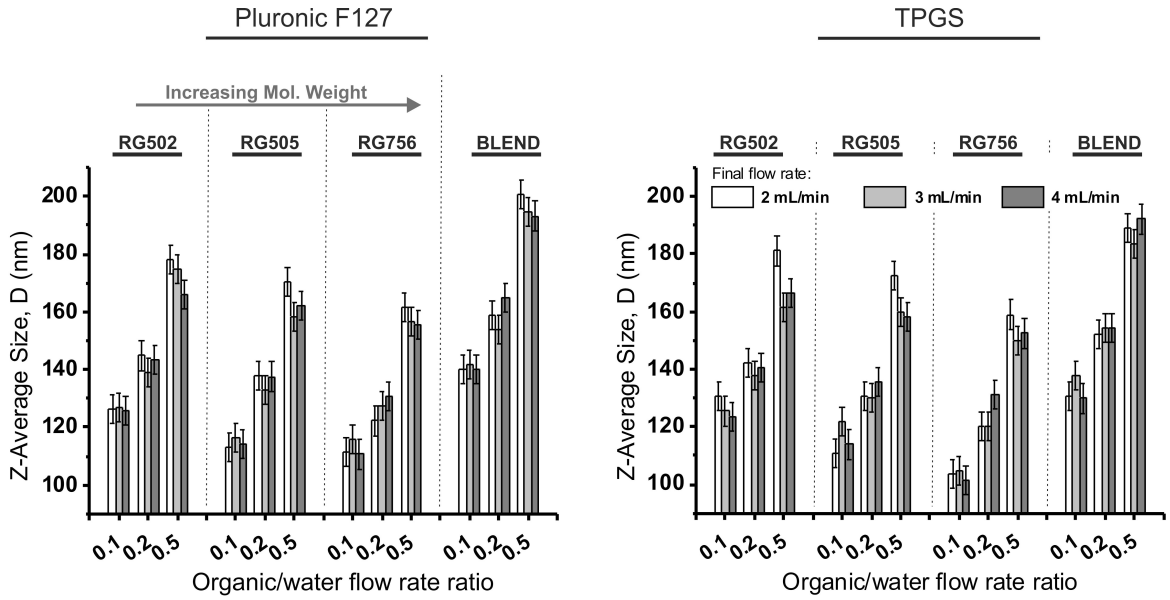

Figure 6—2. Nanoparticle size as a function of PLGA molecular weight, total flow rate and organic/water flow rate ratio in nanoprecipitation experiments performed in microfluidics, using Pluronic® F127 (***left***) or TPGS (***right***) as surfactants at a concentration of 0.010, 0.013, 0.014 % wt. for organic/water flow rate ratios 0.1, 0.2 and 0.5, respectively (entries from #5 to #40 in Table 1). Please note that before the measurement all samples were passed through a 0.22 μm-filter after acetone evaporation, unless otherwise stated.

The nanoparticle size depended very significantly (50-60 nm increase) on the flow rate ratio, which reflects the acetone/water balance at the mixing point, whereas the total flow rate had no influence on size. It is apparent that a larger presence of organic solvent (higher flow rate ratio) increased particle size, consistent with previous literature as discussed in the introduction. We ascribe the larger size primarily to a slower phase separation due to delayed mixing (from around 30 ms at a ratio=0.1 to about 600 ms at a ratio=0.5); although at this stage agglomeration due to inelastic collisions between acetone-swollen particles could not be excluded, we have substantially discounted this possibility after field flow fractionation (FFF) analysis, see later the use of AF4.

Increasing the PLGA molecular weight generally led to smaller particles (see also Figure 6—3A), which may be a reflection of a more rapid precipitation due to decreasing polymer solubility with larger molecular weight. The effect of a broader dispersity from the blended polymer produced a more pronounced effect, with much larger nanoparticles than the two polymers (RG502 and RG505) used individually. It is noteworthy that the molecular weight probably had an effect on the nanoparticle ζ potential (Figure 6—3B); for example, particles made of the smaller RG502 showed a more negative ζ potential than those made of the larger RG756, which may be due to the higher amount of terminal groups: although the two polymers are supposed to be ester terminated, a certain degree of hydrolysis is likely. However, the flow rate ratio (i.e. the acetone content) also seemed to have a major role and

the nanoparticles exhibited increasingly negative potentials with increasing flow rate ratio (and increasing particle size), although sample-to-sample comparison does not deliver statistically significant differences. We speculate that, by permitting longer-range motions of polymer chains, slower precipitation processes may allow a higher local concentration of the charged end groups at the water interface.

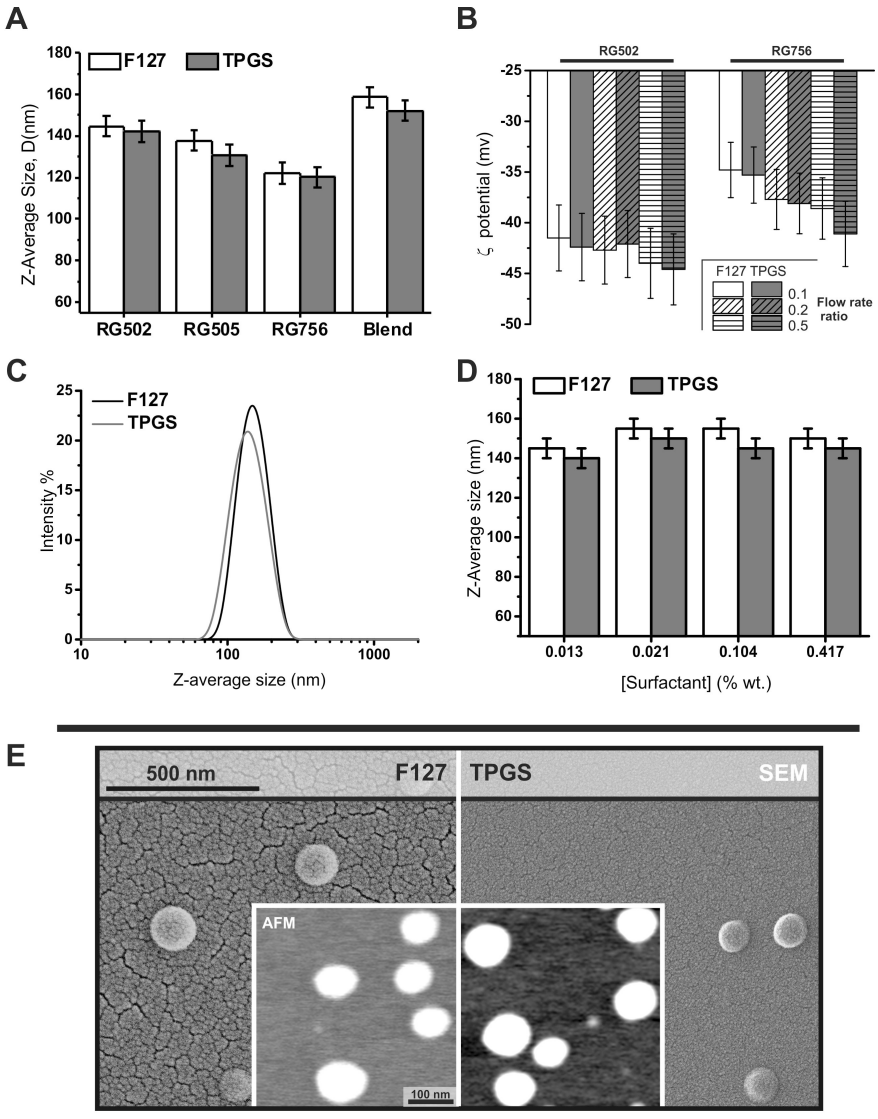

Figure 6—3. ***A.*** Z-average size of nanoparticles produced using different PLGA samples (total flow rate = 2 mL/min; organic/water flow rate ratio = 0.2, surfactant concentration 0.013% wt.; entry #6, #9, #12, #15, in Table 1). ***B.*** ζ potentials of RG502 and RG756; 0.013 % wt. Pluronic® F127 and TPGS. ***C.*** Representative examples of the size distributions (DLS) of nanoparticles produced with 0.013% wt. surfactant (entry #6, in Table 1). ***D.*** Z-average size of RG502 nanoparticles as a function of surfactant concentration; at higher concentrations, e.g. 5% wt. (see Supporting Information, Figure 6—10 top right), TPGS-containing nanoparticles still showed a similar size. ***E.*** SEM and tapping mode AFM images showing PLGA nanoparticles obtained with the two emulsifiers (entry #6, in Table 1). Please note that all samples shown were filtered through 0.22 µm PES membrane, but this approved sterilization method [34], did not have any effect on their size (see Supporting Information, Figure 1SI).

The identity of the surfactant did not appear to play any significant role on the nanoparticles (compare Figure 6—2 left and right panel, see also the complete distributions in Figure 6—3C and AFM/SEM pictures in Figure 6—3E). Using RG502, we have further investigated the effect of the amount of surfactant used, employing concentrations (0.013, 0.021, 0.104, 0.417 % wt.) that are all below the CMC of Pluronic® F127 and all above that of TPGS but one (0.013 % wt.); therefore, the former is in a soluble, non-aggregated state at the moment of mixing, while the latter is in form of micelles. The nanoparticle size, however, was not significantly affected by these chemical and physical differences (Figure 6—3D), although one may argue that TPGS provided marginally smaller sizes. It is noteworthy that at a much higher concentration (5% wt.), Pluronic® F127 seemed to produce larger nanoparticles, with an average size > 200 nm (see Supporting Information, Figure 6—10). However, this is likely to be an artefact, due to the much larger (about double) viscosity a 5% Pluronic® solution compared to water (see Supporting Information, caption to Figure 6—10); since this effect would halve the diffusion coefficient (Stokes-Einstein equation), the hydrodynamic size would appear to double. By centrifuging and re-suspending the particles the excess surfactant can be removed (see the ratio between PLGA and surfactant in Figure 6—4A and 6—4B), therefore lowering the viscosity of the medium, and indeed the size of these particles becomes indistinguishable from those obtained with Pluronic® at lower concentration and with TPGS at any concentration.

Whatever its identity, in most cases the amount of surfactant employed largely exceeded what is necessary for the nanoparticle surface coverage: using a literature estimation (4.3 nm^2/molecule [31]) for the surface area of Pluronic® F127, and 1.3 g/cm^3 as the density of PLGA, one would estimate that a tightly packed surfactant layer adsorbed a 120 nm-sized particle would account for about 16% (1:5.3) of the total mass, but at a 0.013 % wt. this excess is strongly reduced.

The point is whether it is necessary to remove this unbound surfactant: if it is above its CMC, it may produce a heterogeneous formulation with drugs being encapsulated in two differently sized and possibly differently behaving nanocarriers (micelles + nanoparticles). The toxicity of some surfactants may also be a concern, although not in the case of Pluronic® F127 and TPGS at the concentrations used in this study [35, 36]. Therefore, we now describe efforts to minimize issues caused by excess surfactants.

Firstly, we have confirmed that centrifugation removes the free surfactant. Centrifugation is often employed for nanoparticle purification [37-39], and indeed in our case pelleting and re-suspension allowed the majority of the (unbound) surfactant to be removed (Figure 6—4B,

compare solid and striped bars), without affecting the nanoparticle size distribution (Figure 6—4C). After centrifugation, it constituted only 3-5% wt. of the nanoparticle mass with no significant changes if the procedure was repeated (compare solid red and dashed black lines in Figure 6—4A), which indicates that on one hand, its layer is not very tight and, on the other, that one centrifugation step is sufficient to remove the vast majority of the free surfactant. Secondly, we have demonstrated that the excess surfactant was not needed to stabilize the particles, which after re-suspension did not undergo any significant aggregation for up to 40 days (see Supporting Information, Figure 6—11). It is worth noting, however, that during centrifugation/resuspension a significant fraction of the polymer (30-50% wt., Figure 6—4D) was lost, most likely due to incomplete redispersion and adhesion to the plastic ware. In the case of drug-loaded carriers this also implies a significant loss of active pharmaceutical principles, which, would be difficult to recycle due to requiring a separation step. It would therefore be advantageous to employ preparative conditions that do not necessarily require such a purification, in particular when, as in our case, the surfactant(s) are not toxic and can be present below their CMC.

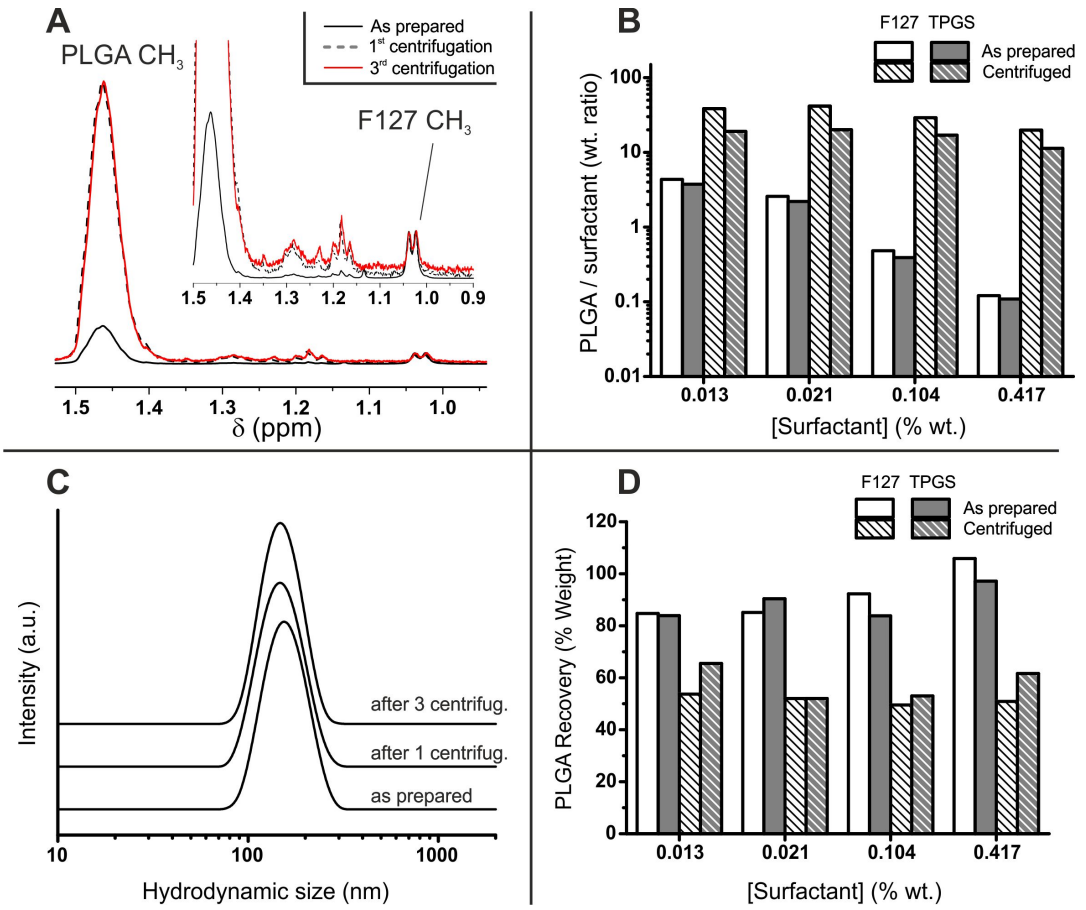

Figure 6—4. ***A.*** ^{1}H NMR spectra (area of methyl resonances) recorded in *d*6-DMSO after freeze drying RG502/Pluronic® F127 nanoparticles ([F127] = 0.013 % wt., flow rate ratio: 0.2, entry #6. PLGA recovery = 26%, PLGA/surfactant wt. ratio before and after centrifugation = 0.01 and 0.03, respectively -data not shown-) immediately after preparation (and acetone evaporation, solid black line), after filtration (dashed black line, it completely overlaps with the sold line showing that the filtration does not alter the overall composition of the formulation) and after centrifugation and resuspension (solid red line); the inset shows a magnified view of the resonance of the PLGA methyl group. ***B.*** RG502/surfactant weight ratio in the materials recovered after preparation and after centrifugation (in both cases the nanoparticles have been filtered), as a function of identity and concentration of the surfactant (flow rate ratio: 0.2). ***C.*** The size distribution (DLS) for entry #6 in Table 1 shows that the nanoparticles are substantially unaltered after a variable numbers of centrifugation steps (0, 1 and 3). ***D.*** The amount of PLGA present in the formulation can be calculated from the dry weight of the latter and knowing the PLGA/surfactant ratio; after centrifugation on average 40% of the initial material is lost, most likely due to irreversible agglomeration in the pellet or adhesion to centrifuge tube surfaces (entry #6).

Secondly, we have focused on establishing a rapid method to confirm the presence of micelles co-dispersed with nanoparticles. Unfortunately, DLS when used as a stand-alone tool was not able to detect them, even when the surfactant concentration was largely above the CMC (see for example Figure 6—5A, *top left*). This is due to the ensemble nature of DLS and the disparity in total scattering intensity of small particles or micelles compared to the larger 100-200 nm particles, which dominate the total scattering intensity ($I \propto d^6$).

In order to achieve a higher sensitivity, we have therefore employed DLS as an on-line detector for AF4 (Figure 6—5); due to the separation via FFF, colloidal objects with different

hydrodynamic size can be analyzed independently from each other, which potentially avoids artefacts due to larger nanoparticles dominating the scattering profile and hindering the analysis of smaller objects.

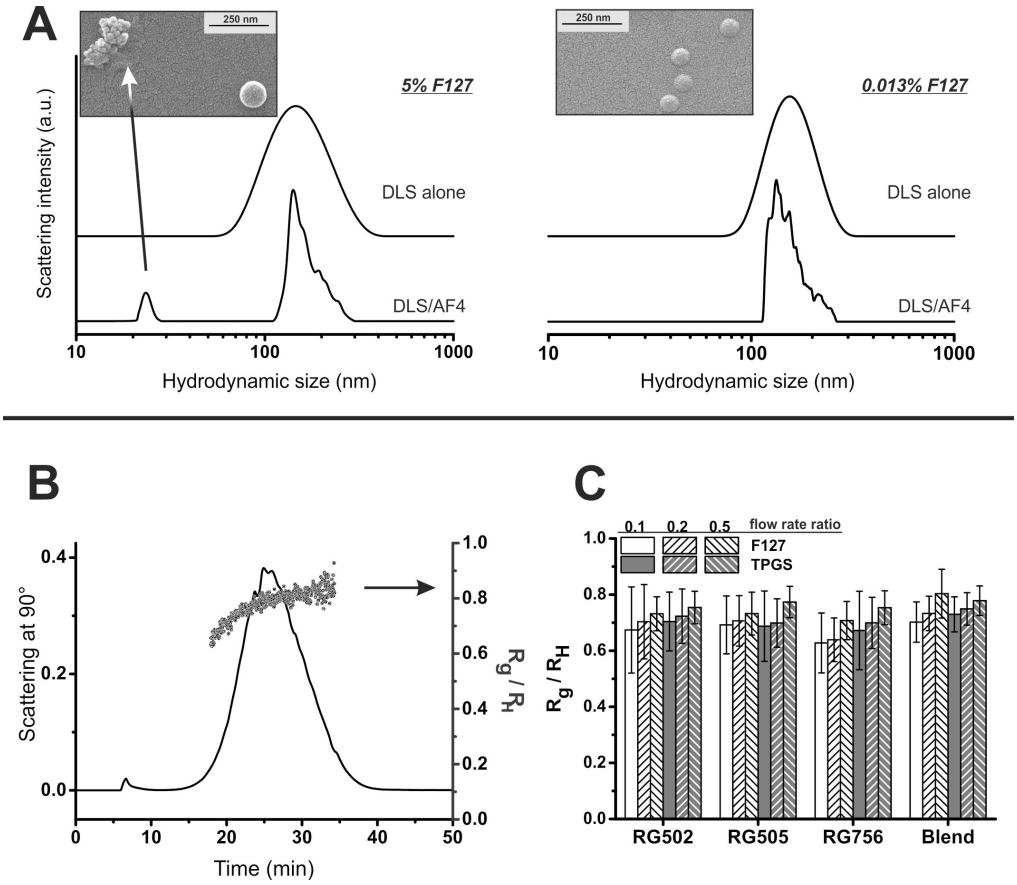

Figure 6—5. ***A.*** Size distributions obtained using DLS as a stand-alone (top graphs) and as an on-line detector for AF4 (bottom graphs) for two nanoparticle systems prepared using different Pluronic® F127 concentrations ([RG502] = 0.05 %wt., entry #1 and #6). At 5% wt. Pluronic® (in the water phase feed, corresponding to a final concentration of 4.167 % wt., i.e. above its CMC) and before centrifugation (after acetone evaporation), a peak at around 25 nm can be seen, and correspondingly aggregates of similarly small objects can be spotted in SEM images. At low surfactant concentration (0.015 % wt. feed, corresponding to a final concentration of ≈ 0.013 % wt., well below CMC), no peak was detected in AF4 and correspondingly only nanoparticles were seen in SEM. ***B.*** Scattering intensity at 90° (static light scattering) and Rg/R_H ratios from the FFF analysis (MALLS, UV and DLS used as detectors) of #6 entry. The shape factor is relatively constant throughout the size distribution. ***D.*** Rg/R_H ratios for various formulations (entries from #5 to #16 in Table 1): all values are close to 0.7, indicating spherical particles. Please note that data are reported as the time averaged R_g/R_h value and standard deviation recorded in one elution.

Indeed, AF4/DLS was able to show the presence of the Pluronic® F127 micelles when above its CMC (Figure 6—5A, left), and their absence below the CMC (Figure 6—15B, *right*), whereas DLS alone was unable to detect them in both conditions (compare top and bottom curves). Incidentally, due to the more reliable size distributions obtained via FFF, it is possible to confirm that nanoparticles are of low polydispersity: 85-90% (depending on the system) of the intensity distribution is contained in the 100-200 nm interval.

To our knowledge, this is one of the first examples of AF4 being successfully applied to the analysis of heterogeneous colloidal mixtures [40]; its possibly most important advantage over stand-alone DLS is the more accurate hydrodynamic size distribution, but it should be noted that the DLS short analysis times are also advantageous and allow it to be used as an in-line detector for the microfluidic-assisted nanoprecipitation process (Figure 6—6). Another strength of AF4 analysis is the ability to combine DLS with multi-angle static light scattering; the resulting shape factor (defined as the Rg/R_H ratio, see Figure 6—5B) distribution is important to assess the morphological homogeneity of the nanoparticles: if nanoparticles form and then later aggregate in clusters, the corresponding shape factor is expected to be significantly larger than that of a perfect sphere (0.775 [41]). In our preparations, its values were always comprised in the 0.67-0.8 interval, independent of the identity of the surfactant and of the PLGA used (Figure 6—5C); this discounts the hypothesis that particles obtained at high acetone content may have a larger size due to late aggregation in the microfluidic channels (see above).

Finally, for all further experiments we have chosen to employ nanoparticle formulations produced with a Pluronic® or TPGS concentration in the feed of 0.015% wt. (overall 0.013% wt. in the nanoparticle dispersions, entries #6 and #12 in Table 6—1), without purifying them via centrifugation in order to minimize the loss of material.

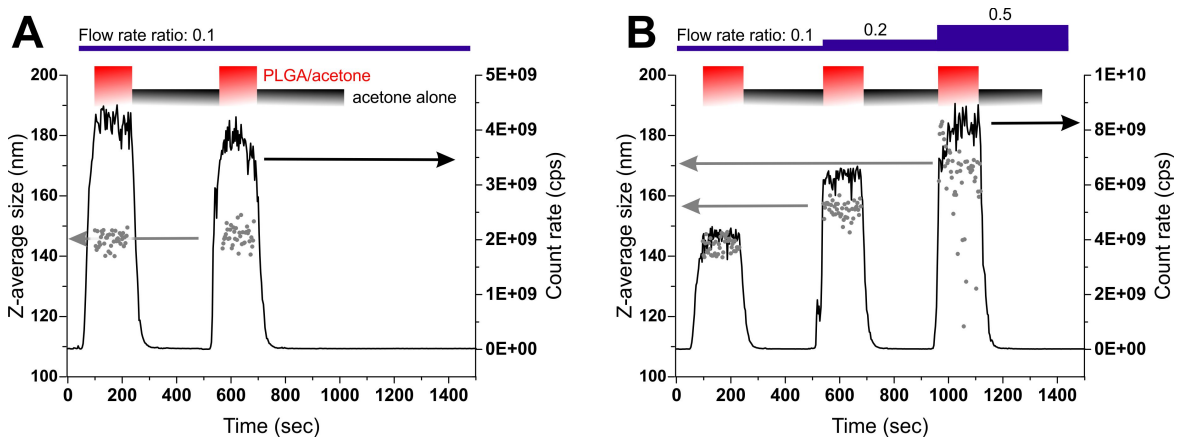

Figure 6—6. DLS measurements performed in-line during microfluidic-assisted nanoprecipitation experiments (flow-through cell sequentially connected to the microfluidic chip). *A.* Reproducibility: the feed of the organic phase was repeatedly alternated from pure acetone to a PLGA acetone solution (entry #5 in Table 1), without significantly affecting the average size (left) and the scattering intensity (right) of the nanoparticles in the mixed 1:10 acetone/water environment. *B.* Tunability: in successive polymer/no polymer alternations, the flow rate ratio was increased (entries #5, #6 and #7 in Table 1), showing the expected increase in nanoparticle size (and scattering intensity).

Under these conditions, free surfactant is still present in the dispersion (about 70-80% of their total amount; compare before and after centrifugation at 0.013 % wt. surfactant in Figure 6—4B), but this is hardly a concern: their low concentration ensures both the absence of micelles (confirmed by AF4) and a negligible toxicity. Clearly, should surfactants with lower CMC, higher toxicity, and/or presence of cell-targeting ligands be used, purification via centrifugation would become necessary.

6.4.3. Drug release

PXT was co-solubilized with PLGA in the acetone phase at a concentration corresponding to a 5% wt. theoretical loading. This achieved encapsulation efficiencies around 65-70%; the resulting PXT concentration of 3-3.5% wt. is probably close to its maximum solubility in PLGA, since higher PXT concentration in the feed led to markedly lower efficiencies (data not shown). The presence of PXT did not affect nanoparticle size and ζ-potential, independent of the polymer or surfactant used (Table 6—2).

Table 6—2. Physico-chemical characteristics, PXT loading and encapsulation efficiency of drug-loaded nanoparticles.

System	Size (nm)	ζ potential (mV)	Theor. loading (%wt.)	Actual loading (%wt.)	EE (%) [a]	τ_1 (h) [b]	τ_2 (h) [b]	Early/ late release [c]	Burst (%) [d]
F127/RG502	145±5	-43±3	5	3.5	70	11±8	57±70	1.4±2.3	27±14
F127/RG756	120±5	-38±3	5	3.3	66	9±3	86±120	2.3±1.5	26±12
TPGS/RG502	140±5	-42±3	5	3.2	65	5±2	93±35	0.9±0.2	32±8
TPGS/RG756	120±5	-38±3	5	3.6	73	6±1	94±18	2.0±0.2	35±2

[a] Encapsulation efficiency.

[b] The release kinetics was fitted with a double exponential equation of the kind of $[y]_t = [y]_\infty - A_1 \exp\left(-\frac{t}{\tau_1}\right) - A_2 \exp\left(-\frac{t}{\tau_2}\right)$ where [y] is the drug released as a function of time, τ_1 and τ_2 are the characteristic times of the two regimes, and A_1 and A_2 the amounts of drugs correspondingly released. The SDs are obtained by fitting sets of data obtained from three independent measurements per time point (8 time points between 0 and 240 hours). It is noticeable that the data for Pluronic®-containing nanoparticles have a higher SD. The data were fitted using the double exponential decay function (Levenberg Marquardt iteration algorithm) of OriginPro 2015.

[c] Calculated as A_1 / A_2.

[d] Calculated as $100 * ([y]_\infty - A_1 - A_2)/[y]_\infty$.

The PXT release was monitored under sink conditions, it always showed a first order-like kinetics. However, it also significantly deviated from a classical, single exponential behaviour (black dashed curve in Figure 6—6B), which we ascribe to the incipient degradation of the PLGA matrix: upon cleavage of a sizeable number of esters, both the bulk density of hydrophilic groups and the water content increase, eventually leading to matrix plasticization

and thus to higher diffusion coefficient of PXT. A much better fit is obtained with a double exponential model (red curve in Figure 6—7B; equation provided in note b to Table 6— 2), where the second exponential reflects the long-term (> 2 days) release behavior. It should be noted that the second exponential provides a time-averaged picture of a continuous process (degradation) and its characteristic time is typically affected by very large errors, therefore the physical meaning of its parameters should not be over-estimated.

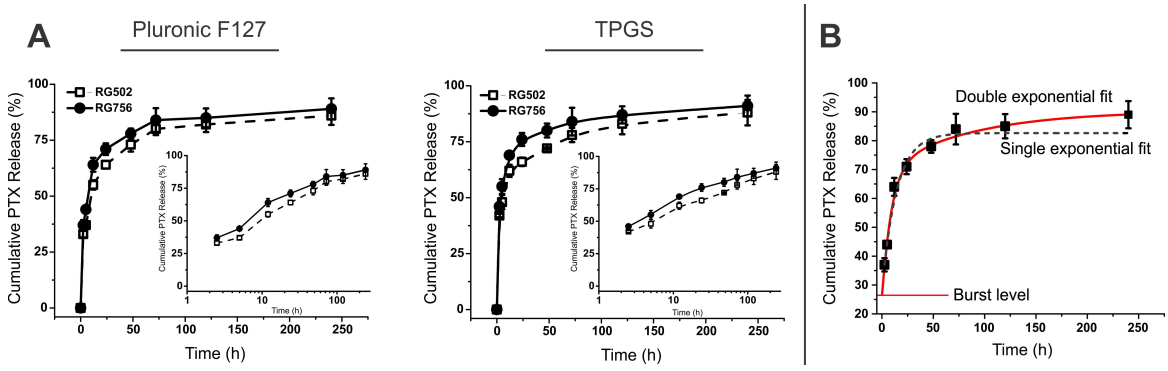

Figure 6—7. ***A***. Drug release profiles for the four nanoparticle systems; the insets report the same data using a semi-log presentation (logarithmic time scale) to show the first-order-like ***B.*** Comparison between experimental release data (F127/RG756 nanoparticles) and fits with single (dashed black line) and double exponential (solid red line).

It is noticeable that:

a) the initial release rate (τ_1) and the burst (extrapolated drug released at time = 0) seem to be respectively slower and smaller with Pluronic® F127. This result, speculatively due to the establishment of a better barrier against diffusion into the water phase, would indicate F127 to be slightly better suited for a sustained release profile. The differences, however, are not sufficiently large to be statistically relevant;

b) the ratio between drug released in the early and in the late phase was higher for RG756 than for RG502, suggesting the latter polymer is somewhat superior for a more sustained release. Nanoparticles of the two polymers were loaded with similar amounts of PXT (Table 6—2), therefore this effect cannot be simply ascribed to different PXT solubilization in the two matrices.

Therefore, it would appear that the presence of TPGS and that of RG756 may increase the amount of early-released drug, although the differences with other formulations are relatively small. We have sought to confirm this point in cell experiments, using HCT-116 as an *in vitro* model, and a formulation identical to Taxol® as a positive control and PXT concentrations ranging from 0.025 to 25 μg/mL (see Supporting Information, Figure 6—12). Indeed, at the

lowest PXT concentration (0.025 μg/mL) and at times < 48 h TPGS/RG756 showed a cytotoxicity similar to that of paclitaxel/Cremophor® EL and higher than the other PXT-loaded PLGA nanoparticles (Figure 6—8A), which we link to the more rapid release of PXT. On the other hand, at longer times and at higher concentrations, all formulations are virtually indistinguishable, most likely because of approaching the solubility of free PXT in the medium.

It is also worth mentioning that, independent of the polymer and surfactant used, that the (non-drug-loaded) PLGA nanoparticles had a much more favorable cytotoxicity profile than Cremophor® EL which is used as a solubilizer in Taxol® (Figure 6—8B).

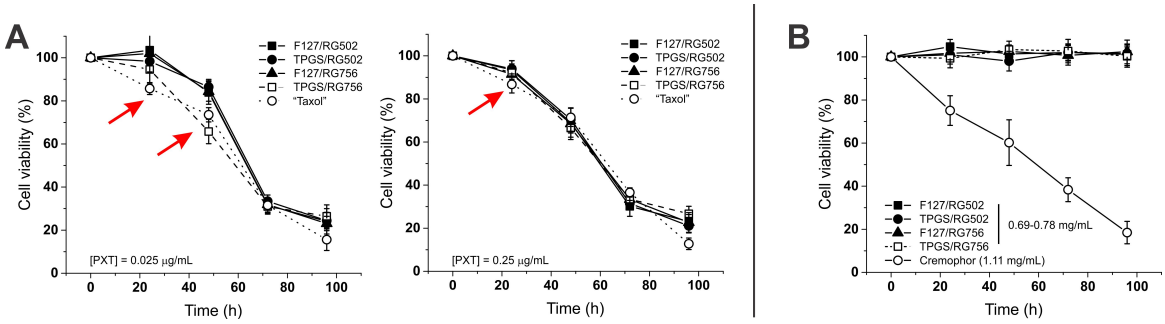

Figure 6—8. ***A.*** HCT-116 viability as a function of time upon exposure to drug-loaded nanoparticles or PXT/Cremophor® EL (similar to Taxol®) at a PXT concentration of 0.025 (left) and 0.25 μg/mL (right). The red arrows indicate the time points when some formulations are significantly more toxic than others; at a 0.25 μg/mL concentration, only PXT/Cremophor® EL at 24 h present a higher toxicity, whereas at higher PXT concentrations all formulations showed the same toxicity at all times. ***B.*** Viability (mitochondrial reductase activity (MTS) normalized against the protein content (BCA assay) to yield a metabolic activity 'per cell') of HCT-116 cells as a function of time upon incubation with similar concentrations of PLGA nanoparticles (no PXT) and Cremophor® EL. The carrier concentrations correspond to those employed in later experiments with a PXT concentration of 25 μg/mL, which was the highest employed in this study.

6.5. Conclusions

PLGA was processed in microfluidic-assisted nanoprecipitation to yield drug-loaded, PEGylated particles with narrow size distribution and a size that depended primarily on the flow rate ratio (water/acetone ratio). We showed that DLS can be used as an in-line quality control tool, and that field flow fractionation (with dynamic and static light scattering detection) allowed for a very accurate colloidal analysis, by providing reliable size and shape factor distributions, and highlighting the presence of surfactant micelles. Finally, the choice of polymer and surfactant had a measurable, although not very large influence on the short-term release of PXT, with higher molecular weight of the PLGA and smaller size of the surfactant apparently causing larger bursts and accelerating the short-term release kinetics.

6.6. Acknowledgments

This work was supported by AstraZeneca through the establishment of the NorthWest Centre of Advanced Drug Delivery (NoWCADD) at the University of Manchester. AFM and SEM images were acquired at the BioAFM and at the Bioimaging facilities (University of Manchester), respectively. The authors would like to thank Dr Tobias Starborg, Christopher Leon Valdivieso and Iwan Roberts for useful discussions about SEM images, and Dr Nigel Hodson for useful discussions about AFM images. Dr. Gennari, Mr. Rios de la Rosa and Dr. d'Arcy acknowledge financial support respectively from financial support from the EU FP7 project UniVax (grant number 601738), the North-West Nanoscience (NoWNano) Doctoral Training Centre (EPSRC grant EP/G03737X/1) and EPSRC for a Doctoral Prize Fellowship.

6.7. References

[1] S.M. D'Addio, R.K. Prud'homme, Controlling drug nanoparticle formation by rapid precipitation Adv Drug Deliver Rev 63(6) (2011) 417-426.

[2] S. Schubert, J.T. Delaney, U.S. Schubert, Nanoprecipitation and nanoformulation of polymers: from history to powerful possibilities beyond poly(lactic acid), Soft Matter 7(5) (2011) 1581-1588.

[3] E. Lepeltier, C. Bourgaux, P. Couvreur, Nanoprecipitation and the "Ouzo effect": Application to drug delivery devices, Adv Drug Deliver Rev 71 (2014) 86-97.

[4] M. Ciofalo, A. Brucato, F. Grisafi, N. Torraca, Turbulent flow in closed and free-surface unbaffled tanks stirred by radial impellers, Chem Eng Sci 51(14) (1996) 3557-3573.

[5] T. Kumaresan, J.B. Joshi, Effect of impeller design on the flow pattern and mixing in stirred tanks, Chem Eng J 115(3) (2006) 173-193.

[6] T. Mahmud, J.N. Haque, K.J. Roberts, D. Rhodes, D. Wilkinson, Measurements and modelling of free-surface turbulent flows induced by a magnetic stirrer in an unbaffled stirred tank reactor, Chem Eng Sci 64(20) (2009) 4197-4209.

[7] R. Karnik, F. Gu, P. Basto, C. Cannizzaro, L. Dean, W. Kyei-Manu, R. Langer, O.C. Farokhzad, Microfluidic platform for controlled synthesis of polymeric nanoparticles, Nano Lett 8(9) (2008) 2906-2912.

[8] N. Kolishetti, S. Dhar, P.M. Valencia, L.Q. Lin, R. Karnik, S.J. Lippard, R. Langer, O.C. Farokhzad, Engineering of self-assembled nanoparticle platform for precisely controlled combination drug therapy, Proc Natl Acad Sci U.S.A. 107(42) (2010) 17939-17944.

[9] P.M. Valencia, O.C. Farokhzad, R. Karnik, R. Langer, Microfluidic technologies for accelerating the clinical translation of nanoparticles, Nat Nanotechnol 7(10) (2012) 623-629.
[10] N. Anton, F. Bally, C.A. Serra, A. Ali, Y. Arntz, Y. Mely, M.J. Zhao, E. Marchioni, A. Jakhmola, T.F. Vandamme, A new microfluidic setup for precise control of the polymer nanoprecipitation process and lipophilic drug encapsulation, Soft Matter 8(41) (2012) 10628-10635.
[11] R.C.S. Bicudo, M.H.A. Santana, Production of hyaluronic acid (HA) nanoparticles by a continuous process inside microchannels: Effects of non-solvents, organic phase flow rate, and HA concentration, Chem Eng Sci 84 (2012) 134-141.
[12] J.M. Lim, N. Bertrand, P.M. Valencia, M. Rhee, R. Langer, S. Jon, O.C. Farokhzad, R. Karnik, Parallel microfluidic synthesis of size-tunable polymeric nanoparticles using 3D flow focusing towards in vivo study, Nanomed-Nanotechnol 10(2) (2014) 401-409.
[13] M. Rhee, P.M. Valencia, M.I. Rodriguez, R. Langer, O.C. Farokhzad, R. Karnik, Synthesis of Size-Tunable Polymeric Nanoparticles Enabled by 3D Hydrodynamic Flow Focusing in Single-Layer Microchannels, Adv Mater 23(12) (2011) H79-H83.
[14] J. Cheng, B.A. Teply, I. Sherifi, J. Sung, G. Luther, F.X. Gu, E. Levy-Nissenbaum, A.F. Radovic-Moreno, R. Langer, O.C. Farokhzad, Formulation of functionalized PLGA-PEG nanoparticles for in vivo targeted drug delivery, Biomaterials 28(5) (2007) 869-876.
[15] T. Betancourt, B. Brown, L. Brannon-Peppas, Doxorubicin-loaded PLGA nanoparticles by nanoprecipitation: preparation, characterization and in vitro evaluation, Nanomedicine-UK 2(2) (2007) 219-232.
[16] C. Fonseca, S. Simoes, R. Gaspar, Paclitaxel-loaded PLGA nanoparticles: preparation, physicochemical characterization and in vitro anti-tumoral activity, J Control Release 83(2) (2002) 273-286.
[17] T. Govender, S. Stolnik, M.C. Garnett, L. Illum, S.S. Davis, PLGA nanoparticles prepared by nanoprecipitation: drug loading and release studies of a water soluble drug, J Control Release 57(2) (1999) 171-185.
[18] L. Martin-Banderas, E. Saez-Fernandez, M.A. Holgado, M.M. Duran-Lobato, J.C. Prados, C. Melguizo, J.L. Arias, Biocompatible gemcitabine-based nanomedicine engineered by Flow Focusing (R) for efficient antitumor activity, Int J Pharm 443(1-2) (2013) 103-109.
[19] H. Xie, Z.G. She, S. Wang, G. Sharma, J.W. Smith, One-Step Fabrication of Polymeric Janus Nanoparticles for Drug Delivery, Langmuir 28(9) (2012) 4459-4463.

[20] L.H. Hung, S.Y. Teh, J. Jester, A.P. Lee, PLGA micro/nanosphere synthesis by droplet microfluidic solvent evaporation and extraction approaches, Lab Chip 10(14) (2010) 1820-1825.

[21] J. Cheng, B.A. Teply, I. Sherifi, J. Sung, G. Luther, F.X. Gu, E. Levy-Nissenbaum, A.F. Radovic-Moreno, R. Langer, O.C. Farokhzad, Formulation of functionalized PLGA-PEG nanoparticles for in vivo targeted drug delivery, Biomaterials 28(5) (2007) 869-76.

[22] Y.M. Wang, H. Sato, I. Adachi, I. Horikoshi, Preparation and characterization of poly(lactic-co-glycolic acid) microspheres for targeted delivery of a novel anticancer agent, taxol, Chemical & pharmaceutical bulletin 44(10) (1996) 1935-40.

[23] C. Fonseca, S. Simoes, R. Gaspar, Paclitaxel-loaded PLGA nanoparticles: preparation, physicochemical characterization and in vitro anti-tumoral activity, Journal of controlled release : official journal of the Controlled Release Society 83(2) (2002) 273-286.

[24] F. Danhier, N. Lecouturier, B. Vroman, C. Jerome, J. Marchand-Brynaert, O. Feron, V. Preat, Paclitaxel-loaded PEGylated PLGA-based nanoparticles: In vitro and in vivo evaluation, J Control Release 133(1) (2009) 11-17.

[25] S.C. Lee, K.M. Huh, J. Lee, Y.W. Cho, R.E. Galinsky, K. Park, Hydrotropic polymeric micelles for enhanced paclitaxel solubility: In vitro and in vivo characterization, Biomacromolecules 8(1) (2007) 202-208.

[26] A. Finkelstein, D. McClean, S. Kar, K. Takizawa, K. Varghese, N. Baek, K. Park, M.C. Fishbein, R. Makkar, F. Litvack, N.L. Eigler, Local drug delivery via a coronary stent with programmable release pharmacokinetics, Circulation 107(5) (2003) 777-784.

[27] J.B. Knight, A. Vishwanath, J.P. Brody, R.H. Austin, Hydrodynamic focusing on a silicon chip: Mixing nanoliters in microseconds, Phys Rev Lett 80(17) (1998) 3863-3866.

[28] H. Song, J.D. Tice, R.F. Ismagilov, A microfluidic system for controlling reaction networks in time, Angewandte Chemie 42(7) (2003) 768-72.

[29] B. Herranz-Blanco, E. Ginestar, H.B. Zhang, J. Hirvonen, H.A. Santos, Microfluidics platform for glass capillaries and its application in droplet and nanoparticle fabrication, International Journal of Pharmaceutics 516(1-2) (2017) 100-105.

[30] R. Basak, R. Bandyopadhyay, Encapsulation of hydrophobic drugs in Pluronic F127 micelles: effects of drug hydrophobicity, solution temperature, and pH, Langmuir 29(13) (2013) 4350-6.

[31] Y.N. Lin, P. Alexandridis, Temperature-dependent adsorption of pluronic F127 block copolymers onto carbon black particles dispersed in aqueous media, J Phys Chem B 106(42) (2002) 10834-10844.

[32] Y.Y. Guo, J. Luo, S.W. Tan, B.O. Otieno, Z.P. Zhang, The applications of Vitamin E TPGS in drug delivery, Eur J Pharm Sci 49(2) (2013) 175-186.
[33] Z.P. Zhang, S.W. Tan, S.S. Feng, Vitamin E TPGS as a molecular biomaterial for drug delivery, Biomaterials 33(19) (2012) 4889-4906.
[34] European-Medicine-Agency, Guideline on the sterilisation of the medicinal product, active substance, excipient and primary container, (2016).
[35] S.F. Khattak, S.R. Bhatia, S.C. Roberts, Pluronic F127 as a cell encapsulation material: Utilization of membrane-stabilizing agents, Tissue Eng 11(5-6) (2005) 974-983.
[36] A. Yan, A. Von Dem Bussche, A.B. Kane, R.H. Hurt, Tocopheryl polyethylene glycol succinate as a safe, antioxidant surfactant for processing carbon nanotubes and fullerenes, Carbon 45(13) (2007) 2463-2470.
[37] B. Kowalczyk, I. Lagzi, B.A. Grzybowski, Nanoseparations: Strategies for size and/or shape-selective purification of nanoparticles, Curr Opin Colloid In 16(2) (2011) 135-148.
[38] J.P. Novak, C. Nickerson, S. Franzen, D.L. Feldheim, Purification of molecularly bridged metal nanoparticle arrays by centrifugation and size exclusion chromatography, Anal Chem 73(23) (2001) 5758-5761.
[39] J.M. Chan, L.F. Zhang, K.P. Yuet, G. Liao, J.W. Rhee, R. Langer, O.C. Farokhzad, PLGA-lecithin-PEG core-shell nanoparticles for controlled drug delivery, Biomaterials 30(8) (2009) 1627-1634.
[40] P. Iavicoli, P. Urban, A. Bella, M.G. Ryadnov, F. Rossi, L. Calzolai, Application of Asymmetric Flow Field-Flow Fractionation hyphenations for liposome-antimicrobial peptide interaction, J Chromatogr A 1422 (2015) 260-269.
[41] J.P. Patterson, M.P. Robin, C. Chassenieux, O. Colombani, R.K. O'Reilly, The analysis of solution self-assembled polymeric nanomaterials, Chem Soc Rev 43(8) (2014) 2412-2425.,

6.8. Supporting Information

Table 6—3. Resomer® PLGAs used in this study.

Prod. No.	RESOMER®	Lactide/glycolide molar ratio [a]	Molecular weight range (kDa) [a]	Inherent viscosity (dl/g) [a]	Tg (°C) [a]	End group [a]
719889	RG 502	50:50	7-17	0.16-0.24	42-46	Alkyl ester
739960	RG 505	50:50	54-69	0.61-0.74	48-52	Ester
719927	RG 756S	75:25	76-116	0.71-1.0	49-55	Ester terminated

[a] according to supplier specifications

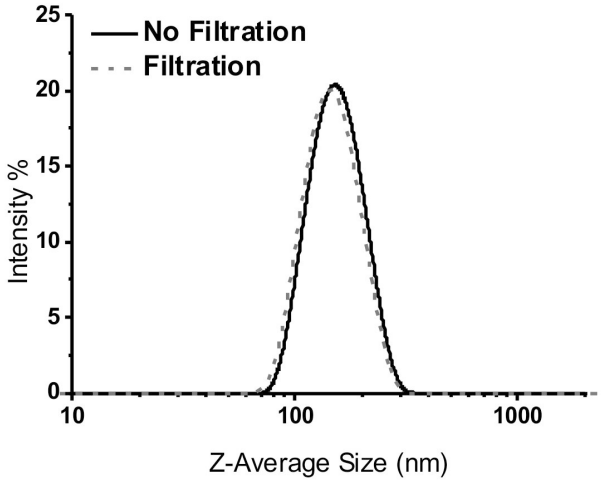

Figure 6—9. Size distribution of RG502 nanoparticles (entry #6, surfactant = TPGS) before and after sterile filtration (0.22 μm pores).

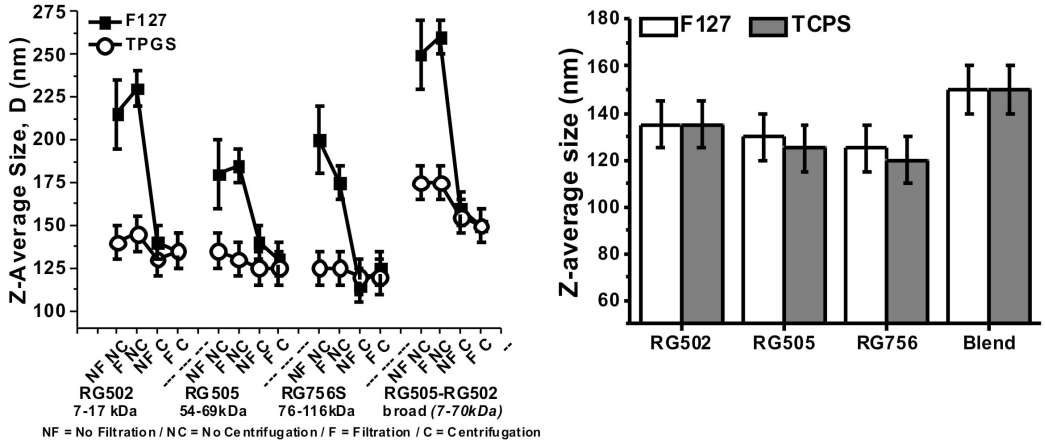

Figure 6—10. Effect of centrifugation and filtration on the size of nanoparticles prepared using 5% wt. water solutions of the two surfactants. Nanoparticles obtained with Pluronic® F127 showed a larger size than the TPGS-based ones before centrifugation (left), but not after centrifugation (right: these are the same data presented with the F C label in the left panel). We believe all nanoparticles to be similar in size, which is also similar to that of particles prepared using much smaller surfactant concentrations (0.013 to 0.417% wt., see Figure 6—3D in the main text); we ascribe this apparently size effect to two causes: 1) the higher viscosity of the medium containing a large excess of Pluronic® (dynamic viscosity of 5, 0.5, 0.1, 0.02 and 0.01 % wt. Pluronic® solutions in water = 2.3697, 1.003, 1.001, 0.8897, 0.8881 mPa s, respectively; dynamic viscosity of 0.5, 0.1, 0.02 and 0.01 % wt. TPGS solutions in water = 0.9151, 0.9047, 0.8854, 0.8838 mPa s, respectively; dynamic viscosity of water = 0.8904 mPa s. Measurements performed at 25°C using a Anton Paar AMVn automated micro viscometer), 2) a transient aggregation mediated by Pluronic® micelles. It is also noteworthy that in no case 0.22 μm filtration affected the nanoparticle size.

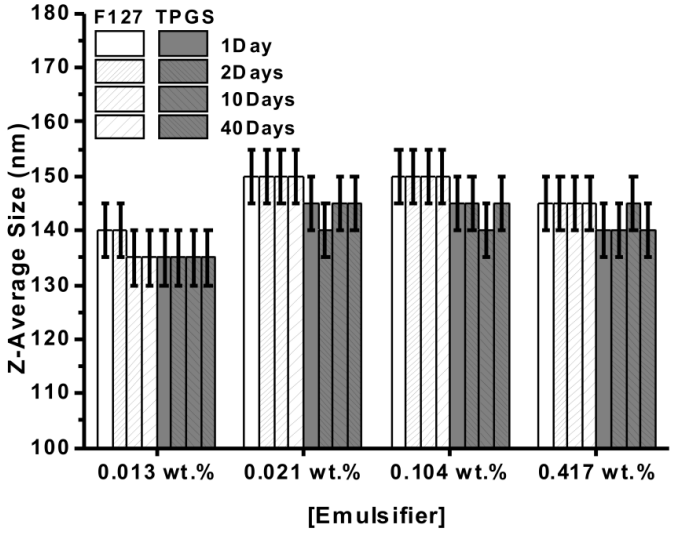

Figure 6—11. Size of RG502 nanoparticles (entry #2, #3, #4 and #6 in Table 1) recorded as a function of time in MilliQ water.

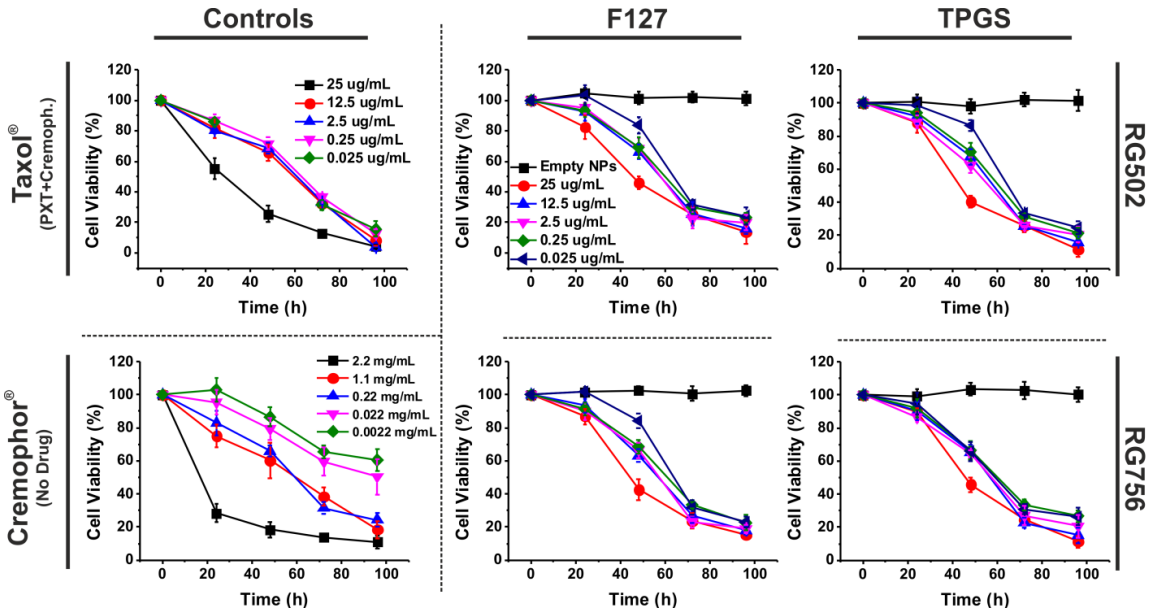

Figure 6—12. HCT-116 cells were incubated with different concentrations of PXT/Cremophor® EL (identical to Taxol®; controls column, top), its vehicle Cremophor® EL (Controls column, bottom) and PXT-loaded nanoparticles; their viability was assessed as MTS activity and normalized against the protein content at different time points (24h, 48h, 72h and 96h). Non-treated cells were used as control at each time point. (n = 3).